

Synthesis of Photoresponsive Nucleosides and Their Incorporation into
Oligonucleotides: Targeting Androgen Receptor and NF- κ B Transcription Factors

A Dissertation
SUBMITTED TO THE FACULTY OF
UNIVERSITY OF MINNESOTA
BY

Nicholas B. Struntz

IN PARTIAL FULFILLMENT OF THE REQUIREMENTS
FOR THE DEGREE OF
DOCTOR OF PHILOSOPHY

Dr. Daniel Harki

February 2016

© Nicholas B. Struntz 2016

Acknowledgements

I would like to thank first and foremost my advisor, Professor Daniel Harki. As your first graduate student, we really took a chance on each other. I have learned invaluable skills, both scientific and otherwise, from being in your laboratory, and I hope to have returned the favor as your student. I could not have asked for a better mentor.

I would also like to thank our many collaborators over the years for their contributions and helpful conversations, which allowed the science in this thesis to flourish. I would like to thank Professor Andrew Harned, Professor Reuben Harris, Dr. Beverly Ostrowski (Minnesota NMR Center), Dr. Defeng Tian (Institute for Therapeutics Discovery and Development), Professor Courtney Aldrich, the Minnesota Supercomputing Institute (MSI), the Analytical Biochemistry Core Facility of the Masonic Cancer Center, Professor Scott Dehm, and a special thanks to Professor Carston Wagner who was my co-advisor for two years during my training grant. I would also like to thank Professor Chengguo Xing and Professor Mark Distefano for being on my committee and helping me navigate through graduate school and beyond.

During my graduate studies, I had the opportunity to work with many talented students and post doctoral researchers, both in the Harki laboratory and surrounding laboratories, that were excellent sounding boards, answered many questions, and made my time here very enjoyable. I also wanted to thank the Department of Medicinal Chemistry, which really was a perfect fit for my research interests and goals. This was the place I needed to be.

I wanted to acknowledge the people that influenced my professional path in order to get me here. I wanted to thank my high school chemistry teacher James Christensen. From the first time I learned chemistry from you, I knew that chemistry was my passion. I knew it was where I needed to be. You not only gave me a foothold in chemistry, but you taught me many lessons about life that I didn't know or chose not to know as a punk teenager. I also wanted to thank my undergraduate advisor Professor Victor Nemykin. You singled me out of my general chemistry class and introduced me to the world of organic chemistry research. From that point on, I knew that I wanted to synthesize and utilize small molecules for probing cellular biology. Thank you for taking that chance on me.

Lastly, I wanted to acknowledge both the NIH Chemistry-Biology Interface Training Grant (5 T32 GM008700-12) and the American Heart Association Predoctoral Fellowship (13PRE14640004 & 15PRE22950024) for financial support for research over the years.

Dedication

I would like to dedicate this thesis to those that have made my achievements possible. To my parents, Mike Struntz, Sarah Struntz, Kim Morfitt, and Bart Morfitt, your constant love and encouragement not only allowed me to excel, but also carried me during the tough times. I am forever indebted to you for all that you've done and continue to do for me. I also wanted to thank my little sister and brother, Jessica Peightal and Austin Struntz, for being great siblings and even better friends. To my grandparents, Maxine Obitz and the late Richard Obitz, Marie Struntz and the late Lawrence Struntz, some of the best memories I have are from my childhood with you. I will always cherish the memories including woodworking with grandpa and swimming up north at the cabin. To all of my remaining friends and family, thank you for being part of my life, for you are what makes life great and enjoyable.

Finally, I would like to dedicate this to my wife, Heather. Words cannot describe how important you are to me. Your constant love and encouragement barely scratches the surface on how you have lifted me up, time and time again, and helped me succeed. You have changed me from the inside out and made me a better person. I look forward to so many new adventures with you. We have so many great things ahead of us. I am so incredibly lucky to share my life with you and I know that I will have lived a great life, as long as you're beside me. You continuously bring joy into my life and I always feel you with me in my heart. I love you so very much.

Abstract

The sequencing of the human genome suggests that transcription factors (TFs) make up one of the largest classes of human proteins, revealing that there are over 2000 genes that code for transcription factors. The pivotal roles of TFs in cell biology become quite apparent when one or more of these regulatory mechanisms becomes mutated or altered. For example, the androgen receptor (AR) transcription factor plays a pivotal role in prostate carcinogenesis and progression. Additionally, the inflammatory response of the NF- κ B transcription factor proteins results in the transcription of many genes, which play pivotal roles in carcinogenesis. There are several approaches to modulate and study transcription factor activity and biochemistry. Utilizing cis element DNA decoys to sequester TFs is one approach to directly modulate transcription factors. Introducing these synthetic double-stranded DNA decoys containing TF binding sites into cells effectively sequesters TFs and inhibits their target gene expression. Over the past couple of decades, numerous reports have validated utilizing this approach. For example, a phosphorthioate STAT3 DNA decoy has entered the “first-in-human” Phase 0 clinical trials for the treatment of head and neck squamous cancer. STAT3 expression and cell viability was reduced in the head and neck cancers injected with the decoy compared to the saline control. Combining the spatial and temporal resolution of caging technology with the DNA decoy strategy for the inhibition of transcription factor activity can yield an approach for the very precise ability to photochemically regulate gene expression, which has potential as a therapeutic agent and tool for probing biological pathways.

This thesis will focus on efforts to develop several novel DNA-based and small molecule-based probes to investigate the biochemistry of TFs and their signaling pathways. Chapter 2 discusses the synthesis and characterization of caged DNA decoys that target the Androgen Receptor (AR). Caged DNA decoys successfully captured AR in LNCaP lysate when irradiated with light. Chapter 3 introduces the complement to caging technology, which is catch and release DNA decoys (CRDDs). CRDDs capture transcription factors, by binding and sequestering them, and then a pulse of light photochemically destroys the CRDD, permitting release of the TF. Several 7-nitroindole (7-NI, **1.47**) nucleobase mimics were incorporated into NF- κ B-directed DNA decoys, which still allowed the capture of the p50-p65 NF- κ B proteins. Irradiation with 350 nm light drives the release of the p50-p65 NF- κ B. The capture and photochemical release of an endogenous transcription factor is demonstrated for the first time. Chapter 4 continues the work of Chapter 3 by developing second-generation nucleobase mimics for use in CRDDs. Addition of molecular recognition properties on a photo-responsive monomer is hypothesized to increase binding affinity to capture endogenous TFs. 8-Nitroguanosine contains this added molecular recognition, is more stable within duplex DNA, and also displayed similar photochemical depurination properties. Chapter 5 outlines work developing photoswitchable nucleobases that transpose their hybridization properties upon photolysis. Chapter 6 highlights work to determine the mechanistic NF- κ B inhibitory properties of several Cryptocaryone analogues, which were found to inhibit the NF- κ B translocation to the nucleus. Appendix A focuses on the characterization of the

enantioselectivity of guanosine monophosphate synthetase (GMPS), a crucial enzyme in nucleotide biosynthesis.

Table of Contents

Acknowledgements	i
Dedication	ii
Abstract	iii
Table of Contents	vi
List of Tables	ix
List of Figures	x
List of Schemes	xiii

Chapter 1: APPROACHES FOR MODULATING TRANSCRIPTION FACTORS CULMINATING IN PHOTOCHEMICAL SPATIOTEMPORAL CONTROL OF NF- κ B WITH CAGED DNA DECOYS

1.1.1	Transcription Factor DNA Binding Domains.....	2
1.1.2	Transcription Factor Trans-activator Domains.....	4
1.1.3	Endogenous Modulation of Transcription Factors.....	6
1.1.4	Ligand Modulation of Transcription Factors and the Androgen Receptor.....	7
1.1.5	Inhibitory Proteins and Post-translational Modulation of TFs and NF- κ B.....	9
1.1.6	Oncogenic Gene Expression and Transcription Factors.....	11
1.2.1	Indirect Transcription Factor Modulators.....	12
1.2.2	Modulation of TFs Through the Inhibition of the Surface Receptor or Extracellular Signaling Molecules.....	14
1.2.3	Modulation of TFs Through the Inhibition of Upstream Signaling Targets.....	15
1.2.4	Modulation of TFs Through the Inhibition of Nuclear Translocation.....	16
1.2.5	Modulation of TFs Through the Inhibition of Epigenetic Targets.....	16
1.3.1	Direct Transcription Factor Modulators.....	17
1.3.2	Small Molecule Transcription Factor Modulators.....	19
1.3.3	Peptide or Peptidomimetic Transcription Factor Modulators.....	21
1.3.4	Modulation of TFs Through Small Molecule DNA Binders.....	23
1.3.5	Modulation of TFs Through mRNA Regulation.....	24
1.4	DNA Decoys.....	25
1.5	Caging Technology.....	31
1.6	Caged DNA Decoys.....	39
1.7	Preface to this Thesis.....	43

Chapter 2: ANDROGEN RECEPTOR-DIRECTED CAGED DNA DECOYS

2.1	Androgen Receptor (AR) DNA Decoys.....	46
2.2	Oligonucleotide Synthesis.....	47
2.3	Thermal Melting Analysis.....	49
2.4	Kinetics of Uncaging.....	50
2.5	Capturing AR Utilizing Caged DNA Decoys.....	52
2.6	Cellular Location of DNA Decoys Utilizing Confocal Microscopy.....	54
2.7	Conclusions and Future Work.....	54
2.8	Experimental Section.....	56

Chapter 3: 7-NITROINDOLE (7-NI) CONTAINING NF- κ B-DIRECTED ‘CATCH AND RELEASE DNA DECOYS’ (CRDDs)

3.1	Catch and Release DNA Decoys (CRDDs) and the NF- κ B Signaling Pathway..	65
3.2	CRDD Design and Synthesis.....	68
3.3	Thermal Melting Analysis.....	72
3.4	Capture of NF- κ B by CRDDs.....	74
3.5	Kinetics of Depurination.....	79
3.6	Photochemical Catch and Release of NF- κ B.....	80
3.7	Conclusions and Future Work.....	82
3.8	Experimental Section.....	83

Chapter 4: THE 8-NITROGUANOSINE NUCLEOBASE FOR INCORPORATION INTO SECOND-GENERATION CATCH AND RELEASE DNA DECOYS (CRDDs)

4.1	Rationale.....	96
4.2	Nucleoside and Oligonucleotide Synthesis.....	97
4.3	Thermal Melting Analysis.....	100
4.4	Proof of Uncaging.....	103
4.5	Conclusions and Future Work.....	104
4.6	Experimental Section.....	104

Chapter 5: PHOTOSWITCHABLE NUCLEOBASES THAT TRANSPOSE HYBRIDIZATION PREFERENCES

5.1	Rationale.....	110
5.2.1	Isatin Scaffold.....	112

5.2.2	Isatin Synthesis.....	114
5.2.3	Isatin Photochemical Tautomerization.....	115
5.3	Conclusions and Future Work.....	116
5.4	Experimental Section.....	117

Chapter 6: BICYCLIC CYCLOHEXENONES AS INHIBITORS OF NF- κ B SIGNALING

6.1	Rationale.....	123
6.2	Cytotoxicity of Cryptocaryone Analogues and Inhibition of NF- κ B Gene Expression Utilizing a Reporter Assay.....	126
6.3	Thiol Reactivity of Cryptocaryone Analogues.....	130
6.4	Inhibition of NF- κ B Nuclear Translocation by Western Blot Analysis, ELISA, and RT-PCR.....	132
6.5	Conclusions and Future Work.....	135
6.6	Experimental Section.....	135

References.....	145
------------------------	------------

Appendix A: INHIBITION OF GUANOSINE MONOPHOSPHATE SYNTHETASE BY THE SUBSTRATE ENANTIOMER L-XMP

A.1	Rationale.....	194
A.2	L-XMP Synthesis.....	196
A.3	GMPS Expression and Kinetic Analysis of GMPS by HPLC and UV-Vis.....	197
A.4	Inhibition of GMPS by L-XMP.....	200
A.5	Docking Analysis of L-XMP.....	202
A.6	Anti-malarial Activity of L-XMP Analogues.....	204
A.7	Conclusions and Future Work.....	206
A.8	Experimental Section.....	207

Appendix B: SPECTRAL DATA FOR SYNTHESIZED COMPOUNDS

B.1	Chapter 2 Compounds.....	222
B.2	Chapter 3 Compounds.....	228
B.3	Chapter 4 Compounds.....	241
B.4	Chapter 5 Compounds.....	247
B.5	Appendix A Compounds.....	251

List of Tables

Table 1.1. Modulation of TFs by DNA decoys.	29
Table 2.1. Thermal melting of 2.2-2.4.	49
Table 3.1 Thermal melting of duplex DNA containing the nitroindoles.	72
Table 3.2 Thermal stability of synthesized CRDDS.	73
Table 4.1. Thermal melting of duplex DNA containing 8-NG.	100
Table 6.1. Results of NF- κ B reporter and cytotoxicity assays performed with 6.10-6.12.	130
Table A.1. Kinetic parameters of GMPS enantiomer substrates D-XMP and L-XMP.	199
Table A.2. GMPS inhibition data of known inhibitors and xanthosine analogues.	201
Table A.3. Antimalarial data of known inhibitors and xanthosine analogues.	206

List of Figures

Figure 1.1. Four superclasses of structural motifs that bind DNA.	2
Figure 1.2. Recruitment of transcriptional machinery to activate gene expression.	5
Figure 1.3. Signal induced activation of transcription factors.	6
Figure 1.4. Androgen receptor signaling pathway.	8
Figure 1.5. The canonical NF- κ B pathway.	10
Figure 1.6. Indirect transcription factor modulators.	13
Figure 1.7. Structure of conophylline.	14
Figure 1.8. Structure of imatinib.	15
Figure 1.9. Structure of SN50.	16
Figure 1.10. Structure of I-BET151.	17
Figure 1.11. Direct transcription factor modulators.	18
Figure 1.12. Structures of Tamoxifen and Enzalutamide.	19
Figure 1.13. Structures of Myc/Max antagonists.	20
Figure 1.14. Structures of C/EBP α DNA binding domain inhibitors.	21
Figure 1.15. Wild-type p53 peptide fragment and the SAH peptide inhibitor.	21
Figure 1.16. Peptide lead and peptidomimetic inhibitor of STAT3.	22
Figure 1.17. Small molecule polyamides that inhibit NF- κ B p50-p65 and AR.	23
Figure 1.18. STAT3 antisense oligonucleotide AZD9150.	24
Figure 1.19. Inhibition of gene expression by DNA decoys.	25
Figure 1.20. Hairpin and dumbbell oligonucleotide structures.	28

Figure 1.21. Common 2-NB derivatives.	34
Figure 1.22. Two-photon uncaging of an inhibitor with 800 nm light.	35
Figure 1.23. Different approaches to caging DNA/RNA.	36
Figure 1.24. Light regulated gene expression strategies.	37
Figure 1.25. Deiters' caged DNA decoy strategy.	40
Figure 1.26. Thermal stability of caged hairpin and dumbbell DNA.	40
Figure 1.27. EMSAs demonstrating light activation of NF- κ B DNA decoys.	41
Figure 1.28. Photochemical activation of NF- κ B-mediated SEAP expression.	42
Figure 2.1. Introduction of caged AR-directed DNA decoys.	47
Figure 2.2. Synthesized DNA decoys with varying degrees of NPOM caging.	48
Figure 2.3. Photolytic decay curve of 2.1 .	51
Figure 2.4. Photo-products of 2.3 .	51
Figure 2.5. Electrophoretic mobility shift assays (EMSAs) with 2.2-2.4 .	53
Figure 3.1. Catch and Release DNA Decoy strategy.	66
Figure 3.2. A Catch and Release DNA Decoy (CRDD) targeting the NF- κ B transcription factor.	68
Figure 3.3. 7-Nitroindole-containing nucleotides.	69
Figure 3.4. Synthesized decoys 3.10-3.19 .	71
Figure 3.5. EMSAs to characterize CRDD protein binding ability.	75
Figure 3.6. Electrophoretic mobility shift assays supershifting experiments.	76
Figure 3.7. Electrophoretic mobility shift assays with 3.10-3.16 .	78
Figure 3.8. Photolytic decay curve of CRDD 3.15 (350 nm light).	79
Figure 3.9. Photo-products of CRDD 3.15 (350 nm light).	80

Figure 3.10. Quantitative electrophoretic mobility shift assay with CRDD 3.15 .	81
Figure 3.11. Western blots and EMSA for irradiation controls.	81
Figure 3.12. NF- κ B reporter assay in CHO cells.	83
Figure 4.1. Synthesized oligonucleotides.	99
Figure 4.2. Hoogsteen base pairing between <i>syn</i> 8-oxo-G 4.15 and <i>anti</i> adenosine.	101
Figure 4.3. Photolysis of 4.14 .	103
Figure 5.1. X-ray crystal structure of DNA.	112
Figure 5.2. Isatin G-to-A mimic scaffold.	113
Figure 5.3. NMR photolysis experiment of the caged isatin scaffold.	115
Figure 5.4. Hypothetical thermal stability experiments of isatin scaffold.	116
Figure 6.1. Structures of cryptocaryone and analogues.	122
Figure 6.2. Initial Screening of Compounds 6.4-6.9 for NF- κ B Inhibitory Activity.	124
Figure 6.3. Cellular NF- κ B luciferase reporter assay in A549 cells.	127
Figure 6.4. Cysteamine reaction assay using compound 6.10 .	131
Figure 6.5. Western blot analysis of compound-treated cells.	132
Figure 6.6. Enhanced potency of enantioenriched 6.11* .	134
Figure A.1. HPLC analysis of L-XMP conversion to L-GMP by GMPS.	197
Figure A.2. Initial velocities versus substrate plots for D-XMP and L-XMP.	199
Figure A.3. Inhibition experiments.	200
Figure A.4. Docking of adenylated intermediates L-GMP in GMPS.	202
Figure A.5. Molecular contacts from the docking study.	203
Figure A.6. Purified GMPS.	215

List of Schemes

Scheme 1.1. Modifications to DNA to improve its serum and intracellular stability.	27
Scheme 1.2. Caging technology utilized for spatiotemporal resolution of ATP.	31
Scheme 1.3. Mechanism of photolytic release of 2-NB 32 .	33
Scheme 2.1. Photolytic decay mechanism of NPOM caging group.	52
Scheme 2.2. Synthesis of TR-labeled AR-directed DNA.	54
Scheme 3.1. Synthesis of 7-nitroindole-containing phosphoramidite 3.9 .	70
Scheme 4.1. Second-generation 8-nitroguanosine (8-NG) depurination probe for use in CRDDs.	97
Scheme 4.2. Synthesis of 8-nitroguanosine.	97
Scheme 4.3. Synthesis of 2'- α -fluoro-8-nitro-2'-deoxyguanosine phosphoramidite.	98
Scheme 5.1. Example of chemical modifications to increase the frequency of nucleobase tautomers.	110
Scheme 5.2. Synthesis of the benzyl protected caged isatin imine 5.18 .	114
Scheme A.1. Enzymatic reaction catalyzed by GMPS.	194
Scheme A.2. Synthesis of L-XMP A.10 .	196
Scheme A.3. Synthesis of L-XMP prodrug A.15 .	205

Chapter 1

APPROACHES FOR MODULATING TRANSCRIPTION FACTORS CULMINATING IN PHOTOCHEMICAL SPATIOTEMPORAL CONTROL OF NF- κ B WITH CAGED DNA DECOYS

The figures of Section 1.6 are reprinted (adapted) with permission from Govan, J. M.; Lively, M. O.; Deiters, A. Photochemical Control of DNA Decoy Enables Precise Regulation of Nuclear Factor κ B activity. *J Am Chem Soc* **2011**, 133, 13176-82. Copyright 2011 American Chemical Society.

1.1.1 Transcription Factor DNA Binding Domains

The sequencing of the human genome suggests that transcription factors make up one of the largest classes of human proteins, revealing that there are over 2000 genes that code for transcription factors.¹ Transcription factors have several distinct families of three-dimensional structural motifs that recognize and bind DNA, which can be divided into four superclasses (**Figure 1.1**).^{2,3} Superclass 1 DNA binding domains contain three basic, but distinct motifs, centralizing around a pair of dimerized α -helices forming sequence-specific interactions with the major groove of DNA. One major class of these is the basic leucine zipper (bZIP) motifs characteristic in TFs such as Activator Protein 1 and cAMP Response Element-binding Protein (CREB, PDB: 1DH3, **1.1**).⁴ Another is the basic helix-loop-helix (bHLH) motif characteristic in TFs such as MyoD, aryl hydrocarbon receptor nuclear translocator (ARNT), and hypoxia-inducible factor 1 α (HIF1 α , PDB: 4ZPR, **1.2**).⁵ The last major motif in superclass 1 is the helix-loop-helix-leucine zipper (bHLH-ZIP) including the E2F, Mad, and c-Myc-Max TFs (PDB: 1NKP, **1.3**).⁶ Superclass 2 comprises of zinc-coordinating DNA binding domains that are often folded into compact structures known as zinc fingers. Zinc fingers are made up of different α -helices and β -sheets whereby zinc is required to stabilize the protein folds creating a finger-like structure that interacts with the major groove of DNA. Nuclear receptors (estrogen receptor, androgen receptor PDB: 1R4I, **1.4**, etc.)⁷ are a major class of transcription factors that bind DNA via zinc fingers. Superclass 3 motifs are series of β -sheets that are able to interact with the major groove of DNA. This superclass is made up

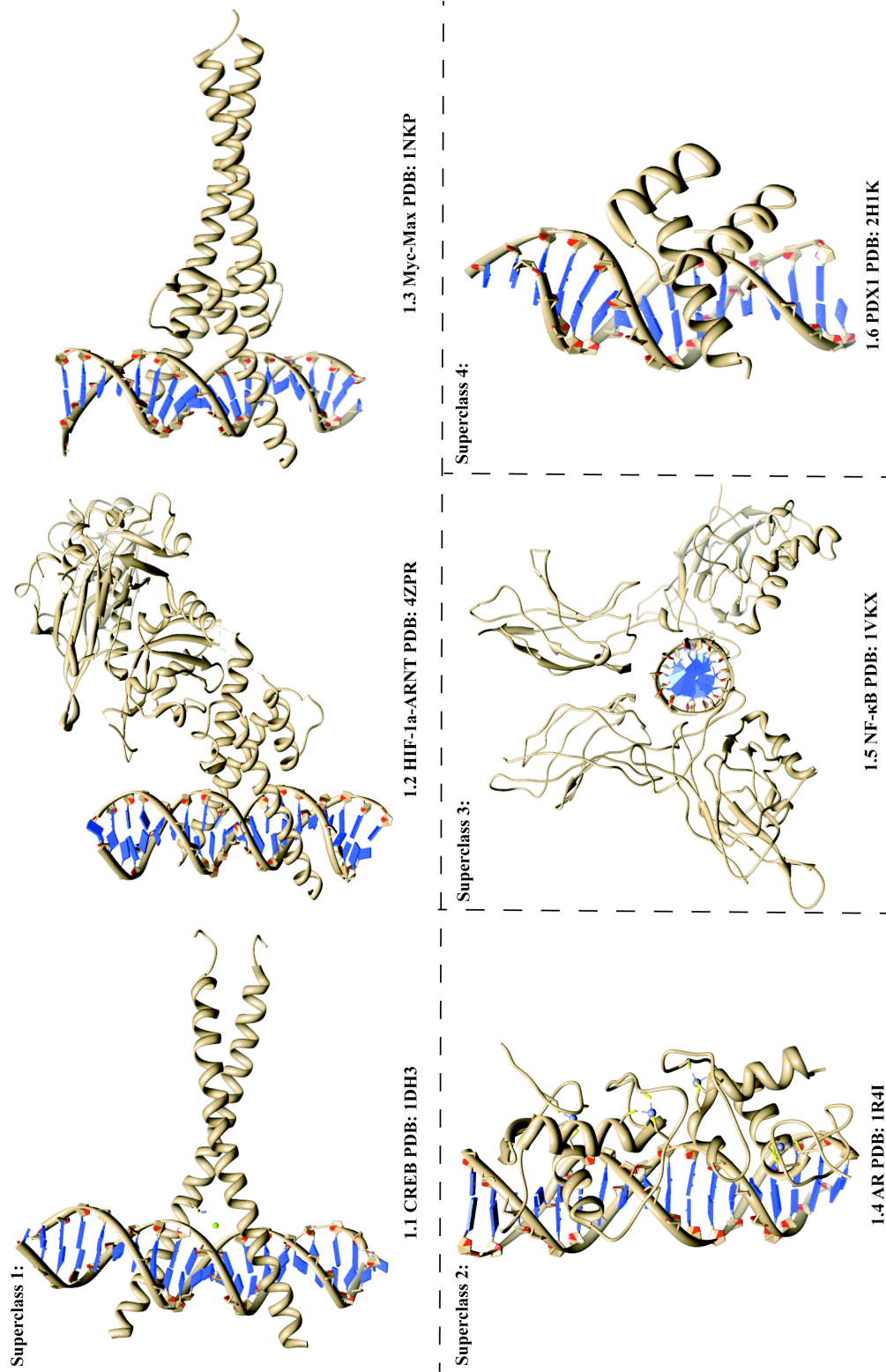


Figure 1.1. Four superclasses of structural motifs that bind DNA. Superclass 1 contains motifs centered around dimerized α -helices that interact with the major groove of DNA. Superclass 2 comprises zinc-coordinating DNA binding domains. Superclass 3 motifs interact with the major groove of DNA. Superclass 4 includes the helix-turn-helix motifs where the second “recognition” helix interacts with the major groove.

of 11 classes of TFs including Nuclear Factors of Activated T cells (NF-ATs), Signal Transducer and Activator of Transcription 3 (STAT-3), and Nuclear Factor- κ of Activated B cells (NF- κ B). The NF- κ B protein largely exists as a p50-p65 heterodimer (PDB: 1VKX, **1.5**).⁸ Superclass 4 motifs consist of helix-turn-helix folds, where the majority of the recognition and binding to DNA is accomplished by the second α -helix, known as the recognition helix.⁹ Nearly 800 homeodomain-containing sequences have been identified including 116 that are implicated in disease.¹⁰ For example, many mutations in pancreatic and duodenal homeobox 1 (PDX1, PDB: 2H1K, **1.6**)¹¹ have been linked to type II diabetes.¹²

Each superclass often has a conserved primary sequence conferring similar DNA binding sites to which each protein binds. Amino acid differences in the sequence give rise to specificity among each family.¹³ In some instances, a single amino acid change can dictate specificity. For example, substitution of residue 9 on the recognition α -helix in the Bicoid Activator Protein no longer activated Bicoid targets, suggesting that residue 9 is crucial for the specific binding of Bicoid Activator Protein to DNA.¹⁴ These residues can act either directly on the DNA or by influencing the interactions of other residues with DNA. Specific DNA recognition can be achieved through these multiple mechanisms.

1.1.2 Transcription Factor Trans-activator Domains

The domains of TFs involved protein-protein interactions with transcriptional machinery, identified as trans-activator domains, stimulate transcription after binding to a specific sequence of DNA. These activation domains function by interacting with RNA polymerase II (Pol II), various other basal transcription factors such as TFIIB and TFIID, and other proteins essential for transcription by recruiting them to the promoter for activation of gene expression (**Figure 1.2**). This recruitment drives the rate of transcription; thereby increasing the overall transcriptional activity after DNA binding in a very controlled manner, which ultimately determines the spatial and temporal expression of genes for development, homeostasis, and response to external stimuli.^{3,15,16} Activation domains can either interact directly with these proteins or indirectly with co-activator proteins, which then interact with the transcriptional machinery. For example, the Elk1 transcription factor binds to a Sur2 subunit of a co-factor called mediator, which is then able to recruit Pol II and basal transcription factors

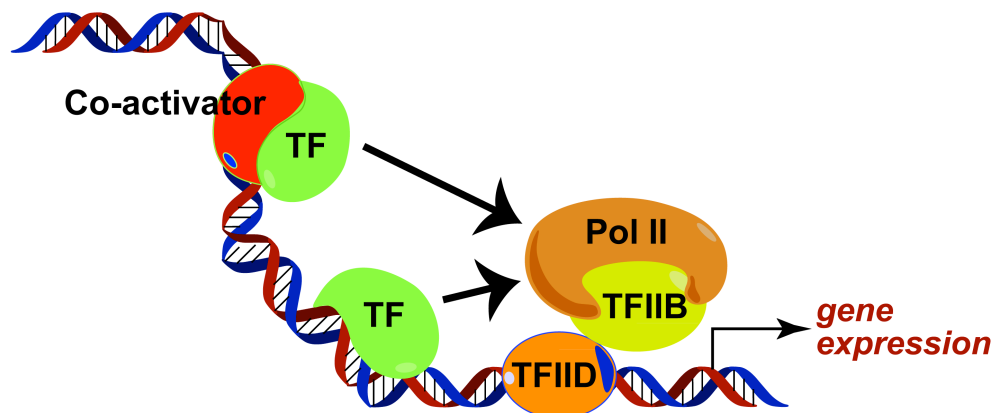


Figure 1.2. Recruitment of transcriptional machinery to activate gene expression. Gene-specific TFs can recruit basal TFs (such as TFIIB and TFIID) and RNA polymerase II (Pol II) either directly or indirectly with co-activator proteins.

TFIIB, TFIIE, TFIIIF, and TFIIH to Gal4 DNA binding sites, resulting in activation of transcription in murine embryonic stem cells.¹⁷

1.1.3 Endogenous Modulation of Transcription Factors

Endogenous modulation of TFs and their gene expression is a main component that dictates which genes are being transcribed in every cellular context and

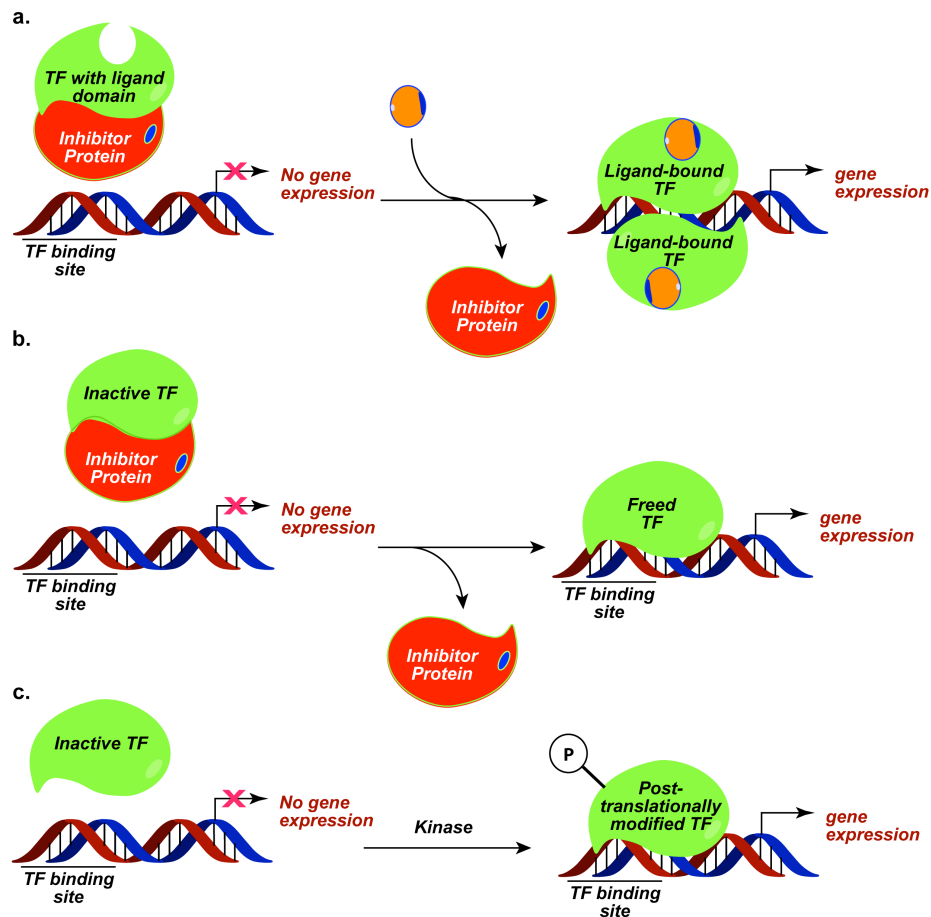


Figure 1.3. Signal induced activation of transcription factors. (a) Nuclear hormone receptor binding the hormone ligand induces dissociation of inhibitor and allows the TF to bind DNA to activate gene expression. (b) TFs bound to an inhibitory protein are rendered inactive until either the TF or the inhibitory protein are signaled to be degraded or conformationally changed, releasing the TF to activate gene expression. (c) Post-translational modifications to the TF induce conformational change allowing the TF to bind DNA.

in response to diverse stimuli.¹⁸ Endogenous regulation of TFs can occur through the control of transcription and synthesis of the TF, epigenetic control through chromatin remodeling, and through multiple mechanisms of post-translational activation including phosphorylation, other co-activators, and even other TFs. In many cases, the TF is regulated by synthesis depending on the cell or tissue type. For example, the MyoD transcription factor is only synthesized in skeletal muscle cells. When MyoD was overexpressed in undifferentiated fibroblast cells, the cells differentiated into skeletal muscle cells showing MyoD's role in the induction of skeletal muscle specific gene expression.^{19,20} Additionally, histone and chromatin modulation is a way to administer transcriptional control, which includes histone acetyltransferases and histone deacetylases.²¹

A considerable extent of TF modulation occurs through signal-induced activation for a rapid and amplified response to a stimulus. This occurs through several different mechanisms including ligand binding, degradation or changes of the inhibitory proteins, post-translational modifications including phosphorylation of the transcription factor and dimerizations with other TFs, or combinations of the three (**Figure 1.3**).

1.1.4 Ligand Modulation of Transcription Factors and the Androgen Receptor

Nuclear hormone receptors (androgen, glucocorticoid, retinoid, and prostaglandin receptors) are a superfamily of transcription factors that are modulated by small lipophilic hormones. As their name implies, the hormone receptors reside in the

nucleus and heat shock proteins bind many members of this class, rendering them inactive state. Binding of the hormone ligand results in a conformational change in the receptor, causing dissociation of heat shock protein in many cases, allowing the transcription factor to bind DNA as a homodimer, thus activating gene expression (Figure 1.3a).^{22,23}

The androgen receptor (AR) transcription factor plays a pivotal role in the development and function of the prostate. Prostate carcinogenesis and progression is distinctively contingent on AR signaling (Figure 1.4).²⁴ Androgens including testosterone are synthesized in the body and distributed through the blood stream (Figure

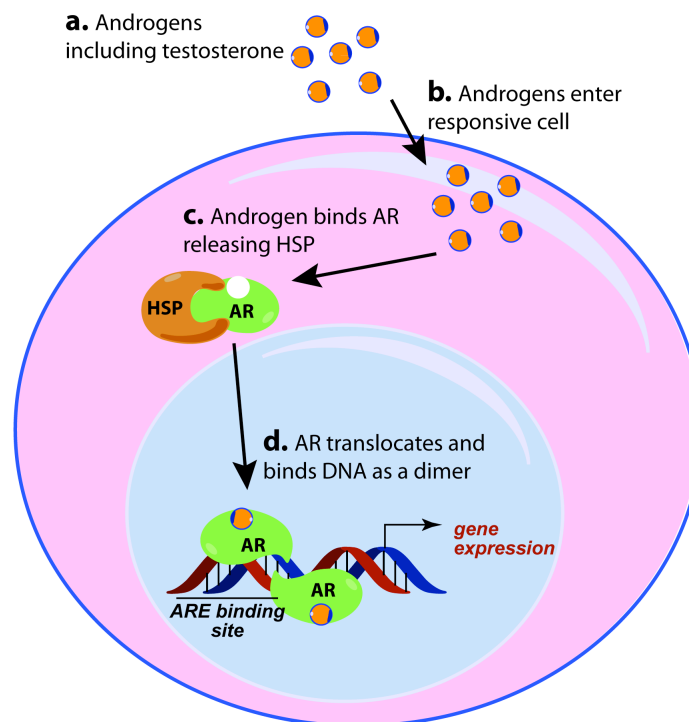


Figure 1.4. Androgen receptor signaling pathway. (a) Androgens including testosterone are synthesized in the body and distributed through the blood stream. (b) Androgens diffuse into androgen responsive cells. (c) Heat shock protein (HSP) inhibits AR activation. Upon binding testosterone or other androgens, HSP dissociates from AR. (d) Free AR is allowed to translocate to the nucleus and bind the ARE sequence as a homodimer to activate gene expression.

1.4a). Androgens diffuse into androgen responsive cells (**Figure 1.4b**). Heat shock protein (HSP) inhibits AR activation. Upon binding testosterone or other androgens, HSP dissociates from AR (**Figure 1.4c**). Free AR is allowed to translocate to the nucleus and bind the Androgen Response Element (ARE) sequence as a homodimer to activate gene expression (**Figure 1.4d**).

1.1.5 Inhibitory Proteins and Post-translational Modulation of TFs and NF-κB

Another level of control that is imposed endogenously on several transcription factors (NF-κB, HIF-1, E2F, MDM4) is their binding to an inhibitory protein either in the cytosol or in the nucleus. These transcription factors are in an inactive state until conformational change in the transcription factor itself, degradation of the inhibitory protein, or conformation change of the inhibitory protein, often due to phosphorylation, disrupts the protein-protein interactions of the transcription factor and inhibitor protein, thus freeing the transcription factor to translocate into the nucleus or dimerize, if needed, bind DNA, and activate gene expression (**Figure 1.3b**).²⁵

The other major regulatory pathway of transcription factors is post-translational modifications. This can be seen with the Signal Transducer and Activator of Transcription 3 (STAT3) transcription factors. Upon exposure to interleukin-6, STAT3 is phosphorylated on a tyrosine residue by the JAK family of kinases. This allows the STAT3 transcription factor to dimerize, translocate into the nucleus, bind to DNA, and activate gene expression (**Figure 1.3c**).²⁶

A combination of both inhibitory proteins and post-translational modifications modulate NF- κ B activity. Since their discovery by Sen and Baltimore in 1986,²⁷ the NF- κ B family of transcription factors have been linked to myriad cellular processes such as proliferation, differentiation, and immune responses to pathogens.^{25,28,29} In the canonical pathway of NF- κ B signaling (**Figure 1.5**), a p50-p65 NF- κ B heterodimer is sequestered in the cytoplasm by the protein I κ B α . Following extracellular stress signals or pathogens, the activated IKK α /IKK β /NEMO complex (IKK) phosphorylates I κ B α , which induces

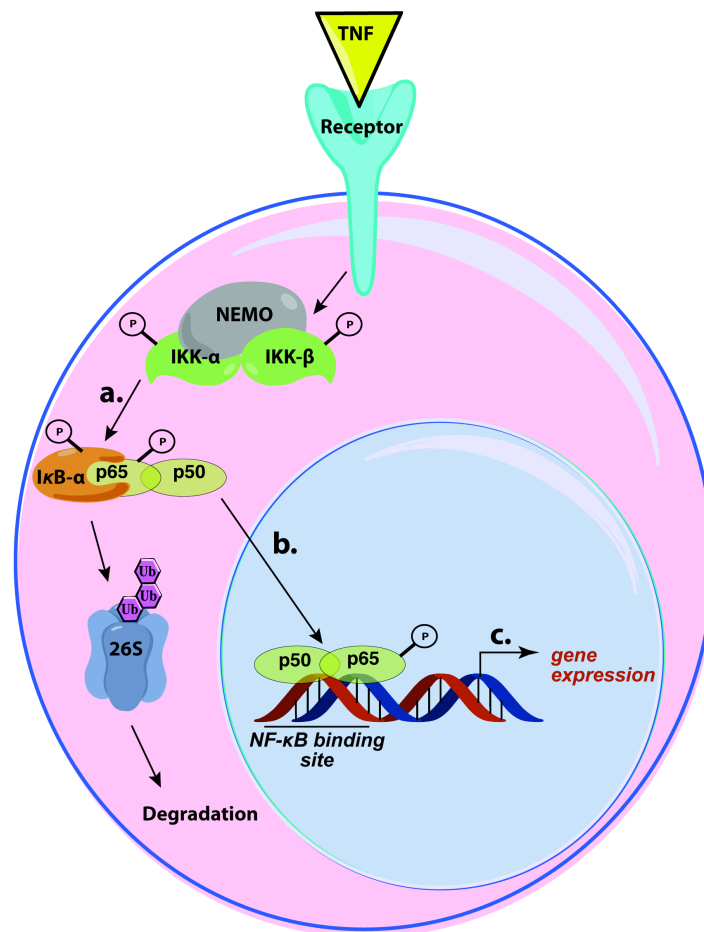


Figure 1.5. The canonical NF- κ B pathway. Small molecule stimuli such as TNF bind to their receptor, which leads to the activation of the IKK complex. (a) The IKK complex phosphorylates I κ B α , which then gets polyubiquitinated and sent to the 26S proteasome for degradation. p65 is further activated by phosphorylation. (b-c) The freed NF- κ B heterodimer translocates to the nucleus to activate gene expression.

ubiquitination and subsequent degradation of I κ B α by the 26S proteasome.^{25,30,31} Protein Kinase A then phosphorylates the p65 subunit, which additionally activates NF- κ B by promoting transcriptional co-activators (**Figure 1.5a**). An exposed nuclear localization sequence on p65 resulted from I κ B α degradation, which alters the cellular p50-p65 equilibrium from exclusively cytosolic to nuclear (**Figure 1.5b**).³² In the nucleus the p50-p65 heterodimer can activate the expression of genes with NF- κ B binding sites in their promoters, including genes coding for inflammatory response such as adhesion molecules, chemokines, MMP, and cytokines (**Figure 1.5c**).^{25,30,31,33-35}

1.1.6 Oncogenic Gene Expression and Transcription Factors

The pivotal roles of TFs in cell biology become quite apparent when one or more of these regulatory mechanisms becomes mutated or altered.³⁶ The aberrant change in gene expression patterns result in the emergence of clinical manifestations including developmental disorders, immune disorders, metabolic disorders, as well as carcinogenesis.^{3,37} Oncogenetics, the study of understanding the genes associated with the susceptibility of malignancies, has uncovered that about one-third of the identified cellular oncogenes code for DNA-binding proteins that act as gene-specific TFs.³⁸⁻⁴¹

For example, AR was found to promote site-specific double stranded DNA breaks, which induces nonrandom translocations driving prostate carcinogenesis in some cases.^{42,43} Prostate cancer has become one of largest causes of cancer-related mortality of men in the western world, with nearly 220,000 new cases estimated annually.⁴⁴ Many

patients progress to a castration-resistant (CRPC) stage where current primary therapies are inadequate, due to mutations, often in the ligand-binding domain of AR, leading to constitutive hyperactivation.⁴⁵ Inhibition of AR in CRPC, preventing its function to activate cancer-related genes, results in cellular arrest and subsequent death.⁴⁶

Additionally, the NF- κ B proteins are referred to as “the master regulators at the center of inflammation” and their inflammatory response results in the transcription of many genes, which play pivotal roles in carcinogenesis.³⁰ NF- κ B has been found to control genes for tumor proliferation, angiogenesis, invasion, metastasis, chemoresistance, and radioresistance.⁴⁷ NF- κ B is constitutively active in most tumor cells and its inhibition results in stopping of cancer growth leading to tumor reduction.⁴⁸

1.2.1 Indirect Transcription Factor Modulators

There are several approaches to modulate and study transcription factor activity and biochemistry. Transcription factors can be targeted either indirectly or directly. Several methods have been developed to inhibit TFs indirectly (**Figure 1.6**). Induction of signaling pathways that affect TF activity can be modulated by inhibiting the extracellular signaling molecules or their cell surface protein receptors, thereby, controlling downstream cellular gene expression (**Figure 1.6a**). Since transcription factors are focal points for intracellular signaling, one common method of modulation is to inhibit an upstream target in the signaling pathway, thus indirectly impeding TF

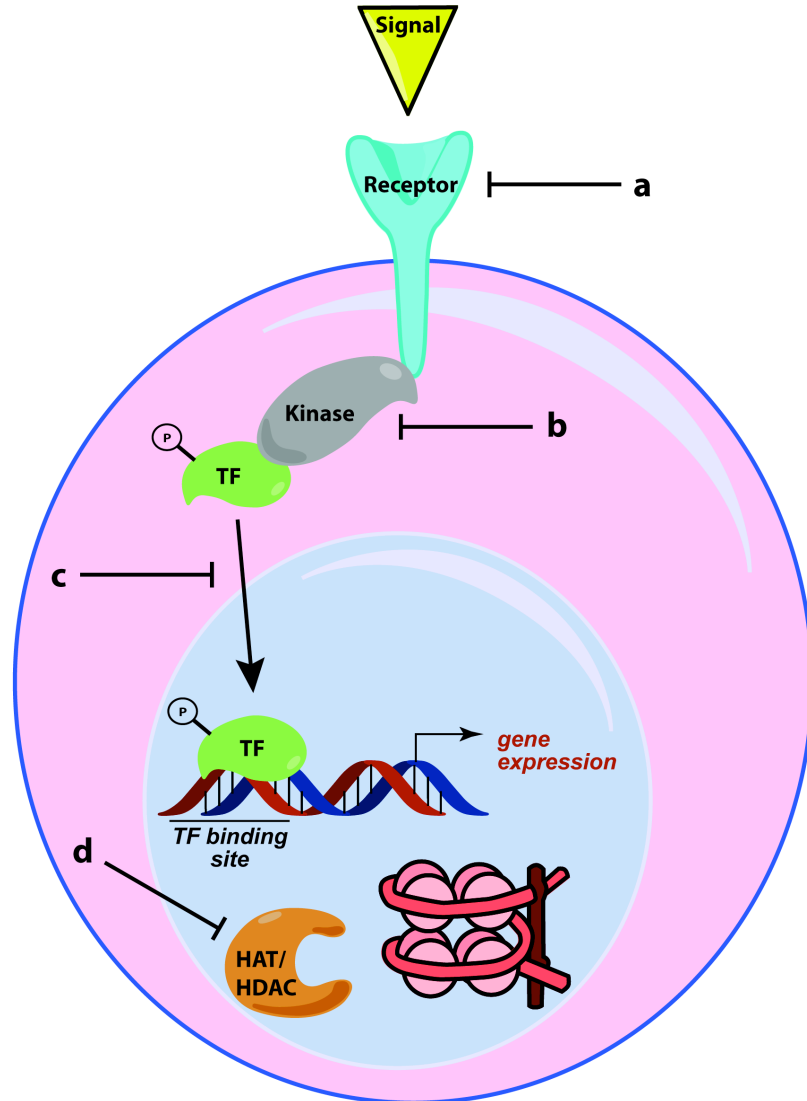


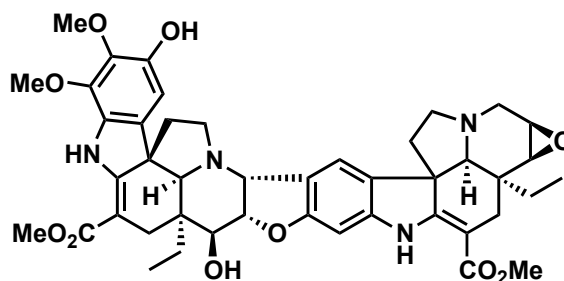
Figure 1.6. Indirect transcription factor modulators. (a) Modulation of extracellular signaling molecules or surface receptors. (b) Inhibition of upstream targets including kinases. (c) Inhibition of nuclear translocation. (d) Inhibition of epigenetic targets including HATs and HDACs.

activity (**Figure 1.6b**). Additionally, activation of several signaling pathways result in post-translational modification to the TF, allowing TF translocation from the cytosol to the nucleus via nuclear location signals, thus resulting in activation of gene expression. Inhibiting this translocation to the nucleus is another method to reduce transcription

factor activity (**Figure 1.6c**).⁴⁹ Lastly, targeting epigenetic regulation, such as controlling histone modifications, has been shown to inhibit the activity of several transcription factors indirectly (**Figure 1.6d**).⁵⁰

1.2.2 Modulation of TFs Through the Inhibition of the Surface Receptor or Extracellular Signaling Molecules

Many cell surface receptors can be inhibited or down regulated to prevent the activation of downstream signaling pathways that eventually activate gene-specific TFs (**Figure 1.6a**). A small molecule screen for TNF- α inhibitors uncovered the molecule conophylline **1.7**, which prevented NF- κ B activation, including its phosphorylation and the degradation of I κ B α by significantly reducing the expression of TNF- α surface receptors (**Figure 1.7**).⁵¹ Another way this can be accomplished is by interfering with the ability of the extracellular signaling molecules to bind and activate the receptor. Several anti-TNF- α antibodies including infliximab (REMICADE) and etanercept (Enbrel) have made it into clinical trials and are FDA approved for the treatments of rheumatoid



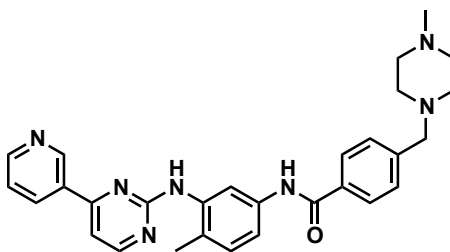
1.7

Figure 1.7. Structure of conophylline.

arthritis and psoriasis by inhibiting the NF- κ B inflammatory response.⁵²

1.2.3 Modulation of TFs Through the Inhibition of Upstream Signaling Targets

Kinases and other upstream signaling proteins are frequently targeted for therapeutic modulation of TF activity and have been very successful in clinical applications to treat aberrantly active oncogenic gene expression (**Figure 1.6b**). One of the more famous examples is the small molecule imatinib **1.8**, which is marketed by Novartis as Gleevec (**Figure 1.8**). Imatinib targets the tyrosine-kinase BCR-Abl, which is aberrantly activated in multiple cancers including Philadelphia chromosome-positive and chronic myelogenous leukemia (CML).⁵³ Hyperactivation of this upstream kinase results in the activation of several downstream TFs including NF- κ B, STAT3, and CCAAT/enhancer-binding protein- α (C/EBP α).⁵⁴⁻⁵⁶ This inhibition of BCR-Abl results in tumor suppression, leading to a five-year survival rate of 80% of chronic myeloid leukemia (CML) patients.⁵⁷

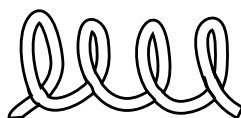


1.8

Figure 1.8. Structure of imatinib.

1.2.4 Modulation of TFs Through the Inhibition of Nuclear Translocation

Controlling the sub-cellular localization of TFs is a strategy for specific signaling pathway inhibition (**Figure 1.6c**).⁴⁹ For example, sequestration of the NF- κ B proteins in the cytosol prevents activation of NF- κ B-directed gene expression. This can be accomplished through the inhibition of nuclear import proteins with peptide mimics of nuclear location sequences (NLSs). NLSs are short peptides on proteins that mediate the nuclear import of proteins by binding to their receptors on the nuclear envelope. The NF- κ B NLS peptide SN50 (**1.9**) competitively inhibited NF- κ B activation at a concentration of 100 μ g/mL in mice, which significantly reduced the nuclear induction of NF- κ B, demonstrating that the sequestration of NF- κ B in the cytosol is a valid strategy for TF modulation. (**Figure 1.9**).⁵⁸



SN50 H-AAVALLPAVLLALLAPVGRKRQKLMP-OH

1.9

Figure 1.9. Structure of SN50.

1.2.5 Modulation of TFs Through the Inhibition of Epigenetic Targets

Targeting epigenetic regulation is a strategy to inhibit the activity of several transcription factors indirectly (**Figure 1.6d**). One example is the small molecule I-

BET151 **1.10**, a bromodomain inhibitor, which prevents the recognition of epigenetic modifications, and resulted in irreversibly suppressing development of type-1 diabetes in NOD mice (**Figure 1.10**). The inhibition of the BET subfamily of bromodomains with I-BET151 suppressed NF- κ B-directed pro-inflammatory gene expression by inhibiting TNF- α induced pathway activation.⁵⁹

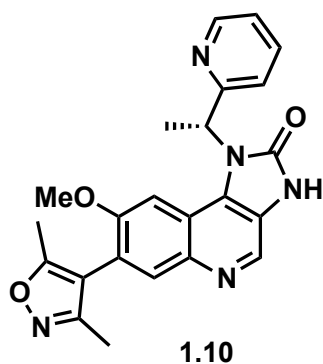


Figure 1.10. Structure of I-BET151.

1.3.1 Direct Transcription Factor Modulators

Transcription factor activity can be modulated by indirect methods; however, they are largely non-specific. Cellular signaling cascades are complex and often involve cross talk between pathways. The result of indirect inhibition, then, affects several transcription factors.⁶⁰ Since many transcription factors are both oncogenic themselves and are the focal points for aberrant gene expression that confers many of the hallmarks of cancer progression, the selective inhibition of TFs serve as the most direct targets for therapeutic development.^{38,61,62} In this way, even several upstream oncogene mutations would be neutralized with the right transcription factor inhibitor. There are numerous

examples demonstrating that inhibition of TFs preferentially causes cancer cell death versus normal cells because of the redundancies in normal signaling pathways, thus making them excellent therapeutic targets.⁶³

Approaches to modulating TFs directly include the use of small molecules and peptides that block protein-protein interactions preventing dimerization of crucial TFs, translocation to the nucleus, or binding to the DNA (**Figure 1.11b**).⁶⁴ There are also modulators targeting specific sequences of DNA to block TF binding (**Figure 1.11c**), methods involved in mRNA regulation (**Figure 1.11d**), and cis element DNA decoys to sequester TFs preventing gene activation (**Figure 1.11e**).

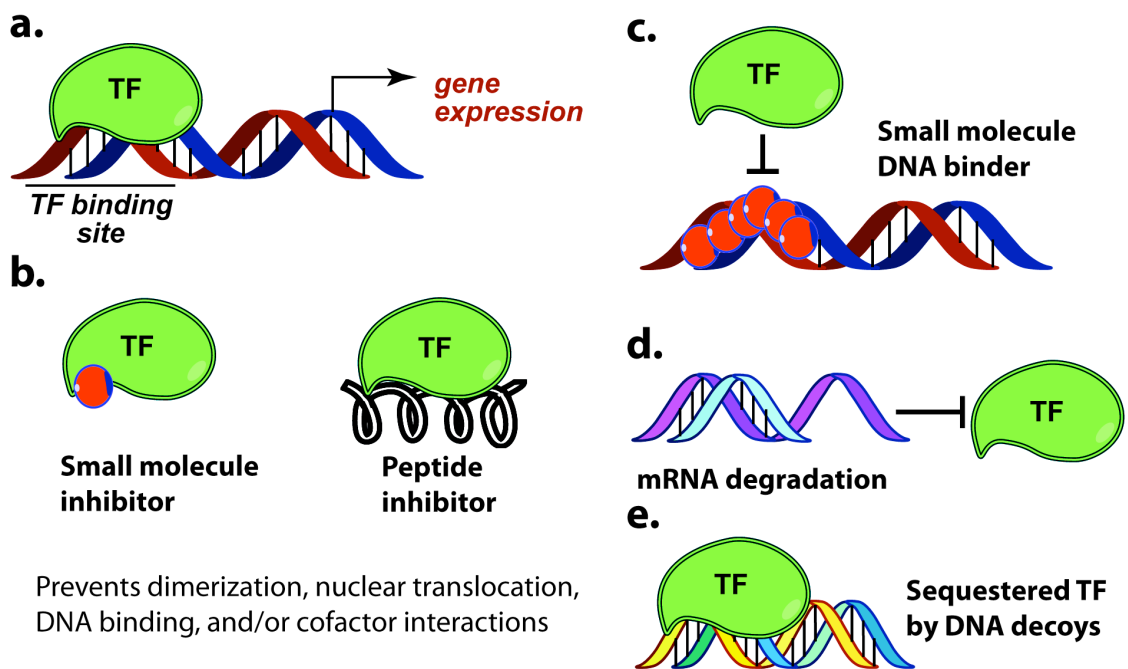


Figure 1.11. Direct transcription factor modulators. (a) Normal TF function. (b) Inhibition of key interactions including dimerization and DNA binding by small molecules or peptides. (c) Small molecule DNA binders blocking TF attachment. (d) mRNA degradation preventing TF synthesis. (e) Cis element DNA decoy sequestering TFs from activating gene expression.

1.3.2 Small Molecule Transcription Factor Modulators

Historically, small molecules have been widely used to directly inhibit therapeutic targets including receptors and kinases that contain binding pockets (**Figure 1.11b**). Since nuclear hormone receptor transcription factors contain a ligand-binding domain, small molecule modulators have been used clinically as agonists, antagonists, and inverse agonists. The estrogen receptor (ER), which is the determining TF driving 75% of breast cancers, can be inhibited with clinical efficacy.⁶⁵ Tamoxifen (**1.11**), an ER antagonist, was introduced into the clinic in the 1980s to treat ER positive breast cancer patients and is one of the most successful targeted therapies, increasing patient's survival rate (**Figure 1.12**).⁶⁶ Similarly to the ER, the androgen receptor (AR), as described above, drives the progression of prostate cancer.⁶⁷ Many therapies have been designed to take advantage of this dependence.⁶⁸ Enzalutamide (**1.12**), which was FDA approved in 2012, increased the overall survival rate of patients by exhibiting multiple mechanisms of action (**Figure 1.12**). Enzalutamide binds to the ligand-binding domain of AR, preventing its activation by testosterone, translocation to the nucleus, and transcriptional activity.⁶⁹

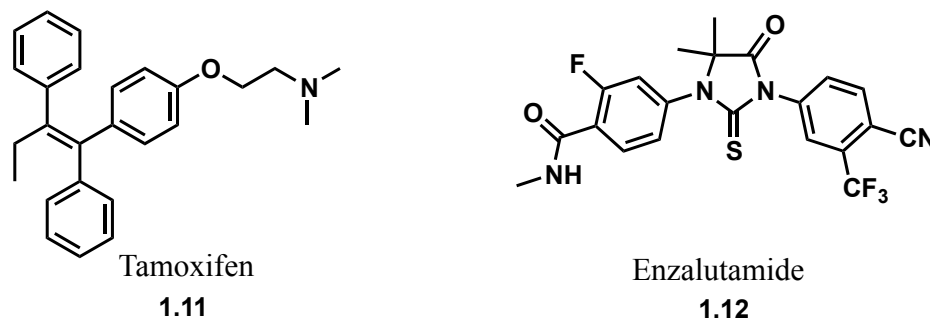


Figure 1.12. Structures of Tamoxifen and Enzalutamide.

With the exception of nuclear hormone receptors, there are relatively few examples of small molecule inhibitors of transcription factors because most transcription factors lack a ligand-binding domain. Thus, direct modulation of such proteins has been difficult due to the fact that they are composed of large, shallow, surfaces, and have even been referred to as ‘undruggable’.^{38,70} Advances in the understanding of the energetics of molecular recognition, both high-throughput and *in silico* screening technologies, and organic synthesis have permitted the ability to inhibit such protein-DNA and protein-protein interactions that have been previously referred to as undruggable.⁷¹⁻⁷⁸ The Koehler lab has developed an unbiased small molecule microarray as a common approach to discover ligand-protein interactions of several types of proteins including TFs.^{79,80} These advancements have paved the way for an exponentially expanding quantity of inhibitors and therapeutic agents. For example, Vogt and co-workers discovered several small molecule antagonists of the Myc/Max protein-protein interaction, which interfered with Myc induced oncogenic transformation (**Figure 1.13**).⁸¹

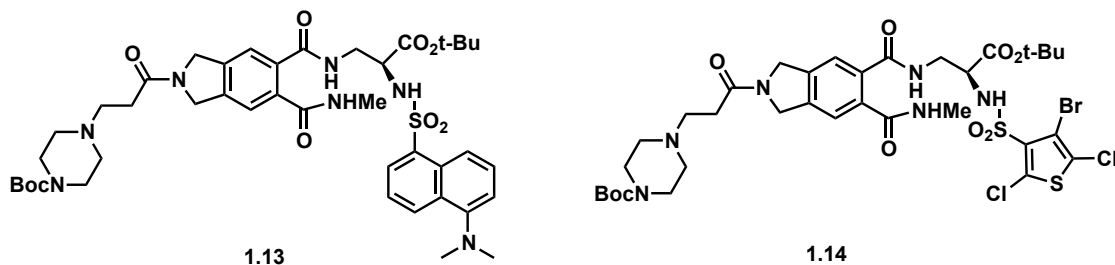


Figure 1.13. Structures of Myc/Max antagonists.

A small molecule inhibitor could also bind to DNA binding domains of TFs and prevent them from binding their target sequences. This strategy has been used to

develop inhibitors of the transcription factor $C/EBP\alpha$. A fluorescent polarization screen was used to identify 39 small molecule inhibitors of the $C/EBP\alpha$ DNA binding domain (Figure 1.14).⁸²

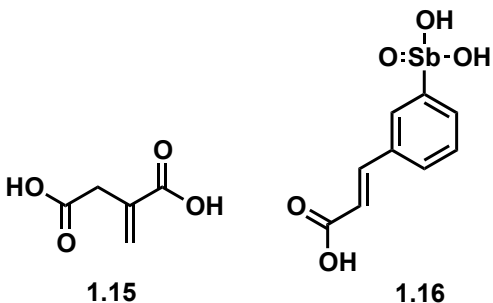
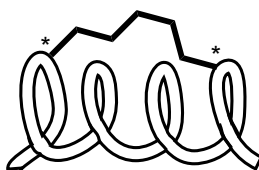


Figure 1.14. Structures of $C/EBP\alpha$ DNA binding domain inhibitors.

1.3.3 Peptide or Peptidomimetic Transcription Factor Modulators

An alternative approach to small molecules blocking protein-protein interactions is through peptide or peptidomimetic inhibitors (Figure 1.11b). This approach has been successful with the *in vivo* targeting of the NOTCH transcriptional



WT p53₁₄₋₂₉ Ac-LSQETFSDLWKLLPEN-NH₂

1.17

WT p53₁₄₋₂₉ Ac-QSQQTF*NDLWRLL*PQN-NH₂

1.18

Figure 1.15. Wild-type p53 peptide fragment and the locked SAH peptide inhibitor. * denotes point of linker attachment to lock the peptide in an alpha helical conformation.

complex in xenograft models, inhibiting the progression of leukemia.⁸³ This strategy has also been utilized in the most well studied TF complex of p53-MDM2. The tumor suppressor p53 upregulates genes responsible for DNA repair, cell-cycle arrest, and apoptosis, which is why p53 mutations are associated with a number of cancers.⁸⁴ The p53 protein is regulated by MDM2, which binds to p53 and blocks its ability to upregulate transcription.^{85,86} A locked, stabilized alpha helix (SAH) peptide inhibitor of MDM2 **1.18**, which mimics the wild-type p53 alpha helix **1.17**, has just moved into phase I clinical trials for patients with advanced malignancies expressing wild-type p53 (**Figure 1.15**).⁸⁶

Limitations to the peptide approach include lack of cell permeability and poor stability due to proteolytic degradation. One way to overcome these limitations is by utilizing peptidomimetics. Peptidomimetic inhibitors combine the advantages of peptides (high efficacy and target selectivity) and small molecules (cell permeable, stable, and bioavailability).⁸⁷ Peptidomimetics function by arranging their three-dimensional conformation in the shallow binding pockets to inhibit protein-protein interactions.⁸⁸ There are a number of peptidomimetic compounds in preclinical and clinical trials. Signal transducer and activator of transcription 3 (STAT3) is an oncogenic TF constitutively

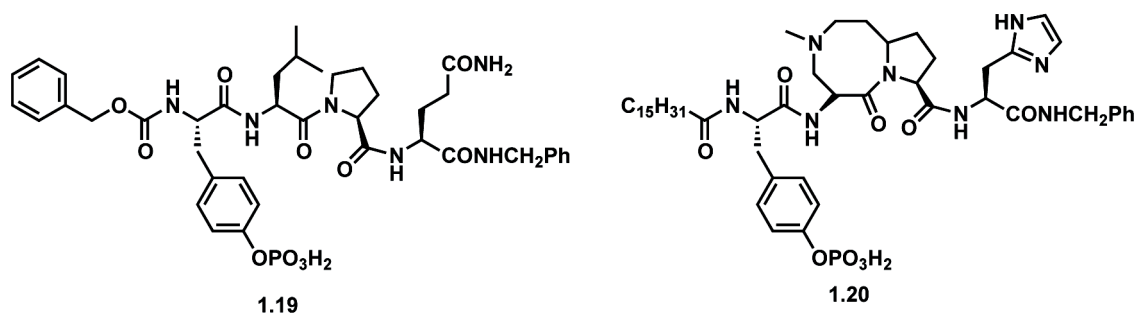


Figure 1.16. Peptide lead and peptidomimetic inhibitor of STAT3.

active in many breast cancers.⁸⁹ Several peptidomimetic compounds have been identified that inhibit STAT3 and cell proliferation (**Figure 1.16**).⁹⁰

1.3.4 Modulation of TFs Through Small Molecule DNA Binders

Another method to directly modulate TF activity is to block it from binding its target sequence by manipulating the DNA structure, thus preventing target gene expression (**Figure 1.11c**). DNA binding pyrrole-imidazole (Py-Im) polyamides have become a great strategy and class of gene modulators. Py-Im polyamides are small molecule minor groove binders that achieve sequence-specific recognition of DNA through hydrogen bonds to DNA. This strategy has been used to rationally design small molecules to inhibit the binding NF- κ B p50-p65 (**1.21**) and the AR (**1.22**) to DNA (**Figure 1.17**).⁹¹⁻⁹³ In addition, because G-quadruplexes are secondary DNA structures formed by guanine-rich sequences and are over-represented in telomeres and transcriptional start sites, small molecules have been used to stabilize G-quadruplexes to inhibit the binding of TFs, such as c-Myc, to DNA.^{94 95}

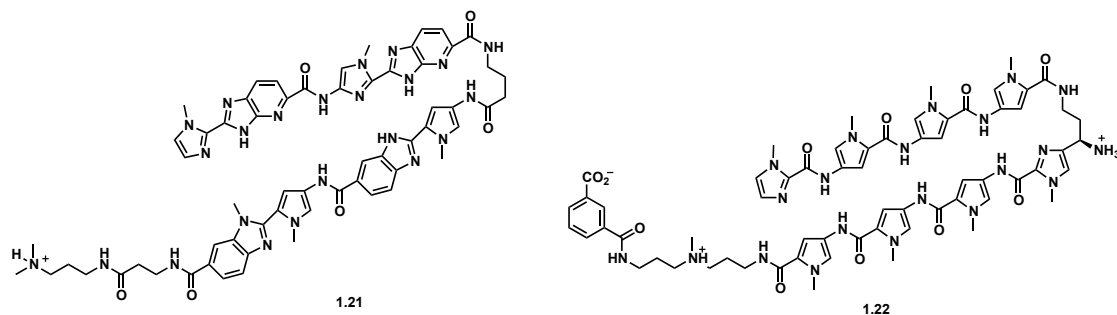


Figure 1.17. Small molecule Py-Im polyamides that inhibit NF- κ B p50-p65 and AR.

1.3.5 Modulation of TFs Through mRNA Regulation

Small interfering RNA (siRNA), short hairpin RNA (shRNA), and antisense oligonucleotides are standard laboratory tools used for mRNA regulation, which can be utilized to target transcription factors to directly downregulate their mRNA expression and subsequent protein synthesis (**Figure 1.11d**). These technologies utilize double-stranded RNAs (dsRNAs) that get processed by the Dicer protein to yield short (~20 base pair) dsRNAs, which can dissociate into two single-stranded RNAs (ssRNAs). This single-stranded RNA is incorporated into the RNA-induced silencing complex (RISC) and is a sequence-specific complement of the target mRNA. Upon hybridizing with the mRNA, a conformational shift allows the catalytic subunit, Argonaute, to cleave the mRNA, which results in inhibition of protein synthesis.⁹⁶⁻⁹⁹ These technologies have limitations associated with cellular uptake and short half-lives, but have tremendous advantages including specificity and efficacy against their targets. For example, the STAT3 antisense oligonucleotide AZD9150 (**1.23**), has undergone phase I clinical trials for advanced lymphoma and solid tumor patients whereby two out of three patients observed a greater than 50% reduction in tumor size by inhibiting STAT3 gene expression (**Figure 1.18**).¹⁰⁰

5'- CTATTTGGATGTCAGC -3'

1.23

Figure 1.18. STAT3 antisense oligonucleotide AZD9150. The nucleotides are locked nucleic acids (LNA, **1.27**), which also contain constrained ethyl groups.¹⁰¹

1.4 DNA Decoys

Utilizing cis element DNA decoys to sequester TFs is another approach to directly modulate transcription factors (**Figure 1.11e**). Previous studies have shown that tandem repeats of DNA in the genome that contain transcription factor binding sites could serve as decoy binding sites, which effectively sequesters a TF and inhibits its target gene expression.¹⁰²⁻¹⁰⁴ This endogenous form of TF competitive inhibition can be replicated exogenously by introducing synthetic double-stranded oligodeoxynucleotides (ODN) containing TF binding sites into cells. These platforms of artificial gene modulation utilizing cis element DNA decoys can be transfected into cells, sequestering their targeted TFs, and alter gene expression by inhibiting their endogenous activity (**Figure 1.19b**).¹⁰⁵ There are several types of DNA decoys, usually ranging from 10-20 base pair ODNs to plasmid DNA containing multiple decoys in the sequence.¹⁰⁶

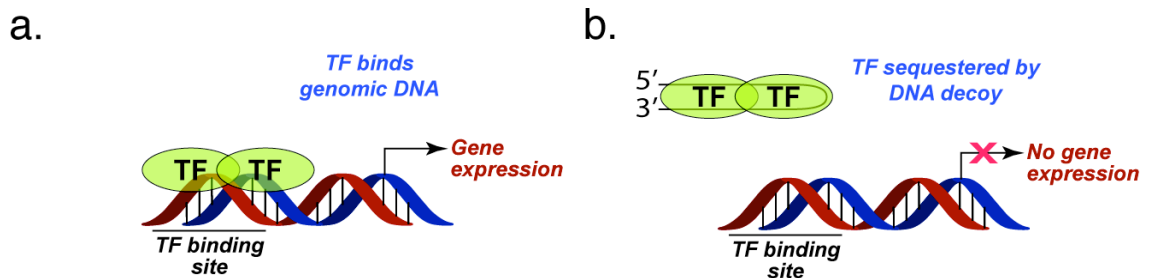


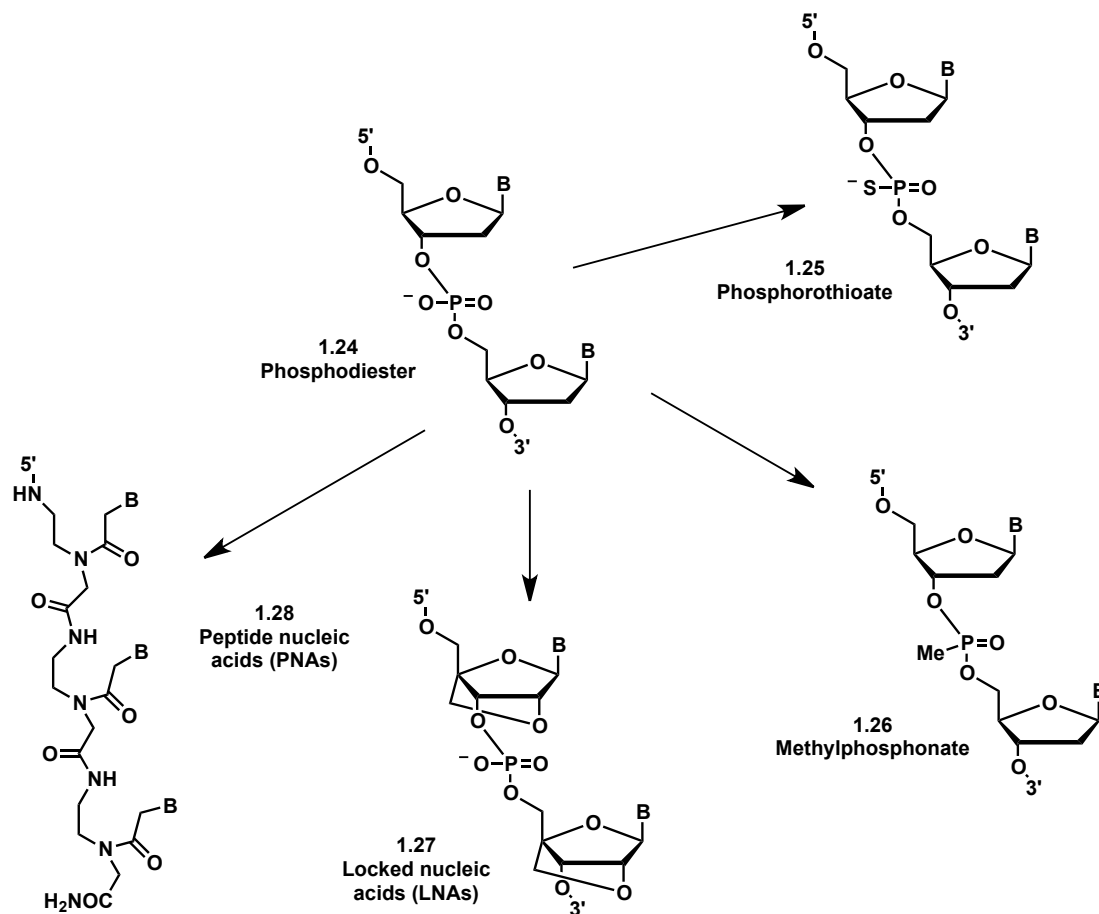
Figure 1.19. Inhibition of gene expression by DNA decoys. (a) TFs able to bind genomic DNA and activate gene expression. (b) DNA decoys sequester TFs thereby reducing its effective concentration and subsequent endogenous activity.

There are numerous advantages to this approach of modulating TFs and gene expression: the TF targets are abundant and identifiable as publications of TFs and their consensus sequences become more common, which is attributable to genome

technologies like chromatin immunoprecipitation sequencing (ChIP-seq),^{107,108} the synthesis of DNA decoys are relatively simple using phosphoramidite chemistry,^{109,110} the DNA binding domains of TFs are unlikely to acquire mutations to achieve resistance, and DNA decoys can be rationally designed to modulate any TF because the only structural information about the TF that is needed is the sequence that it binds.

One major limitation of DNA decoys, or DNA therapeutic agents in general, is their poor cellular uptake. Laboratory techniques such as cationic liposomes, heat shock, and electroporation can be used to introduce foreign DNA into cells; however, these techniques cannot be used *in vivo*. However, there has been progress to rectify this problem. The Hemagglutinating Virus of Japan (HVJ)-liposome method and ultrasound-mediated gene transfer method have demonstrated enhanced gene transfer and uptake of DNA decoys.¹¹¹⁻¹¹⁸ Another major limitation of DNA decoys is their rapid degradation by serum and intracellular nucleases,^{119,120} consequently, there have been several different modifications of DNA decoys to improve their stability (**Scheme 1.1**). Modified phosphodiester bonds (**1.24**), such as replacing a non-bridging oxygen in the phosphate linkages with sulfur to form phosphorothioate (PS) bonds (**1.25**), greatly increases DNA stability.¹²¹ Other modifications to the backbone including methyl phosphate and methyl phosphonate (**1.26**) derivatives have also demonstrated nuclease resistance, giving rise to higher stabilities.^{122,123} Conformational restriction of nucleosides is another successful strategy in designing potent DNA decoys. These locked nucleic acids (LNAs, **1.27**) contain a 2'-O-4'-C-methylene bridge in the sugar of the DNA and have demonstrated added thermal stability and nuclease resistance while retaining their ability to bind

TFs.^{124,125} Peptide nucleic acids (PNAs, **1.28**) are a class of DNA mimics in which the sugar-phosphate backbone is replaced by N-(2-aminoethyl)glycine units and are able to efficiently undergo Watson-Crick hybridization.^{126,127} Recently, PNA-DNA decoy chimeras have been shown to inhibit the NF- κ B and Sp1 TFs and are fully resistant to exonucleases.¹²⁸



Scheme 1.1. Modifications to DNA to improve its serum and intracellular stability. B denotes any nucleobase.

Tethering the two hybridized strands of a DNA decoy together with one or two closed nucleotide loops on the end form either hairpin or dumbbell structures (**Figure 1.20**). These structures exhibit improved nuclease stability, improved sequence

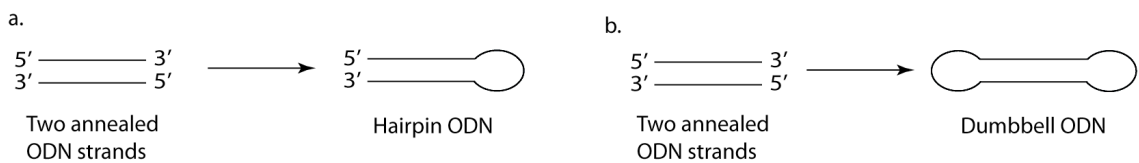


Figure 1.20. (a) Hairpin and (b) dumbbell oligonucleotide structures formed by tethering two oligonucleotide strands together giving more stable and effective complexes.

specificity, cellular uptake, and lowered toxicity.^{119,129} Studies with AP-1 and STAT decoys have demonstrated that hairpin and dumbbell DNA decoys yield significantly greater TF inhibition *in vitro* (78% knockdown with the dumbbell versus 39% knockdown with the phosphorothioate modified). Importantly, they are more stable and effective over phosphorothioate and unmodified DNA decoys *in vivo* as well.¹³⁰⁻¹³² Another advantage of hairpin and dumbbell DNA decoys is an added level of specificity. Changing the sequence of the loop region of a pan STAT dumbbell DNA decoy discriminates it for either STAT1 or STAT3.^{132,133} These studies demonstrate that hairpin and dumbbell DNA decoys are markedly improved over other chemically modified DNA decoys, and therefore, utilization of these decoys are quite relevant for therapeutic intervention and as a tool for further research.

The efficiency and versatility of DNA decoys make it an attractive approach for use as a tool and a possible therapeutic agent. Over the past couple of decades, numerous reports have validated utilizing this approach and the increased utilization over a wide breadth of applications and range in clinical areas.^{134,135} Several targets and applications are summarized in **Table 1.1**.^{20,135-146} Among these are regulating several manifestations of inflammation including cystic fibrosis (NF- κ B),¹⁴⁰ regulating neural stem cell differentiation (HNF4-1 and MAZ-1),¹⁴¹ reducing oxidative

Table 1.1. Modulation of TFs by DNA decoys. Modulating TFs by DNA decoys can effect several cellular processes and as a result, yield numerous therapeutically relevant responses. All decoys are linear double stranded oligonucleotides.				
TF Target	Cellular process regulated by TF	Therapeutic indication	Decoy sequence	Refs
NF-κB	Cytokine expression, oxidant stress response, apoptosis, cell proliferation	Inflammation, ischemia reperfusion, cancer, osteoporosis	5' - CCTTGAAGGGATTTCCTCC - 3' 3' - GGAAC TTCCTAAAGGGAGG - 5'	158,159, 144,143, 140,136
TAR/tat	Viral replication	HIV infection	5' - UGCUAGCCAGAGAGCC - 3' 3' - AGCGAUCGGUCUCUGA - 5'	157
MAZ	Oncogenic expression, Stem cell differentiation	Cancer, neurodegenerative	5' - TATGGGAGGGACT - 3' 3' - ATACCCCTCCCTGA - 5'	156,141
AP1	Oxidant stress response, cell proliferation, differentiation	Cardiac fibroblast proliferation, neointimal hyperplasia	5' - AGCTTGTGAGTCAGAAGCT - 3' 3' - TCGAACACTCAGTCTTCGA - 5'	138,142
EF2	Cell proliferation, cell-cycle regulator	Neoplasia, angiogenesis, inflammation	5' - GATCAAAAAGCGCGAATCAAAAGCGGAATC - 3' 3' - CTAGTTTTCGCGCTTAGTTTTCGCGCTTAG - 5'	155,145, 146
STAT	Cell proliferation	Cancer	5' - CATTTCCTCCGTAATCGAAGATTTCGGGAAAATG - 3' 3' - GTAAAGGGCATTTAGCTTCTAAATGCCCTTTAC - 5'	152,153, 154,139
Sp1	Angiogenic factors	Cancer metastasis	5' - CCCC GGCGGGTCTGGCGGG - 3' 3' - GGGGCCCCCGCCAGACCCGCC - 5'	151
AR	Cell proliferation, prostate development, metastasis	Prostate cancer	5' - TGCAGAACAGCAAGTGCTAGC - 3' 3' - ACGTCTTGCTTCACGATCG - 5'	150
ER	Cell proliferation, cell-cycle regulator, apoptosis	Breast cancer	5'-TAATAGGTACAGTGACCTAGGTACAGTGACCTA- GGTCACAGTGACCTGATTCC - 3'	149
CRP	Cell proliferation, cell-cycle regulator, apoptosis	Cancer, viral diseases	5' - TGACGTCATGACGTCATGACGTC - 3' 3' - ACTGCAGTACTGCAGTACTGCAGT - 5'	147,148

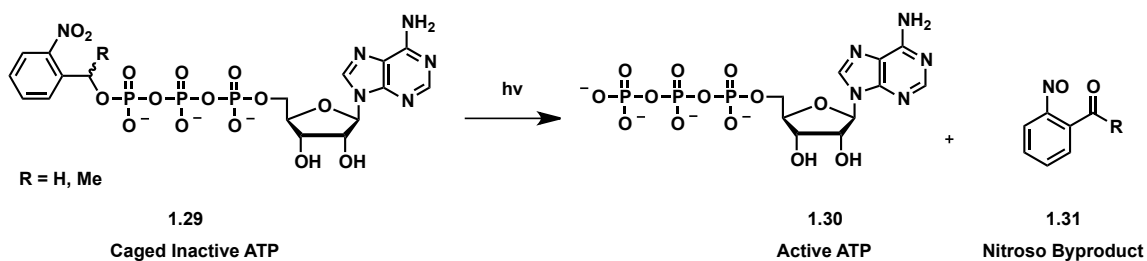
stress-induced cardiac fibroblast proliferation (AP-1),¹⁴² and altering cell-cycle regulatory genes (E2F).^{20,145,146} Since this approach gives an efficient and specific TF inhibition, a wide-ranging list of DNA decoys have been developed to inhibit numerous TFs implicated in cancer growth and development (**Table 1.1**).¹⁴⁷⁻¹⁵⁴ Among these, DNA decoys designed against NF- κ B, Sp1, STAT3, and MAZ have all demonstrated anti-cancer activity over many different cancer types including breast, melanoma, colorectal, pancreatic, and several more.¹⁴⁷⁻¹⁵⁰ Additionally, DNA decoys designed against hormone receptor TFs including the androgen receptor (AR), the estrogen receptor (ER), and the cyclic AMP receptor protein (CRP) have all been shown to induce apoptosis and cell death in several cancer types.^{151,152,155,156}

The DNA decoy approach is also validated in several *in vivo* mice and rat models. Local administration of an NF- κ B decoy to rats induced apoptosis of osteoclasts via Fas signaling, which could be used as a strategy for treatment of conditions such as osteoporosis, peri-articular osteolysis, inflammatory arthritis, and Paget's syndrome.¹⁵⁷ An E2F DNA decoy was administered into rats via HVJ-liposome complexes and demonstrated reduced expression of the *c-myc*, *cdc2*, and *PCNA* genes, which resulted in the inhibition of vascular smooth muscle cell (VSMC) proliferation.¹⁵⁸ More recently, a phosphorthioate STAT3 DNA decoy has entered the "first-in-human" Phase 0 clinical trials for the treatment of head and neck squamous cancer.¹⁵⁹ STAT3 expression and cell viability was reduced in the head and neck cancers injected with the decoy compared to the saline control. Additionally, since systemic administration results in degradation of the decoys, dumbbell STAT3 decoys were synthesized and attached hexaethyleneglycol

linkers to yield a cyclic STAT3 decoy. Intravenous injection of this cyclic decoy inhibited xenograft growth and downregulated STAT3 target genes within the tumor, demonstrating successful systemic administration of DNA decoys.¹⁵⁹ Collectively, the DNA decoy strategy for the inhibition of transcription factor activity can be considered one of the most useful approaches for both a therapeutic for disease progression and as a tool to examine molecular mechanisms.

1.5 Caging Technology

To obtain spatiotemporal resolution of DNA decoy function, an external trigger that enables precise activation or deactivation is needed. Light is an ideal external trigger as it is highly selective, easily and precisely controlled in time, space, and intensity, and, if done correctly, is harmless to biological systems. Strategies to develop such a trigger for biochemical experiments have been investigated since the 1970s when J. F. Hoffman synthesized an adenosine triphosphate (ATP) derivative with a 2-nitrobenzyl photolabile group (**Scheme 1.2, 1.29**).¹⁶⁰ This otherwise active molecule is rendered inactive by appendage of the 2-NB photolabile masking (or caging, which was coined by Hoffman) molecule, which disrupts key molecular recognition properties

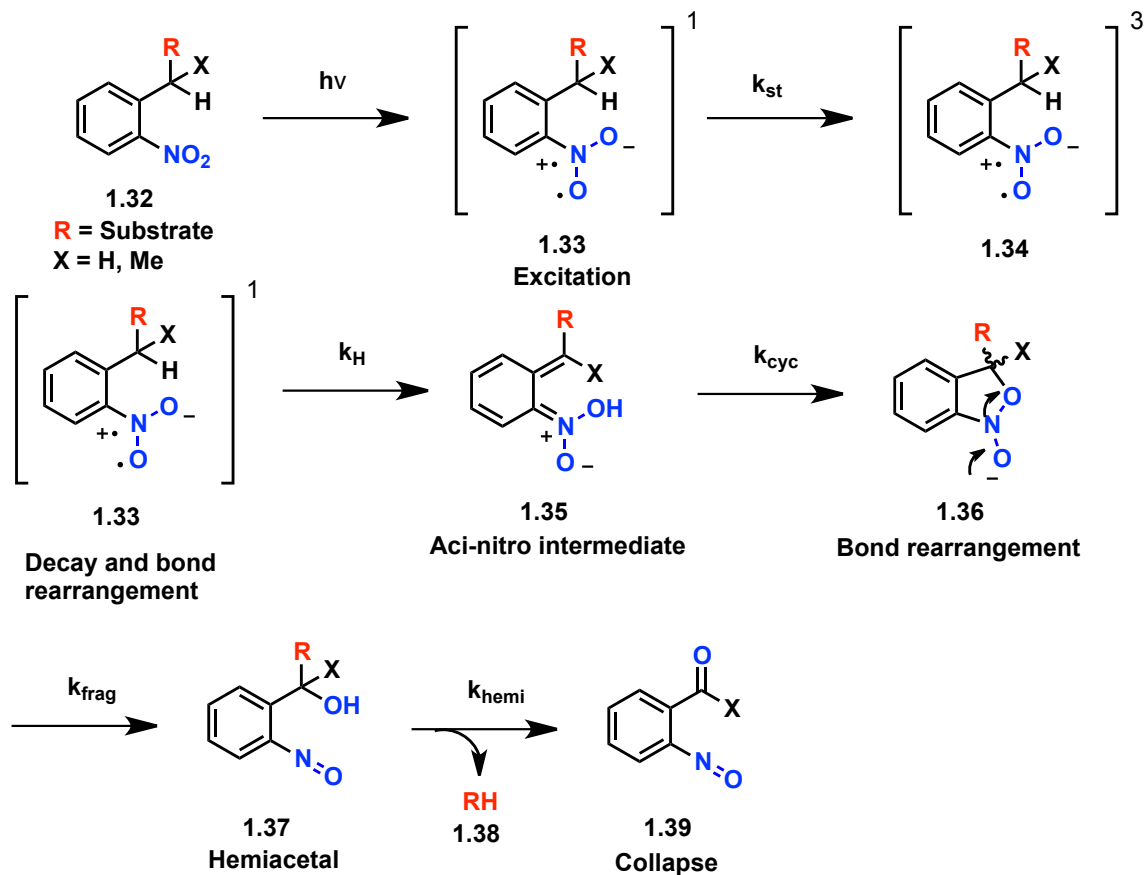


Scheme 1.2. Caging technology utilized for spatiotemporal resolution of ATP.

between the molecule and its target as a result of steric interference. Photolysis of the molecule renders the system active by liberating the caging group (**1.31**) and regenerating the original, bioactive ATP molecule (**1.30**). Early studies with this caged ATP demonstrated spatial and temporal control over a biological system and single turnovers of a sodium pump could be observed.¹⁶¹ 2-NB caging groups had been used previously as organic synthesis protecting groups.¹⁶² Since then, a myriad of applications have been developed utilizing this technology from the analysis of neurological processes to studying secondary messengers and cellular signaling molecules, proteins, and nucleic acids, all achieving a higher level of control of cellular processes.¹⁶³⁻¹⁶⁸

Over 80% of the publications on caging technology are applications of the most widely used 2-nitrobenzyl (2-NB, **1.32**) photolabile molecule or its derivatives.¹⁶⁹ The events from the absorption of light and eventual release of the substrate have been subdivided into five major steps (**Scheme 1.3**).¹⁷⁰ The first step is excitation to form the diradical **1.33** at a rate of $2 \times 10^7 \text{ s}^{-1}$. 2-NB has a strong UV absorbance with a λ_{max} at 275 nm.¹⁷¹ The excited singlet can either undergo intersystem crossing to the triplet state **1.34** at the rate k_{ST} (10^9 s^{-1}) or undergo hydrogen atom abstraction at the rate k_{H} ($\sim 10^9 \text{ s}^{-1}$).¹⁷⁰ The triplet state cannot undergo hydrogen atom abstraction. After a bond rearrangement, the product of hydrogen atom abstraction is aci-nitro intermediate **1.35**. This intermediate is stable enough to be observed and kinetic rate studies have been performed extensively on this intermediate demonstrating its sensitivity to pH.¹⁷² Several tautomers and isomers exist of the aci-nitro intermediate, but it has been demonstrated that the E,E isomer cyclizes directly to form the oxazole intermediate **1.36**. The rate at which the oxazole is

formed (k_{cyc}) is immediately followed by the formation of the nitroso species or the ring-opening to the hemiacetal intermediate **1.37** (k_{frag} , $\sim 5000 \text{ s}^{-1}$).¹⁷¹ The last step is the collapse of the hemiacetal releasing the substrate **1.38** and the nitroso by-product **1.39**, which is the rate-limiting step (k_{hemi} , 0.11 s^{-1}) of the photo-uncaging process.¹⁷¹



Scheme 1.3. Mechanism of photolytic release of 2-NB **1.32**. The five-step mechanism includes the excitation of the nitro-group with light yielding the diradical **1.33**. The radical performs a hydrogen atom abstraction followed by a rearrangement to give the aci-nitro intermediate **1.35**. Bond rearrangement leads to heterocyclic intermediate **1.36**, which fragments to yield hemiacetal nitroso **1.37**. The final rate-limiting step is the collapse of the hemiacetal releasing the substrate **1.38** and the nitroso by-product **1.39**.

Several requirements need to be met to yield a good caging group like 2-NB: it should be easy to synthesize and introduce to a wide array of substrates; it should be stable under physiological conditions; it should have a large molar extinction coefficient (ϵ) for photoactivation; it should photoactivate at a wavelength that reduces the amount of photodamage; this photoactivation should result in a large percentage of photo-uncaging quantified by the quantum yield (ϕ); and finally, the photo by-product should not be toxic.¹⁶⁴ Copious amounts of papers have been published in the last 10 years presenting modifications to caging scaffolds, changing one or several of these properties. Considerable work has been done modifying the 2-NB scaffold to make it more efficient (**Figure 1.21**).¹⁷³⁻¹⁸⁰ Various functional groups such as hydroxyl, carboxylic acid, or phosphate groups can be protected with 2-NB (**1.40**). Oxycarbonyl derivatives of 2-NB allow amino groups to be protected (**1.41**). Addition of a benzyl substituent of the 2-NB group is also very common. Addition of a methyl substituent to form the 2-

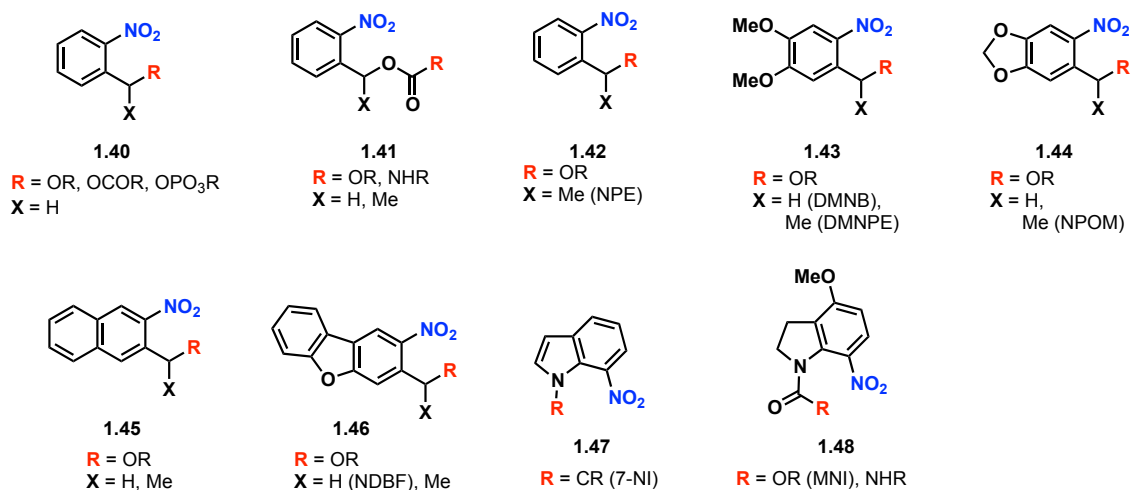


Figure 1.21. Common 2-NB derivatives. 2-NB **1.40** can be used to protect several different functional groups. Functionalization of 2-NB with an oxycarbonyl group **1.41** allows amines to be protected. Addition of a benzylmethyl substituent **1.42** increases efficacy of the 2-NB. Addition of electron donating groups (**1.43-1.44**) or increased aromaticity (**1.45-1.46**) enhances absorptivity of the 2-NB. Additional scaffolds including 7-nitroindole and indoline (**1.47-1.48**) have demonstrating efficient caging.

nitrophenylethyl (2-NPE, **1.42**) caging group demonstrates a higher photo-release rate than 2-NB (34300 s^{-1} for 2-NPE compared to 600 s^{-1} for 2-NB).¹⁶⁹ Addition of electron donating aryl substituents, such as a catechol (**1.43**) or piperonal (NPOM, **1.44**) enhance the absorptivity of the scaffold increasing the λ_{max} up to 365 nm.^{176,181} Similarly, substitution of the phenyl group with other aromatic groups that contain more conjugation such as naphthalene (**1.45**) or dibenzofuran (NDBF, **1.46**) have shown to red-shift to 350-400 nm.¹⁷⁸ 7-Nitroindole (7-NI, **1.47**) and 4-Methoxyl-7-nitroindolinyl (MNI, **1.48**) photolabile groups have also been identified as efficient caging groups.¹⁸² MNI caged glutamate was used in spatial temporal resolution of the neurotransmitter.¹⁸³

An alternative to single-photon uncaging like 2-NB, is two-photon uncaging, where light equaling twice the wavelength of the maximum absorption of the caging group is applied, such as using 730 nm light to uncage a photolabile molecule with a maximum absorption at 365 nm. These caging groups have resulted in improvements of spatiotemporal resolution as well as increased tissue penetration.¹⁸⁴ Numerous biological studies have utilized this technology. One example is the caging of a farnesyltransferase inhibitor with the two-photon uncaging coumarin-based thiol-protecting group (**1.49**).

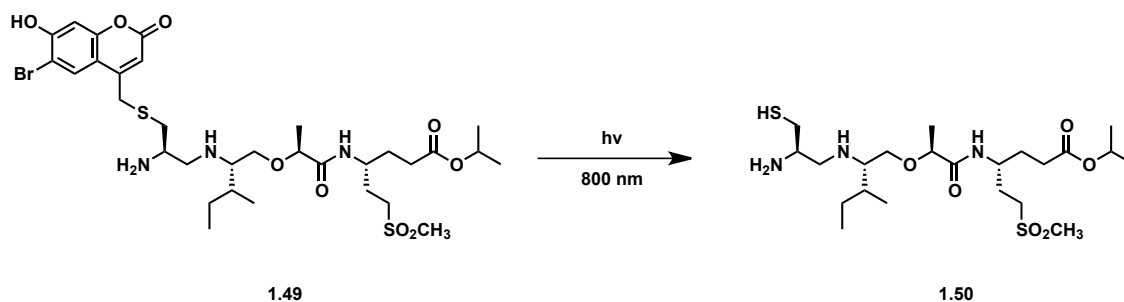


Figure 1.22. Two-photon uncaging of a farnesyltransferase inhibitor with 800 nm light.

Irradiation with 800 nm light yielded two-photon uncaging producing the free farnesyltransferase inhibitor (**1.50**) in Ciras-3 fibroblasts to inhibit Ras localization and alter cell morphology.¹⁸⁵

Relatively new in the history of caging technology, is the application of caging DNA, RNA, and their analogues. Depending on the application, the caging group can be introduced on the nucleobase (blocking key molecular recognition interactions, **1.51**), as the nucleobase (leaving an abasic site when photocleaved, **1.52**), on the ribose sugar (**1.53**), on the phosphodiester backbone (**1.54**), or as an internal photolabile linker (resulting in fragmented products when cleaved, **1.55**).^{164,186,187}

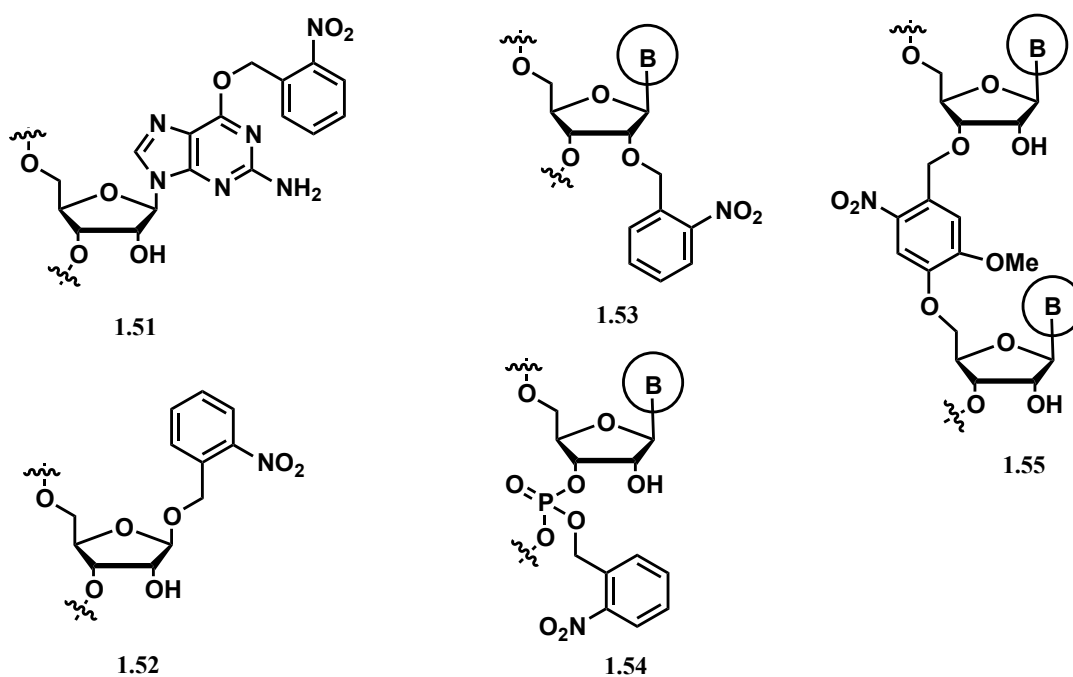


Figure 1.23. Different approaches to caging DNA/RNA. The caging group can be placed on the nucleobase **1.51**, as the nucleobase **1.52**, on the ribose sugar **1.53**, on the phosphodiester backbone **1.54**, or as an internal photocleavable linker **1.55**. B denotes any nucleobase.

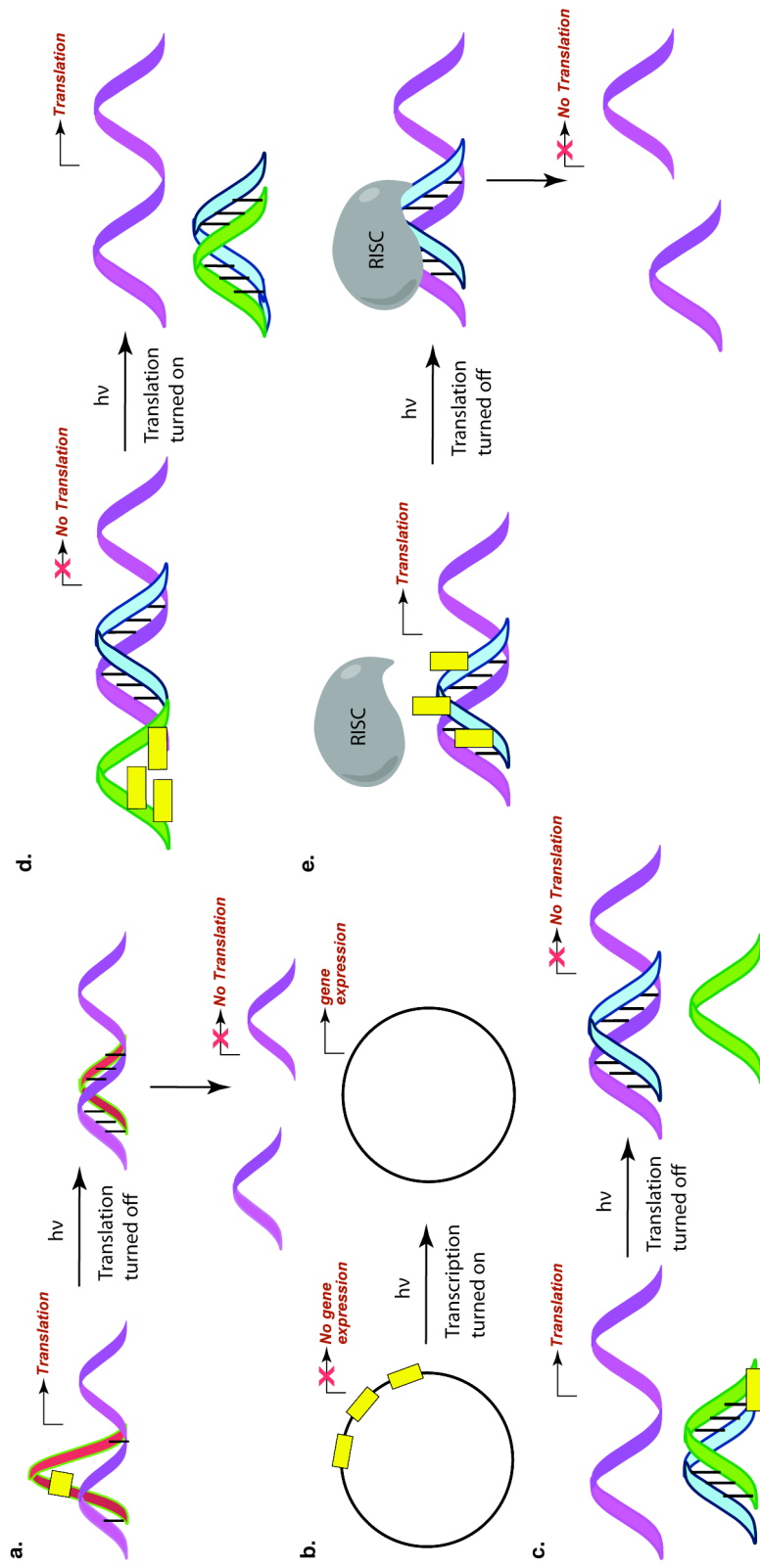


Figure 1.24. Light regulated gene expression strategies. (a) Light activated DNazymes degrade mRNA to silence gene expression. (b) Light induced activation of transcription by releasing caging groups on DNA. (c) Double stranded antisense strand with photocleavable linker. Photolysis cleaves the two strands allowing complementary strand to bind mRNA and deactivate translation. (d) Single stranded caged antisense strand permitted to bind mRNA. Photolysis drives self-hybridization of the antisense strand, obstructing its activity, thus turning on translation. (e) Caged siRNA binds to its mRNA target, but caged groups prevent the binding of the RISC complex. Photolysis and removal of the caged groups allow binding of the RISC complex and degradation of mRNA.

The effects of nucleobase caging have been widely studied and demonstrate a perturbation in duplex stability with the addition of multiple caged groups.¹⁸⁸ Caged guanosine and caged cytosine have used light to induce the formation of G-quadruplexes and light-trigger aptamers that contain antidote activity.^{189,190} This caging approach has been used extensively to control gene expression in a spatial and temporal manner (**Figure 1.24**). For example, caged nucleobases have been used to photochemically activate DNAzymes to degrade mRNA and silence protein synthesis (**Figure 1.24a**).¹⁹¹ In a similar manner, caging technology has been used to photoinduce T7 RNA polymerase transcription both by incorporation of caging groups on the oligonucleotide and on the polymerase (**Figure 1.24b**).^{192,193} One major approach to regulate gene expression is through antisense and siRNA. Caged antisense and siRNA have been used widely to knockdown gene expression spatiotemporally both in cells and in zebrafish and *Xenopus* Embryos.¹⁹⁴⁻¹⁹⁶ This is realized by a few of different mechanisms. One early and widely used application is the use of the photocleavable backbone by insertion of a caging linker in the RNA backbone (**Figure 1.24c**).¹⁹⁷ Duplex RNA is introduced with a photocleavable linker and unable to bind mRNA thus leaving translation active. Upon photolysis, the RNA is cleaved, yielding a single complementary strand that can bind mRNA, thus deactivating translation. Alternatively, caging groups attached to the nucleobase on an antisense RNA strand can prevent self-hybridization, yielding an active antisense strand. Photolysis and removable of the caged groups drives self-hybridization, obstructing its antisense activity, effectively activating translation (**Figure 1.24d**).¹⁹⁸ As another method of gene expression control, caging groups introduced on the

phosphodiester backbone and nucleobases can interfere with the formation of the siRNA-RISC complex necessary to cleave the mRNA. Photolysis, and removal of the photolabile groups, permits the RISC complex to bind, cleave the mRNA, and deactivate translation (**Figure 1.24e**).^{199,200}

1.6 Caged DNA Decoys

Combining the spatial and temporal resolution of caging technology with the DNA decoy strategy for the inhibition of transcription factor activity can yield an approach for the very precise ability to photochemically regulate gene expression, which has potential as a therapeutic agent and tool for probing biological pathways. Deiters and co-workers developed a caged NF- κ B-directed DNA decoy to photochemically control NF- κ B gene expression.²⁰¹ It was hypothesized that caging groups would disrupt Watson-Crick base pairing, thus rendering the decoy inactive. Photolysis of the caging groups would then restore duplex formation, permitting NF- κ B binding, thus sequestering the TF, leading to inhibition of gene expression (**Figure 1.25**). Deiters incorporated several NPOM (**1.44**) caging groups into hairpin and dumbbell DNA decoys that resulted in disruption of duplex formation, which is demonstrated by thermal melting studies. When four caging groups were incorporated into the hairpin decoy (**Figure 1.26.D4**), or just three in the dumbbell (**Figure 1.26.D6**), all duplex formation is abolished. Upon irradiation with light (350 nm for 10 minutes in buffer), the caging groups were removed

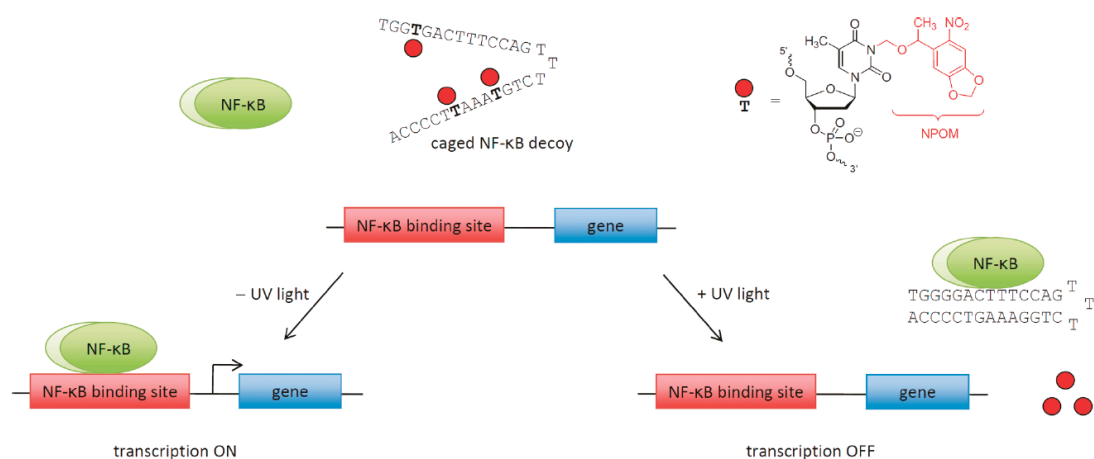


Figure 1.25. Adopted with permission from *J. Am. Chem. Soc.* **2011**, *133*, 13176. The caging groups disrupted Watson-Crick base pairing, thus rendering the decoy inactive. Irradiation and removal of the caging groups restored duplex formation, permitting NF-κB binding, thus sequestering the TF, leading to inhibition of gene expression.

DNA	Sequence	$T_m / ^\circ\text{C}$	
		-UV	+UV
D2	5' TGGGGACTTTCCAG [†] _T ACCCCTGAAAGGTC _T	84.4 ± 0.0	-
D3	5' TGGGGACT T TCCAG [†] _T ACCC T GAAAGG T C _T	54.4 ± 1.7	81.8 ± 0.6
D4	5' TGGGGACT TT TCCAG [†] _T ACCC T GAAAGG T C _T	NA	83.1 ± 0.6
D5	5' T [†] TGGGGACTTTCCAG [†] T [†] T ACCCCTGAAAGGTC [†] T	74.8 ± 0.6	-
D6	5' T [†] TGGGGACTT T CCAG [†] T [†] T ACCC T GAAAGG T C [†] T	NA	73.8 ± 1.5
D7	5' T [†] T GGGGACTT T CCAG [†] T [†] T ACCC T GAAAGG T C [†] T	NA	74.4 ± 0.9

Figure 1.26. Adopted with permission from *J. Am. Chem. Soc.* **2011**, *133*, 13176. Thermal stability of caged hairpin and dumbbell DNA decoys before and after photolysis. A bold **T** denotes a caged thymidine nucleotide and NA indicated no melting temperature could be measured.

and hybridization can now occur, restoring the duplex stability seen in the non-caged DNA decoys (**D2**).

To identify the proficiency of binding of the DNA decoys to NF- κ B *in vitro*, the electrophoretic mobility shift assay (EMSA) was used (**Figure 1.27**). If a binding event occurs, the higher molecular weight complex (DNA + protein) will hinder its progression down the gel, hence is “shifted” up the gel from the unbound DNA. The addition of nuclear extract containing NF- κ B proteins to non-caged DNA decoys promotes binding and is specific as no binding was seen with a scrambled DNA decoy (**Figure 1.27**, lanes **2** and **10**). The same addition of nuclear extract to the caged DNA decoy showed no appreciable binding event, demonstrating the caging groups provided sufficient perturbation to abolish transcription factor binding affinity (**Figure 1.27**, lanes **4**, **7**, **12**, and **15**). Irradiation with light, removal of the caging groups, and formation of

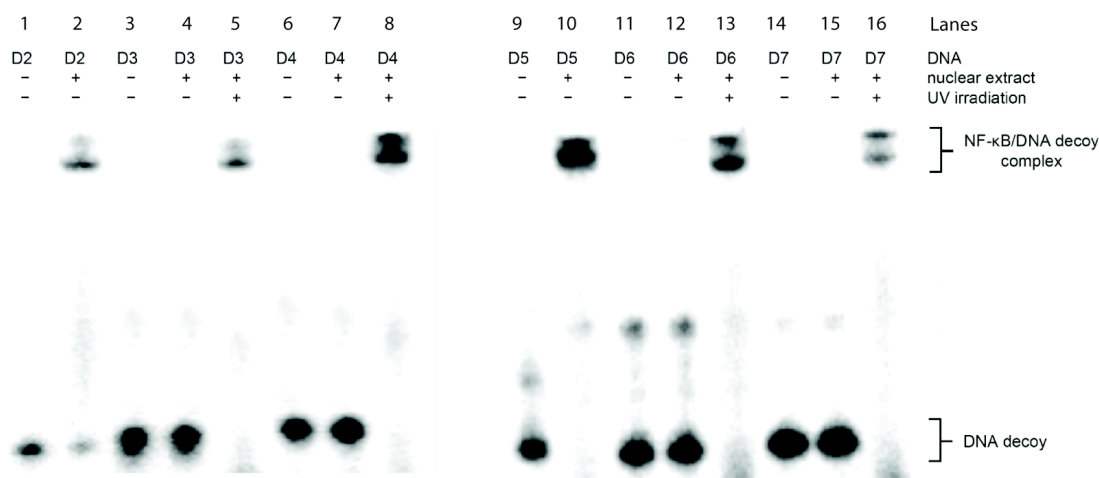


Figure 1.27. Adapted with permission from *J. Am. Chem. Soc.* **2011**, *133*, 13176. EMSAs demonstrating light activation of NF- κ B DNA decoys. Caged decoys do not induce a gel shift (lanes **4**, **7**, **12**, and **15**). Irradiation with light restores duplex DNA and induces a gel shift demonstrating NF- κ B binding *in vitro* (lanes **5**, **8**, **13**, and **16**).

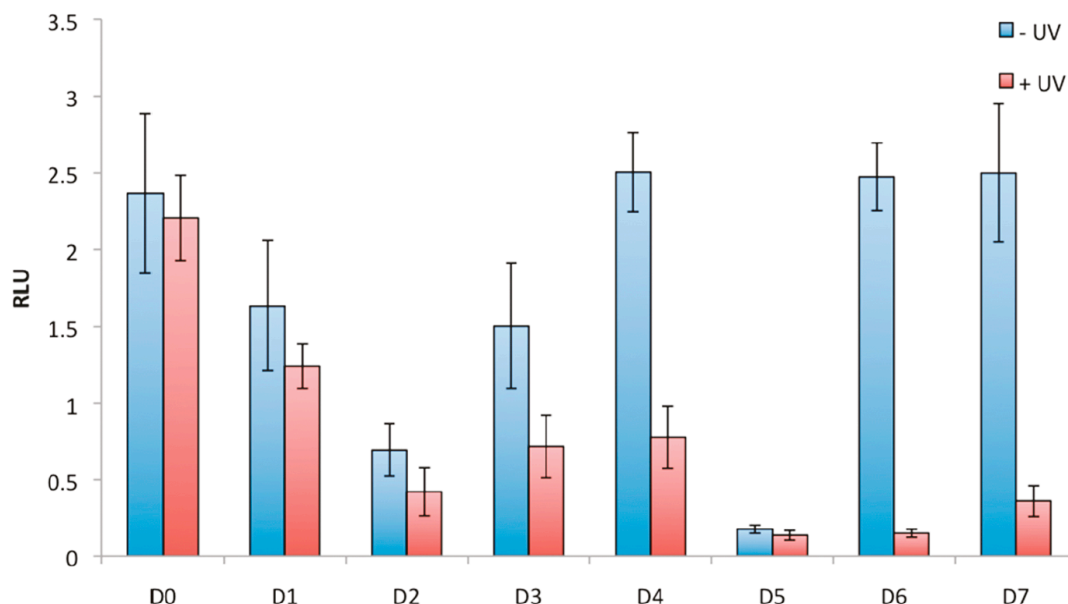


Figure 1.28. Adapted with permission from *J. Am. Chem. Soc.* **2011**, *133*, 13176. Photochemical activation of NF- κ B-mediated SEAP expression. Transfection of caged DNA decoys with no duplex formation demonstrated no inhibition of NF- κ B-mediated SEAP expression. UV irradiation for 2 min restores the structure and function of the DNA decoys within the cells and resulted in effective sequestering of NF- κ B, leading to inhibition of SEAP expression.

duplex hairpin or dumbbell DNA decoys, restores their binding affinity and demonstrated capture of NF- κ B (**Figure 1.27**, lanes **5**, **8**, **13**, and **16**).

The DNA decoys were then transfected into NF- κ B/SEAP HEK293 cells to investigate the photochemical control of gene expression within mammalian cells (**Figure 1.28**). The transfection of native decoys (**Figure 1.28.D2**, **D5**) into the HEK293 cells down-regulated NF- κ B-mediated gene expression by 60% or 100% compared to the scrambled control (**Figure 1.28.D0**). The introduction of caged DNA decoys with no duplex formation (**Figure 1.26.D4**, **D6**, **D7**) demonstrated no inhibition of NF- κ B-mediated SEAP expression. UV irradiation for 2 min restored the structure and function of the DNA decoys within the cells and resulted in effective sequestering of NF- κ B,

leading to inhibition of SEAP expression. This caged DNA decoy approach enables the precise deactivation of gene expression in both a spatial and time-resolved manner, which have great potential as therapeutic agents and will enable the study of gene function in biological pathways.

1.7 Preface to this Thesis

The following chapters disclose my efforts to develop several novel DNA-based and small molecule-based probes to investigate the biochemistry of transcription factors and their signaling pathways. Chapter 2 discusses the synthesis and characterization of caged DNA decoys that target the Androgen Receptor (AR). Caged DNA decoys with 6 and 8 NPOM (**1.44**) caging groups successfully captured AR in LNCaP lysate when irradiated with light. Chapter 3 introduces a complement to caging technology, which are catch and release DNA decoys (CRDDs). CRDDs capture transcription factors, by binding and sequestering them, and then a pulse of light photochemically destroys the CRDD, permitting release of the TF. Several 7-nitroindole (7-NI, **1.47**) nucleobase mimics were incorporated into NF- κ B-directed DNA decoys, which still allowed the capture of the p50-p65 NF- κ B proteins. Irradiation with 350 nm light drives the release of the p50-p65 NF- κ B. The capture and photochemical release of an endogenous transcription factor is demonstrated for the first time. Chapter 4 continues the work of Chapter 3 by developing second-generation nucleobase mimics for use in CRDDs. Addition of molecular recognition properties on a photo-responsive monomer

was hypothesized to increase binding affinity to capture endogenous TFs. 8-Nitroguanosine contains this added molecular recognition, is more stable within duplex DNA, and also displayed similar photochemical depurination properties. Chapter 5 outlines work developing photoswitchable nucleobases that transpose their hybridization properties upon photolysis. Chapter 6 highlights work with determining the mechanistic NF- κ B inhibitory properties of several Cryptocaryone analogues, which were found to inhibit the NF- κ B translocation to the nucleus. Appendix A focuses on the characterization of the enantioselectivity of guanosine monophosphate synthetase (GMPS), a crucial enzyme in nucleotide biosynthesis.

Chapter 2

ANDROGEN RECEPTOR-DIRECTED CAGED DNA DECOYS

This work was performed in collaboration with Mr. Matthew Bockman and Professor Daniel A. Harki. In this work, Mr. Matthew Bockman was responsible for synthesizing oligonucleotides **2.3** and **2.4** and obtaining their melting temperatures, which is shown in **Table 2.1**.

2.1 Androgen Receptor (AR) DNA Decoys

As discussed in **Chapter 1.1.4**, AR is activated by the binding of androgens, which allows translocation to the nucleus, and activation of gene expression (**Figure 1.4**). Prostate carcinogenesis and its progression is contingent on AR signaling and activation, thus has been exploited for therapy development. Enzalutamide (**1.12**), which was FDA approved in 2012, binds to the ligand-binding domain of AR, preventing its activation, and increasing overall survival. Despite the benefit on survival of Enzalutamide, approximately one quarter of prostate cancer patients will develop resistance due to AR gene mutations and amplifications, up-regulation of AR synthesis, and/or altering signaling pathway with cross talk to AR signaling.²⁰² Developing DNA decoys to sequester AR is an approach to circumvent resistance since the DNA binding domain of AR is less prone to mutations, and will therefore avoid several of these mechanisms of resistance. Classical DNA response elements of nuclear hormone receptors contain inverted repeats of 5'-AGAACA-3', but extensive research has discovered several AR-distinct androgen receptor elements (ARE) that have contributed to consensus sequences useful for targeting the ARE.²⁰³ With this information readily available, ARE DNA decoys can be a strategy employed to inhibit AR.^{151,204} Kuratsukuri and co-workers synthesized double stranded DNA with the 21 base pair ARE sequence of the prostate specific antigen (PSA) gene.¹⁵¹ This decoy shifted active AR protein from LNCaP nuclear lysate, demonstrating specific binding in an electrophoretic mobility shift assay (EMSA). The decoy was also transfected into LNCaP cells, inhibiting key

downstream AR-driven genes including prostate specific antigen (PSA), which induced apoptosis. The spatiotemporal resolution of caging technology on AR-directed DNA decoys would yield a powerful tool to interrogate AR-signaling and a possible therapeutic agent. Therefore, we designed and synthesized caged DNA decoys to AR. Kinetic studies determined the speed and efficiency of this process, demonstrating full uncaging within one minute; however, incomplete uncaging was observed. Nonetheless, caged DNA decoys with 6 and 8 NPOM (**1.44**) caged groups successfully captured AR in LNCaP lysate following irradiation with light.

2.2 Oligonucleotide Synthesis

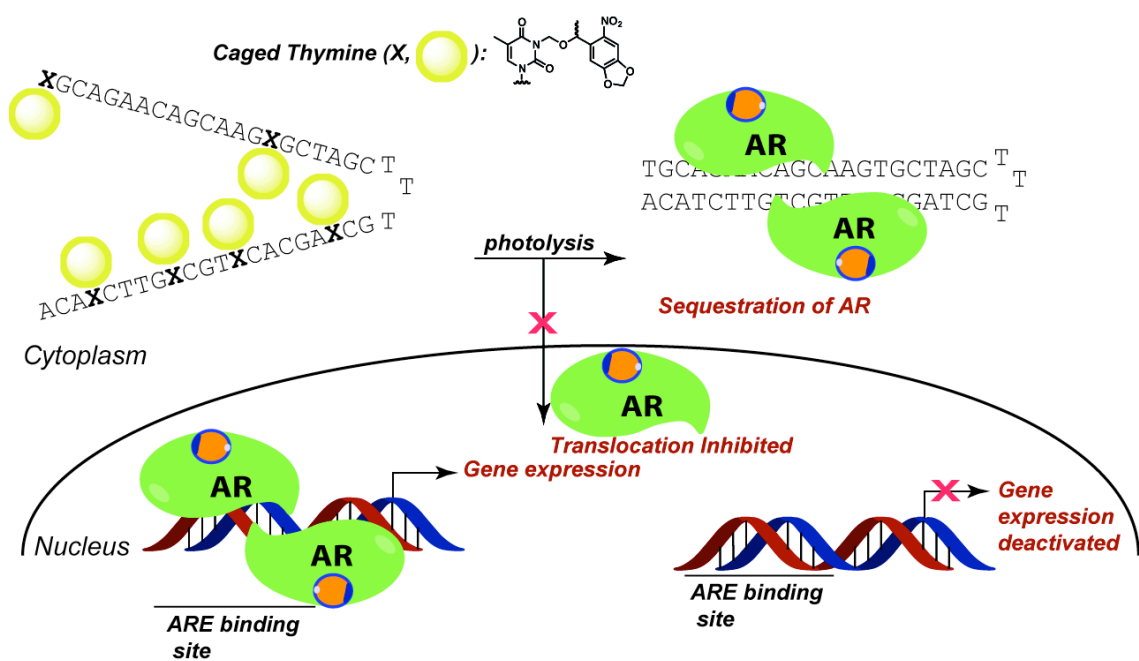


Figure 2.1. Introduction of caged AR-directed DNA decoys. Introduction of caged groups prevent duplex hybridization and AR binding. Upon photolysis and removal of the caging groups, hybridization of the DNA decoy is restored, and AR is sequestered, effectively deactivating gene expression.

We designed caged AR-directed DNA decoys based on the ARE sequence of PSA and utilized a three-thymine loop to yield hairpin DNA decoys that are expected to be stable and efficient (**Figure 2.1**). Introduction of caged groups was hypothesized to prevent duplex hybridization and AR binding based on previous caged DNA examples.²⁰¹ Upon photolysis of the caging groups, hybridization of the DNA decoy is restored, which is hypothesized to sequester AR, and effectively deactivate gene expression.

The NPOM (**1.44**) caging group was developed in 2006,²⁰⁵ has been previously used in caged DNA applications,²⁰⁶ and the phosphoramidite has been made commercially available by Glen Research. With the phosphoramidite in hand, we synthesized several DNA decoys under standard solid-phase DNA synthesis conditions, incorporating this caged thymine in place of native thymines in key positions to block hybridization (**Figure 2.2**). We synthesized decoy **2.1** with one NPOM caging group installed, to study kinetics of uncaging for one group within duplex DNA (**Section 2.5**). As mentioned, the 21 base pair sequence of the ARE of PSA was synthesized as a hairpin with a three-thymine loop (**2.2**) The incorporation of 6 and 8 NPOM caging groups into



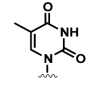
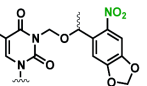
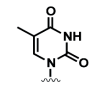
Figure 2.2. Synthesized DNA decoys with varying degrees of NPOM caging. **X** denotes an NPOM caged thymine.

this hairpin was envisioned to be sufficient in order to disrupt duplex formation yielding the ability of spatiotemporal control of AR binding (**2.3** and **2.4**, respectively).

2.3 Thermal Melting Analysis

The thermal stability of the AR-directed DNA decoys containing the NPOM caging groups and their corresponding deprotected products were studied by UV thermal melting experiments (**Table 2.1**).²⁰⁷ The native 45-mer DNA decoy is very thermally stable ($T_m = 86.4$ °C). Incorporation of NPOM caging groups located on both sides of the duplex introduces much more steric hindrance than just on a single side, especially when they are positioned close to one another. Previous studies have shown that complete disruption of DNA hybridization requires a caging group every 4-6 nucleotides throughout the sequence.^{191,208} The introduction of 6 NPOM caged thymines (**2.3**) located

Table 2.1. Thermal melting of **2.2-2.4** demonstrating DNA duplex destabilization from incorporation of NPOM caging groups and restoration of stability upon irradiation with light. Thermal melting experiments were performed in 10 mM sodium cacodylate, 10 mM KCl, 10 mM MgCl₂, 5 mM CaCl₂, pH 7.0 buffer. Mean \pm SD (n = 4).

dsDNA sequence =		2.3		2.4	
		5' - X GCAGAACAGCAAG X GCTAGC _T	5' - X GCAGAACAGCAAG X G X AGC _T		
		3' -ACA X CTTG X CGT X CACG X CG _T	3' -ACA X CT X G X CGT X CACG X CG _T		
Nucleobases		$T_m / ^\circ\text{C}$	$\Delta T_m / ^\circ\text{C}$	$T_m / ^\circ\text{C}$	$\Delta T_m / ^\circ\text{C}$
X = T (2.2)		86.4 (± 0.5)	—	86.4 (± 0.5)	—
X = Caged T		68.1 (± 1.0)	-18.3 (± 1.0)	51.4 (± 3.9)	-35.0 (± 3.9)
X = Photo-lyzed T		86.2 (± 0.3)	—	85.9 (± 0.5)	—

on both sides of the duplex lowers thermal stability of the caged decoy to 68.1 °C compared to the 86.4 °C of the native decoy ($\Delta T_m = -18.3$ °C). Even more perturbed, incorporation of 8 NPOM caged thymines (**2.4**) dramatically lowers thermal stability ($\Delta T_m = -35.0$ °C). Photolysis of both caged DNA decoys resulted in the recovery of thermal stability ($T_m = 86.2$ °C and 85.9 °C, respectively). Similarly to the caged DNA decoys in **Chapter 1.6**, the loss of thermal stability was hypothesized to confer to loss of binding affinity towards AR since duplex DNA is required for TF binding.

2.4 Kinetics of Uncaging

To characterize the kinetics and the identities of the photo-products resulting from irradiation of the caged DNA decoys, we utilized liquid chromatography-mass spectrometry (LC-MS) analysis of an irradiated aqueous sample. As shown in **Figure 2.3**, irradiation of **2.1**, with a single NPOM caging group, yielded fast photolysis ($t_{1/2} = 0.9$ min; 350 nm light; light intensity: 2.38×10^{-8} ein $\text{cm}^{-2}\text{s}^{-1}$). The quantum yield (Φ) of **2.1** was determined to be 0.051, which is comparable to the literature value ($\Phi = 0.094$).²⁰⁹ After 5 minutes of irradiation, very little caged decoy remained, demonstrating efficient uncaging. AR Decoys **2.3** and **2.4** with 6 and 8 caged groups were irradiated similarly to decoy **2.1**. Unexpectedly, multiple products formed upon irradiation (**Figure 2.4**). From the mass spectrum, it was determined that these products were the result of incomplete photolytic decay, whereas 1-4 methoxy groups are still attached to the nucleobase. It is hypothesized that photolysis produces free alcohol **2.7**, and instead of releasing

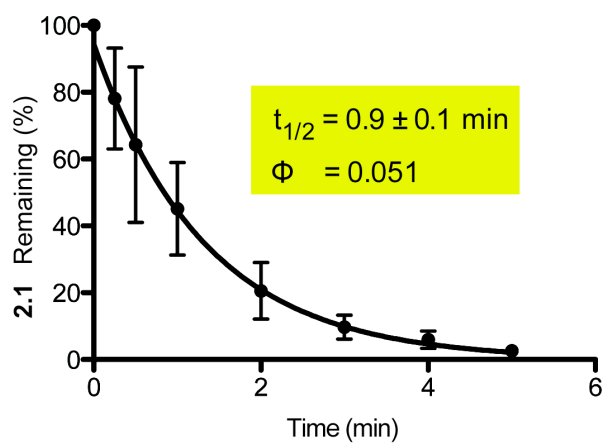


Figure 2.3. Photolytic decay curve of **2.1** with calculated half-life and quantum yield ($R^2 = 0.99$).

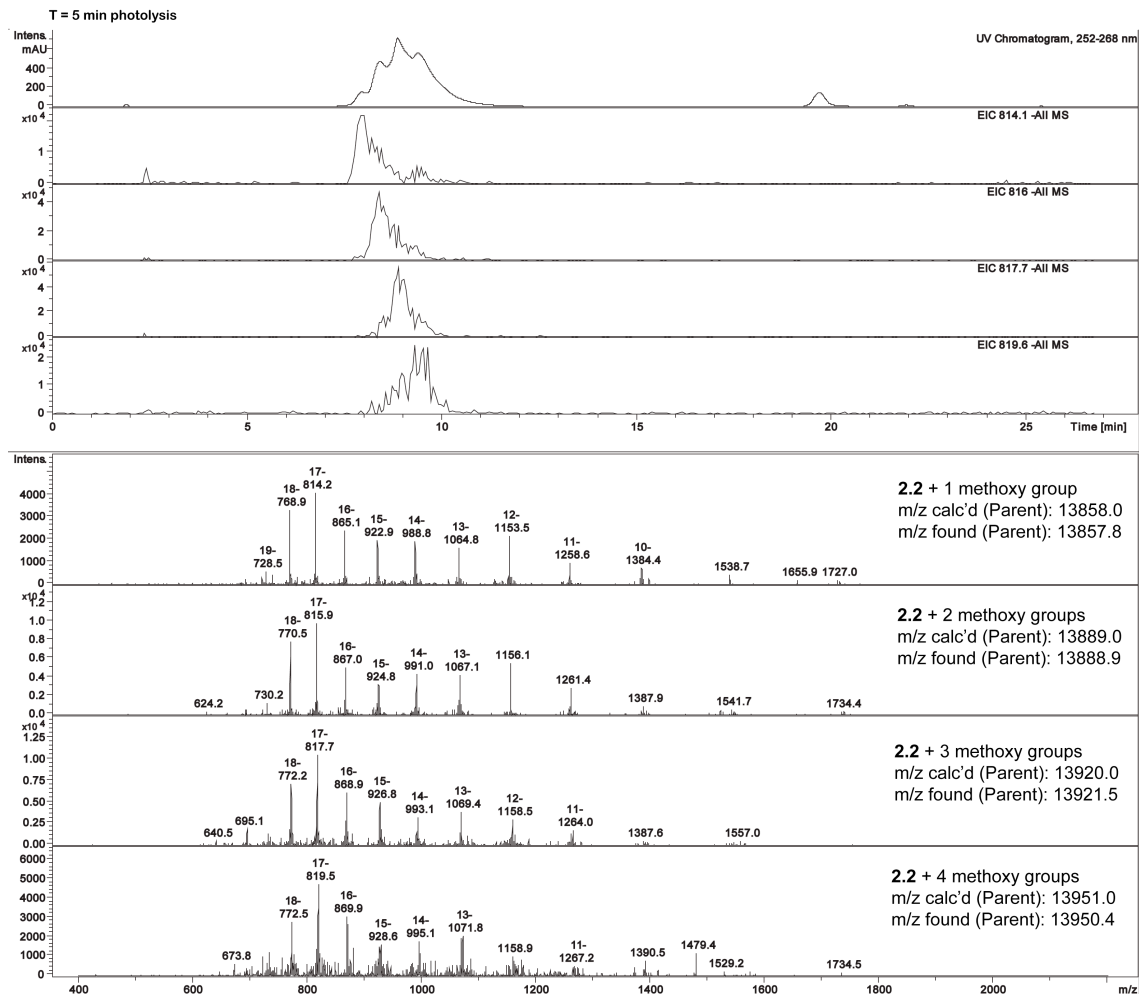
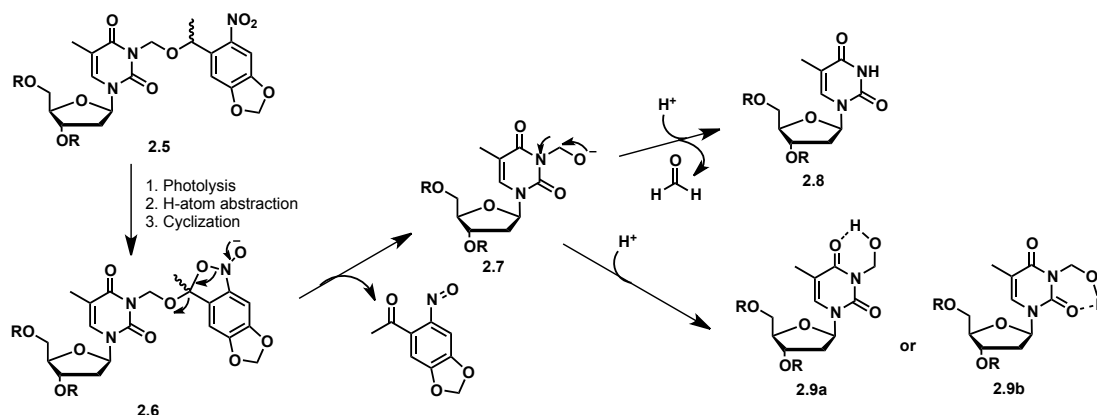


Figure 2.4. Photo-products of **2.3** demonstrating the failed release of formaldehyde resulting in formation of multiple products. Analysis of photo-products at $t = 5$ min from experiment shown in **Figure 2.3**.

formaldehyde to yield the native thymine **2.8**, the pendant methoxy group engages in a six-membered ring that is stabilized by an intramolecular hydrogen-bond (**2.9**, **Scheme 2.1**). Brief preliminary studies suggests pH dependence, where a low pH (pH 3-5) prevents formaldehyde release while a high pH (pH 10-13) encourages formaldehyde release yielding the native decoy complex.



Scheme 2.1. Photolytic decay mechanism of NPOM caging group leading to either formation of the native thymine **2.8** or the residual methoxy group getting trapped in the six-membered ring **2.9**.

2.5 Capturing AR Utilizing Caged DNA Decoys

We next evaluated the ability of the AR-directed decoys to capture AR by electrophoretic mobility shift assays (EMSAs). ^{32}P -labeled **2.2-2.4** were added to a solution of testosterone induced LNCaP lysate and protein binding was measured. Native AR-directed DNA decoy **2.2** exhibited the appropriate band shift demonstrating AR binding (**Figure 2.5, lane 2**). Addition of LNCaP lysate to the 6 or 8 caged DNA decoys, **2.3** and **2.4**, were unable to bind the protein efficiently (**Figure 2.5, lanes 4 and 7**). Irradiation of **2.3** and **2.4** with 350 nm light for 5 minutes, resulted in partial restoration

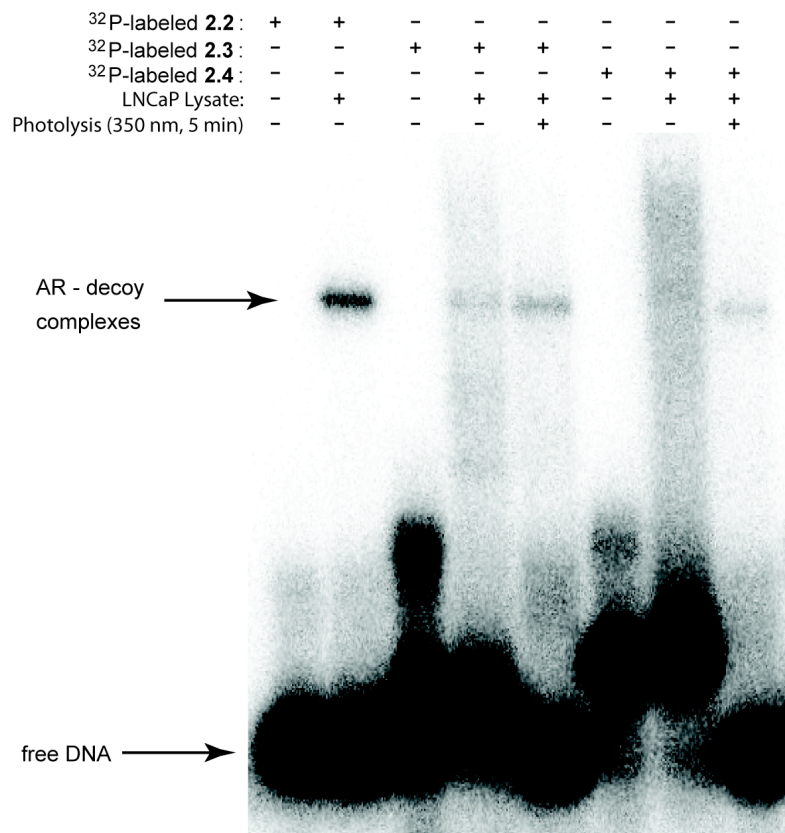
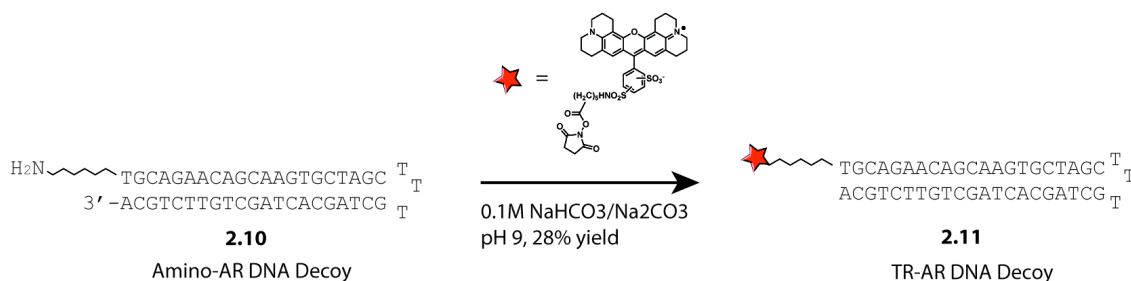


Figure 2.5. Electrophoretic mobility shift assays with **2.2-2.4**. $5'$ - 32 P-labeled **2.2** incubated with AR rich LNCaP lysate demonstrated the ability to bind AR (**lane 2**). $5'$ - 32 P-labeled **2.3-2.4** incubated with LNCaP lysate were unable to bind the protein with efficiency (**lanes 4 and 7**). Irradiation of samples followed by addition of LNCaP lysate demonstrated capture of the AR protein (**lanes 5 and 8**).

the native complex as discussed above. Addition of lysate to the photolyzed **2.3** and **2.4** yields evidence of protein binding (**Figure 2.5, lanes 5 and 8**). The binding events following photolysis are weaker than native **2.2** (**Figure 2.5, lane 2**), presumably because of the incomplete photolytic decay to the native decoy.

2.6 Cellular Location of DNA Decoys Utilizing Confocal Microscopy

With evidence demonstrating that our decoys can capture the AR protein, we synthesized a Texas Red (TR) labeled AR-directed DNA decoy to detect whether the decoy could be transfected into LNCaP cells and where within the cell the decoys would be distributed. We purchased the 5'-C₆-amino derivative of the native decoy **2.2**, decoy **2.10**, and conjugated it to the NHS-ester of Texas Red (TR), yielding AR decoy **2.11**. In future studies, this decoy will be transfected into LNCaP cells to determine sub-cellular location and transfection efficiency of the DNA decoys.



Scheme 2.2. Synthesis of TR-labeled AR-directed DNA decoys for confocal microscopy studies.

2.7 Conclusions and Future Work

Hairpin DNA decoys were designed to tightly bind and sequester the AR protein. Addition of NPOM caging groups to these decoys created steric interactions, which reduced their duplex stability and dramatically affected their affinity for AR. Photolysis of **2.3** and **2.4** restores the duplex, providing evidence for the photochemical sequestration of AR. Thermal melting analysis and electrophoretic mobility shift assays

were used to characterize the caged decoys **2.3** and **2.4**. The introduction of 6 NPOM caged thymines (**2.3**) lowers thermal stability of the caged decoy to 68.1 °C compared to the 86.4 °C of the native decoy ($\Delta T_m = -18.3$ °C). Even more perturbed, incorporation of 8 NPOM caged thymines (**2.4**) dramatically lowers thermal stability ($\Delta T_m = -35.0$ °C). This result was very encouraging, which demonstrates lack of thermal stability and duplex formation needed to abolish AR binding affinity. Kinetic studies determined the speed of this process, demonstrating loss of caging groups within one minute; however, the major product formed was not the native decoy **2.2**. Due to incomplete uncaging, multiple methoxy adducts remained on the decoy. This result is believed to have hindered the binding of AR in the EMSA assays (**Figure 2.5, lanes 5 and 8**) and is a major limitation of this technology. One method currently being investigated to overcome this limitation is by synthesizing O⁶-linked NPOM thymines lacking the methoxy linker, thus removing the intermediate in the photolytic decay process leading to methoxy adducts. This simpler uncaging method should result in improved protein binding similar to native **2.2**. Other than switching caging methods, other future directions for this project will include transfections of the decoys into mammalian cells. We will be using variety of chemical transfection reagents and electroporation methods to transfect the DNA decoys into LNCaP cells to sequester the AR in mammalian cells. The TR-labeled AR-directed decoy will allow characterization of transfection efficiency. Overall, this AR-directed caged DNA decoy strategy enabled the precise capture of AR in a spatiotemporal manner, which can have great potential as therapeutic agents and will enable the study of the AR gene function in biological pathways.

2.8 Experimental Section

2.8.1 Solid-Phase DNA Synthesis. Oligonucleotides were synthesized using standard solid-phase phosphoramidite chemistry on an Applied Biosystems 394 DNA/RNA synthesizer.²¹⁰ All phosphoramidites, solvents, and solid supports (1.0 μmol) were purchased from Glen Research Corporation. Following the synthesis, the resin was transferred to a fritted reaction vessel. Concentrated aqueous ammonium hydroxide (2.5 mL) was added and the vessel was placed in a shaker for 18 hours at room temperature. After deprotection, the solution was filtered into a centrifuge tube (10 mL) and distilled water (2 mL) was added. The ammonium hydroxide was evaporated *in vacuo* (samples were transferred to microcentrifuge tubes and placed in a SpeedVac) and the remaining solution was purified by HPLC (see below). After purification, the oligonucleotides were desalted with DNase/RNase free H₂O using Illustra NAP-5 columns (Sephadex G-25 DNA grade, GE Healthcare) according to manufacturer instructions. The desalted oligonucleotides were quantified by UV-Vis (A_{260} , using predicted molar extinction coefficients for native dNTPs and $\epsilon=5,000 \text{ M}^{-1} \text{ cm}^{-1}$ for NPOM at 260 nm) and confirmed by LC-MS (see below). The purity was assessed by HPLC reinjection of the purified oligonucleotides (see **Appendix B** for chromatograms).

Oligonucleotide **2.1**. Purity = 87.7% (260 nm). MS calc'd 9741.1, found 9741.6 (parent)

Oligonucleotide **2.2**. Purity = 88.6% (260 nm). MS calc'd 13827.0, found 13827.8 (parent)

Oligonucleotide **2.3**. Purity = 96.9% (260 nm). MS calc'd 15163.4, found 15163.2 (parent)

Oligonucleotide **2.4**. Purity = 86.0% (260 nm). MS calc'd 15609.2, found 15610.4 (parent)

Oligonucleotide **2.10**. Purity = 75.2% (260 nm). MS calc'd 14015.2, found 14015.7 (parent)

Oligonucleotide **2.11**. Purity = 91.4% (260 and 589 nm). MS calc'd 14708.0, found 14721.2 (parent)

2.8.2 HPLC Purification & LC-MS Analysis. Oligonucleotides were HPLC purified on an Agilent 1200 series instrument equipped with a diode array detector and a PLRP-S column (8 μm , 100 \AA , 4.6 x 150 mm, Agilent Technologies). The analysis method (2.750 mL/min flow rate) involved isocratic 100 mM TEAA (aqueous, pH 7.0, Sigma-Aldrich; 0 to 5 mins) followed by a linear gradient to 10% 100 mM TEAA:MeCN (1:1, 5 to 10 mins) and finally a linear gradient of 30% to 70% 100 mM TEAA:MeCN (1:1, 10 to 45 mins). Wavelengths monitored = 215 nm and 260 nm. LC-MS was performed on an Agilent 1100 series HPLC instrument equipped with an Agilent MSD SL Ion Trap mass spectrometer (operating in negative ion mode). A Zorbax SB-C18 column (5 μm , 300 \AA , 0.5 x 150 mm, Agilent Technologies) was used for LC-MS analysis. The analysis method (15 $\mu\text{L}/\text{min}$ flow rate) involved 15 mM aqueous NH_4OAc containing 2% MeCN followed by a linear gradient of 2% to 25% MeCN (0 to 15 mins) and 25% to 60% MeCN (15 to 25 mins). Wavelengths monitored = 215 nm and 260 nm.

2.8.3 Thermal Melting Analysis. Thermal melting analyses were performed on a temperature-controlled Agilent Cary 100 UV-Vis spectrophotometer containing a 6-cell block with a path length of 1 cm. A degassed aqueous solution of 10 mM sodium cacodylate, 10 mM KCl, 10mM MgCl₂, and 5 mM CaCl₂ (pH 7.0) was used as analysis buffer.²¹¹ Oligonucleotides (1 nmol) were mixed in the buffer (1 mL). Before data collection, samples were heated to 90 °C and cooled to a starting temperature of 30 °C with a 5 °C/min ramp. Data points were recorded at $\lambda = 260$ nm every 12 seconds on a 0.5 °C/min ramp from 30 °C to 90 °C. After data collection, the sample was cooled back down to 30 °C on a 5 °C/min ramp. The method was repeated to obtain a technical replicate. The experiment was repeated to obtain a biological replicate (n=4 total analyses). The reported thermal melting temperatures (T_m) were calculated from the maximum of the first derivative of the denaturation curve (Cary WinUV Thermal Application; v 4.20). Mean T_m values (with standard deviation) were calculated in Microsoft Excel from the individual T_m values obtained from each replicate (n = 4).

2.8.4 Photolysis, Exponential Decay, and Quantum Yield Analysis. DNA photolysis experiments were carried out using a Rayonet photochemical reactor (RMR-600, Southern New England Ultraviolet Co.) fitted with two, 350 nm bulbs. To enable quantitative analysis of photochemical decay of DNA decoys, calibration plots for each DNA decoy were generated. Increasing concentrations of each DNA decoy (0.55, 1.65, 4.94, 14.81, 44.44, 133.33 pmol) were added to a fixed concentration of a non-modified

DNA oligonucleotide (5'-TAACTA-3', 100 pmol) and analyzed by extracted ion current (EIC) LC-MS (masses monitored at -9 charge state for decoys).²¹² A calibration plot was created by plotting the ratio of decoy:standard area under the curve (AUC) versus DNA decoy concentration, yielding calibration plots with a slope-intercept equation of $R^2 > 0.99$.

Quantitative analysis of DNA decoy photolysis was performed by dissolving the DNA decoy (800 pmol) in DNase/RNase free H₂O and then adding the solution to conical pulled point vial inserts (250 μ L; Agilent, 8010-0125). Vessels containing the aqueous DNA solution was placed into the photochemical reactor and irradiated (light intensity: 2.38×10^{-8} ein $\text{cm}^{-2} \text{s}^{-1}$; calculated as described below). Aliquots (4 μ L) were taken at several time points (0, 0.25, 0.5, 1, 2, 3, 4, 5 min), diluted with standard (1 μ L) and then analyzed by LC-MS. The concentration of the decoy species from irradiation were determined by fitting the decoy/standard ratios from each sample into the slope-intercept equation from the calibration plot to yield the amount of decoy (pmol) in sample (performed in Microsoft Excel). This process was repeated for each prominent molecular ion observed in the photolysis sample. Furthermore, this quantitative analysis method assures comparable ionization properties for the photolyzed products in comparison to the non-irradiated sample. First order decay analysis (GraphPad Prism; v5.0b) was then fitted to the data (percentage of starting material over time) to obtain the decay equation and half-life ($t_{1/2}$) of the DNA decoy. Mean $t_{1/2}$ values (with standard deviation) were calculated in Microsoft Excel from the fitting of the decay curve with the individual data points obtained from each replicate ($n = 4$).

Quantum yield (Φ) calculations were carried out to determine the efficiency of photolysis of caged **2.2.1** (eq. 1). The intensity of the light source (I , eq. 2) was determined using $K_3[Fe(C_2O_4)_3]$ actinometry as previously described.^{213,214} In brief, a solution of $K_3[Fe(C_2O_4)_3] \cdot 3H_2O$ in distilled H_2O (6 M, 2 mL) was irradiated for 180 seconds in the Rayonet equipped with two, 350 nm bulbs. After irradiation, the sample was transferred to a volumetric flask (25 mL). To the flask was added aqueous buffer (3 mL; recipe to make a 500 mL solution of aqueous buffer: 300 mL of 1.0 M NaOAc, 180 mL of 1.0 M H_2SO_4 , and 20 mL distilled H_2O), phenanthroline solution (3 mL of 0.1% v/v phenanthroline in distilled H_2O), KF solution (1 mL of a 2.0 M solution), and distilled water (~18 mL, to 25 mL). The solution was placed in the dark for 1 hour. A non-irradiated sample was prepared in the same manner. After 1 hour, the solutions were transferred to a cuvette and the A_{510} was measured for both samples. The Rayonet light intensity was then calculated using eq. 2 (2.38×10^{-8} ein $cm^{-2} s^{-1}$). The extinction coefficient at 350 nm (ϵ_{350}) of caged decoy **2.2.1** was calculated by UV-Vis absorbance using the Beer-Lambert law ($5077 M^{-1} cm^{-1}$). The irradiation time for 90% conversion ($t_{90\%}$) of the DNA decoy was calculated from the first order decay equation (above). Quantum yield was then calculated using eq. 1 to give a value less than one.²¹⁵

$$\text{(Eq. 1)} \quad \Phi = (I * \sigma * t_{90\%})^{-1}$$

where σ ($cm^2 mol^{-1}$) is equal to $1000 * \epsilon_{350}$ of the DNA decoy

$$\text{(Eq. 2)} \quad I \text{ (ein } cm^{-2} s^{-1}) = (V_1 * V_3 * \Delta A_{510}) / (1000 \text{ (mL/l)} * \epsilon_{510} * V_2 * \Phi_{Fe} * t)$$

where V_1 is the volume of $K_3[Fe(C_2O_4)_3]$ irradiated (mL); V_2 is the volume of the $K_3[Fe(C_2O_4)_3]$ solution transferred to the volumetric flask (mL); V_3 is the volume of the volumetric flask (mL); ΔA_{510} is the difference in absorbances at 510 nm between the irradiated and non-irradiated samples; ϵ_{510} is the extinction coefficient of $K_3[Fe(C_2O_4)_3]$ at 510 nm ($11,100 \text{ cm}^{-2} \text{ s}^{-1}$)²¹³; Φ_{Fe} is the quantum yield of $K_3[Fe(C_2O_4)_3] \cdot 3H_2O$ (1.21)²¹³; and t is the time irradiated (s).

2.8.5 ³²P Radiolabeling. DNA decoys in DNase/RNase free water were annealed by heating to 95 °C in a heating block for 5 minutes, followed by slow cooling to room temperature. To a microcentrifuge tube (1.7 mL) was added the annealed DNA decoy (50 pmol) and T4 polynucleotide kinase (PNK) buffer (5 μ L of a 10X solution, Thermo Scientific). DNase/RNase-free H₂O was added to yield a final volume of 40 μ L. The reaction tube was placed into a shielded rack then [γ -³²P]-ATP (5 μ L; 6,000 Ci/mmol, Perkin Elmer) was added. PNK was diluted in DNase/RNase-free H₂O (1:10) then added to the reaction (5 μ L). The reaction was briefly mixed, centrifuged (to remove any material from cap), and then placed in a 37 °C heat block for 30 minutes. Heating to 70 °C for 30 minutes in the second heat block was then used to inactivate the kinase. The radioactive reaction mixture was transferred to an Illustra MicroSpin G-50 column (GE Healthcare, prepared according to vendor instructions) and centrifuged at 1500 rpm for 20 seconds to yield ³²P-labeled oligonucleotides. The radioactivity of the oligonucleotides were quantified (counts/min/ μ L) by transferring an aliquot to an

Eppendorf tube followed by analysis on a Beckman LS 6500 multi-purpose scintillation counter (dry counting).

2.8.6 Electrophoretic Mobility Shift Assay (EMSA). Binding reactions containing binding buffer (2 μL of a 10X solution; 10X solution: 100 mM Tris, 10 mM EDTA, 500 mM NaCl, and 10% NP-40),⁹² sheared salmon sperm DNA (1 μL of a 1.0 $\mu\text{g}/\mu\text{L}$ solution), and DNase/RNase free H_2O (to a final volume of 20 μL) were prepared in microcentrifuge tubes (0.65 mL) and incubated on ice for 30 mins. ^{32}P -labeled DNA decoys (1 μL , 25,000 counts/min/ μL) were added to the binding reaction. Binding reactions were then transferred to glass HPLC vial inserts (each 20 μL binding reaction was pipetted into individual inserts) and irradiated (with the exception of non-irradiated control samples) in the Rayonet with two 350 nm bulbs (2.28×10^{-8} ein $\text{cm}^{-2} \text{s}^{-1}$) at room temperature. The samples were taken out of the Rayonet at various time points and transferred (~20 μL volume) to a new microcentrifuge tube (0.65 mL). Testosterone induced LNCaP lysate (1 μL of a 4.0 $\mu\text{g}/\mu\text{L}$ solution, Active Motif) was added to the binding reaction. All samples and controls were then incubated at room temperature for 20 min. Loading dye (2 μL , 10X solution; 0.5X TBE, 40% glycerol, 2 mg/mL Orange G dye, Sigma) was added to each reaction and samples were loaded onto a 5% non-denaturing PAGE gel that was pre-run at 200 V for 1 hr in 0.5X TBE. Samples were electrophoresed at 200V until the loading dye was $\sim 3/4$ down the gel. The gel was transferred to filter paper (Bio-Rad; the plates were pried apart and the gel was placed on the wetted filter paper), covered with plastic wrap and cellophane (Bio-Rad), and dried

for 1 hr (Gel Air Dryer, Bio-Rad). The gel was transferred to a phosphorimager screen overnight and then analyzed on a Typhoon FLA 7000 biomolecular imager (GE Healthcare). Images were analyzed using Image Quant TL software (v 7.0, GE Healthcare).

2.8.7 Texas Red Conjugation. The amino-modified oligonucleotide **2.10** (0.1 μ mol of free primary amines) was dissolved in 0.7 mL DNase/RNase free H₂O. 10X conjugation buffer (1M NaHCO₃/Na₂CO₃, pH 9, 0.1 mL) was added to the oligonucleotide. A freshly prepared 10 mg/mL solution of active Texas Red NHS ester (Molecular Probe) in DMF (0.2 mL) was added to the reaction mixture. The mixture was vortexed and reacted with a stir bar for 24 hours. The reaction was HPLC purified and desalted to afford **2.11** (28 nmol, 28% yield).

Chapter 3

7-NITROINDOLE (7-NI) CONTAINING NF- κ B-DIRECTED ‘CATCH AND RELEASE DNA DECOYS’ (CRDDs)

This work was performed in collaboration with Bryant Keller and Professor Daniel A. Harki. In this work, Bryant Keller was responsible for synthesizing the 6-nitroindole phosphoramidite and oligonucleotide **3.23**.

3.1 ‘Catch and Release’ DNA Decoys (CRDDs) and the NF- κ B Signaling Pathway

The caged DNA decoy examples in **Chapter 1.6** and **Chapter 2** demonstrate the precise activation of decoys in a spatiotemporal manner, which has potential as therapeutic agents and may enable the studies specific TFs by deactivation of their signaling pathways. However, biochemical signaling pathways are extremely complex and involve inter-pathway cross talk, which complicates their study and analysis. For instance, it has been demonstrated that the transcription factor Nuclear Factor Kappa B (NF- κ B) is constitutively activated in prostate cancer and regulates AR expression.^{216,217} NF- κ B interacts and cooperates with more than 40 other TFs in cancer.⁴⁷ Additionally, it has been shown that oscillation in NF- κ B signaling controls the dynamics of gene expression, and therefore, it is quite difficult to obtain more than a snapshot of the function of these types of transcription factors.^{218,219} Given the real-time complexity of cellular signaling pathways and the limitations of current technologies, including engineered cell lines,²²⁰ there is a need for chemical tools to study the activation of gene-specific TFs in a spatiotemporal manner.

To study the activation of TF pathways, biomedical researchers typically dose cells with exogenous stimulatory ligands, such as small molecules or proteins, to activate specific pathways of interest. One example is tumor necrosis factor (TNF), which is widely used to activate the canonical NF- κ B pathway. However, it has been shown that TNF activates more than the NF- κ B pathway, including the MAP kinase and death receptor pathways (**Figure 3.1ai**).^{60,221} Therefore, the utilization of signaling molecules

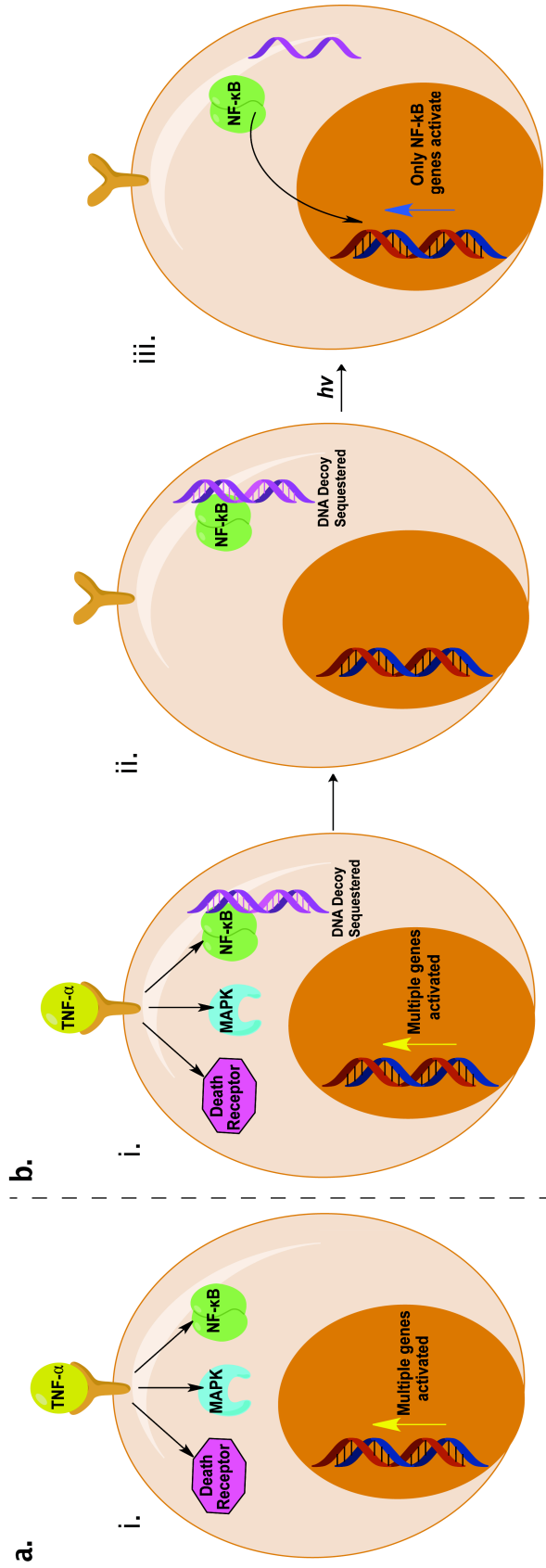


Figure 3.1. Catch and Release DNA Decoy strategy. (a) TNF- α addition results in the induction of multiple pathways including NF- κ B (b) i. TNF- α addition results in the induction of multiple pathways including NF- κ B. ii. NF- κ B sequestered in cytoplasm by a DNA decoy. iii. Photolytic release of NF- κ B allowing translocation and the activation of NF- κ B target genes.

such as TNF can result in the incorrect assignment of a subset of NF- κ B-controlled cellular processes due to other signaling pathways being stimulated in addition to the desired (NF- κ B) target (**Figure 3.1a**).

This problem can be overcome through a ‘catch and release’ mechanism of NF- κ B sequestering, re-establishment of equilibrium, then photochemical release allowing exclusive activation of NF- κ B driven genes in a spatiotemporal manner (**Figure 3.1b**). As discussed in **Chapter 1.4**, the DNA decoy strategy can be considered one of the most useful approaches to examine molecular mechanisms of TFs and their specific signaling pathways. This has been demonstrated utilizing a cAMP response element (CRE)-directed DNA decoy and analyzing alterations in gene expression by DNA microarrays. The CRE-directed decoy sequestered the TF, which resulted in the up-regulation of the AP-2 β and other genes involved in development and cell differentiation, and down-regulated different clusters of genes involved in cell proliferation and transformation. This indicates that CRE transcription favors tumor growth and may serve as a target to treat cancer.²²² We hypothesized that a photo-responsive ‘on-to-off’ DNA decoy could sequester NF- κ B in the cytoplasm following TNF- α stimulation (**Figure 3.1bi**). DNA decoys are known to have half-lives of ~3 days *in vitro* and ~5 days *in vivo*,²²³ therefore, we predicted that the cell would re-establish an equilibrium following withdraw of the signaling ligand (**Figure 3.1bii**). Finally, the NF- κ B transcription factor could be then released from the DNA decoy photochemically (**Figure 3.1biii**) to yield exclusive activation of NF- κ B target genes after nuclear translocation. This ‘Catch and Release’ approach could then allow for an in-depth understanding of the mechanisms that activate

gene expression and precise mapping of complex signaling pathways and their cross talk, such knowledge could be valuable information for the understanding of disease processes and for the development of therapeutic agents.^{37,224}

3.2 CRDD Design and Synthesis

We developed a novel class of DNA decoys, termed ‘Catch and Release DNA Decoys (CRDDs)’, that capture and release DNA-binding proteins using a light trigger (**Figure 3.2**). Unlike caged DNA decoys, CRDDs are an ‘on-to-off’ platform that utilizes light to promote photochemical destruction of the DNA decoy and dissociation of the protein-DNA complex. Our design utilizes depurination-competent mimics of natural nucleobases that when incorporated into a DNA decoy function as natural nucleobases and enable decoy binding to its designed protein target. However, CRDD photolysis results in formation of multiple abasic sites within the decoy, as well as truncated decoys resulting from β - and δ -elimination at abasic sites, yielding a modified CRDD that possesses significantly diminished affinity for its design protein target. Consequently, CRDD photolysis enables release of the sequestered protein target.

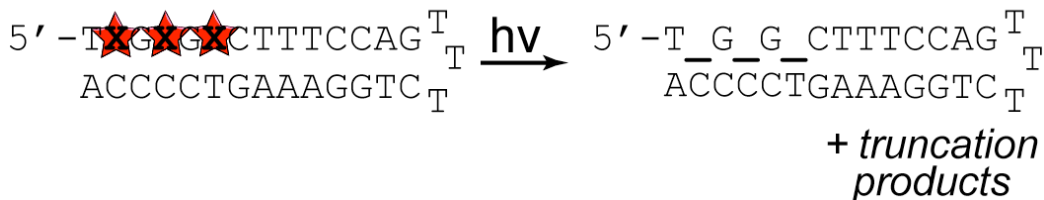


Figure 3.2. A Catch and Release DNA Decoy (CRDD) targeting the NF- κ B transcription factor. Photolysis of DNA decoys containing photo-responsive nucleotides (X with stars) with UV-light (hv) results in formation of abasic sites () and strand cleavage products (not shown).

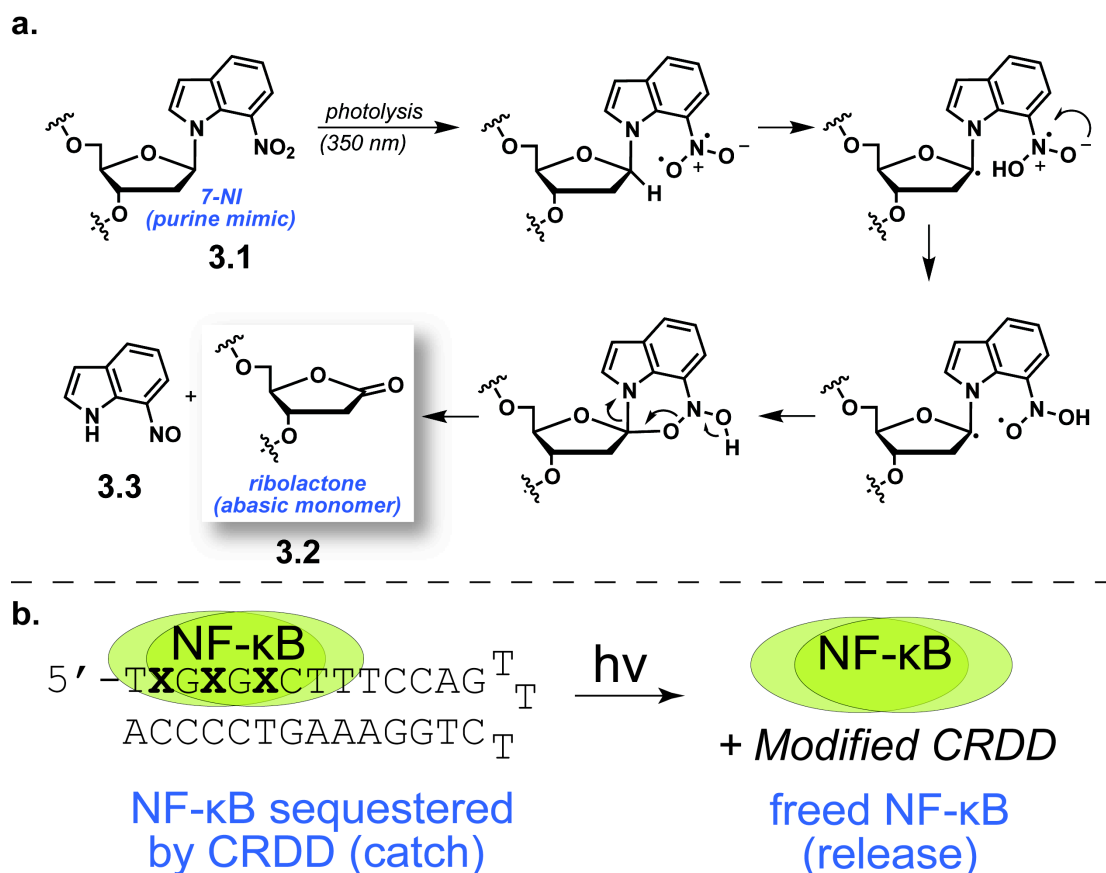
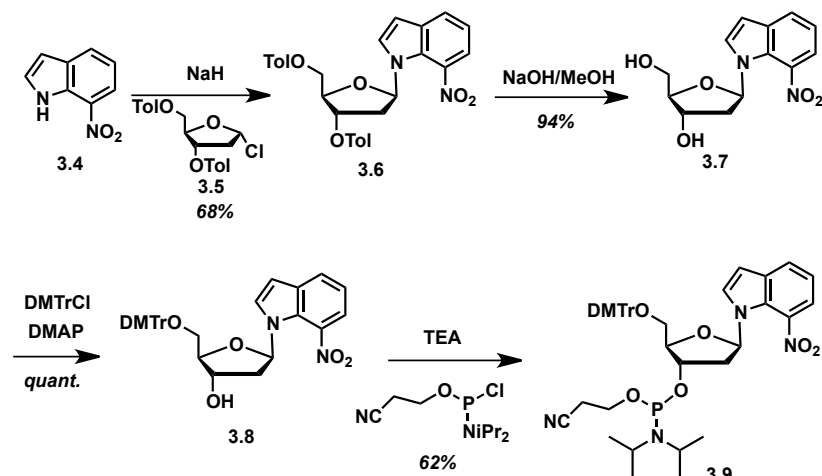


Figure 3.3. (a) 7-Nitroindole-containing nucleotides (**3.1**) depurinate with UV-light resulting information of 2'-deoxyribose-5-phosphate **3.2** and 7-nitrosoindole (**3.3**) products. (b) Incorporation of three 7-nitroindole nucleotides ($X = 3.1$) into a DNA decoy sequence known to target the NF- κ B proteins still permit protein binding (catch). Photolysis of the decoy with UV-light (350 nm) results in the formation of multiple abasic sites and truncation products that have lowered affinity for the protein, thereby enabling dissociation of the NF- κ B-CRDD complex (release).

Incorporation of 2-nitrobenzylethers in place of native nucleobases in DNA oligonucleotides has been utilized as a strategy to generate abasic sites photochemically with sequence specificity.²²⁵⁻²²⁷ Additionally, 7-nitroindole (**3.1**) has been shown to photochemically depurinate in DNA oligonucleotides, through formation of a diradical, hydrogen atom abstraction, heterocycle formation and degradation similar to the 2-NB mechanism (**Scheme 1.3**), yielding a 2'-deoxyribose-5-phosphate (**3.2**) abasic site in DNA, which can undergo β - and δ -elimination resulting in strand cleavage, and a 7-nitrosoindole (**3.3**)

by-product (**Figure 3.3a**).²²⁸⁻²³¹ Given the obvious structural similarities between indole heterocycles and purine nucleobases, which is further reinforced by work demonstrating that 5-nitroindole can serve as a ‘universal base’ in DNA²³² and that both 5- and 7-nitroindole nucleobases can be enzymatically recognized by Klenow fragment DNA polymerase I,²³³ we hypothesized that 7-nitroindole may suitably mimic natural purines in established DNA decoys that bind the NF- κ B proteins. Furthermore, we hypothesized that photolysis of the NF- κ B-decoy complex would enable protein release through photochemical destruction of the decoy as previously described (**Figure 3.3b**).

The synthesis of phosphoramidite **3.9** starting from 7-nitroindole (7-NI, **3.4**) can be prepared in four steps as previously described (**Scheme 3.1**).^{228,234} S_N2 displacement of 3',5'-*O*-toluoyl-1'- α -chloro-2'-deoxyribose **3.5** with the sodium salt of 7-nitroindole (**3.4**) yields the protected 7-NI nucleoside **3.6**. Deprotection of the toluoyl protecting groups, followed by 5'-hydroxyl protection with 4,4'-dimethoxytrityl chloride afforded **3.8**. Finally, incorporation of the phosphoramidite on the 3'-hydroxyl group of the



Scheme 3.1. Synthesis of 7-nitroindole-containing phosphoramidite **3.9**.

nucleoside yielded 7-nitroindole-2'-deoxyribose phosphoramidite **3.9**, which is now ready for incorporation into CRDDs by solid-phase oligonucleotide synthesis.

The NF- κ B signaling pathway regulates scores of cellular processes associated with inflammation, cell survival and proliferation, and aberrant NF- κ B activity is frequently found in cancer, cardiovascular disease, and autoimmune diseases.²³⁵ Given the fundamental role of NF- κ B signaling in many human diseases, as well as strong precedence for the development of NF- κ B-targeted DNA decoys,²³⁶⁻²⁴⁰ including caged reagents,²⁰¹ we developed our first CRDD against the NF- κ B proteins. The four purine site of the NF- κ B consensus sequence (5'-GGGRNYYYCC-3', where R is a purine, Y is a pyrimidine, and N is any nucleotide) is crucial for DNA binding of p50.²⁴¹ Therefore, we utilized established NF- κ B decoy **3.10**²⁰¹ as our base hairpin sequence for optimizing NF- κ B-targeted CRDDs (**Figure 3.4**). One-to-three purines included in or flanking the 4-

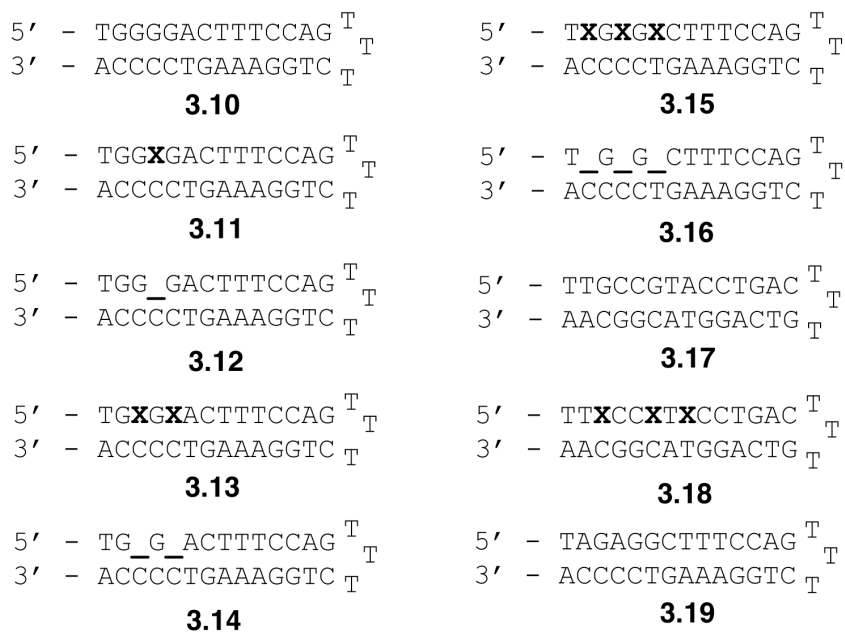
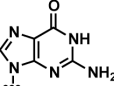
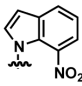
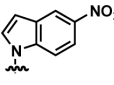
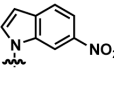


Figure 3.4. Synthesized decoys **3.10-3.19** (X = **3.1**; = **3.2**).

G site were replaced with 7-NI nucleotides, yielding CRDDs **3.11**, **3.13**, and **3.15**. The substitutions of the 7-NIs were also placed in succession to amplify the result of multiple depurination events in a concentrated area. These decoys were synthesized using **3.9** under standard solid-phase DNA synthesis conditions. Photolysis of **3.11**, **3.13**, and **3.15**, followed by purification afforded decoys **3.12**, **3.14**, and **3.16** containing one, two, and three abasic sites, respectively. A control scrambled DNA decoy **3.17** and scrambled CRDD containing three 7-NI nucleotides **3.18** were also synthesized, as well a DNA decoy with three base pair mismatches **3.19** in place of the three 7-NI nucleotides.

3.3 Thermal Melting Analysis

Table 3.1 Thermal melting of duplex DNA containing the 7-nitroindole **3.21** and 6-nitroindole **3.23** nucleotides. DNA containing the 5-nitroindole nucleotide **3.22**, an established universal base,²³² was used as a control. Thermal melting experiments performed in 10 mM sodium cacodylate, 10 mM KCl, 10 mM MgCl₂, 5 mM CaCl₂, pH 7.0 buffer.²¹¹ Mean \pm SD (n = 4) are shown.

dsDNA sequence =					
		5' - CCTTTTT X TTTTTGG - 3'			
		3' - GGAAAAA Y AAAAACC - 5'			
Nucleobases		Y = G	Y = A	Y = C	Y = T
X = G (3.20)		47.4 (\pm 0.7)	45.9 (\pm 0.8)	57.3 (\pm 0.5)	48.5 (\pm 0.5)
X = 7-NO ₂ Indole (3.21)		40.3 (\pm 0.4) [-7.1]	42.8 (\pm 0.5) [-3.1]	42.1 (\pm 0.2) [-15.2]	42.1 (\pm 0.5) [-6.4]
X = 5-NO ₂ Indole (3.22)		44.7 (\pm 0.3) [-2.7]	46.2 (\pm 0.6) [0.3]	49.8 (\pm 0.5) [-7.5]	45.8 (\pm 0.4) [-2.7]
X = 6-NO ₂ Indole (3.23)		43.8 (\pm 0.5) [-3.6]	46.4 (\pm 0.7) [0.5]	47.3 (\pm 0.4) [-10.0]	45.4 (\pm 0.4) [-3.1]

The thermal stability of DNA duplexes and hairpins containing the 7-NI nucleobase was studied by UV thermal melting experiments and compared to native guanine **3.20**.²⁰⁷ First, 7-NI was singly incorporated into oligonucleotide **3.21** and thermal melting of duplex DNA containing all natural nucleotides hybridized to 7-NI was measured. In addition, the DNA stability of duplexes containing 5-nitroindole **3.22** and 6-nitroindole **3.23** nucleobases was included for comparison (**Table 3.1**).^{207,231,232} In comparison to G-C pairing, incorporation of 5-nitroindole **3.22** into duplex DNA in place of guanine decreases stability ($\Delta T_m = -7.5$ °C), while 6-nitroindole **3.23** is more destabilizing ($\Delta T_m = -10.0$ °C), and 7-nitroindole **3.21** is even more destabilizing ($\Delta T_m = -15.2$ °C). However, 7-Nitroindole **3.21** is the only nucleotide able to undergo photochemical depurination.

Table 3.2 Thermal stability of synthesized NF- κ B-directed (**3.10-3.16**), scramble (**3.17** and **3.18**), and three base pair mismatch (**3.19**) CRDDs. Thermal melting of **3.10-3.16** demonstrating DNA duplex destabilization resulting from incorporation of 7-nitroindoles (CRDDs **3.11**, **3.13**, and **3.15**) and more predominantly, abasic sites (CRDDs **3.14** and **3.16**). Thermal melting of **3.17-3.19** demonstrating scramble DNA duplex destabilization resulting from incorporation of 7-nitroindoles (**3.18**) and destabilization from incorporation of base pair mismatches (**3.18**). Thermal melting experiments were performed in 10 mM sodium cacodylate, 10 mM KCl, 10 mM MgCl₂, 5 mM CaCl₂, pH 7.0 buffer. Mean \pm SD (n = 4).

DNA	$T_m / ^\circ\text{C}$	$\Delta T_m / ^\circ\text{C}$	DNA	$T_m / ^\circ\text{C}$	$\Delta T_m / ^\circ\text{C}$
3.10	82.6 (± 0.4)	—	3.15	70.4 (± 0.4)	-12.2 (± 0.6)
3.11	78.5 (± 0.5)	-4.1 (± 0.7)	3.16	66.8 (± 2.2)	-15.8 (± 2.2)
3.12	81.1 (± 0.1)	-1.5 (± 0.4)	3.17	85.1 (± 0.1)	—
3.13	72.3 (± 0.4)	-10.3 (± 0.6)	3.18	72.7 (± 0.5)	-9.9 (± 0.5)
3.14	70.3 (± 0.8)	-12.3 (± 0.9)	3.19	72.2 (± 0.3)	-10.4 (± 0.3)

Thermal melting of CRDDs **3.11**, **3.13**, and **3.15** and the stability of their corresponding abasic photoproducts **3.12**, **3.14**, and **3.16** were then performed (**Table 3.2**). The introduction of a single 7-NI nucleotide into the CCRD **3.11** decreased duplex stability as expected ($\Delta T_m = -4.1$ °C), but photochemical introduction of the abasic site in **3.12** increased stability compared to **3.11** ($\Delta T_m = +2.6$ °C). From this result, it was hypothesized that more than one abasic site would be needed to sufficiently disrupt duplex formation and overall binding affinity after depurination. The thermal stabilities of **3.13** and **3.15** were lower in comparison to non-modified decoy **3.10** ($\Delta T_m = -10.3$ °C and -12.2 °C, respectively), yet both are sufficiently stable ($T_m = 72.3$ °C and 70.4 °C, respectively). As anticipated, photochemical introduction of multiple abasic sites forming **3.14** (two abasic sites) is destabilizing to duplex DNA ($\Delta T_m = -12.3$ °C compared to **3.10**; $\Delta T_m = -2.0$ °C compared to **3.13**) and even greater for **3.16** ($\Delta T_m = -15.8$ °C compared to **3.10**; $\Delta T_m = -3.6$ °C compared to **3.15**), which contains three abasic sites. The thermal stability of scramble **3.18** containing three 7-NIs was lower in comparison to non-modified scramble decoy **3.17** ($\Delta T_m = -9.9$ °C), similarly to the incorporation of 7-NIs into the CRDDs. Three base pair mismatch **3.19** in place of the three 7-NI nucleotides also displayed a lowered T_m compared to native **3.10** ($\Delta T_m = -10.4$ °C).

3.4 Capture of NF- κ B by CRDDs

We next evaluated the ability of the decoys to capture NF- κ B proteins by electrophoretic mobility shift assays (EMSAs). ³²P-end-labeled **3.10**, **3.15**, and **3.17-3.19**

were added to a solution of recombinant p50-p65 proteins and protein binding was measured. The NF- κ B directed DNA decoys exhibited specific binding toward the NF- κ B proteins, as little binding occurred with the scramble and base pair mismatch decoys **3.17-3.19** (**Figure 3.5**).

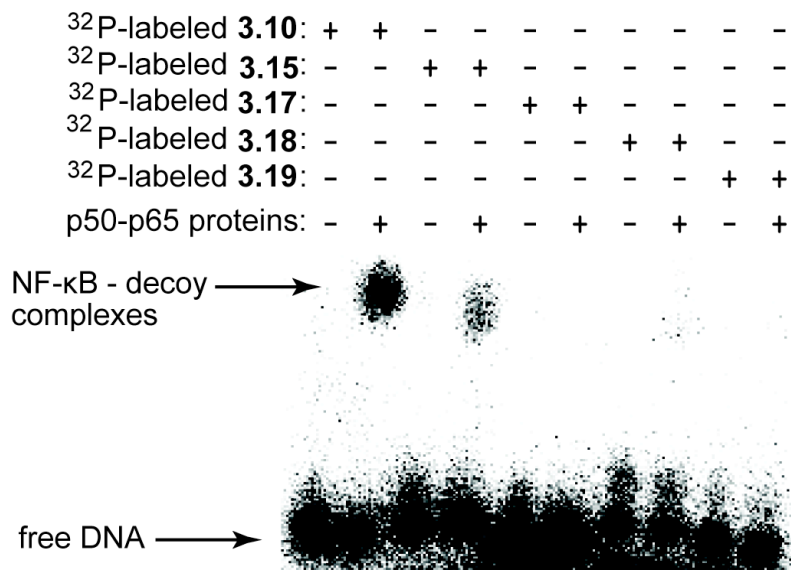


Figure 3.5. EMSA to characterize CRDD protein binding ability. 5'-³²P-labeled **3.10** (NF- κ B decoy without 7-NI modifications), **3.15** (NF- κ B decoy with three 7-NI modifications), **3.17** (scramble decoy without 7-NI modifications), **3.18** (scramble decoy with three 7-NI modifications), and **3.19** (NF- κ B decoy with three natural base pair mismatch modifications) incubated with p50-p65 recombinant proteins results in the formation of NF- κ B-**3.10** and NF- κ B-**3.15** complexes. Scramble decoys **3.17** and **3.18** as well as three base pair mismatch **3.19** show no affinity towards p50-p65.

To characterize the NF- κ B complexes responsible for binding to DNA decoys, supershifting EMSAs were carried out (**Figure 3.6**). p50 utilized in all experiments is a partially truncated recombinant protein (35-381; 433 amino acids for wild-type enzyme). The p65 recombinant protein utilized in these experiments is primarily the DNA-binding domain with a N-terminal GST tag (1-306; 551 amino acids for wild-type enzyme). Addition of p50 antibody to NF- κ B-**3.10** complexes completely supershifted the band, indicating that p50 protein is present in all complexes bound to **3.10** (**Figure 3.6a**).

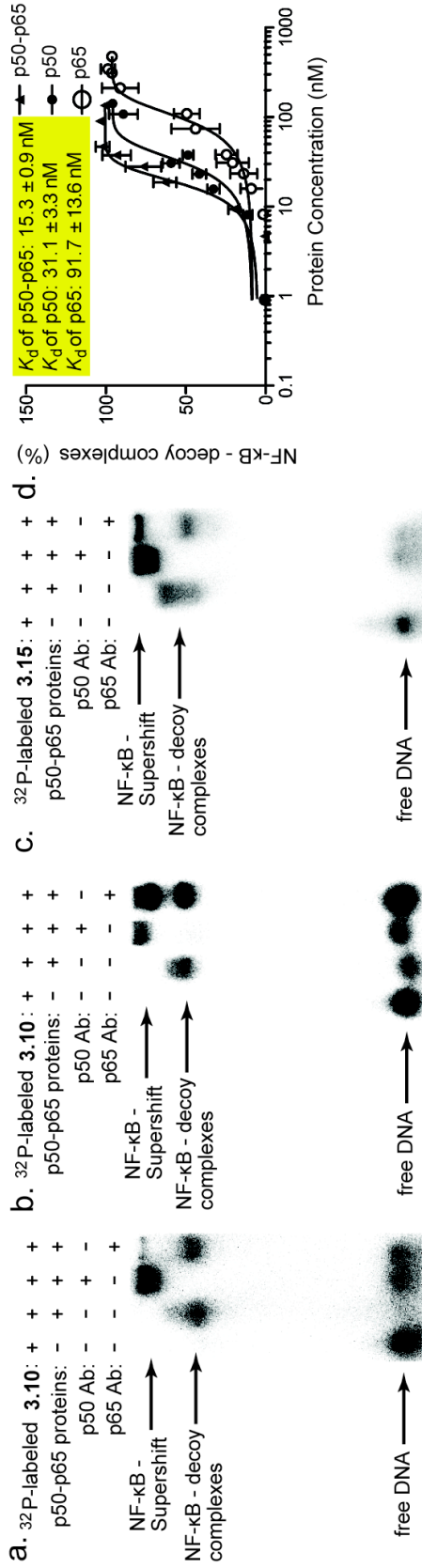


Figure 3.6. EMSA supershifting experiments. (a and c) $5'$ - 32 P-labeled **3.10** or **3.15** incubated with recombinant p50 protein (Enzo Life Sciences, BML-UW9885-0050, amino acids 35-381), recombinant p65 protein (Sino Biological, 12054-H09E, amino acids 1-306), p50 antibody (Santa Cruz Biotechnology, sc-7178 x), or p65 antibody (Santa Cruz Biotechnology, sc-8008 x) displays formation of the NF- κ B-DNA decoy supershift complexes. (b) $5'$ - 32 P-labeled **3.10** incubated with recombinant p50 protein (Enzo Life Sciences, BML-UW9885-0050, amino acids 35-381), recombinant p65 protein (Active Motif, 31302, amino acids 1-537), p50 antibody (Santa Cruz Biotechnology, sc-7178 x), or p65 antibody (Santa Cruz Biotechnology, sc-8008 x) displays formation of the NF- κ B-DNA decoy supershift complexes. Sciences-Sino Biological) proteins, p50-p50 (Enzo Life Sciences) homodimer proteins, and p65-p65 (Sino Biological) homodimer proteins. (d) Quantitative EMSA analysis to measure equilibrium dissociation (K_d) constants for **4** with p50-p65 heterodimer and p50 and p65 homodimer proteins. Recombinant p50 (35-381) and p65 (1-306) proteins used in this study. Mean \pm SD (n = 3).

However, addition of p65 antibody only partially supershifted the NF- κ B complex (**Figure 3.6a**). These data suggest that the observed NF- κ B-**3.10** complex is comprised of both p50-p65 heterodimers (supershift) and p50-p50 homodimers (shift), which is consistent with previously studies.²⁴² The supershift experiment was repeated with a near full-length p65 recombinant protein (1-537), which confirmed these results (**Figure 3.6b**). The ability of CRDD **3.15** (containing three 7-NIs) to bind the NF- κ B complexes was similarly confirmed by EMSA supershift analysis (**Figure 3.6c**) To support these EMSA results, we performed quantitative EMSA titrations with NF- κ B proteins to obtain equilibrium dissociation constants for all three possible NF- κ B complexes with native DNA decoy **3.10** (**Figure 3.6d**). The p50-p65 heterodimer demonstrated the highest binding affinity ($K_d = 15.3$ nM). The p50 and p65 homodimer proteins were also measured ($K_d = 31.1$ nM and 91.7 nM, respectively), revealing the p65 homodimer has a 6-fold lower binding affinity for **3.10** than the p50-p65 heterodimer, which is consistent with a previous study.²⁴³ Therefore, our studies of CRDD binding to NF- κ B proteins are sampling a mixture of both p50 and p65 heterodimers and homodimers.

As shown in **Figure 3.7a**, CRDDs **3.11**, **3.13**, and **3.15** demonstrated the ability to bind the NF- κ B complex similarly to native decoy **3.10**. Decoys **3.12** and **3.14**, however, retain the ability to bind despite containing one and two abasic sites. Decoy **3.16**, containing three abasic sites, demonstrated no observable complex formation upon addition of proteins. This result revealed that the photochemical transformation of **3.15** to **3.16** abolishes NF- κ B binding, and therefore, we utilized this compound for further studies.

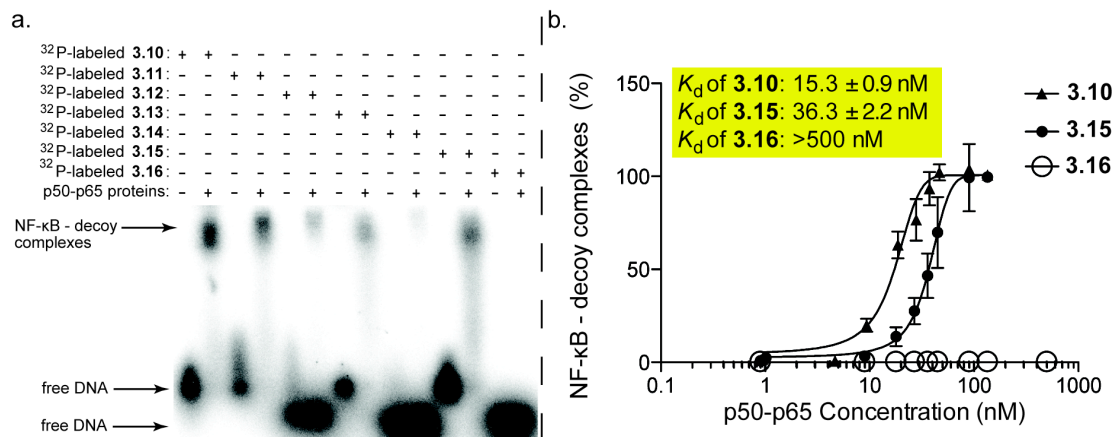


Figure 3.7. (a) Electrophoretic mobility shift assays with **3.10-3.16**. $5'$ - 32 P-labeled **3.10-3.16** incubated with p50-p65 (Sino Biological) recombinant proteins displays formation of the NF- κ B-CRDD complexes. NF- κ B binding is observed until three abasic sites are formed (i.e., **10**). (b) Quantitative EMSA analysis to measure equilibrium dissociation (K_d) constants for **3.10**, **3.15**, and **3.16** with recombinant p50-p65 proteins.

To corroborate our EMSA results, we performed quantitative EMSA titrations with NF- κ B proteins and **3.10**, **3.15**, and **3.16** to obtain equilibrium dissociation constants for our probes. DNA decoy **3.10** ($K_d = 15.3$ nM) and CRDD **3.15** ($K_d = 36.2$ nM) exhibited comparable binding affinities for the NF- κ B proteins (**Figure 3.7b**). Quantitative analysis using densitometry revealed approximately ~50% decrease in signal of CRDD **3.15** compared to native **3.10** (**Figure 3.7a**), which is consistent with a lower K_d (**Figure 3.7b**). Remarkably, CRDD **3.16**, which contains three abasic sites in the p50 recognition domain, exhibited no observable binding to the NF- κ B proteins ($K_d > 500$ nM). These data further support our model by which CRDD depurination ablates protein recognition.

3.5 Kinetics of Depuration

To characterize the kinetics and the identities of the photo-products resulting from irradiation of **3.15**, we utilized liquid chromatography-mass spectrometry (LC-MS) analysis of an irradiated aqueous sample. As shown in **Figure 3.8**, irradiation of **3.15** yielded fast photolysis ($t_{1/2} = 1.2$ min; 350 nm light; light intensity: 5.66×10^{-8} ein $\text{cm}^{-2}\text{s}^{-1}$) whereby 90% of **3.15** was converted to photo-products within 4.5 minutes. The quantum yield (Φ) of **3.15** was determined to be 0.0104, which is comparable, albeit slower, than 6-nitropiperonyloxymethyl (NPOM)-protected thymine ($\Phi = 0.094$).²⁰⁹

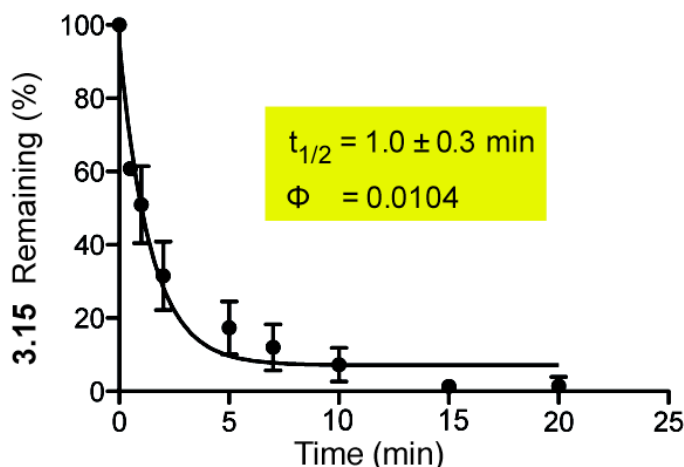


Figure 3.8. Photolysis of CRDD **3.15** (350 nm light). Samples analyzed by ion-extracted LC-MS. Photolytic decay curve of **3.15** with calculated half-life and quantum yield ($R^2 = 0.97$).

After 25 minutes of irradiation of CRDD **3.15**, very little decoy remained and multiple abasic decoys and truncation products resulting from β - and δ -elimination were detected (**Figure 3.9**). As expected, formation of decoys with one abasic site increases immediately, peaks around 5 minutes, and decreases as multiple abasic sites are formed.

Decoys with one, two, and three abasic sites (**3.24**, **3.25**, and **3.16**, respectively) were observed after 25 minutes of irradiation. These abasic decoys result in approximately 65% of the total number of photo-products formed (**Figure 3.9**, dashed lines). Several truncated products (**3.26-3.29**) are formed by β and δ -eliminations of the 3' and 5' phosphates, due to the instability of the abasic lactones within DNA.²³⁰ Of these truncated products, 2-6 nucleotides are cleaved from the 5'-end of the decoy (**Figure 3.9**, solid lines). Consequently, photolysis of **3.15** results in substantial modification to the essential 4-G NF- κ B binding site, which disrupts protein-CRDD binding.

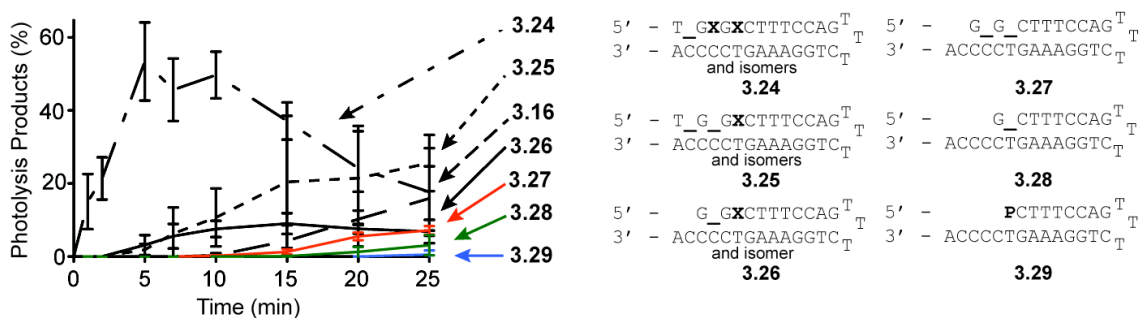


Figure 3.9. Photolysis of CRDD **3.15** (350 nm light). Samples analyzed by ion-extracted LC-MS. Formation of abasic sites and truncation products **3.16** and **3.24-3.29** resulting from photolysis of **3.15** (**P** = 5'-phosphate). Dashed line denotes full-length DNA decoys containing abasic products and solid lines denote truncation products (some contain abasic sites as well). Isomers denote constitution isomers resulting from photolysis of **3.15** (e.g., **X** and **_** are in different arrangements). Mean \pm SD (n = 4). An LC-MS chromatogram of the photo-products from irradiation of **9** can be found in **Appendix B**.

3.6 Photochemical Catch and Release of NF- κ B

To assess the ability of CRDD **3.15** to release the NF- κ B complex photochemically, a solution of ³²P-labeled **3.15** and recombinant proteins were incubated in binding buffer, followed by treatment with 350 nm light. Photolysis of the **3.15**-NF- κ B

complex, over time, drives release of the transcription factor upon formation of abasic sites and truncated products of the DNA decoy (**Figure 3.10a**). After 4 minutes of irradiation of the **3.15**-NF- κ B complex, approximately 50% of the NF- κ B proteins are released even through the protein is in large excess (**Figure 3.10b**). Recovery of the complex can be obtained by additional 32 P-labeled **3.15**, demonstrating the viability of NF- κ B to bind DNA after irradiation with light.

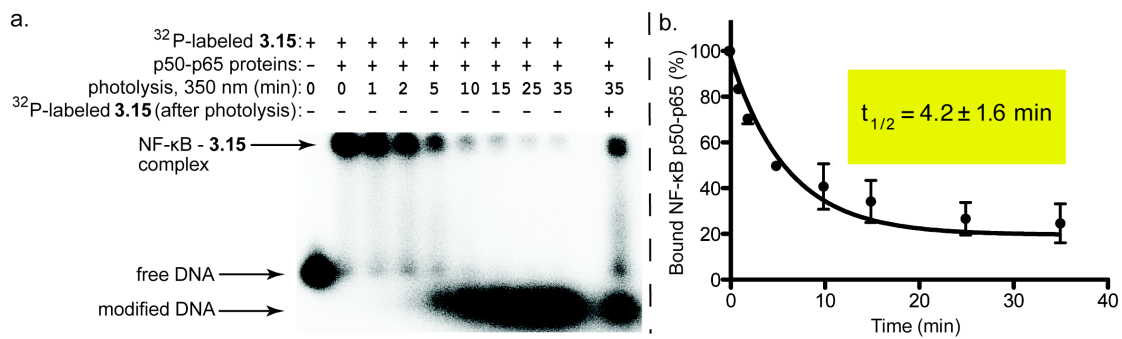


Figure 3.10. Quantitative electrophoretic mobility shift assay with CRDD **3.15**. (a) $5'$ - 32 P-labeled **3.15** incubated with NF- κ B proteins yields complex formation (catch, $t = 0$ min), which is dissociated upon photolysis with 350 nm light (release) in a time-dependent manner. Recovery of the NF- κ B-**3.15** complex can be obtained by addition of 32 P-labeled **3.15**. (b) Densitometry of EMSAs yielding half-life of NF- κ B release ($R^2 = 0.93$). Mean \pm SD. ($n = 3$).

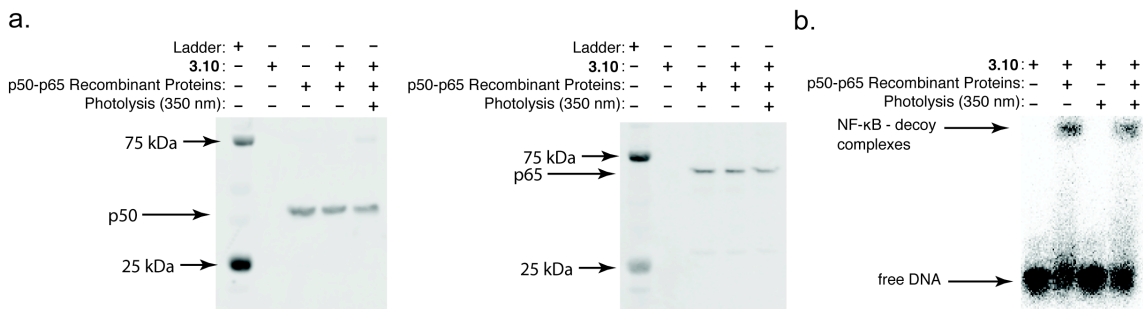


Figure 3.11. (a) Western blots for p50 (left) and p65 (right) following irradiation of NF- κ B recombinant p50 protein (Enzo Life Sciences, BML-UW9885-0050, amino acids 35-381), recombinant p65 protein (Sino Biological, 12054-H09E, amino acids 1-306) at 350 nm for 60 minutes. (b) EMSA of NF- κ B recombinant p50 protein (Enzo Life Sciences, BML-UW9885-0050, amino acids 35-381), recombinant p65 protein (Sino Biological, 12054-H09E, amino acids 1-306) with $5'$ - 32 P-labeled **4** following irradiation of proteins at 350 nm for 60 minutes.

Additionally, western blot (**Figure 3.11a-3.11b**) and EMSA (**Figure 3.11c**) analysis of p50 and p65 proteins following subjection to the photolysis conditions (350 nm light, in H₂O) reveals no apparent damage to proteins.

3.7 Conclusions and Future Work

We demonstrate for the first time the capture and photochemical release of an endogenous transcription factor heterodimer using a novel photo-responsive Catch and Release DNA Decoy (CRDD). Photolysis of CRDD **3.15** resulted in formation of abasic sites and truncated products abolishing affinity for NF- κ B protein binding. These results have demonstrated that CRDDs can be used to effectively capture and spatiotemporally release TFs.

The EMSA experiments demonstrated the ability of the 7-nitroindole decoy **3.15** to catch, photochemically release, and recapture NF- κ B *in vitro* (**Figure 3.10a**). Future work will demonstrate the ability of our ‘catch and release’ NF- κ B decoys to work in cell culture. We will utilize a commercial cell line (CHO/GFP-NF- κ B-p65, Affymetrix RC2001), which is a stable, p65-GFP reporter cell lines that is useful in monitoring the cellular activity of NF- κ B. Under basal conditions, the NF- κ B dimer is sequestered in the cytoplasm **Figure 3.12**. Induction of the signaling pathway by addition of IL-1 β results in NF- κ B activation and nuclear translocation. This is evident by visualizing our data in **Figure 3.12** where the GFP signal overlays with the nuclear stain (Hoechst33342, H33342) following IL-1 β activation. We will utilize this cell line to study catch and

release by fluorescently-labeled CRDDs. We expect to see overlap of our fluorescently-labeled CRDDs and p65-GFP when transfected into this cell line. Irradiation of the CRDD will result in dissociation of NF- κ B and we expect to visualize the nuclear translocation of the p65-GFP.

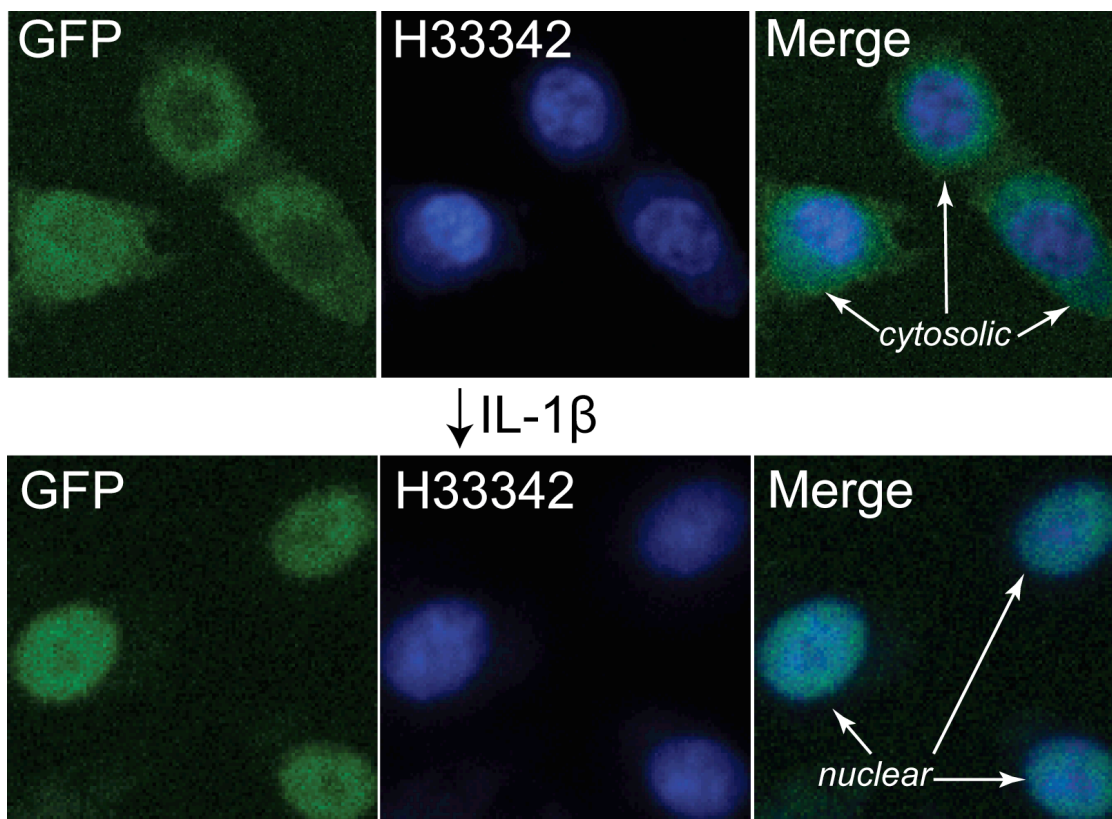


Figure 3.12. NF- κ B reporter assay in CHO cells. (Top) p65-GFP is visualized in the cytoplasm, yielding distinct localization versus H33342 (nuclear stain). Induction of NF- κ B results nuclear translocation of p65-GFP, as evidenced by co-localization of the GFP signal and H33342.

3.8 Experimental Section

3.8.1 Chemical Synthesis.

General. Chemical reagents were typically from Sigma-Aldrich or Acros and used without additional purification unless explicitly noted. Reactions were performed under

an atmosphere of dry N₂ unless otherwise noted. Silica gel chromatography was performed on a Teledyne-Isco Combiflash Rf-200 instrument utilizing Redisep Rf Gold High Performance silica gel columns (Teledyne-Isco) or self-packed columns with SiliaFlash 60Å silica gel (SiliCycle). Nuclear magnetic resonance (NMR) spectroscopy employed a Bruker AvanceII+ instrument operating at 400 MHz (for ¹H), 100 MHz (for ¹³C), or 161 MHz (for ³¹P) at ambient temperature. Chemical shifts are reported in parts per million and normalized to internal solvent peaks or tetramethylsilane ($\delta = 0$ ppm).

1-(2'-Deoxy-3',5'-di-*O*-*p*-toluoyl- β -ribofuranosyl)-7-nitroindole (3.6): Prepared as previously described.^{244,245}

1-(2'-Deoxy- β -ribofuranosyl)-7-nitroindole (3.7): Prepared as previously described.^{244,245}

1-(2'-Deoxy-5'-dimethoxytrityl- β -ribofuranosyl)-7-nitroindole (3.8): Prepared as previously described.^{244,245}

1-(2'-Deoxy-3'-(2-cyanoethyl-N,N-diisopropylphosphoramidite-5'-dimethoxytrityl- β -ribofuranosyl)-7-nitroindole (3.9): Prepared as previously described.^{244,245}

3.8.2 Solid-Phase DNA Synthesis. Oligonucleotides were synthesized using standard solid-phase phosphoramidite chemistry on an Applied Biosystems 394 DNA/RNA

synthesizer.²¹⁰ 7-Nitroindole (7-NI) phosphoramidite was synthesized as previously described.^{244,245} All other phosphoramidites, solvents, and solid supports (1.0 μmol) were purchased from Glen Research Corporation. 7-NI was incorporated into the oligonucleotide by a manual coupling, whereas all other nucleotides were incorporated with automated couplings. Automated DNA synthesis was paused immediately prior to incorporation of 7-NI and the solid support was removed from the synthesizer. To achieve a manual coupling, 7-NI phosphoramidite (15 mg) was dissolved in anhydrous MeCN (200 μL), loaded into a syringe (1 mL), and attached to one side of the solid support. A second syringe (1 mL) was loaded with Activator (600 μL , Glen Research Corp.) and attached to the other end of the solid support. The solutions were then mixed through the solid support vessel manually by the two syringes for 20 min. Afterwards, the solid support vessel was drained, washed with anhydrous MeCN (1 mL) and returned to the synthesizer. This procedure for manual coupling was performed for all 7-NI incorporations. Following the synthesis, the resin was transferred to a fritted reaction vessel. Concentrated aqueous ammonium hydroxide (2.5 mL) was added and the vessel was placed in a shaker for 18 hours at room temperature. After deprotection, the solution was filtered into a centrifuge tube (10 mL) and distilled water (2 mL) was added. The ammonium hydroxide was evaporated *in vacuo* (samples were transferred to microcentrifuge tubes and placed in a SpeedVac) and the remaining solution was purified by HPLC (see below). After purification, the oligonucleotides were desalted with DNase/RNase free H₂O using Illustra NAP-5 columns (Sephadex G-25 DNA grade, GE Healthcare) according to manufacturer instructions. The desalted oligonucleotides were

quantified by UV-Vis (A_{260} , using predicted molar extinction coefficients for native dNTPs and $\epsilon=5,900 \text{ M}^{-1} \text{ cm}^{-1}$ for 7-NI at 260 nm) and confirmed by LC-MS (see below). The purity was assessed by HPLC reinjection of the purified oligonucleotides (see **Appendix B** for chromatograms).

Oligonucleotide **3.10**. Purity = 95.9% (260 nm). MS calc'd 9502.2, found 9501.6 (parent)

Oligonucleotide **3.11**. Purity = 97.9% (260 nm). MS calc'd 9513.2, found 9513.9 (parent)

Oligonucleotide **3.12**. Purity = 95.8% (260 nm). MS calc'd 9367.1, found 9368.1 (parent)

Oligonucleotide **3.13**. Purity = 98.6% (260 nm). MS calc'd 9524.2, found 9524.7 (parent)

Oligonucleotide **3.14**. Purity = 98.4% (260 nm). MS calc'd 9232.9, found 9233.1 (parent)

Oligonucleotide **3.15**. Purity = 98.5% (260 nm). MS calc'd 9551.2, found 9551.7 (parent)

Oligonucleotide **3.16**. Purity = 96.1% (260 nm). MS calc'd 9114.8, found 9113.5 (parent)

Oligonucleotide **3.17**. Purity = 93.0% (260 nm). MS calc'd 9502.2, found 9502.0 (parent)

Oligonucleotide **3.18**. Purity = 95.3% (260 nm). MS calc'd 9551.2, found 9550.8 (parent)

Oligonucleotide **3.19**. Purity = 94.5% (260 nm). MS calc'd 9486.2, found 9486.4 (parent)

Oligonucleotide **3.21**. Purity = 93.0% (260 nm). MS calc'd 4557.0, found 4556.8 (parent)

Oligonucleotide **3.23**. Purity = 87.5% (260 nm). MS calc'd 4557.0, found 4556.5 (parent)

3.8.3 HPLC Purification & LC-MS Analysis. Procedure outlined in **Chapter 2.8.2**.

3.8.4 Thermal Melting Analysis. Procedure outlined in **Chapter 2.8.3**.

3.8.5 Photolysis, Exponential Decay, and Quantum Yield Analysis. DNA photolysis experiments were carried out using a Rayonet photochemical reactor (RMR-600, Southern New England Ultraviolet Co.) fitted with eight, 350 nm bulbs. To enable quantitative analysis of photochemical decay of DNA decoys, calibration plots for each DNA decoy were generated. Increasing concentrations of each DNA decoy (0.55, 1.65, 4.94, 14.81, 44.44, 133.33 pmol) were added to a fixed concentration of a non-modified DNA oligonucleotide (5'-TAACTA-3', 100 pmol) and analyzed by extracted ion current (EIC) LC-MS (masses monitored at -9 charge state for decoys).²¹² A calibration plot was created by plotting the ratio of decoy:standard area under the curve (AUC) versus DNA decoy concentration, yielding calibration plots with a slope-intercept equation of $R^2 > 0.99$.

Quantitative analysis of DNA decoy photolysis was performed by dissolving the DNA decoy (800 pmol) in DNase/RNase free H₂O and then adding the solution to conical pulled point vial inserts (250 μ L; Agilent, 8010-0125). Vessels containing the aqueous DNA solution was placed into the photochemical reactor and irradiated (light intensity: 5.66×10^{-8} ein $\text{cm}^{-2} \text{s}^{-1}$; calculated as described below). Aliquots (4 μ L) were taken at several time points (1, 2, 5, 7, 10, 15, 20, 25 min), diluted with standard (1 μ L) and then analyzed by LC-MS. The concentration of the decoy species from irradiation were determined by fitting the decoy/standard ratios from each sample into the slope-intercept equation from the calibration plot to yield the amount of decoy (pmol) in sample. This process was repeated for each prominent molecular ion observed in the photolysis sample. Furthermore, this quantitative analysis method assures comparable

ionization properties for the photolyzed products in comparison to the non-irradiated sample. First order decay analysis (GraphPad Prism; v5.0b) was then fitted to the data (percentage of starting material over time) to obtain the decay equation and half-life ($t_{1/2}$) of the DNA decoy. Mean $t_{1/2}$ values (with standard deviation) were calculated from the fitting of the decay curve with the individual data points obtained from each replicate ($n = 4$).

Quantum yield (Φ) calculations were carried out to determine the efficiency of photolysis of CRDD **3.15** (eq. 1). The intensity of the light source (I , eq. 2) was determined using $K_3[Fe(C_2O_4)_3]$ actinometry as previously described.^{213,214} In brief, a solution of $K_3[Fe(C_2O_4)_3] \cdot 3H_2O$ in distilled H_2O (6 M, 2 mL) was irradiated for 180 seconds in the Rayonet equipped with eight, 350 nm bulbs. After irradiation, the sample was transferred to a volumetric flask (25 mL). To the flask was added aqueous buffer (3 mL; recipe to make a 500 mL solution of aqueous buffer: 300 mL of 1.0 M NaOAc, 180 mL of 1.0 M H_2SO_4 , and 20 mL distilled H_2O), phenanthroline solution (3 mL of 0.1% v/v phenanthroline in distilled H_2O), KF solution (1 mL of a 2.0 M solution), and distilled water (~18 mL, to 25 mL). The solution was placed in the dark for 1 hour. A non-irradiated sample was prepared in the same manner. After 1 hour, the solutions were transferred to a cuvette and the A_{510} was measured for both samples. The Rayonet light intensity was then calculated using eq. 2 (5.66×10^{-8} ein $cm^{-2} s^{-1}$). The extinction coefficient at 350 nm (ϵ_{350}) of CRDD **3.15** was calculated by UV-Vis absorbance using the Beer-Lambert law ($7070 M^{-1} cm^{-1}$). The irradiation time for 90% conversion ($t_{90\%}$) of

the DNA decoy was calculated from the first order decay equation (above). Quantum yield was then calculated using **eq. 1** to give a value less than one.²¹⁵

$$\text{(Eq. 1)} \quad \Phi = (I \cdot \sigma \cdot t_{90\%})^{-1}$$

where σ ($\text{cm}^2 \text{mol}^{-1}$) is equal to $1000 \cdot \epsilon_{510}$ of the DNA decoy

$$\text{(Eq. 2)} \quad I (\text{ein cm}^{-2} \text{s}^{-1}) = (V_1 \cdot V_3 \cdot \Delta A_{510}) / (1000 (\text{mL/l}) \cdot \epsilon_{510} \cdot V_2 \cdot \Phi_{\text{Fe}} \cdot t)$$

where V_1 is the volume of $\text{K}_3[\text{Fe}(\text{C}_2\text{O}_4)_3]$ irradiated (mL); V_2 is the volume of the $\text{K}_3[\text{Fe}(\text{C}_2\text{O}_4)_3]$ solution transferred to the volumetric flask (mL); V_3 is the volume of the volumetric flask (mL); ΔA_{510} is the difference in absorbances at 510 nm between the irradiated and non-irradiated samples; ϵ_{510} is the extinction coefficient of $\text{K}_3[\text{Fe}(\text{C}_2\text{O}_4)_3]$ at 510 nm ($11,100 \text{ cm}^{-2} \text{ s}^{-1}$)²¹³; Φ_{Fe} is the quantum yield of $\text{K}_3[\text{Fe}(\text{C}_2\text{O}_4)_3] \cdot 3\text{H}_2\text{O}$ (1.21)²¹³; and t is the time irradiated (s).

3.8.6 ³²P Radiolabeling. Procedure outlined in **Chapter 2.8.5.**

3.8.7 Electrophoretic Mobility Shift Assay (EMSA). Binding reactions containing binding buffer (2 μL of a 10X solution; 10X solution: 100 mM Tris, 10 mM EDTA, 500 mM NaCl, and 10% NP-40),⁹² recombinant p50 protein (0.5 μL ; 0.50 $\mu\text{g}/\mu\text{L}$, Enzo Life Sciences, BML-UW9885-0050, amino acids 35-381), recombinant p65 protein (0.5 μL ; 0.50 $\mu\text{g}/\mu\text{L}$ Sino Biological, 12054-H09E, amino acids 1-306), and DNase/RNase free H_2O (to a final volume of 20 μL) were prepared in microcentrifuge tubes (0.65 mL) and incubated on ice for 30 mins. ³²P-labeled DNA decoys (1 μL , 25,000 counts/min/ μL) were added to the binding reaction and then incubated at 37 °C for 10 mins.

For catch and release, binding reactions were then transferred to glass HPLC vial inserts (each 20 μL binding reaction was pipetted into individual inserts) and irradiated (with the exception of non-irradiated control samples) in the Rayonet with eight 350 nm bulbs (5.66×10^{-8} ein $\text{cm}^{-2} \text{s}^{-1}$) at room temperature. The samples were taken out of the Rayonet at various time points and transferred ($\sim 20 \mu\text{L}$ volume) to a new microcentrifuge tube (0.65 mL). For rebinding studies (**Figure 3.10a**, lane **10**), additional ^{32}P -labeled DNA was added to only that sample (1 μL , 25,000 counts/min/ μL of DNA). All samples and controls were then incubated at 37 $^{\circ}\text{C}$ for 2 hours.

For supershift experiments, binding reactions containing recombinant p50 proteins (0.5 μL ; 0.50 $\mu\text{g}/\mu\text{L}$, Enzo Life Sciences, BML-UW9885-0050, amino acids 35-381), recombinant p65 protein (0.5 μL ; 0.50 $\mu\text{g}/\mu\text{L}$ Sino Biological, 12054-H09E, amino acids 1-306 (**Figure 3.6a** and **Figure 3.6b**) or 2.5 μL ; 0.10 $\mu\text{g}/\mu\text{L}$ Active Motif, 31302, amino acids 1-537 (**Figure 3.6c**)), p50 antibody (10 μL ; 200 $\mu\text{g}/0.1 \text{ ml}$, Santa Cruz Biotechnology, sc-7178 x), or p65 antibody (10 μL ; 200 $\mu\text{g}/0.1 \text{ ml}$, Santa Cruz Biotechnology, sc-8008 x) were prepared in microcentrifuge tubes (0.65 mL) and incubated on ice for 60 mins. ^{32}P -labeled DNA decoys (1 μL , 25,000 counts/min/ μL) were added to the binding reaction and then incubated at 37 $^{\circ}\text{C}$ for 10 mins.

For binding constant studies (**Figure 3.6d** and **Figure 3.7b**), DNA concentration was held constant (20,000 counts/min/ μL) and titrated with increasing p50-p65 heterodimer, p50-p50 homodimer, or p65-p65 homodimer at various concentrations (0, 0.90 nM, 9.00 nM, 17.98 nM, 26.98 nM, 35.97 nM, 44.96 nM, 89.92 nM, 134.88 nM, and 179.84 nM; 500 nM was only used for decoy **3.16**).²⁴³ Recombinant p50 protein was

from Enzo Life Sciences (BML-UW9885-0050, amino acids 35-381) and recombinant p65 protein was from Sino Biological (12054-H09E, amino acids 1-306). The fraction of DNA bound in each reaction was determined by dividing the densitometry of each bound band by the total densitometry of the bound and free bands. These fractions were then plotted on a semi-logarithmic plot (GraphPad Prism; v5.0b) and the equilibrium dissociation constants were calculated. Mean \pm SD. (n = 3).

For photochemical stability studies, binding reactions containing binding buffer, recombinant p50 protein (0.5 μ L; 0.50 μ g/ μ L, Enzo Life Sciences, BML-UW9885-0050, amino acids 35-381), recombinant p65 protein (0.5 μ L; 0.50 μ g/ μ L Sino Biological, 12054-H09E, amino acids 1-306), and DNase/RNase free H₂O (to a final volume of 19 μ L) were prepared in microcentrifuge tubes (0.65 mL) and incubated at room temperature for 10 mins. The sample to be irradiated (19 μ L) was pipetted into a glass HPLC vial insert and irradiated in the Rayonet with eight 350 nm bulbs (5.66×10^{-8} ein cm⁻² s⁻¹) at room temperature for 1 hr. The sample was then transferred to a new microcentrifuge tube. ³²P-labeled DNA decoys (1 μ L, 25,000 counts/min/ μ L) were added to the binding reaction and then incubated at 37 °C for 10 mins.

Loading dye (2 μ L, 10X solution; 0.5X TBE, 40% glycerol, 2 mg/mL Orange G dye, Sigma) was added to each reaction and samples were loaded onto a 5% non-denaturing PAGE gel that was pre-run at 200 V for 1 hr in 0.5X TBE. Samples were electrophoresed at 200V until the loading dye was \sim ³/₄ down the gel. The gel was transferred to filter paper (Bio-Rad; the plates were pried apart and the gel was placed on the wetted filter paper), covered with plastic wrap and cellophane (Bio-Rad), and dried

for 1 hr (Gel Air Dryer, Bio-Rad). The gel was transferred to a phosphorimager screen overnight and then analyzed on a Typhoon FLA 7000 biomolecular imager (GE Healthcare). Images were analyzed using Image Quant TL software (v 7.0, GE Healthcare).

3.8.8 Western Blots. Binding reactions were prepared as described above for EMSA analysis, except the binding buffer was omitted. Western blots were performed as previously described.²⁴⁶ The sample to be irradiated (20 μL) was pipetted into a glass HPLC vial insert and irradiated in the Rayonet with eight 350 nm bulbs (5.66×10^{-8} $\text{ein cm}^{-2} \text{ s}^{-1}$) at room temperature for 1 hr. The sample was then transferred to a new microcentrifuge tube. To each sample was added NuPAGE 4X LDS sample buffer (5 μL , Invitrogen) and NuPAGE 10X sample reducing agent (2 μL , Invitrogen) and the samples were heated to 99 °C for 5 minutes. Protein samples were separated on a gradient 4-12% SDS-PAGE gel (Invitrogen) using MES SDS running buffer (NuPAGE), and then electrotransferred to a polyvinylidene difluoride membrane (Immobilon). The membrane was transferred to a heat-sealed bag containing Odyssey blocking buffer (5 mL, LI-COR Biotech.) to block the membrane overnight at 4 °C. Proteins were detected by incubation with primary antibodies for p65 (5 μL ; Santa Cruz Biotechnology, sc-372) and p50 (30 μL ; Enzo Life Sciences, ALX-804-043-C100) in a heat-sealed bag containing blocking buffer (5 mL) overnight at 4 °C. The membrane was then briefly washed by gentle rocking in ddH₂O (50 mL, 1 min, total 5x), and then incubated with IRDye 800 anti-rabbit (5 μL ; LI-COR Biotech., 926-32211) and IRDye 680 anti-mouse (5 μL ; LI-COR

Biotech., 926-68020) conjugated secondary antibodies together in a heat-sealed bag containing blocking buffer (5 mL) for 2 hours at room temperature. The membrane was again washed via gentle rocking in ddH₂O (50 mL, 1 min, total 5x). The immunocomplexes were visualized using the Odyssey classic infrared imaging system (LI-COR Biotech.).

3.8.9 Protocol for Mammalian Cell Culture. All cell lines were maintained in a humidified 5% CO₂ environment at 37 °C. CHO/NFκBp65-GFP cells (Affymetrix/Panomics #RC2001) were cultured in Hams F12K media supplemented with 10% fetal bovine serum (FBS, Gibco), penicillin (100 I.U./mL), streptomycin (100 μg/mL), and hygromycin (100 μg/mL, Roche, 10843555001) at a density of 2×10⁵ - 2×10⁶ cells/mL. This cell line (Affymetrix/Panomics #RC2001) was designed for the study of p65 translocation and was developed by co-transfection of an expression vector for a fusion protein of turboGFP and human NFκBp65 as well as pHyg. GFP+ cells are selected by culturing the cells with hygromycin B.

3.8.10 Confocal Microscopy. CHO/NF-κBp65-GFP cells were grown in a T75 culture flask to 70-80% confluency. The CHO/NF-κBp65-GFP cells were detached from the surface of the T75 culture flask using trypsin-EDTA solution. After the cells are detached, media was added to inactivate the trypsin and transfer this solution to a 15 mL tube. The cell density was determined using a hemocytometer and spin down the cells at 125 × g for 5 minutes. The CHO/NF-κBp65-GFP cells were resuspended in fresh media

at a density of 10,000 cells/mL. 200 μ L of this cell solution was added to the appropriate number of wells in an 8-well glass slide (Sigma Aldrich, C7057-1PAK). The plate was incubated on a level, vibration-free table for 1 hour at room temperature (20-25°C) to ensure an even distribution of cells throughout each well. After the cells are attached evenly in each well, the plate was incubated at 37°C and 5% CO₂ for 18-24 hours. The appropriate wells were induced with 10 ng/mL TNF- α (or IL-1 β) for 30 minutes. After incubation, the media was replaced in each well with 100 μ L of Hoechst 33342 (#B2261-100MG, 1:10,000 dilution) staining solution and incubated for 30 minutes at room temperature in the dark. The Hoechst staining solution was replaced in each well with 100 μ L of fresh media. The cells were imaged on the Zeiss Cell Observer Spinning Disk confocal microscope using the provided protocol utilizing the Phase II channel, blue channel for nuclear stain, and green channel for GFP-p65. The data was worked up on the NIS Elements Viewer (version 4.11.0) software.

Chapter 4

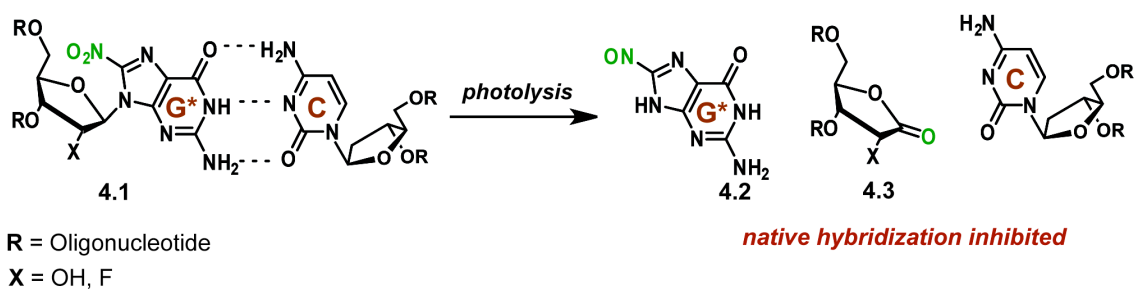
THE 8-NITROGUANOSINE NUCLEOBASE FOR INCORPORATION INTO SECOND-GENERATION CATCH AND RELEASE DNA DECOYS (CRDDs)

This work was performed in collaboration with Professor Daniel A. Harki

4.1 Rationale

The 7-nitroindole (7-NI) nucleobase **3.1** has allowed us to ‘catch and release’ the NF- κ B transcription factor (TF) complex when incorporated into a DNA decoy (**Figure 3.10**). However, 7-NI destabilizes duplex formation, such as **3.15**, which contains three 7-NIs incorporated compared to non-modified decoy **3.10** ($\Delta T_m = -12.2$ °C), and shows lower binding affinity to the protein than the native bases (~50%, **Figure 3.7**). It has been noted before that the worst steric repulsion effects involving purines occurs as a result of modification to the N3 atoms.²⁴⁷ As an example of this steric repulsion, N3-methyladenine, a cytotoxic lesion, has been demonstrated to block DNA polymerization.²⁴⁸ Since the 7-nitro group of **3.1** is in similar space as the N3 of purines, we hypothesize the 7-nitro group sterically perturbs duplex formation by pushing the aromatic ring out of favorable stacking, therefore, leading to the negative effects seen in duplex stability and protein binding affinity. Additionally, 7-NI is incapable of hydrogen bonding and selective hybridization with natural nucleobases, thus reducing molecular interactions between the DNA-protein interface, which decreases the overall binding affinity. 8-Nitroguanosine has been studied as a chemical probe for protein S-guanylation.^{249,250} 8-Nitroguanosine (8-NG, **4.1**) was envisioned to contain the depurination properties of the 7-NI nucleobase, while positioning the nitro group away from the hybridization face by placing it in the C8 positions of purines, which is shown to be solvent accessible in **Figure 5.1**, thus reducing the steric repulsions. Additionally, 8-NG has a full hydrogen-bond profile on the hybridization face, which is hypothesized to

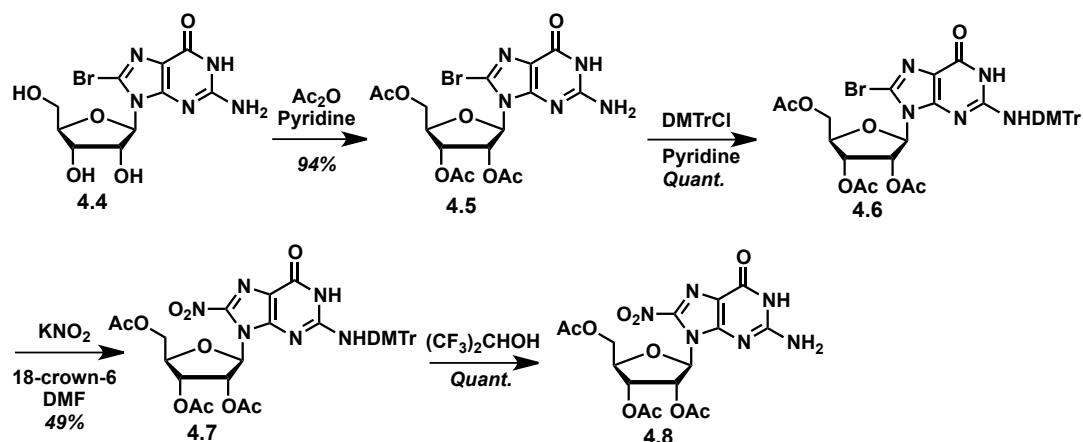
increase the amount of molecular interactions with TFs. Photolysis of 8-NG **4.1** is predicted to follow a similar mechanism as 7-NI (**Figure 3.3a**) to produce the nitroso guanine photo-byproduct **4.2**, and an abasic lactone (**4.3**, **Scheme 4.1**). To test these hypotheses, we prepared 2'- α -fluoro-8-nitro-2'-deoxyguanosine phosphoramidite **4.13**, which was then incorporated into oligonucleotide **4.14**. This oligonucleotide was demonstrated to be more stable than the 7-NI oligonucleotide **3.21**, and kept the photolytic uncaging properties, producing the abasic lactone **4.16** and the truncation product **4.17** upon photolysis.



Scheme 4.1. Second-generation 8-nitroguanosine (8-NG) depurination probe for use in CRDDs.

4.2 Nucleoside and Oligonucleotide Synthesis

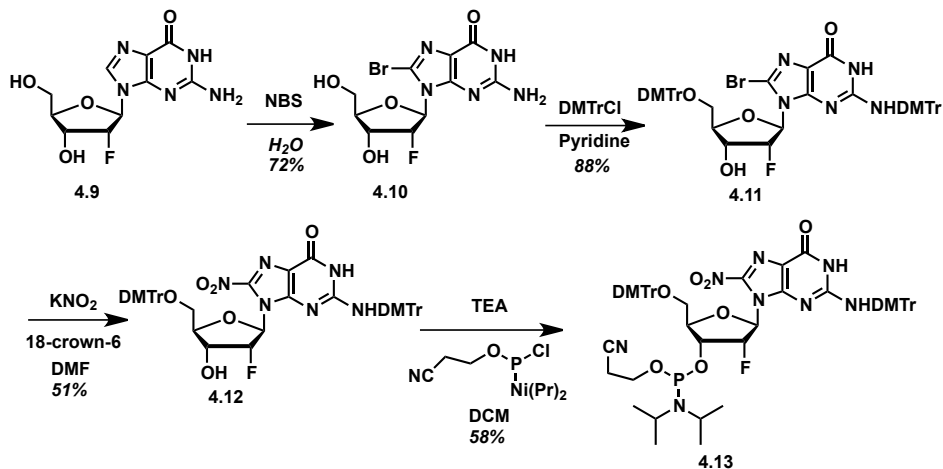
8-Bromoguanosine **4.4** was utilized to synthesize the acetylated 8-nitroguanosine **4.8** (**Scheme 4.2**). Acetic anhydride was used to protect 8-bromoguanosine **4.4** to give 2,3,5-tri-O-acetyl-8-bromoguanosine **4.5** in 94% yield. The exocyclic amine of **4.5** was protected with 4,4'-dimethoxytrityl chloride to afford **4.6** in quantitative yield. Nitration of **4.6** with potassium nitrite gave **4.7** in 49% yield, and a very mild deprotection of the DMT using 1,1,1,3,3,3-hexafluoro-2-propanol gave **4.8** in quantitative yield.²⁵¹



Scheme 4.2. Synthesis of 8-nitroguanosine.

Nitration of the 8-position of guanine renders the nucleoside unstable ($t_{1/2} = 5$ min in H_2O) due to a longer glycosidic bond (1.523 Å of **4.8** compared to 1.473 Å of **4.6**).²⁴⁹ Incorporation of a 2'- α -fluorine on the sugar restores stability by slightly shortening the glycosidic bond, which dramatically increased its stability ($t_{1/2} = 45$ days in 0.05 M sodium phosphate buffer).²⁴⁹ With this in mind, 2'- α -fluoro-8-nitro-2'-deoxyguanosine phosphoramidite **4.13** was hypothesized to remain stable enough for incorporation into CRDDs (**Scheme 4.3**).²⁴⁹ Initially, 2'- α -fluoro-2'-deoxyguanosine **4.9** was brominated utilizing NBS to achieve 8-bromo-2'- α -fluoro-2'-deoxyguanosine **4.10** in 72% yield. Similarly to **Scheme 4.2**, both the exocyclic amine and 5'-hydroxyl group of **4.10** were protected with 4,4'-dimethoxytrityl chloride with 88% yield to afford protected **4.11**, which was then nitrated to afford protected 2'- α -fluoro-8-nitro-2'-deoxyguanosine **4.12** in 51% yield. Finally, incorporation of the phosphoramidite on the 3-hydroxyl group of the nucleoside provided 2'- α -fluoro-8-nitro-2'-deoxyguanosine phosphoramidite **4.13** after

rigorous purification in 58% yield, which is now ready for incorporation into a set of CRDDs.



Scheme 4.3. Synthesis of 2'- α -fluoro-8-nitro-2'-deoxyguanosine phosphoramidite.

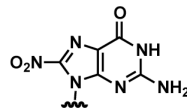
Similarly to the 7-NI oligonucleotide **3.21**, 2'- α -fluoro-8-nitro-2'-deoxyguanosine **4.13** was incorporated into oligonucleotide **4.14** to measure the thermal melting of duplex DNA containing all natural nucleotides hybridized to 8-NG. In addition, the 8-oxo-2'-deoxyguanosine (8-oxoG) phosphoramidite was purchased and used in the synthesis of the oligonucleotide **4.15** for comparative stability studies.

dsDNA sequence =

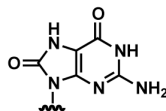
5' -CCTTTTT X TTTTTGG-3'

Nucleobases

X = 8-NO₂
Guanosine
(**4.14**)



X = 8-Oxo-
Guanosine
(**4.15**)



X = Abasic
(**4.16**)

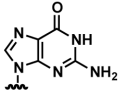
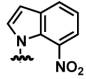
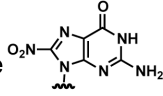
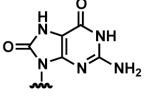


Figure 4.1. Synthesized oligonucleotides.

4.3 Thermal Melting Analysis

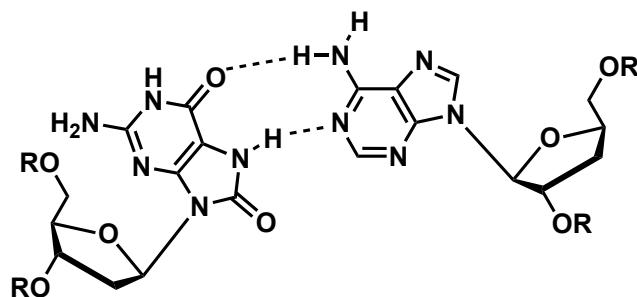
UV thermal melting experiments were used to determine the relative stability of 8-NG **4.14** compared to the 7-nitroindole oligonucleotide **3.21** (Table 4.1).^{207,231,232} 8-NG **4.14** has a clear preference when base paired against C than the other three bases due to Watson-Crick base pairing ($T_m = 46.9$ °C against C compared to $T_m = 40.9$ °C against G, $T_m = 37.3$ °C against A, and $T_m = 38.1$ °C against T). This is a dramatic shift from the universal nitroindole bases, which base pair appreciably against all four bases. In comparison to G-C pairing, incorporation of 8-NG into oligonucleotide **4.14** still decreases stability compared to G ($\Delta T_m = -10.4$ °C), however, is quite more stable than

Table 4.1. Thermal melting of duplex DNA containing the 7-nitroindole, 2'- α -fluoro-8-nitro-2'-deoxyguanosine, and 8-oxo-2'-deoxyguanosine nucleotides. Thermal melting experiments performed in 10 mM sodium cacodylate, 10 mM KCl, 10 mM MgCl₂, 5 mM CaCl₂, pH 7.0 buffer.²¹¹ Mean \pm SD (n = 4) are shown.

dsDNA sequence =					
		Y = G	Y = A	Y = C	Y = T
	5' -CCTTTTT X TTTTTGG-3' 3' -GGAAAAA Y AAAAACC-5'				
Nucleobases		Y = G	Y = A	Y = C	Y = T
X = G		47.4 (± 0.7)	45.9 (± 0.8)	57.3 (± 0.5)	48.5 (± 0.5)
X = 7-NO ₂ Indole (3.21)		40.3 (± 0.4) [-7.1]	42.8 (± 0.5) [-3.1]	42.1 (± 0.2) [-15.2]	42.1 (± 0.5) [-6.4]
X = 8-NO ₂ Guanosine (4.14)		40.9 (± 0.8) [-6.5]	37.3 (± 0.4) [-8.6]	46.9 (± 0.7) [-10.4]	38.1 (± 0.6) [-10.4]
X = 8-Oxo- Guanosine (4.15)		43.7 (± 0.4) [-3.7]	50.6 (± 1.1) [4.7]	53.3 (± 0.4) [-4.0]	45.6 (± 0.4) [-2.9]

7-nitroindole ($\Delta\Delta T_m = +4.8$ °C). This added duplex stability is hypothesized to confer to a higher protein-DNA binding affinity than 7-NI when incorporated into CRDDs, especially when multiple 8-NG monomers are incorporated.

A potential limitation of **4.14**, however, is the steric hindrance of the nitro group over the sugar, preventing the nucleobase from occupying the *anti* position. 8-Oxo-2'-deoxyguanosine **4.15** is known to exist partially in the *syn* conformation, which places the oxo group into the hybridization interface.^{252,253} During the *syn* conformation, the nucleobase undergoes Hoogsteen base-pairing, accepting hydrogen bonds from the top face of adenosine, leading to an increased stability with mismatched nucleotides (**Figure 4.2**). If the nitro group of **4.14** is also in the *syn* conformation, it may prevent the nitro group from being in proximity to the anomeric proton it needs to abstract or destabilize molecular recognition interactions. Thermal analysis is informative of this *syn-anti* preference. 8-Oxo-2'-deoxyguanosine **4.15** has clear preferences when base paired against C or A (Watson-Crick and *anti* vs. Hoogsteen and *syn* preferences, respectively) than the other two bases ($T_m = 53.3$ °C against C and $T_m = 50.6$ °C against A compared to $T_m = 43.7$ °C against G and $T_m = 45.6$ °C against T). This clearly demonstrates that 8-



4.15
R = Oligonucleotide

Figure 4.2. Hoogsteen base pairing between *syn* 8-oxo-G **4.15** and *anti* adenosine.

oxo-G is undergoing both Watson-Crick and Hoogsteen base pairing, validating that 8-oxo-G exists in both an *anti* and *syn* conformation. To identify what conformation 8-NG **4.14** exists in, a direct comparison of 8-NG **4.14** to that of 8-oxo-G **4.15** reveals that the thermal stability of **4.14** against A is largely decreased by existing primarily in the *anti* conformation ($\Delta T_m = -8.6$ °C compared to G), whereby the thermal stability of **4.15** against A actually increases ($\Delta T_m = +4.7$ °C compared to G) due to existing partially in the *syn* conformation and undergoing Hoogsteen base pairing. This provides evidence that 8-NG **4.14** undergoes traditional Watson-Crick base pairing (seen in **Scheme 4.1**).

4.4 Proof of Uncaging

To demonstrate whether or not 2'- α -fluoro-8-nitro-2'-deoxyguanosine **4.1** would depurinate within duplex DNA, the oligonucleotide **4.14** was annealed with its complementary strand. Irradiation (350 nm light; light intensity: 5.66×10^{-8} ein $\text{cm}^{-2}\text{s}^{-1}$) of **4.14** yielded photolytic breakdown of the nucleotide, completing its conversion to the corresponding abasic **4.16** and a truncation product **4.17** within 30 minutes (**Figure 4.3**). **Figure 4.3a** displays the LC traces of **4.14** and the formed photo-products. **Figure 4.3b** shows the MS traces of the corresponding oligonucleotides.

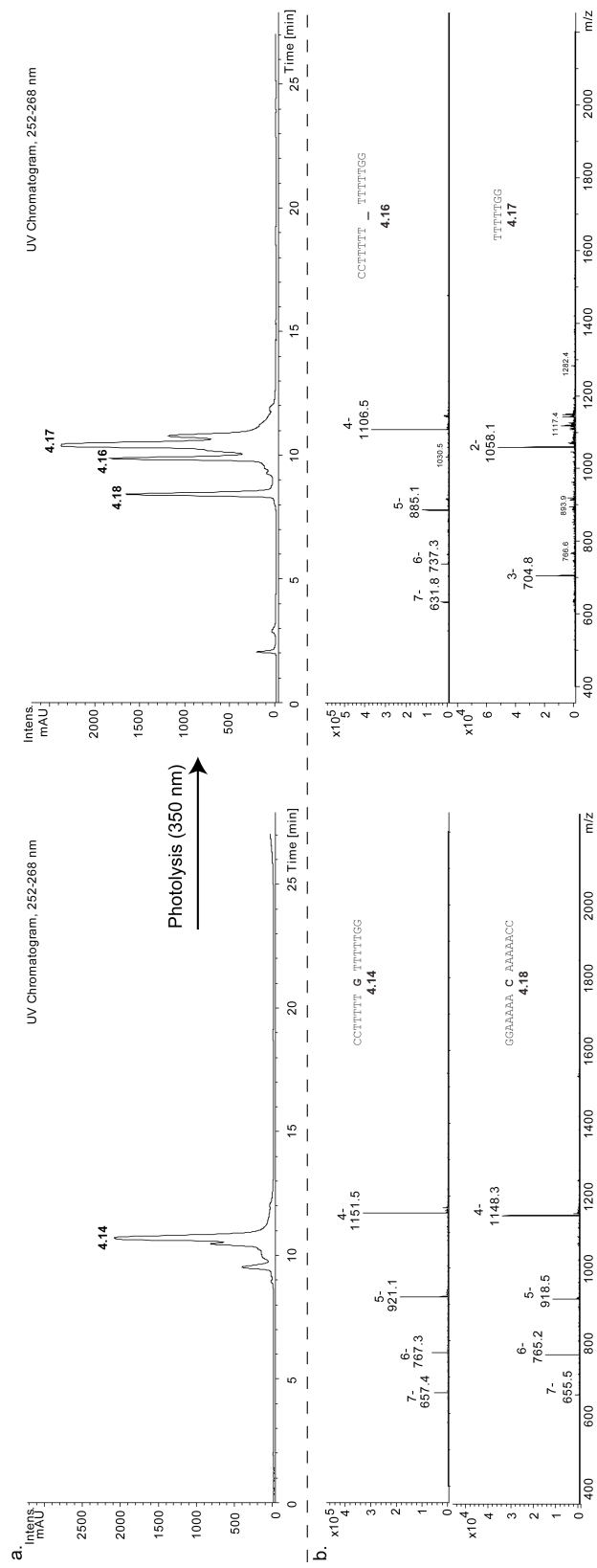


Figure 4.3. Photolysis of **4.14** as a double-stranded oligomer demonstrating that 8-NG can undergo photolysis within a duplex, forming the corresponding abasic site **4.16** and a truncation product **4.17**. (a) LC traces of **4.14** and the formed photo-products. (b) MS traces of the corresponding oligonucleotides.

4.5 Conclusions and Future

The second-generation probe, 2'- α -fluoro-8-nitro-2'-deoxyguanosine **4.1**, contains added molecular recognition capabilities, yielding greater duplex stability. Going forward, we will synthesize our second-generation catch and release DNA decoys to sequester and release TFs such as NF- κ B. Our prediction is that a greater duplex stability, in addition to added molecular recognition, will give higher affinity DNA-protein interactions, which will increase the efficiency of the catch and release DNA decoys. This tighter binder will result in a greater difference in binding affinity after photolysis and formation of abasic sites yielding a more efficient probe. A more efficient probe will give us a higher degree of binding and subsequent release, resulting in lower dosing required in order to sequester cellular TFs.

4.6 Experimental Section

4.6.1 Chemical Synthesis.

General. Procedure outlined in **Chapter 3.8.1**. (see **Appendix B** for chromatograms).

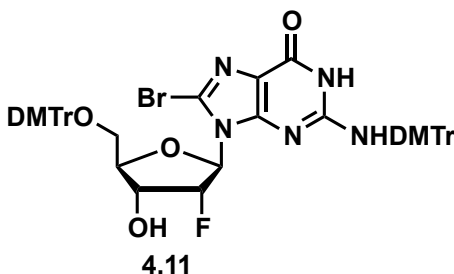
2',3',6'-O-acetyl-8-bromo-guanosine (4.5). Prepared as previously described.²⁴⁹

2',3',6'-O-acetyl-2-dimethoxytrityl-8-bromo-guanosine (4.6). Prepared as previously described.²⁴⁹

2',3',6'-O-acetyl-2-dimethoxytrityl-8-nitro-guanosine (4.7). Prepared as previously described.²⁴⁹

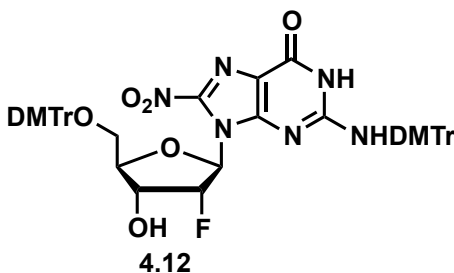
2',3',6'-O-acetyl-8-nitro-guanosine (4.8). Prepared as previously described.²⁴⁹

8-bromo-2'- α -fluoro-2'-deoxyguanosine (4.10). Prepared as previously described.²⁴⁹



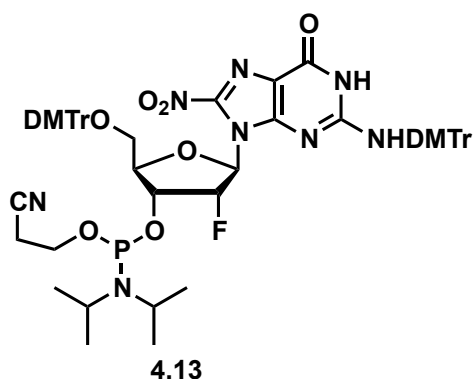
8-bromo-2,6'-dimethoxytrityl-2'- α -fluoro-2'-deoxyguanosine (4.11). 8-bromo-2'- α -fluoro-2'-deoxyguanosine (**4.10**, 2.55 g, 7.01 mmol) was dissolved in pyridine (10 mL) and evaporated three times to remove any water. It was then re-dissolved in pyridine (10 mL) and charged with a catalytic amount of DMAP (85.5 mg, 0.70 mmol). 4,4'-dimethoxytrityl chloride (5.23 g, 15.4 mmol) was added in portions and stirred at room temperature for 24 hours. It was diluted with ddH₂O (200 mL) and extracted with DCM (200 mL). The organic layer was washed with saturated aqueous NaHCO₃ (200 mL) and brine (200 mL). The resultant organic layer was dried (Na₂SO₄), and concentrated *in vacuo*. The residue was purified by column chromatography on silica gel (gradient of 0-5% methanol in DCM). It was concentrated *in vacuo* to yield an orange foam (3.85 g,

56.8% yield over two steps. ^1H NMR (CDCl_3): δ = 8.60 (dt, 4 H, J = 1.8 Hz, 6.00 Hz), 7.67 (tt, 2 H, J = 1.8 Hz, 7.6 Hz, 15.2 Hz), 7.45-6.60 (m, 20H), 5.66 (d, 1H, J = 24.1 Hz), 4.85 (dd, 1H, J_{H-H} = 3.5 Hz, J_{H-F} = 54.1 Hz), 3.86 (ddd, 1H, J = 2.85 Hz, 6.1 Hz, 9.3 Hz), 3.78 (t, 2H, J = 1.8 Hz, 4.8 Hz), 3.73 (s, 6H), 3.72 (s, 6H), 3.58 (m, 5H) 3.27 (m, 1H), 3.13 (dd, 1H, J = 6.24 Hz, 10.7 Hz); ^{13}C NMR (CDCl_3): δ = 158.5, 158.3, 157.4, 151.3, 150.8, 136.0, 130.1, 130.0, 128.1, 127.8, 126.9, 122.9, 118.0, 113.13, 91.8, 90.3, 87.9, 87.6, 86.4, 80.9, 55.2, 30.6, 19.1, 13.7; HRMS-ESI $^-$ m/z $[\text{M}-\text{H}]^-$ calc'd for $\text{C}_{52}\text{H}_{46}\text{BrFN}_5\text{O}_8$: 966.2519, found: 966.2527.



2,6'-dimethoxytrityl-2'- α -fluoro-8-nitro-2'-deoxyguanosine (4.12). 8-bromo-2,6'-dimethoxytrityl-2'- α -fluoro-2'-deoxyguanosine (**4.11**, 357 mg, 0.370 mmol) was dissolved in DMF (10.00 mL) and heated to 90 °C. Potassium nitrite (313 mg, 3.68 mmol) and 18-crown-6 (972 mg, 3.68 mmol) was added to the solution and stirred for 24 hours. It was diluted with ddH₂O (50 mL) and extracted with DCM (50 mL). The organic layer was washed with saturated aqueous brine (50 mL). The resultant organic layer was dried (Na_2SO_4), and concentrated *in vacuo*. The residue was purified by column chromatography on silica gel (gradient of 0-5% methanol in DCM). It was concentrated *in vacuo* to yield an orange foam (0.175 g, 49% yield, 68% yield BRSM). ^1H NMR

(CDCl₃): δ = 7.37-6.95 (m, 18H), 6.72 (m, 4H), 6.61 (m, 4H), 5.58 (d, 1H, J = 23.6 Hz), 4.72 (dd, 1H, J_{H-H} = 3.5 Hz, J_{H-F} = 57.4 Hz), 3.76 (m, 1H), 3.69 (s, 3H), 3.68 (s, 3H), 3.61 (s, 3H), 3.60 (s, 3H), 3.30 (d, 1H, J = 10.45 Hz), 3.15 (m, 2H); ¹³C NMR (CDCl₃): δ = 158.8, 158.6, 158.4, 147.3, 139.4, 135.9, 130.8, 130.1, 129.9, 129.7, 129.1, 128.6, 128.1, 127.8, 127.8, 127.1, 113.2, 87.1, 86.3, 81.4, 55.3, 30.6, 19.1, 13.7; HRMS-ESI m/z [M-H]⁻ calc'd for C₅₂H₄₆FN₆O₁₀⁻: 933.3265, found: 933.3341.



2-Cyanoethyl-*N,N*-diisopropylphosphoramidite-2,6'-dimethoxytrityl-2'- α -fluoro-8-nitro-2'-deoxyguanosine (4.13). 2,6'-dimethoxytrityl-2'- α -fluoro-8-nitro-2'-deoxyguanosine (**4.12**, 166 mg, 0.18 mmol) was put into an Abderhalden with P₂O₅ and dried for 24 hours. It was then dissolved in dry DCM (5 mL) and charged with four molecule sieves and stirred at room temperature for 1 hour. Distilled triethylamine (96 μ L, 0.69 mmol) and 2-Cyanoethyl-*N,N*-diisopropylchlorophosphoramidite (160 μ L, 0.69 mmol) were added and stirred at room temperature for 2 hours. Silica gel, deactivated with triethylamine, was added to the resultant reaction mixture and was concentrated *in vacuo*. The residue was purified by column chromatography on silica gel (gradient of 0-5% methanol in DCM). It was concentrated *in vacuo* to yield an orange foam (63.7 mg,

32% yield). ^1H NMR (CDCl_3): $\delta = 7.51\text{-}7.15$ (m, 22H), 6.85-6.75 (m, 4H), 6.23 (s, 1H), 4.08 (m, 5H), 3.49 (m, 4H), 2.69 (m, 2H), 1.25 (t, 12H, $J = 7.05$ Hz); ^{13}C NMR (CDCl_3): $\delta = 162.9, 158.4, 158.3, 149.3, 147.6, 139.8, 130.2, 130.0, 129.2, 129.2, 128.2, 127.8, 127.8, 127.7, 126.8, 117.1, 113.0, 113.0, 112.9, 81.2, 58.3, 55.1, 50.1, 45.8, 45.3, 30.8, 22.9, 19.9, 9.0$; ^{31}P NMR $\delta = 150.84$ (s, 1P) HRMS-ESI $^-$ m/z $[\text{M-H}]^-$ calc'd for $\text{C}_{61}\text{H}_{64}\text{FN}_8\text{O}_{11}\text{P}^-$: 1133.4343, found: 1133.4591.

4.6.2 Solid-Phase DNA Synthesis. Procedure outlined in **Chapter 3.8.2.** (see **Appendix B** for chromatograms).

Oligonucleotide **4.14.** Purity = 90.9% (260 nm). MS calc'd 4608.9, found 4609.5 (parent)

Oligonucleotide **4.15.** Purity = 85.9% (260 nm). MS calc'd 4561.9, found 4563.2 (parent)

4.6.3 HPLC Purification & LC-MS Analysis. Procedure outlined in **Chapter 2.8.2.**

4.6.4 Thermal Melting Analysis. Procedure outlined in **Chapter 2.8.3.**

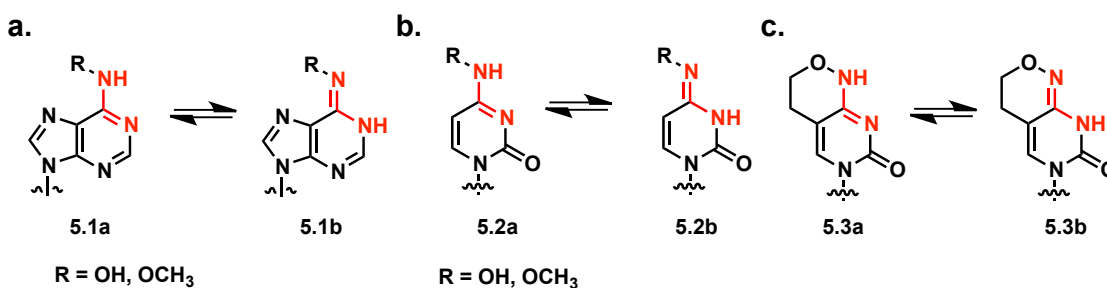
Chapter 5

PHOTOSWITCHABLE NUCLEOBASES THAT TRANSPOSE HYBRIDIZATION PREFERENCES

This work was performed in collaboration with Professor Daniel A. Harki

5.1 Rationale

Noticeably missing from our toolbox of reagents for studying DNA and RNA structure/function properties are photoswitchable nucleotides: non-natural nucleosides (and –tides) that can base pair with a cognate purine or pyrimidine and then switch base pairing preferences after treatment with light (e.g., the designed ligand base pairs with cytosine and administration of light triggers a switch in binding preference for thymine). As opposed to the caged nucleobases (**Chapter 1.6 and 2**) or CRDDs (**Chapter 3**), which are either ‘off-to-on’ or ‘on-to-off’ triggered systems, non-natural photoswitchable nucleobases are designed to be functionally active before and after photolysis. Non-natural nucleobases that transpose their hybridization properties upon photolysis were designed based upon the established ability of nucleosides to adopt, albeit infrequently, different tautomeric forms.^{254,255} Watson and Crick postulated that DNA mutations could occur by the mispairing of minor tautomers, which was later termed the “rare tautomer” hypothesis for DNA replication because of the rare occurrence of natural nucleobase tautomers.²⁵⁶ Chemical modifications can be used to increase the populations of these “rare” tautomers (**Scheme 5.1**). For example, converting the exocyclic amines of



Scheme 5.1. Examples of chemical modifications to increase the frequency of nucleobase tautomers.

adenines or cytosines to hydroxylamine or methoxyamines, shift the tautomeric equilibrium from the amino to the imino tautomers (**Scheme 5.1a-b**).²⁵⁷⁻²⁶³ The P nucleobase is an analogue of the hydroxylamine cytosine, where the hydroxyl group is tethered to make a 6-membered ring and prevent *syn-anti* isomerization (**Scheme 5.1c**).²⁶⁴⁻²⁶⁸ The P nucleotide and oligonucleotides have been utilized in numerous applications including substrates for DNA polymerases, primers for DNA synthesis, and viral mutagens.²⁶⁹⁻²⁷¹

The ability of these systems to transpose their hybridization preferences exploits differences in ground state energies (ΔG_{rel}) between discrete tautomers. Locking of the high-energy tautomer through appendage of a photolabile caging group yields a nucleobase that will hybridize to a native purine or pyrimidine. Photolysis of the caging group removes the barrier for nucleobase tautomerization and enables return to its lowest energy structure, which results in formation of a modified nucleobase with a different hydrogen-bonding profile. These reagents then base pair with their new complement purine or pyrimidine.

The position of the caging group should be away from the hydrogen-bonding face of the nucleobase to minimize the steric hindrance to the complementary nucleobases. The x-ray crystal structure of the DNA sequence 5'-CCAAGCTTGG-3' reveals that C₅ and C₆ of pyrimidines and C₇ and C₈ of purines are solvent exposed and point into the major groove, therefore, the addition of the caging group to these positions should minimize any steric interactions (**Figure 5.1**, PDB: 1en3).²⁷²

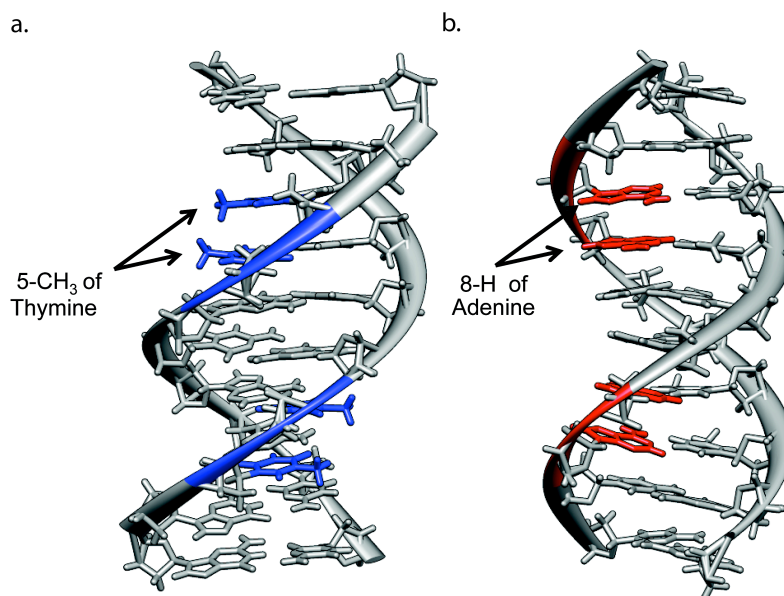


Figure 5.1. X-ray crystal structure of the DNA sequence 5'-CCAAGCTTGG-3' (PDB: 1n3). (a) Solvent exposed 5-CH₃ of thymine (shown in blue). (b) Solvent exposed 8-H of adenine (shown in red).

We designed and have successfully made benzyl protected isatin nucleobase that contains a locked, high energy, imine tautomer. Photolysis of this isatin has been shown to release the high-energy imine tautomer and isomerize to the lower energy amine tautomer.

5.2.1 Isatin Scaffold

One example of this strategy is shown in **Figure 5.2**. Enolate trapping of the higher energy tautomer of the isomerizable isatin system with 2-nitrobenzyl (**1.40**), locks the tautomer in one hydrogen-bonding arrangement, yielding a non-natural guanosine mimic **5.4**. Photolysis of the 2-NB group followed by isomerization of the nucleobase to the lower energy tautomer, yields a new hydrogen-bonding conformation as a non-natural

adenosine mimic **5.5**. The mechanism of photochemical tautomerization can follow traditional 2-NB uncaging (**Scheme 1.3**). Irradiation with light produces a diradical **5.7** that undergoes a hydrogen atom abstraction **5.8** and rearranges to the heterocyclic intermediate **5.10**. This intermediate breaks down, releases the nitroso by-product **5.11** and rearranges the electrons from the imine to the nitrogen, which is protonated, yielding the amino group **5.12** (**Figure 5.2b**). Calculated differences in ground state energies of the two possible isatin tautomers utilizing density functional theory calculations (B3LYP/DFT, 6-31G* basis set, Spartan) reveals a clear preference for one tautomer over the other ($\Delta G_{\text{rel}} = 34.4$ kcal/mol, **Figure 5.2c**). We utilize these relatively simple ground state energy calculations to predict the lowest energy and predominant tautomer when designing new nucleobases for synthesis. The position of the caging moiety is also essential in our design since this modification cannot interfere with nucleobase hybridization. To avoid the steric disruption of hybridization that occurs with caged

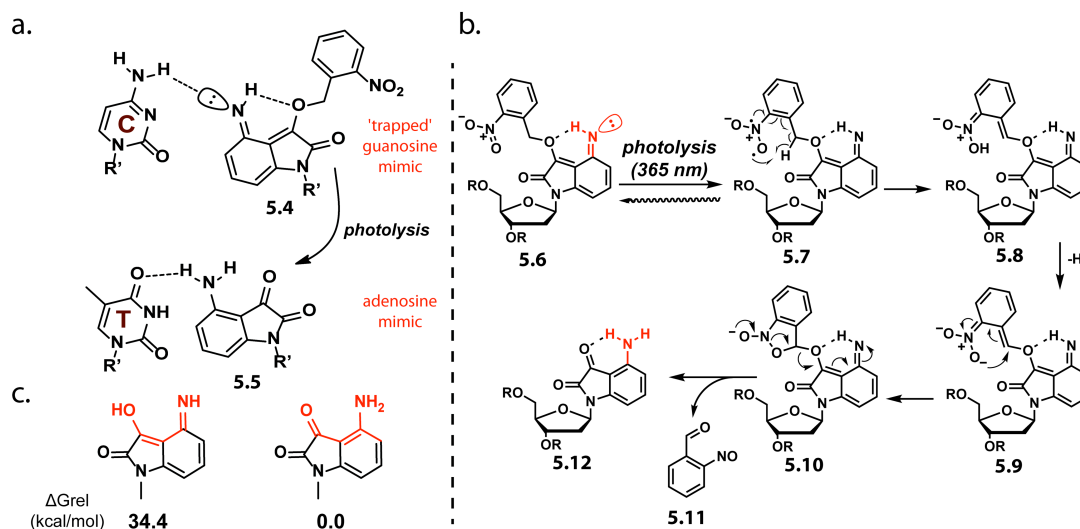
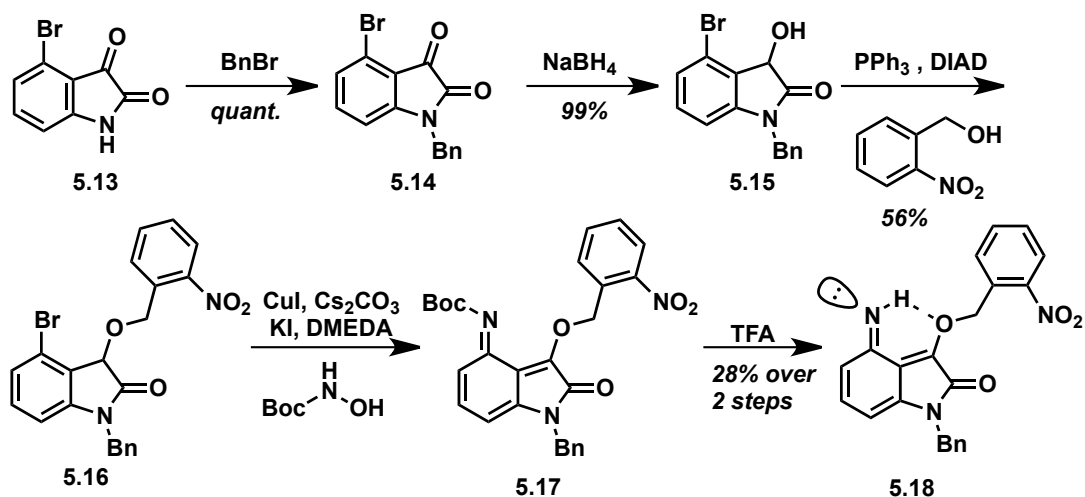


Figure 5.2. (a) Isatin G-to-A mimic scaffold. (b) Calculated relative stabilities of the tautomers of the isatin photoswitch. (c) Proposed mechanism of photochemical tautomerization. R' = ribose sugar. R = oligonucleotide.

nucleobases, we rationalized that appending the photolabile molecule to the 3-position of isatin would not significantly disrupt DNA hybridization since this position of the heterocycle would be expected to project into the major groove in duplex DNA, akin to the region in space occupied by the 8-position of native purines.

5.2.2 Isatin Synthesis

To this point, we have successfully made benzyl protected isatin nucleobase **5.18** (Scheme 5.2). Benzyl protection of 4-bromoisatin **5.13** followed by reduction of the 3-position ketone of intermediate **5.14** proceeded smoothly to deliver alcohol **5.15**. Alkylation with the requisite 2-NB caging group (**1.40**) provided intermediate **5.16**. Coupling of Boc protected hydroxylamine to the isatin heterocycle by copper catalyzed carboamination followed by spontaneous dehydration delivered **5.17**,²⁷³ which was immediately deprotected to yield the trapped non-natural guanosine mimic imine **5.18**.



Scheme 5.2. Synthesis of the benzyl protected caged isatin imine **5.18**.

5.2.3 Isatin Photochemical Tautomerization

With **5.18** in hand we conducted preliminary photolysis experiments to demonstrate the ability of the nucleobase to tautomerize (**Figure 5.3**). Compound **5.18** was dissolved in CDCl₃ and a ¹H NMR spectrum was acquired. Upon photolysis at 254 nm over 4 hours, we see complete elimination of proton H_A (internally hydrogen bonded imine proton) from the tautomerization to the amine **5.19** and large chemical shifts of the 2-NB protons upon production of the predicted nitroso aldehyde **5.20**. This experiment suggests the ability to photochemically tautomerize a trapped non-natural guanosine

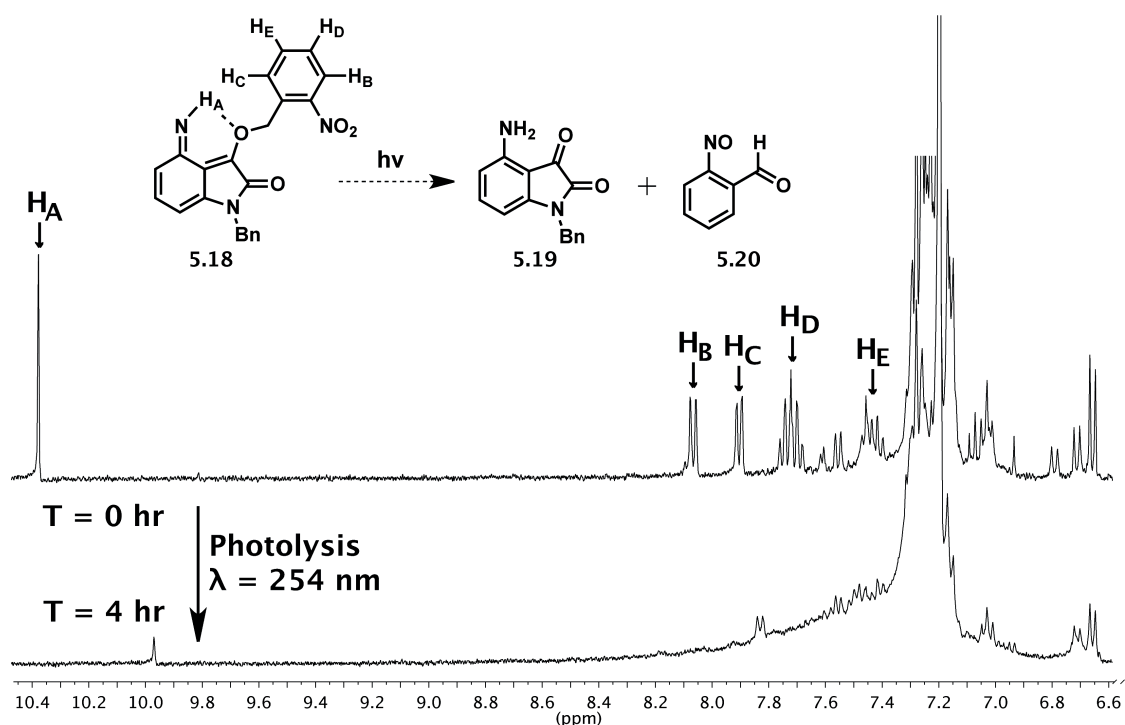


Figure 5.3. NMR photolysis experiment of the caged isatin scaffold demonstrating tautomerization from the imine **5.18** to the amine **5.19**.

mimic imine to a lower energy amine derivative, yielding a non-natural adenosine mimic, although more definitive experiments are needed to fully characterize this process.

5.3 Conclusions and Future Work

We synthesized the non-natural guanosine mimic imine **5.18** and demonstrated that it is able to photochemically tautomerize to the lower energy amine derivative, yielding a non-natural adenosine mimic. Future work will include synthesizing the phosphoramidite of the isatin scaffold **5.7**. Once incorporated in oligonucleotides, we will utilize thermal DNA denaturation (T_m) to characterize the DNA oligos bearing our photoswitchable nucleosides. A decrease in duplex DNA T_m confers destabilization of

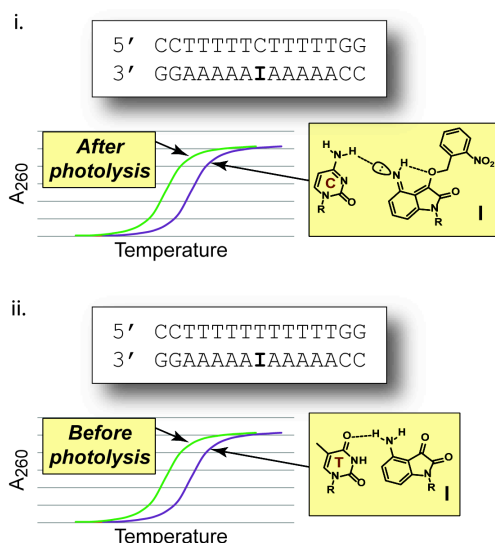


Figure 5.4. The photoswitchable isatin heterocycle is incorporated into DNA oligos by solid-phase synthesis, and isatin-functionalized duplex DNAs are measured for stability by thermal denaturation studies (melting temperature, T_m , experiments). (i) Hypothetical example of the isatin photoswitch base-paired with its designed complement cytosine. Photolysis of this sample switches the isatin to an adenine mimic, lowering T_m . (ii) Mispairing of the isatin photoswitch with thymine; however, photolysis of the isatin heterocycle yields the adenine mimic, which forms a favorable base-pair with adenine and increases the T_m . R = ribose

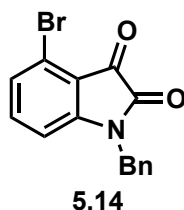
the duplex, whereas an increase in T_m signifies enhanced stabilization. An illustration of this technique is shown in **Figure 5.4**, where incorporation of the ‘trapped’ isatin photoswitchable nucleoside (**Figure 5.4ai**) into a DNA oligo and base pairing opposite its designed complement, cytosine, in duplex DNA is predicted to yield a favorable T_m . However, photolysis of this sample will switch the hybridization preference of the isatin nucleobase to an adenine mimic that will exhibit a lower T_m due to mispairing with cytosine. Conversely, mispairing of the ‘trapped’ isatin heterocycle across from thymine can be quantified by simply using another DNA strand (**Figure 5.4aii**). Photolysis of this sample will then convert the isatin nucleobase into an adenine mimic, which should form a favorable base pair with thymine and yield an increase in duplex T_m upon a second analysis of the sample. These experiments allow us to quickly triage newly synthesized photoswitchable probes for their base pairing preferences. In addition to these studies, other photoswitchable scaffolds will be developed.

5.4 Experimental Section

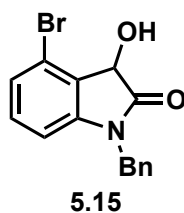
5.4.1 *Ab initio* calculations. Energy minimized three-dimensional conformations were generated for each compound using the calculations function of Spartan Student Edition (Version 4.1.1, Build 132) utilizing density functional theory calculations (B3LYP/DFT, 6-31G* basis set). Energies were normalized to the lowest energy structure.

5.4.2 Chemical Synthesis.

General. Procedure outlined in **Chapter 3.8.1.** (see **Appendix B** for chromatograms).

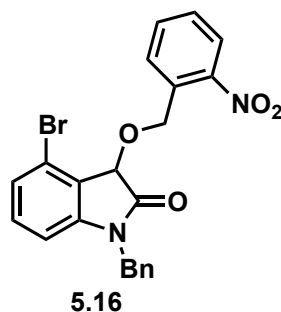


1-Benzyl-4-bromoisatin (5.14). Sodium Hydride (326 mg, 8.49 mmol) was added to a slurry of 4-bromoisatin (1.28 g, 5.66 mmol) in DMF (10 mL) and stirred at room temperature for 10 minutes. Benzylbromide (1.01 mL, 8.49 mmol) was added dropwise and stirred at room temperature for 15 minutes. The mixture was poured into cold stirring brine (150 mL) and the orange precipitate was filtered to give **5.14** (1.78 g, quantitative yield). ^1H NMR (CDCl_3): $\delta = 7.37\text{-}7.29$ (m, 6H), 7.22 (d, 1H, $J = 8.15$ Hz), 6.72 (d, 1H, $J = 7.8$ Hz), 4.94 (s, 2H); ^{13}C NMR (CDCl_3): $\delta = 180.6, 157.3, 152.2, 138.3, 134.1, 133.3, 129.1, 128.6, 128.3, 127.4, 121.7, 116.5, 109.7, 100.0, 44.1$; HRMS-ESI m/z $[\text{M}+\text{Na}]^+$ calc'd for $\text{C}_{15}\text{H}_{10}\text{BrNO}_2\text{Na}^+$: 337.9787, found: 337.9815.

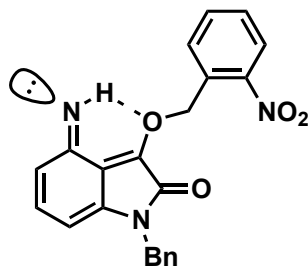


1-Benzyl-4-bromo-3-hydroxy-isatin (5.15). Sodium borohydride (18 mg, 0.47 mmol) was added to a solution of **5.14** (100 mg) in MeOH/DCM (1:1, 10 mL) at 0 °C and stirred for 1 hour. It was quenched with 1N HCl (10 mL), concentrated *in vacuo*, extracted with

ethyl acetate (10 mL), and SiO₂ purified (100% DCM) to give **5.15** (100 mg, 99%). ¹H NMR (CDCl₃): δ = 7.34-7.27 (m, 5H), 7.17 (d, 1H, *J* = 9.3 Hz), 7.08 (t, 1H, *J* = 7.9 Hz), 6.65 (d, 1H, *J* = 7.8 Hz), 5.17 (s, 1H), 4.87 (m, 2H); ¹³C NMR (CDCl₃): δ = 174.8, 144.8, 134.8, 131.4, 128.9, 127.9, 127.3, 126.5, 120.5, 108.5, 100.0, 70.3, 60.4, 44.0, 14.2; HRMS-ESI⁺ m/z [M+Na]⁺ calc'd for C₁₅H₁₂BrNO₂Na⁺: 339.9944, found: 339.9888.



1-Benzyl-4-bromo-3-(2-nitrobenzyl)-isatin (5.16). 2-Nitrobenzyl alcohol (73 mg, 0.471 mmol) and triphenylphosphine (124 mg, 0.47 mmol) were added to a solution of **5.15** (100 mg, 0.31 mmol) in THF (15 mL) at room temperature. DIAD (0.093 mL, 0.47 mmol) was added dropwise to the reaction mixture and stirred for 24 hours. The reaction was quenched with H₂O (15 mL), extracted with DCM (50 mL) and washed with brine (20 mL), then SiO₂ purified (gradient of 0-40% ethyl acetate in hexanes) to give **5.16** (80.0 mg, 56%). ¹H NMR (CDCl₃): δ = 8.11 (dd, 1H, *J* = 1.3 Hz, 8.1 Hz), 7.75 (m, 1H), 7.68 (td, 1H, *J* = 1.35 Hz, 7.5 Hz), 7.48 (dt, 1H, *J* = 1.55 Hz, 3.55 Hz), 7.34-7.27 (m, 3H), 7.19-7.11 (m, 3H), 6.72 (m, 1H), 6.59 (m, 1H), 5.30 (s, 2H), 4.94 (s, 2H), 2.78 (t, 1H, *J* = 6.55 Hz); ¹³C NMR (CDCl₃): δ = 171.2, 134.1, 133.2, 129.8, 129.0, 128.9, 128.4, 127.8, 127.6, 127.4, 127.2, 127.1, 70.1, 62.3, 60.4, 44.4, 21.1, 14.2; HRMS-ESI²⁻ m/z [M-2H]²⁻ calc'd for C₂₂H₁₅BrN₂O₄²⁻: 225.0113, found: 225.0990.



5.18

1-Benzyl-4-imine-3-(2-nitrobenzyl)-isatin (5.18). A 10 mL Schlenk flask was oven dried, cooled, and then charged with **5.16** (45 mg, 0.10 mmol), CuI (1.9 mg, 0.01 mmol), KI (33 mg, 0.20 mmol), Boc-protected hydroxylamine (17 mg, 0.14 mmol), dimethylethylenediamine (5 μ L, 0.05 mmol). The flask was evacuated and refilled with nitrogen. The reagents were dissolved in DMF (5 mL) and cesium carbonate (46 mg, 0.14 mmol) was added. The reaction was heated to 110 $^{\circ}$ C and stirred for 6 hours. The reaction was filtered and evaporated to afford crude **5.17**.

Trifluoroacetic acid (6 μ L, 0.08 mmol) was added dropwise to a solution of crude **5.17** (25 mg, 0.05 mmol) in DCM (5 mL) at room temperature. The reaction was concentrated *in vacuo*, then SiO₂ purified (gradient of 0-5% methanol in DCM) to give **5.18** (11 mg, 28% over two steps). ¹H NMR (CDCl₃): δ = 10.37 (s, 1H), 8.05 (d, 1H, J = 8.28 Hz), 7.89 (dd, 1H, J = 2.0 Hz, 7.4), 7.73 (m, 1H), 7.71 (dt, 1H, J = 0.96 Hz, 7.28 Hz, 9.04 Hz), 7.45 (t, 1H, J = 5.32), 7.34-7.14 (m, 4H), 7.03 (t, 1H, J = 7.96 Hz), 6.66 (d, 1H, J = 8.84 Hz), 5.23 (s, 2H), 4.87 (s, 2H); ¹³C NMR (CDCl₃): δ = 206.9, 148.3, 138.3, 130.8, 129.1,

129.0, 128.6, 128.3, 128.1, 127.4, 127.2, 53.4, 44.1, 31.9, 29.7, 22.7, 22.0, 14.2; HRMS-ESI m/z [M-H]⁻ calc'd for C₂₂H₁₇N₃O₄⁻: 387.1219, found: 387.1174.

Chapter 6

BICYCLIC CYCLOHEXENONES AS INHIBITORS OF NF- κ B SIGNALING

This work has been published by the American Chemical Society:
The full text is reprinted with permission from Hexum, J. K.; Tello-Aburto, R.; Struntz, N. B.; Harned, A. M.; Harki, D. A. Bicyclic Cyclohexenones as Inhibitors of NF-kappaB Signaling. *ACS Med Chem Lett* **2012**, 3, 459-464. Copyright 2012 American Chemical Society.

This work was performed in collaboration with Mr. Joseph Hexum, Dr. Rodolfo Tello-Aburto, Professor Andrew M. Harned, and Professor Daniel A. Harki

6.1 Rationale

Transient induction of the nuclear factor- κ B (NF- κ B) transcription factors is an essential step in the immune response to pathogens, resulting in the expression of genes associated with cellular proliferation, differentiation, and survival, as well as activating the cellular inflammatory response.²⁷⁴⁻²⁷⁶ Equally important is the ability of cells to down-regulate or terminate this activity.²⁷⁵ Constitutive NF- κ B activation has been observed in a spectrum of human cancers, such as acute and chronic myeloid leukemias, prostate, breast, lung, and brain cancers.⁴⁷ Chronic inflammation resulting from constitutive NF- κ B activation has been strongly implicated in the carcinogenesis of tissues from these organ sites.^{48,277-279} Consequently, the NF- κ B signaling pathway has become an important therapeutic target for developing the next-generation of small molecule anticancer agents.²⁷⁷

There have been numerous efforts aimed at identifying natural products with activity against the NF- κ B pathway.²⁸⁰⁻²⁸³ Many of these natural products contain reactive moieties (e.g. enones) that can capture nucleophiles and inhibit signaling through a covalent mechanism.^{284,285} Drugs that function through a covalent mechanism are widely used in the pharmaceutical industry and at least 39 FDA-approved medicines can be classified as ‘covalent drugs.’²⁸⁶ One recently identified natural product NF- κ B inhibitor with a reactive enone moiety is cryptocaryone (**6.1**).²⁸⁷⁻²⁸⁹ Researchers at the National Cancer Institute reported that **6.1** inhibits degradation of the NF- κ B repressor protein I κ B α in B lymphocytes with high constitutive IKK (I κ B kinase complex) activity (**Figure**

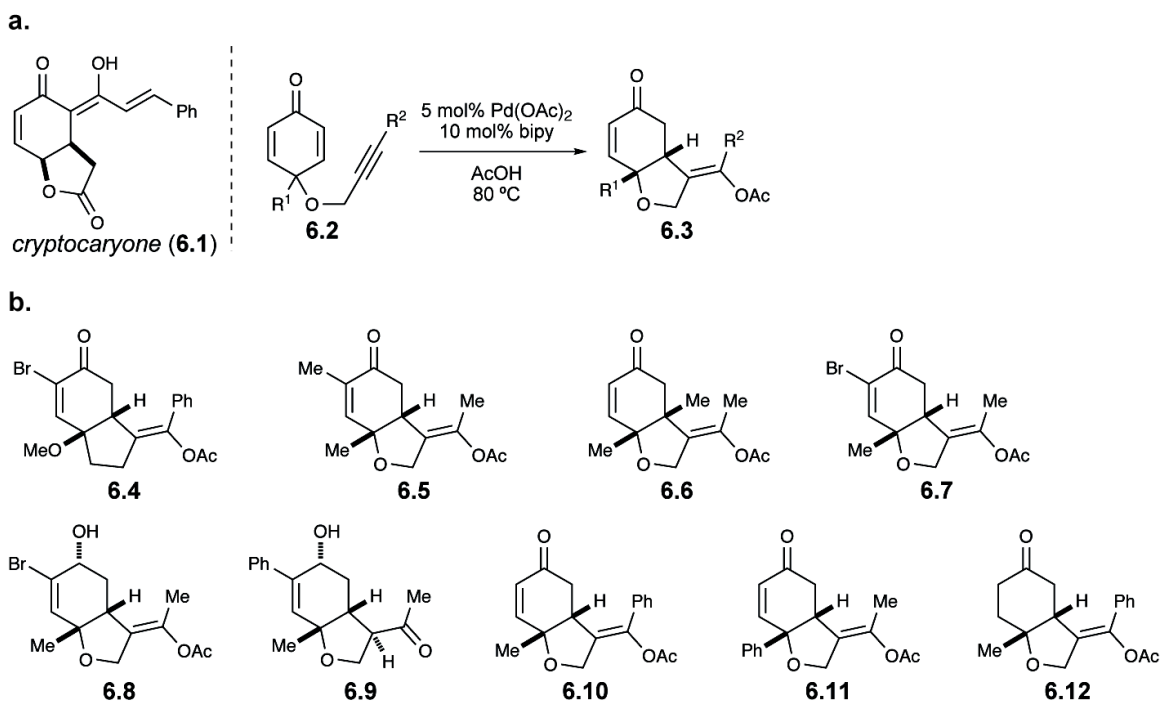


Figure 6.1. (A) Structure of cryptocaryone (**6.1**) and methodology for the preparation of the bicyclic enones of interest. (B) Analogues **6.4-6.12** (racemic) screened for NF- κ B inhibitory activity.

1.5).²⁹⁰ As discussed above, activated IKKs phosphorylate I κ B repressor proteins, targeting them for ubiquitination and degradation by the 26S proteasome. Freed p50-p65 (NF- κ B) heterodimers can then translocate to the nucleus and activate the expression of NF- κ B target genes.^{73,274,279} Accordingly, inhibiting the degradation of I κ B proteins by small molecules such as cryptocaryone (**6.1**) is a strategy that can be used to modulate aberrant NF- κ B signaling by inhibiting its translocation to the nucleus (**Figure 1.6c**). Due to this promising activity, enantioselective total syntheses of cryptocaryone have been recently described by both Fujioka²⁹¹ and Helmchen.²⁹²

Our interest in cryptocaryone stems from its structural similarity to a series of compounds we have recently prepared via Pd-catalyzed acetoxylation of alkyne-tethered cyclohexadienones (e.g., **6.2**→**6.3**, **Figure 6.1a**).²⁹³ While **6.3** does not have the

cinnamoyl side chain present in **6.1**, we hypothesized that the structurally similar enone moiety that is present in both **6.1** and **6.3** may yield similar biological activity profiles for both compounds. Previous studies with sesquiterpene lactones that inhibit NF- κ B signaling have revealed covalent Michael adduct formation to exposed cysteine residues on essential NF- κ B proteins, thereby eliminating their enzymatic activity and disrupting the signaling pathway.²⁸³ While cryptocaryone's exact protein target(s) and mechanism of binding (e.g., covalent or non-covalent) are unknown at this time, it is possible that it similarly captures accessible cysteine sulfhydryl groups on key protein(s) involved in NF- κ B signaling and abolishes their function. If this is the case, then structurally analogous compounds to cryptocaryone (**6.1**), such as **6.3**, should also possess NF- κ B inhibitory properties. The presence of the fully substituted carbon atom at the γ -position of the enone in **6.3** does provide some additional steric hindrance that may deter Michael adduct formation in comparison to **6.1**. Undeterred, we investigated the NF- κ B inhibitory activity of several bicyclic enones similar to **6.3** and we also studied their antiproliferative activities against prototypical leukemia and prostate cancer cell lines. The compounds investigated during this study are shown in **Figure 6.1b** and were prepared using methods previously described by the Harned lab. Compounds **6.4-6.11** were all prepared as racemic samples.

6.2 Cytotoxicity of Cryptocaryone Analogues and Inhibition of NF- κ B Gene Expression Utilizing a Reporter Assay

Initial screening of **6.4-6.11** was carried out utilizing a standard NF- κ B luciferase reporter assay in A549 human lung cancer cells. This cell line bears a stably transfected luciferase reporter construct downstream of six repeats of the consensus NF- κ B binding site. Induction of NF- κ B signaling is achieved by treatment with TNF- α , and cell permeable small molecules can inhibit this induced activity. We performed a preliminary screen by treating induced cells with 50 μ M concentrations of **6.4-6.11**. This concentration was selected based upon cryptocaryone's ability to inhibit the degradation of I κ B α at 16 μ M.²⁹⁰ Results from our study found **6.4** to be poorly soluble under the assay conditions, yielding unreliable values, and compounds **6.5-6.9** failed to inhibit induced NF- κ B activity (**Figure 6.2**).

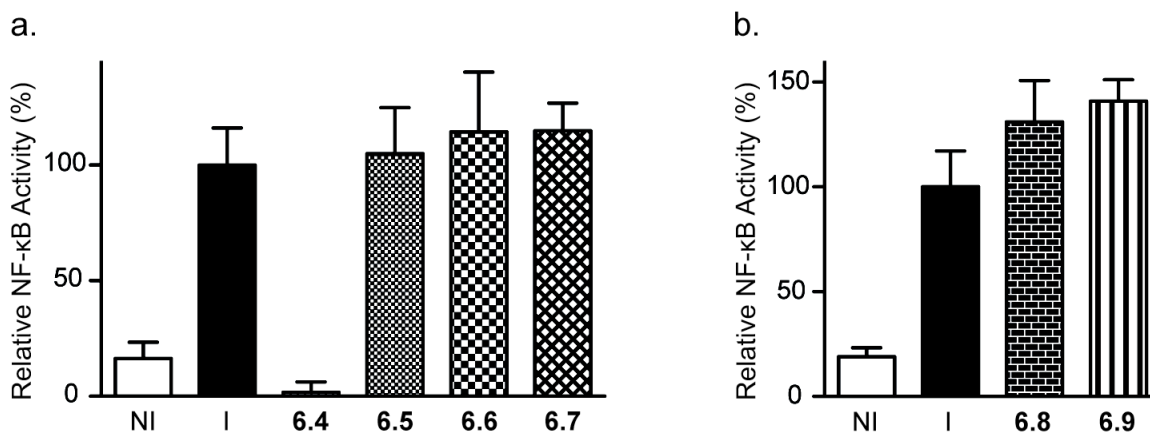


Figure 6.2. Initial Screening of Compounds **6.4-6.9** for NF- κ B Inhibitory Activity. Assay was performed in A549 cells as described below. NI = non-induced control wells, I = cells induced with TNF- α (15 ng/mL). A549 cells are induced with TNF- α (15 ng/mL) and treated with **6.4-6.9** at a concentration of 50 μ M. Notably, **6.4** was poorly soluble in this assay and significant amounts of precipitate were noticed upon serial dilution of the DMSO stock into media.

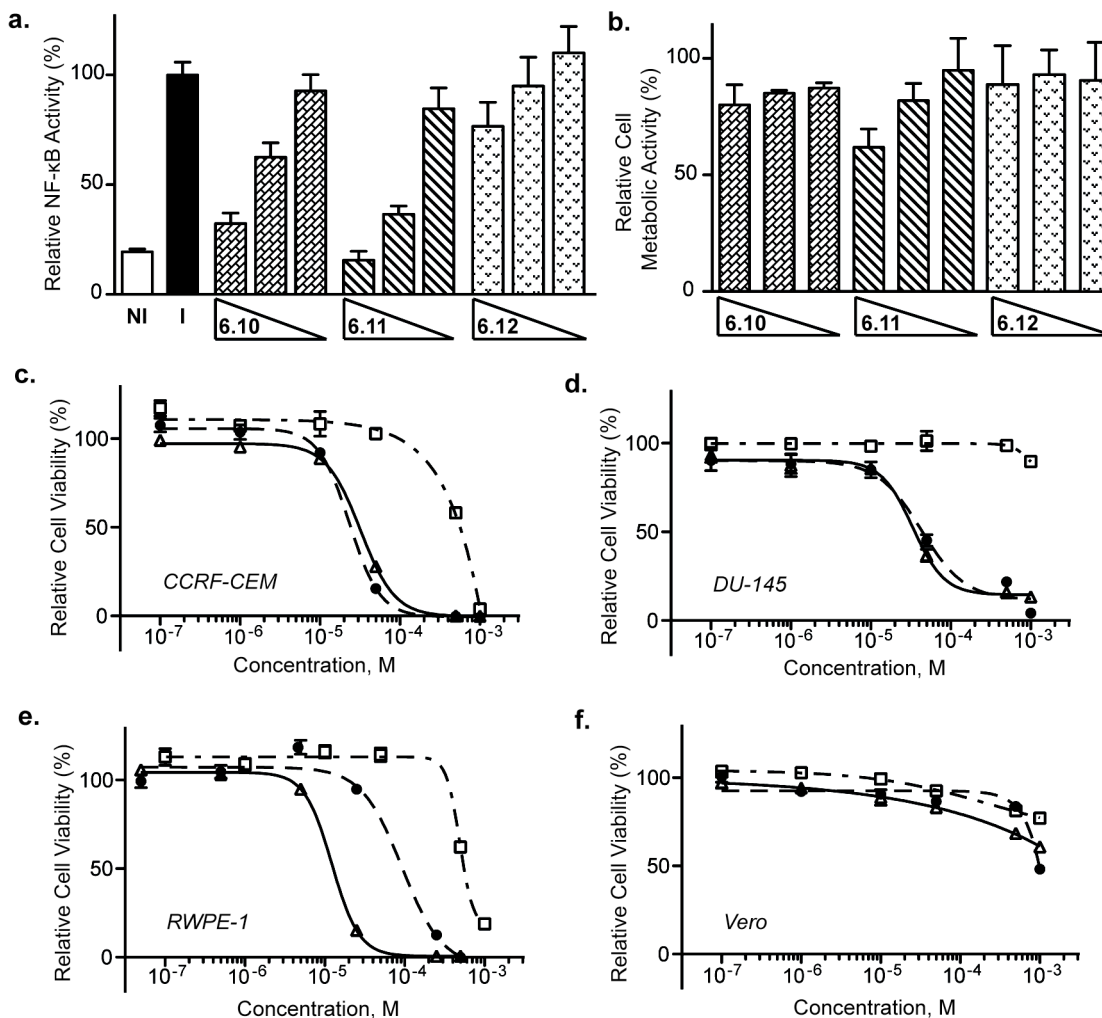


Figure 6.3. (a) Cellular NF-κB luciferase reporter assay in A549 cells. NI = non-induced control cells, I = cells induced with TNF-α. Compound-treated cells are induced with TNF-α and treated with analogues **10-12** at the following concentrations: 100 μM, 50 μM, and 10 μM. (b) Cytotoxicity of **10-12** in the NF-κB Reporter Assay. Cells are treated with **10**, **11**, and **12** at 250 μM, 100 μM, and 50 μM concentrations and cell viability was assessed by Alamar Blue staining. (c-f) Cytotoxicity of **6.10-6.12** against (c) CCRF-CEM cells, (d) DU-145 cells, (e) RWPE-1 cells, and (f) Vero cells. Cells were treated with **6.10** (open triangles), **6.11** (closed circles), and **6.12** (open squares) at various concentrations. Cell viability was measured by Alamar Blue staining.

Gratifyingly, analogues **6.10** and **6.11** both inhibited induced NF- κ B activity (**Figure 6.3a and Table 6.1**). At a concentration of 50 μ M, both compounds inhibited induced NF- κ B activity, with **6.11** (36% residual NF- κ B activity) exhibiting more potent inhibition than **6.10** (62% residual NF- κ B activity) following treatment. The NF- κ B inhibitory activity was not attributable to non-specific cell death as only 5% (for **6.10**) and 10% (for **6.11**) decreases in cell viability were observed following 50 μ M treatment with each compound under identical assay conditions (**Figure 6.3b**). Compound **6.11** completely inhibited NF- κ B activity to non-induced levels at a 100 μ M treatment and was more potent than **6.10** at all concentrations examined.

To determine if **6.10** and **6.11** function through a covalent mechanism of inhibition, the enone moiety of compound **6.10** was reduced to produce the respective cyclohexanone, **6.12** (racemic). If covalent capture of proteins is the mechanism of activity, then compound **6.12** should exhibit diminished NF- κ B inhibitory activity in the A549 luciferase reporter assay. We found that compound **6.12** only reduced NF- κ B activity by 24% (**Figure 6.3a and Table 6.1**) at the highest concentration tested (100 μ M), which is a ~4-fold decrease in potency compared to **6.11**. Therefore, these molecules function, at least in part, through a covalent mechanism of inhibition.

Encouraged by these results we evaluated compounds **6.10-6.12** for their cytotoxicity in two standard human cancer cell lines, DU-145 and CCRF-CEM. DU-145 is a model for hormone-independent prostate cancer and CCRF-CEM is a model for childhood T-cell acute lymphoblastic leukemia. DU-145 cells are known to possess constitutive NF- κ B activity.^{294,295} In addition, these three compounds were tested against

RWPE-1, an immortalized prostate epithelial cell line derived from non-cancerous prostate cells, and Vero, a cell line developed from the kidney of a normal African green monkey (**Figure 6.3e-f**).²⁹⁶⁻³⁰¹ The RWPE-1 and Vero cell lines were utilized in this study to allow us to measure the selectivity of compounds **6.10-6.12**. Selectivity indices are frequently-used metrics that directly compare the potency of a compound in cancer cells to the potency of the same compound in ‘normal’ cells.³⁰²

As shown in **Figure 6.3c-d**, **6.10** and **6.11** exhibited similar cytotoxicities against DU-145 and CCRF-CEM. Both compounds were slightly more potent against CCRF-CEM cells (IC_{50} : **6.10**, **6.11** = 26 μ M) than DU-145 cells (IC_{50} : **6.10** = 34 μ M, **6.11** = 36 μ M) in a 48-hr cytotoxicity assay (**Table 6.1**). The observed IC_{50} values for **6.10** and **6.11** against DU-145 are approximately 15-fold higher than the reported IC_{50} value for cryptocaryone (IC_{50} = 2.3 μ M) in the same cell line.³⁰³ Control compound **6.12** exhibited very little activity against either cell line (IC_{50} values could not be accurately calculated due to lack of potency). This result further confirms that the enone moiety is essential for activity. To measure selectivity indices (SI) for **6.10** and **6.11**, we compared the IC_{50} values for inhibition of DU-145 versus RWPE-1 cells (**Table 6.1**). These values were calculated by dividing the IC_{50} value obtained for each compound against the RWPE-1 cell line by the IC_{50} value obtained for each compound against the DU-145 cell line. Compound **6.10** resulted in an SI value of 0.44, suggesting that this compound is not selective towards DU-145 prostate cancer cells. In contrast, compound **6.11** resulted in an SI value of 2.75. Thus, **6.11** appears to be more selective towards DU-145 cells than RWPE-1 cells, adding to our interest in this analogue.

Table 6.1. Results of NF- κ B reporter and cytotoxicity assays performed with **6.10-6.12**. ^aPercentage (%) NF- κ B activity at various doses is shown relative to the induced, DMSO treated control arbitrarily assigned 100% activity. Mean values of biological triplicate data are shown with propagated standard deviation (\pm SD) from all replicates. ^bIC₅₀ values shown are the mean of three biological replicates. The error values are shown as the standard deviation (\pm SD) of the triplicate data. ^cThe selectivity indices (SI) were calculated by dividing the IC₅₀ value obtained for each compound against the RWPE-1 cell line by the IC₅₀ value obtained for each compound against the DU-145 cell line.

Compound	% NF- κ B Activity ^a		
	100 μ M	50 μ M	10 μ M
6.10	33.9 \pm 10.8	61.6 \pm 10.7	90.9 \pm 13.5
6.11	17.3 \pm 5.1	36.2 \pm 8.2	93.7 \pm 15.5
6.12	76.1 \pm 10.9	94.4 \pm 13.1	109.4 \pm 12.0

Compound	IC ₅₀ (μ M) ^b				SI ^c
	CCRF-CEM	DU-145	Vero	RWPE-1	
6.10	26.4 \pm 7.3	33.7 \pm 5.8	>500	14.8 \pm 2.6	0.44
6.11	26.4 \pm 3.1	35.9 \pm 4.8	>500	98.8 \pm 15.1	2.75
6.12	>500	>500	>500	>500	-

6.3 Thiol Reactivity of Cryptocaryone Analogues

Following the cytotoxicity assays, we decided to further investigate the Michael acceptor mechanism hypothesis for these compounds. Therefore, we performed an NMR experiment in which **6.10** was incubated with cysteamine (**Figure 6.4a**).³⁰⁴ NMR spectra were collected at various timepoints (**Figure 6.4b**). The disappearance of the doublet at 6.06 ppm followed by the disappearance of the doublet at 6.75 ppm provides evidence for a two-step Michael addition of cysteamine into the enone moiety of **6.10**. To confirm the Michael addition adduct had formed, the cysteamine reaction mixture was purified by HPLC and analyzed by mass spectrometry (**Figure 6.4c**).

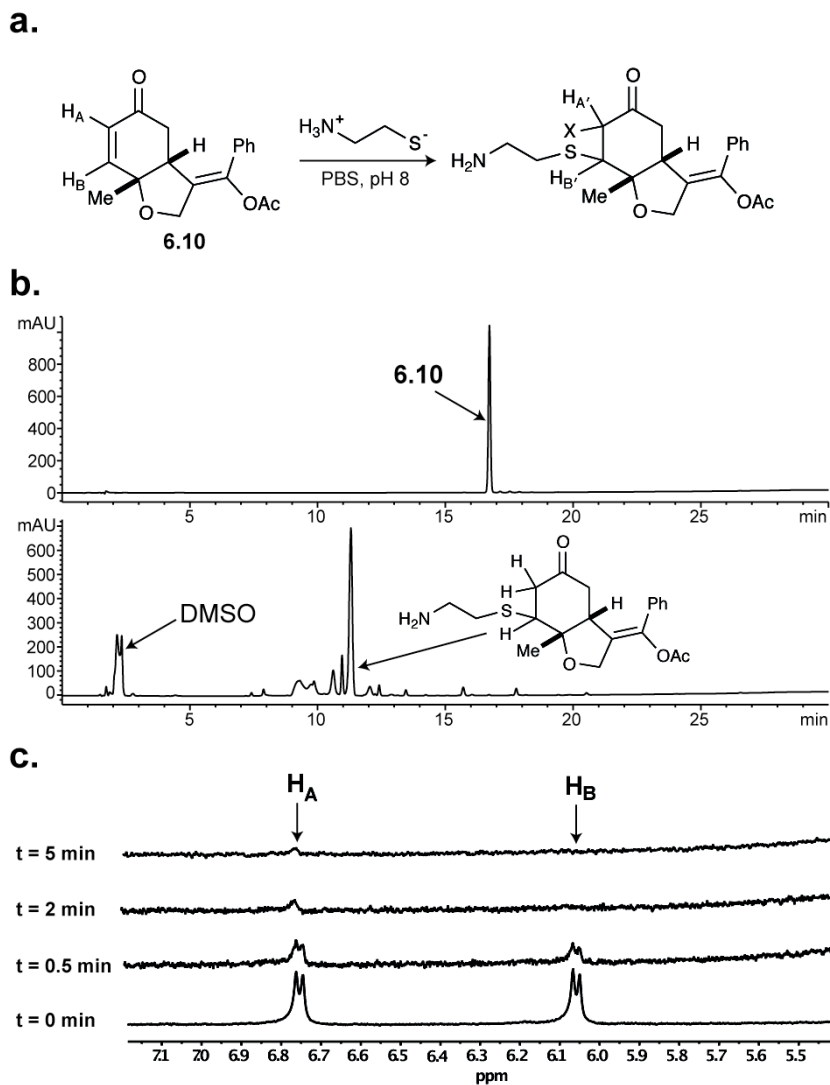


Figure 6.4. Cysteamine reaction assay using compound **6.10**. (a) Reaction of **6.10** with cysteamine. (b) HPLC traces of **6.10** and the cysteamine reaction product. Chromatograms were obtained using a signal wavelength of 254 nm. (c) ^1H NMR spectra for the cysteamine reaction are shown at four different time points (0, 0.5, 2, and 5 minutes). X = H or D (from deuterated solvent).

6.4 Inhibition of NF- κ B Nuclear Translocation by Western Blot Analysis, ELISA, and RT-PCR

To further characterize the mechanism of NF- κ B inhibition by cryptocaryone analogues, we fractionated NF- κ B-induced and compound-treated DU-145 and CCRF-CEM cells and then immunoblotted for p65 protein in the nuclear lysate (**Figure 6.5a and Figure 6.5b**). Decreased p50-p65 nuclear translocation is expected if **6.10** and **6.11** inhibit the degradation of I κ B repressor proteins, whereas no change in nuclear p65 levels should be observed if **6.10** and **6.11** modulate NF- κ B by directly targeting the p50 or p65 protein (e.g., alkylation of NF- κ B proteins by the small molecule abolishes DNA-binding

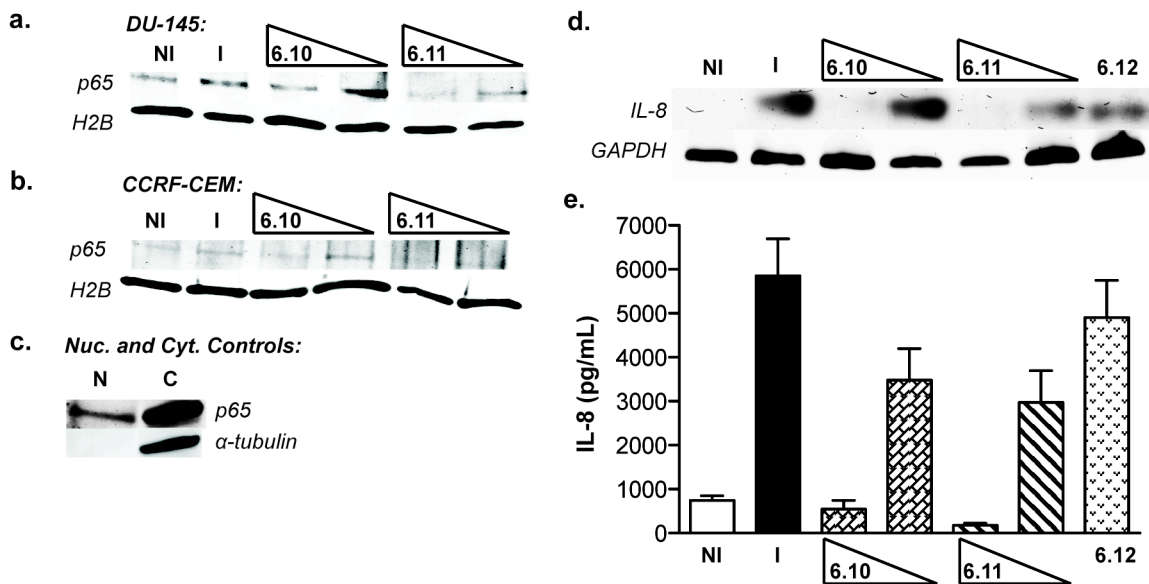


Figure 6.5. Western blot analysis of p65 and histone H2B proteins from nuclear lysate fractions of compound-treated (a) DU-145 cells and (b) CCRF-CEM cells. Cells were dosed with either vehicle control (DMSO; NI and I lanes) or analogues **6.10** or **6.11** (100 μ M and 25 μ M), followed by induction of the NF- κ B pathway with TNF- α . (c) Nuclear (N) and cytoplasmic (C) control blots for DU-145 cells. This blot shows that α -tubulin, a cytoplasmic protein, was not found in the nuclear samples. (d) RT-PCR analysis of IL-8 and GAPDH mRNA from DU-145 cells. (e) Secreted IL-8 protein levels as measured by ELISA. Data shown is mean \pm SEM (standard error of the mean). NI = non-induced cells, I = induced cells. (d-e) Cells were dosed at concentrations of 100 μ M and 33 μ M for **6.10** and **6.11**. Cells were dosed with **6.12** at a concentration of 100 μ M.

capability). Both **6.10** and **6.11** completely inhibited nuclear translocation of p65 at a 100 μ M treatment in NF- κ B-induced DU-145 (**Figure 6.5a**) and CCRF-CEM (**Figure 6.5b**) cell lines. Partial inhibition of p65 nuclear translocation was observed at a 25 μ M treatment of **6.10** and **6.11** in both cell lines. Immunoblotting of our prepared nuclear fractions for α -tubulin, an abundant cytosolic protein, revealed no detectable signal, which verifies that our nuclear p65 lysate samples are not contaminated with cytosolic p65 (**Figure 6.5c**). Based upon these results, we can conclude that cryptocaryone analogues such as **6.10** and **6.11** modulate NF- κ B activity by inhibiting I κ B degradation and p50-p65 heterodimer translocation to the nucleus.

To further evaluate the ability of our molecules to regulate NF- κ B activity in cells, we tested their ability to inhibit the activation of IL-8, a well-known proinflammatory regulator. IL-8 is a chemokine whose expression is driven by NF- κ B binding to the IL-8 promoter and activation of gene expression.³⁰⁵⁻³⁰⁷ DU-145 cells were treated with **6.10-6.12** and NF- κ B was induced by addition of TNF- α . Secreted IL-8 levels in cell media were measured by ELISA.^{308,309} Additionally, we further correlated IL-8 protein levels to IL-8 mRNA levels by semi-quantitative (traditional) RT-PCR analysis. As expected, analysis of IL-8 mRNA and protein levels revealed significant increases in both following NF- κ B induction with TNF- α (**Figure 6.5d-e**). Compound **6.11** was found to inhibit the production of IL-8 mRNA to visibly lower levels than that of **6.10** at the lowest concentration tested (33 μ M). The changes in mRNA levels observed with **6.10** and **11** were mirrored in the amount of secreted IL-8 protein measured. Compound **6.10** abolished IL-8 production to non-induced levels, while

compound **6.11** depleted IL-8 protein levels to nearly undetectable levels at the highest concentration tested. Additionally, control compound **6.12** at 100 μM had an insignificant effect (4,900 pg/mL) on IL-8 levels as compared to **6.10** and **6.11** at 33 μM dose (3,480 pg/mL and 2,970 pg/mL, respectively). These data support the hypothesis that the formation of Michael adducts is vital to the mechanism of NF- κB pathway inhibition for bicyclic cyclohexenones **6.10** and **6.11**. These data also suggest that compound **6.11**, which bears a pendent aromatic ring adjacent to the Michael acceptor, compared to **6.10**, which contains a methyl group, is a better lead compound for further optimization.

With another goal of beginning to establish the stereoisomeric preferences of these compounds, we carried out the enantioselective reaction shown in **Figure 6.6**. To our delight, the use of the chiral bipyridine ligand (-)-iso-PINDY³¹⁰ allowed us to produce enone **6.11*** in 63% ee from precursor **6.13**, with the major enantiomer being the one shown (**Figure 6.6a**). To determine if enantioenriched **6.11** (which we have denoted as **6.11***) possesses enhanced biological potency compared with racemic **6.11**, we repeated the NF- κB reporter assay and cancer cell cytotoxicity experiments with **6.11***.

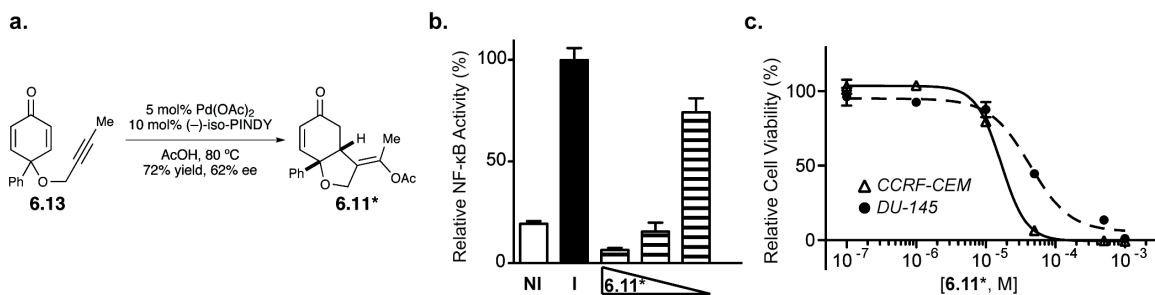


Figure 6.6. Enhanced potency of enantioenriched **6.11***. (a) Synthesis of **6.11***. (b) Cellular NF- κB luciferase reporter assay in A549 cells. NI = non-induced control wells, I = cells induced with TNF- α . Compound-treated cells are induced with TNF- α and treated with analogue **6.11*** at the following concentrations: 100 μM , 50 μM , and 10 μM . (c) Cytotoxicity of **6.11*** against CCRF-CEM (open triangles) and DU-145 human prostate cancer cells (closed circles). Cell viability was measured by Alamar Blue staining.

Interestingly, **6.11*** completely abolished induced NF- κ B signaling to non-induced levels (**Figure 6.6b**), resulting in 18% relative NF- κ B activity at 50 μ M. This constitutes a 2-fold enhancement in potency compared with racemic **6.11**. An enhancement in potency with **6.11*** versus racemic **6.11** was observed in cytotoxicity assays (**Figure 6.6c**) against CCRF-CEM cells ($IC_{50} = 19 \mu\text{M}$), whereas **6.11*** was slightly less active towards DU-145 cells ($IC_{50} = 46 \mu\text{M}$). Unfortunately, (-)-iso-PINDY has not proven to be generally useful for preparing other bicyclic products with high selectivity; therefore, a more thorough study into this effect will have to wait until a more effective ligand is identified.

6.5 Conclusions and Future Work

In conclusion, we have identified a new class of oxygenated bicyclic enones with activity against the NF- κ B signaling pathway. While the cytotoxic and NF- κ B inhibitory activity is modest, it is sufficiently strong to view these compounds as interesting lead compounds for further development. In addition to establishing a more comprehensive structure-activity relationship, we are working to further clarify the exact molecular target(s) of these compounds. All of these results will be reported in due course.

6.6 Experimental Section

6.6.1 Chemical Synthesis. Reference experimental methods for chemical synthesis are available online at: <http://pubs.acs.org/doi/abs/10.1021/ml300034a>

6.6.2 Preparation of Stock Solutions of Compounds 6.4-6.12. Compound stock solutions were prepared in DMSO (100 mM or 200 mM concentrations) and stored at -20° C when not in use. Compound purities were assessed frequently by analytical reverse-phase HPLC analysis and fresh solutions were prepared as needed.

6.6.3 Protocol for Mammalian Cell Culture. All cell lines were maintained in a humidified 5% CO₂ environment at 37 °C. CCRF-CEM cells (ATCC, CCL-119) were cultured in RPMI-1640 media (ATCC) supplemented with 10% fetal bovine serum (FBS, Gibco), penicillin (100 I.U./mL), and streptomycin (100 µg/mL, ATCC) at a density of 2×10^5 - 2×10^6 cells/mL. A549/NF-κB-luc cells (Panomics, RC0002) were cultured in DMEM media (ATCC) supplemented with 10% FBS (Gibco), penicillin (100 I.U./mL), streptomycin (100 µg/mL, ATCC), and hygromycin (100 µg/mL, Roche). DU-145 cells were cultured in EMEM media (ATCC) supplemented with 10% FBS (Gibco), penicillin (100 I.U./mL), and streptomycin (100 µg/mL, ATCC). RWPE-1 cells (ATCC, CRL-11609), which are non-cancerous prostate epithelial cells, were cultured in Keratinocyte Serum-Free Medium (K-SFM; Gibco) supplemented with human recombinant epidermal growth factor (EGF, 5 ng/mL, PeproTech), bovine pituitary extract (BPE, 0.05 mg/mL, PeproTech), penicillin (100 I.U./mL, ATCC), and streptomycin (100 µg/mL, ATCC).

6.6.4 Protocol for NF-κB Reporter Assay. A549/NF-κB-luc cells were seeded at a density of 5,000 cells/well in cell culture media (50 µL) in 96-well white plates with clear bottoms (Costar) 24 h prior to treatment. Compounds were serially diluted in pre-

warmed media and dosed to cells (final volume/well = 100 μ L; final DMSO concentration = 0.5%). Thirty minutes after treating the cells, NF- κ B was induced by adding TNF- α (15 ng/mL final concentration, delivered in PBS; Invitrogen) to the treated wells and the induced control wells. After 7 h, Bright-Glo luciferase reagent (Promega) was added to each well (100 μ L) and the plate was allowed to stand for two minutes. Luminescence measurements were then obtained using an LJL BioSystems HT Analyst plate reader. Background luminescence from reagents (no cell controls) was subtracted. Typical induction yields were \sim 7-fold. Negligible decreases in cell viability ($<$ 15%) were observed with test compounds under these conditions, as measured by colorimetric viability staining (Alamar Blue, Invitrogen). Each experiment was performed in biological triplicate (at minimum) with three technical replicates per experiment. Uncertainty in each % NF- κ B activity value was calculated via the propagated standard error (the square root of the sum of squares of the individual standard deviations). Statistical analyses were performed with Microsoft Excel and the results were plotted with GraphPad Prism (v. 5.0).

6.6.5 Cell Culture Cytotoxicity Assays. CCRF-CEM cells were seeded at a density of 10,000 cells/well in cell culture media (50 μ L) in standard 96-well plates (Costar) 24 h prior to treatment. DU-145 and RWPE-1 cells were seeded at a density of 5,000 cells/well in cell culture media (50 μ L) in standard 96-well plates (Costar). Blank (no cells) wells and control (vehicle control treated) wells were prepared with each experiment. Compounds were serially diluted in pre-warmed media and dosed to cells

(final volume/well = 100 μ L; final DMSO concentration = 0.5%). Approximately 2 h before the end of the treatment period (48 h), AlamarBlue (Invitrogen) cell viability reagent was added to each well (10 μ L). This procedure yields a quantitative measure of cell viability by evaluating the ability of metabolically active cells (which are proportional to the number of living cells) to convert resazurin (non-fluorescent dye) to red-fluorescent resorufin. Fluorescence data were obtained on either a Molecular Devices SpectraMax M2 plate reader or an LJL BioSystems HT Analyst plate reader. Background fluorescence (no cell controls) was subtracted from each well and cellular viability values following compound treatment were normalized to vehicle-only treated wells (control wells only treated with aqueous DMSO, which were arbitrarily assigned 100% viability). Individual IC₅₀ curves were generated by fitting data to the sigmoidal (dose response) function of varied slope in GraphPad Prism (v. 5.0) software. Only curve fits with $r^2 > 0.95$ were deemed sufficient. Each experiment was performed in biological triplicate and mean IC₅₀ values (with standard deviation) were calculated from the individual IC₅₀ values obtained from each replicate.

6.6.6 Cell Fractionation and Western Blotting. CCRF-CEM and DU-145 cells were plated at 4×10^6 cells/well in 6-well culture dishes 24 h before dosing. Cells were then treated with compounds **6.10** and **6.11** for 16 h. The final volume of media/well following compound dosing was 2.25 mL. CCRF-CEM cells were induced with phorbol 12-myristate 13-acetate (PMA, 850 ng/mL, Fisher BioReagents) for the last 4 h of the 16 h dosing.⁴⁷ DU-145 cells were induced with TNF- α (117 ng/mL, Gibco) for the last 2 h

of the 16 h dosing. DU-145 cells were then trypsinized and pelleted, and CCRF-CEM cells were immediately pelleted (500 x g for 5 min, room temperature). The media was decanted and cell pellets were resuspended once in ice-cold phosphate buffered saline (PBS, 1 mL) and pelleted again (500 x g for 5 min, 4 °C). Cell pellets were subsequently lysed in Buffer 1 (400 µL; Buffer 1 components (to make 50 mL): 10 mM HEPES, 10 mM KCl, 1.5 mM MgCl₂, 1 mM DTT, and one tablet of cOmplete (Roche) EDTA-free protease inhibitor cocktail) and incubated on ice for 10 min. The cells were homogenized by passing them through a 28-gauge syringe four times. Cell nuclei were pelleted by centrifugation at maximum speed (21,000 x g) for 5 min at 4 °C. The supernatants (cytosolic extracts) were collected in pre-chilled tubes and stored at -80 °C until further use. The residual pellets were gently washed with PBS without pellet disruption (200 µL) and subsequently resuspended in Buffer 2 (400 µL; Buffer 2 components (to make 50 mL): 20 mM HEPES, 600 mM KCl, 1.5 mM MgCl₂, 1 mM DTT, 0.2 mM EDTA, 25% (v/v) glycerol, and one tablet of cOmplete [Roche] EDTA-free protease inhibitor cocktail) to lyse the nuclei. Samples were incubated on ice and vortexed on the highest setting for 15 sec every 10 min for a total of 40 min. The suspension was centrifuged at maximum speed (21,000 x g) for 10 min at 4 °C. The supernatants (nuclear extracts) were collected in pre-chilled tubes and stored at -80 °C until further use. The protein concentrations were determined using the BCA protein assay kit (Pierce).

Samples of nuclear and cytosolic extracts (30 µg) were combined with NuPAGE 4X LDS sample buffer and NuPAGE 10X sample reducing agent (Invitrogen) and put in heat block at 99 °C for 5 minutes. Protein samples were electrophoresed on a

gradient 4-20% SDS-PAGE gel (BioRad), then electrotransferred to a polyvinylidene difluoride membrane (Immobilon). The membrane was then blocked with Odyssey blocking buffer (LI-COR Biotech.) for 1 h. Proteins were detected by incubation with primary antibodies for p65 (Active Motif, 39283), histone H2B (Active Motif, 61038), and α -tubulin (Active Motif, 39528) in blocking buffer supplemented with 0.1% Tween 20 for 1 h. The membrane was then briefly washed by gentle rocking in a solution of PBS (50 mL, 1 min, total 5x), and then incubated with IRDye 800 anti-rabbit (LI-COR Biotech., 926-32211) and IRDye 680 anti-mouse conjugated secondary antibodies (LI-COR Biotech., 926-68020) in blocking buffer supplemented 0.1% Tween 20 for 1 h. The membrane was again washed via gentle rocking in a solution of PBS (50 mL, 1 min, total 5x). The immunocomplexes were visualized using the Odyssey classic infrared imaging system (LI-COR Biotech.).

6.6.7 Compound Treatment for ELISA and PCR. DU-145 cells were seeded into 24-well plates at a cell density of 2×10^5 cells/well. The plate was dosed with compounds **6.10-6.12** for 24 hours. The cells were induced with TNF- α (117 ng/mL) six hours after the initial dosing, resulting in an 18 hour induction.

6.6.8 IL-8 Enzyme-Linked Immunosorbent Assays. A human IL-8 ELISA kit (Thermo Scientific, EH2IL82) was used to quantitate secreted IL-8 protein levels in NF- κ B-induced DU-145 cells treated with **6.10-6.12**. Following the dosing and induction of DU-145 cells (described above), cell media (500 μ L) was collected from each treated well

and stored at -20 °C until analysis. Immediately prior to analysis, samples were centrifuged at maximum speed (21,000 x g) for 1 minute and then secreted IL-8 protein levels were measured for each sample according to vendor instructions. The absorbance of each sample at 450 nm and 550 nm was collected following addition of the substrate stop solution using a Molecular Devices SpectraMax M2 plate reader. The standard curve was fitted using a 4-parameter logistic (4-PL) algorithm in GraphPad Prism (v. 5.0) software. Unknown samples were plotted against the standard curve to yield IL-8 protein concentrations in pg/mL. Triplicate biological replicates were performed and each bar represents at least 6 individual wells. The data shown in Figure 3 is mean \pm SEM, which was calculated from mean values of each of the three biological replicates. Statistical analyses were performed in Microsoft excel and data was plotted using GraphPad Prism (v. 5.0) software.

6.6.9 mRNA Isolation and Purification. RNeasy Plus Micro Kits (Qiagen, 74034) and QIAshredders (Qiagen, 79654) were used to isolate and purify mRNA from DU-145 cells. Following compound dosing, NF- κ B induction, and harvesting of the cell media (described above), cell monolayers were washed with PBS (1X) and then lysed according to the method described in the RNeasy Plus Micro Kit (β -Mercaptoethanol supplement was included). The samples were then homogenized using QIAshredders according to vendor instructions. mRNA was isolated and purified using the RNease Plus Micro Kit and eluted in RNase-free water (14 μ L). RNA samples were immediately stored at -80 °C.

6.6.10 Reverse Transcription (RT) & Polymerase Chain Reaction (PCR) assays. The RNA concentration and purity of each sample were determined using a NanoDrop instrument (Thermo Scientific). RNA samples with A_{260}/A_{280} ratios ≥ 1.9 were used in PCR assays. The concentration of each mRNA sample within a biological experiment was normalized to the value obtained from the sample with the lowest measured mRNA concentration. Reverse transcription of mRNA into cDNA was carried out using the QuantiTect Reverse Transcription Kit (Qiagen, 205311). Template mRNA was added to gDNA Wipeout Buffer (7X) and RNase-free water for a total volume of 14 μ L (less than 1 μ g of mRNA was added to each sample). Samples were then incubated at 42 °C for 2 minutes (Bio-Rad T100 thermal cycler) and then immediately placed on ice. Next, the entire contents of the previous mix were added to 6 μ L of reverse-transcription master mix, and mRNA was reverse transcribed to cDNA per vendor instructions. cDNA samples were stored at -20 °C immediately following reverse transcription.

The cDNA samples were carried forward to the PCR assays. These assays utilized HotStarTaq DNA Polymerase Kit (Qiagen, 203203) along with a dNTP Mix (Qiagen, 201900). Primers specific to either IL-8 or GAPDH (control) were purchased for Integrated DNA Technologies. The following IL-8 and GAPDH oligonucleotide primers were reported previously in the literature^{277,311} and were used in our study:

IL-8 Forward: 5' – CTC TCT TGG CAG CCT TCC TGA TT – 3'

IL-8 Reverse: 5' – AAC TTC TCC ACA ACC CTC TGC AC – 3'

GAPDH Forward: 5' – GTA AAG TGG ATA TTG TTG CCA TCA – 3'

GAPDH Reverse: 5' – AAA TTC GTT GTC ATA CCA GGA AAT – 3'

Primers (IL-8 and GAPDH) were added to separate HotStarTaq DNA Polymerase master mixes (no extra Mg²⁺ was added) containing PCR Buffer, dNTP mix, HotStarTaq DNA Polymerase, and RNase-free water. An aliquot (2 µL) of the template cDNA obtained from the previous reverse transcription procedures was then added to the master mix in 0.200 mL PCR tubes for a total volume of 100 µL. A total of 27 PCR cycles were performed (on a Bio-Rad T-100 thermal cycler) for both IL-8 and GAPDH according to the following method:

1. *Initial Activation:* 15 minutes at 95 °C
2. *Denaturation:* 1 minute at 94 °C
3. *Annealing:* 1 minute at 54 °C
4. *Extension:* 1 minute at 72 °C
5. *Final Extension:* 10 minutes at 72 °C
6. *Final Hold:* 4 °C

Steps 2-4 were repeated 27 times (27 cycles).

An aliquot of the resulting PCR products (2 µL) was added to loading buffer (8 µL; recipe for loading buffer: 10 mg of orange G, 10 mg of bromophenol blue sodium salt, and 10 mg of xylene cyanol FF in 6 mL of formamide). The samples were then electrophoresed on a 1% agarose gel made in 0.5% TBE buffer (10X TBE components (to make 1 L): 108 g tris base, 55 g boric acid, and 7.4 g EDTA in distilled and deionized water). The agarose gel was stained using SYBR Gold nucleic acid gel stain (Invitrogen)

and then visualized using the Typhoon FLA 7000 (GE Healthcare). Gels were analyzed using ImageQuant TL software (GE, version 7.0).

References:

1. Venter, J. C.; Adams, M. D.; Myers, E. W.; Li, P. W.; Mural, R. J.; Sutton, G. G.; Hamilton, O. S.; Yandell, M.; Evans, C. A.; Holt, R. A.; Gocayne, J. D.; Amanatides, P.; Ballew, R. M.; Huson, D. H.; Wortman, J. R.; Zhang, Q.; Kodira, C. D.; Zheng, X. H.; Chen, L.; Skupski, M.; Subramanian, G.; Thomas, P. D.; Zhang, J.; Miklos, G. L. G.; Nelson, C.; Broder, S.; Clark, A. G.; Nadeau, J.; McKusick, V. A.; Norton, Z.; Levine, A. J.; Roberts, R. J.; Simon, M.; Slayman, C.; Hunkapiller, M.; Bolanos, R.; Delcher, A.; Dew, I.; Fasulo, D.; Flanigan, M.; Florea, L.; Aaron, H.; Hannenhalli, S.; Kravitz, S.; Levy, S.; Mobarry, C.; Reinert, K.; Remington, K.; Abu-Threideh, J.; Beasley, E.; Biddick, K.; Bonazzi, V.; Brandon, R.; Cargill, M.; Chandramouliswaran, I.; Charlab, R.; Chaturvedi, K.; Deng, Z.; Francesco, V. D.; Dunn, P.; Eilbeck, K.; Evangelista, C.; Gabrielian, A. E.; Gan, W.; Ge, W.; Gong, F.; Gu, Z.; Guan, P.; Heiman, T. J.; Higgins, M. E.; Ji, R.-R.; Ke, Z.; Ketchum, K. A.; Lai, Z.; Lei, Y.; Li, Z.; Li, J.; Liang, Y.; Lin, X.; Lu, F.; Merkulov, G. V.; Milshina, N.; Moore, H. M.; Naik, A. K.; Narayan, V. A.; Neelam, B.; Nusskern, D.; Rusch, D. B.; Salzberg, S.; Shao, W.; Shue, B.; Sun, J.; Wang, Z. Y.; Wang, A.; Wang, X.; Wang, J.; Wei, M.-H.; Ron, W.; Xiao, C.; Yan, C.; Alison, Y.; Ye, J.; Zhan, M.; Zhang, W.; Zhang, H.; Zhao, Q.; Zheng, L.; Zhong, F.; Zhong, W.; Zhu, S. C.; Zhao, S.; Gilbert, D.; Baumhueter, S.; Spier, G.; Carter, C.; Cravchik, A.; Woodage, T.; Ali, F.; An, H.; Awe, A.; Baldwin, D.; Baden, H.; Barnstead, M.; Barrow, I.; Beeson, K.; Busam, D.; Carver, A.; Center, A.; Cheng, M. L.; Curry, L.; Danaher, S.; Davenport, L.; Desilets, R.; Dietz, S.; Dodson, K.; Doup, L.; Ferreira, S.; Garg, N.;

Gluecksmann, A.; Hart, B.; Jason, H.; Haynes, C.; Heiner, C.; Hladun, S.; Damon, H.; Houck, J.; Howland, T.; Ibegwam, C.; Johnson, J.; Kalush, F.; Kline, L.; Koduru, S.; Love, A.; Mann, F.; May, D.; McCawley, S.; McLntosh, T.; McMullen, I.; Moy, M.; Moy, L.; Murphy, B.; Nelson, K.; Pfannkoch, C.; Pratts, E.; Puri, V.; Qureshi, H.; Reardon, M.; Rodriguez, R.; Rogers, Y.-H.; Romblad, D.; Ruhfel, B.; Scott, R.; Sitter, C.; Smallwood, M.; Stewart, E.; Strong, R.; Suh, E.; Thomas, R.; Tint; Tse, S.; Vech, C.; Wang, G.; Wetter, J.; Williams, S.; Williams, M.; Windsor, S.; Winn-Deen, E.; Wolfe, K.; Zaveri, J.; Zaveri, K.; Abril, J. F.; Guigó, R.; Campbell, M. J.; Sjolander, K. V.; Karlak, B.; Kejariwal, A.; Mi, H.; Lazareva, B.; Hatton, T.; Narechania, A.; Diemer, K.; Muruganujan, A.; Guo, N.; Sato, S.; Bafna, V.; Istrail, S.; Lippert, R.; Schwartz, R.; Walenz, B.; Yooseph, S.; Allen, D.; Anand, B.; Baxendale, J.; Blick, L.; Caminha, M.; Carnes-Stine, J.; Caulk, P.; Chiang, Y.-H.; Coyne, M.; Dahlke, C.; Mays, A. D.; Dombroski, M.; Donnelly, M.; Ely, D.; Esparham, S.; Fosler, C.; Gire, H.; Glanowski, S.; Glasser, K.; Glodek, A.; Gorokhov, M.; Graham, K.; Gropman, B.; Harris, M.; Heil, J.; Henderson, S.; Hoover, J.; Jennings, D.; Jordan, C.; Jordan, J.; Kasha, J.; Kagan, L.; Kraft, C.; Levitsky, A.; Lewis, M.; Liu, X.; Lopez, J.; Ma, D.; Majoros, W.; McDaniel, J.; Murphy, S.; Newman, M.; Nguyen, T.; Nguyen, N.; Nodell, M.; Pan, S.; Peck, J.; Peterson, M.; Rowe, W.; Sanders, R.; Scott, J.; Simpson, M.; Smith, T.; Sprague, A.; Stockwell, T.; Turner, R.; Venter, E.; Wang, M.; Wen, M.; Wu, D.; Wu, M.; Xia, A.; Zandieh, A.; Zhu, X. The Sequence of the Human Genome. *Science* **2001**, 291, 1304-1351.

2. Emery, J. G.; Ohlstein, E. H.; Jaye, M. Therapeutic Modulation of Transcription Factor Activity. *TRENDS Pharmacol Sci* **2001**, 22, 233-240.
3. Latchman, D. S. Transcription Factors: An Overview. *Int J Biochem Cell Biol* **1997**, 29, 1305-1312.
4. Schumacher, M. A.; Goodman, R. H.; Brennan, R. G. The structure of a CREB bZIP.somatostatin CRE complex reveals the basis for selective dimerization and divalent cation-enhanced DNA binding. *J Biol Chem* **2000**, 275, 35242-7.
5. Wu, D.; Potluri, N.; Lu, J.; Kim, Y.; Rastinejad, F. Structural integration in hypoxia-inducible factors. *Nature* **2015**, 524, 303-308.
6. Nair, S. K.; Burley, S. K. X-ray structures of Myc-Max and Mad-Max recognizing DNA. Molecular bases of regulation by proto-oncogenic transcription factors. *Cell* **2003**, 112, 193-205.
7. Shaffer, P. L.; Jivan, A.; Dollins, D. E.; Claessens, F.; Gewirth, D. T. Structural basis of androgen receptor binding to selective androgen response elements. *Proc Natl Acad Sci U S A* **2004**, 101, 4758-63.
8. Chen, F. E.; Huang, D. B.; Chen, Y. Q.; Ghosh, G. Crystal structure of p50/p65 heterodimer of transcription factor NF-kappaB bound to DNA. *Nature* **1998**, 391, 410-3.
9. Wintjens, R.; Rooman, M. Structural Classification of HTH DNA-binding Domains and Protein – DNA Interaction Modes. *J Mol Biol* **1996**, 262, 294-313.
10. Banerjee-Basu, S.; Ferlanti, E. S.; Ryan, J. F.; Baxevanis, A. D. The Homeodomain Resource: sequences, structures and genomic information. *Nucleic Acids Res* **1999**, 27, 336-337.

11. Longo, A.; Guanga, G. P.; Rose, R. B. Structural basis for induced fit mechanisms in DNA recognition by the Pdx1 homeodomain. *Biochemistry* **2007**, *46*, 2948-57.
12. Staffers, D. A.; Ferrer, J.; Clarke, W. L.; Habener, J. F. Early-onset type-II diabetes mellitus (MODY4) linked to IPF1. *Nat Genet* **1997**, *17*, 138-139.
13. Shore, P.; Whitmarsh Aj Fau - Bhaskaran, R.; Bhaskaran R Fau - Davis, R. J.; Davis Rj Fau - Waltho, J. P.; Waltho Jp Fau - Sharrocks, A. D.; Sharrocks, A. D. Determinants of DNA-binding specificity of ETS-domain transcription factors. *Mol Cell Biol* **1996**, *16*, 3338-3349.
14. Hanes, S. D.; Brent, R. DNA specificity of the bicoid activator protein is determined by homeodomain recognition helix residue 9. *Cell* **1989**, *57*, 1275-1283.
15. Roeder, R. G. The role of general initiation factors in transcription by RNA polymerase II. *Trends Biochem Sci* **1996**, *21*, 327-335.
16. Nikolov, D. B.; Burley, S. K. RNA polymerase II transcription initiation: A structural view. *Proc Natl Acad Sci USA* **1997**, *94*, 15-22.
17. Cantin, G. T.; Stevens, J. L.; Berk, A. J. Activation domain–mediator interactions promote transcription preinitiation complex assembly on promoter DNA. *P Natl Acad Sci USA* **2003**, *100*, 12003-12008.
18. Calkhoven, C. F.; Ab, G. Multiple steps in the regulation of transcription-factor level and activity. *Biochem J* **1996**, *317*, 329-342.
19. Edmondson, D. G.; Olson, E. N. Helix-loop-helix proteins as regulators of muscle-specific transcription. *J Biol Chem* **1993**, *268*, 755-758.

20. Maeshima, Y.; Kashihara, N.; Yasuda, T.; Sugiyama, H.; Sekikawa, T.; Okamoto, K.; Kanao, K.; Watanabe, Y.; Kanwar, Y. S.; Makino, H. Inhibition of mesangial cell proliferation by E2F decoy oligodeoxynucleotide in vitro and in vivo. *J Clin Invest* **1998**, 101, 2589-2597.
21. Spencer, V. A.; Davie, J. R. Role of covalent modifications of histones in regulating gene expression. *Gene* **1999**, 240, 1-12.
22. Tenbaum, S.; Baniahmad, A. Nuclear receptors: Structure, function and involvement in disease. *Int J Biochem Cell B* **1997**, 29, 1325-1341.
23. Lonergan, P.; Tindall, D. Androgen receptor signaling in prostate cancer development and progression. *J Carcinog* **2011**, 10, 20-20.
24. Lonergan, P. E.; Tindall, D. J. Androgen receptor signaling in prostate cancer development and progression. *J Carcinog* **2011**, 10, 20.
25. Hayden, M. S., Ghosh, S. Shared principles in NF-kappaB signaling. *Cell* **2008**, 132, 344-362.
26. Levy, D. E.; Darnell, J. E. STATs: transcriptional control and biological impact. *Nat Rev Mol Cell Biol* **2002**, 3, 651-662.
27. Sen, R., Baltimore, D. Multiple nuclear factors interact with the immune- globulin enhancer sequences. *Cell* **1986**, 46, 705-716.
28. Karin, M.; Greten, F. R. NF-[kappa]B: linking inflammation and immunity to cancer development and progression. *Nat Rev Immunol* **2005**, 5, 749-759.
29. Karin, M. Nuclear factor-[kappa]B in cancer development and progression. *Nature* **2006**, 441, 431-436.

30. Naugler, W. E., Karin, M. NF- κ B and cancer-identifying targets and mechanisms. *Curr Opin Genet Dev* **2008**, 18, 19-26.
31. Karin, M., Yamamoto, Y., Wang, Q. M. The IKK NF-kappa B system: a treasure trove for drug development. *Nat. Rev. Drug Discov.* **2004**, 3, 17-26.
32. Tergaonkar, V., Correa, R. G., Ikawa, M., Verma, I. M. Distinct roles of IkappaB proteins in regulating constitutive NF-kappaB activity. *Nat Cell Biol* **2005**, 7, 921-923.
33. Libby, P. Inflammation in atherosclerosis. *Nature* **2002**, 420, 868-874.
34. Monaco, C., Paleolog, E. Nuclear factor κ B a potential therapeutic target in atherosclerosis and thromboses. *Cardiovascular Res.* **2004**, 61, 671-682.
35. Aggarwal, B. B. Nuclear factor-kappaB the enemy within. *Cancer Cell* **2004**, 6, 203-208.
36. Kontos, C. K.; Scorilas, A.; Papavassiliou, A. G. The role of transcription factors in laboratory medicine. *Clin Chem Lab Med* **2013**, 51, 1563-71.
37. Karamouzis, M. V.; Konstantinopoulos, P. A.; Papavassiliou, A. G. The activator protein-1 transcription factor in respiratory epithelium carcinogenesis. *Mol Cancer Res* **2007**, 5, 109-20.
38. Darnell, J. E., Jr. Transcription factors as targets for cancer therapy. *Nat Rev Cancer* **2002**, 2, 740-9.
39. Mukherjee, S. *The Emperor of All Maladies*. Scribner; Reprint edition: 2011; p 608.
40. Nogués, C. Oncogenetics: How Far, and What for? *B Cancer* **1998**, 85, 243-245.

41. Varmus, H. E. Oncogenes and Transcriptional Control. *Science* **1987**, 238, 1337-1339.
42. Mani, R.-S.; Tomlins, S. A.; Callahan, K.; Ghosh, A.; Nyati, M. K.; Varambally, S.; Palanisamy, N.; Chinnaiyan, A. M. Induced Chromosomal Proximity and Gene Fusions in Prostate Cancer. *Science* **2009**, 326, 1230.
43. Lin, C.; Yang, L.; Tanasa, B.; Hutt, K.; Ju, B.-g.; Ohgi, K. A.; Zhang, J.; Rose, D. W.; Fu, X.-D.; Glass, C. K.; Rosenfeld, M. G. Nuclear Receptor-Induced Chromosomal Proximity and DNA Breaks Underlie Specific Translocations in Cancer. *Cell* **2009**, 139, 1069-1083.
44. Siegel, R. L.; Miller, K. D.; Jemal, A. Cancer statistics, 2015. *CA Cancer J Clin* **2015**, 65, 5-29.
45. Nadiminty, N.; Gao, A. Mechanisms of persistent activation of the androgen receptor in CRPC: recent advances and future perspectives. *World J Urol* **2012**, 30, 287-295.
46. Scher, H. I.; Fizazi, K.; Saad, F.; Taplin, M.-E.; Sternberg, C. N.; Miller, K.; de Wit, R.; Mulders, P.; Chi, K. N.; Shore, N. D.; Armstrong, A. J.; Flaig, T. W.; Fléchon, A.; Mainwaring, P.; Fleming, M.; Hainsworth, J. D.; Hirmand, M.; Selby, B.; Seely, L.; de Bono, J. S. Increased Survival with Enzalutamide in Prostate Cancer after Chemotherapy. *New Engl J Med* **2012**, 367, 1187-1197.
47. Chaturvedi, M. M.; Sung, B.; Yadav, V. R.; Kannappan, R.; Aggarwal, B. B. NF-kappaB addiction and its role in cancer: 'one size does not fit all'. *Oncogene* **2011**, 30, 1615-30.

48. Karin, M. Nuclear factor-kappa B in cancer development and progression. *Nature* **2006**, 441, 431-436.
49. Ziegler, E. C.; Ghosh, S. Regulating inducible transcription through controlled localization. *Sci STKE* **2005**, 2005, re6.
50. Pennisi, E. Opening the Way to Gene Activity. *Science* **1997**, 275, 155-157.
51. Gohda, J.; Inoue J Fau - Umezawa, K.; Umezawa, K. Down-regulation of TNF-alpha receptors by conophylline in human T-cell leukemia cells. *Int J Oncol* **2003**, 23, 1019-6439 (Print).
52. Song, X.; Torphy, T.; Grisowold, D.; Shealy, D. Coming of Age: Anti-Cytokine Therapies. *Mol Interv* **2002**, 2, 36-46.
53. Stegmeier, F.; Warmuth, M.; Sellers, W. R.; Dorsch, M. Targeted Cancer Therapies in the Twenty-First Century: Lessons From Imatinib. *Clin Pharmacol Ther* **2010**, 87, 543-552.
54. Kirchner, D.; Duyster, J.; Ottmann, O.; Schmid, R. M.; Bergmann, L.; Munzert, G. Mechanisms of Bcr-Abl-mediated NF- κ B/Rel activation. *Exp Hematol* **2003**, 31, 504-511.
55. Coppo, P.; Dusanter-Fourt, I.; Millot, G.; Nogueira, M. M.; Dugray, A.; Bonnet, M. L.; Mitjavila-Garcia, M. T.; Le Pesteur, D.; Guilhot, F.; Vainchenker, W.; Sainteny, F.; Turhan, A. G. Constitutive and specific activation of STAT3 by BCR-ABL in embryonic stem cells. *Oncogene* **2003**, 22, 4102-4110.
56. Schuster, C.; Forster, K.; Dierks, H.; Elsässer, A.; Behre, G.; Simon, N.; Danhauser-Riedl, S.; Hallek, M.; Warmuth, M. The effects of Bcr-Abl on C/EBP

transcription-factor regulation and neutrophilic differentiation are reversed by the Abl kinase inhibitor imatinib mesylate. *Blood* **2002**, 101, 655-663.

57. Goldman, J. M.; Marin, D. Is imatinib still an acceptable first-line treatment for CML in chronic phase? *Oncology* **2012**, 26, 901.

58. Das, J.; Chen, C.-H.; Yang, L.; Cohn, L.; Ray, P.; Ray, A. A critical role for NF-[kappa]B in Gata3 expression and TH2 differentiation in allergic airway inflammation. *Nat Immunol* **2001**, 2, 45-50.

59. Fu, W.; Farache, J.; Clardy, S. M.; Hattori, K.; Mander, P.; Lee, K.; Rioja, I.; Weissleder, R.; Prinjha, R. K.; Benoist, C.; Mathis, D. Epigenetic modulation of type-1 diabetes via a dual effect on pancreatic macrophages and β cells. *eLife* **2014**, 3.

60. Banno, M.; Mizuno, T.; Kato, H.; Zhang, G.; Kawanokuchi, J.; Wang, J.; Kuno, R.; Jin, S.; Takeuchi, H.; Suzumura, A. The radical scavenger edaravone prevents oxidative neurotoxicity induced by peroxynitrite and activated microglia. *Neuropharmacology* **2005**, 48, 283-90.

61. Papavassiliou, A. G. Transcription factor-based drug design in anticancer drug development. *Mol Med* **1997**, 3, 799-810.

62. Hanahan, D.; Weinberg, R. A. The Hallmarks of Cancer. *Cell* **2000**, 100, 57-70.

63. Yeh, J. E.; Toniolo, P. A.; Frank, D. A. Targeting transcription factors: promising new strategies for cancer therapy. *Curr Opin Oncol* **2013**, 25, 652-8.

64. Arndt, H.-D. Small Molecule Modulators of Transcription. *Angew Chem Int Edit* **2006**, 45, 4552-4560.

65. Allred, D. C.; Brown, P.; Medina, D. The origins of estrogen receptor alpha-positive and estrogen receptor alpha-negative human breast cancer. *Breast Cancer Res* **2004**, *6*, 240-245.
66. Jordan, V. C. Tamoxifen: a most unlikely pioneering medicine. *Nat Rev Drug Discov* **2003**, *2*, 205-213.
67. Attard, G.; Richards, J.; de Bono, J. S. New strategies in metastatic prostate cancer: targeting the androgen receptor signaling pathway. *Clin Cancer Res* **2011**, *17*, 1649-57.
68. Chen, Y.; Sawyers, C. L.; Scher, H. I. Targeting the androgen receptor pathway in prostate cancer. *Curr Opin Pharm* **2008**, *8*, 440-448.
69. Patel, N. K.; Finianos, A.; Whitaker, K. D.; Aragon-Ching, J. B. Advanced prostate cancer – patient survival and potential impact of enzalutamide and other emerging therapies. *Ther Clin Risk Manag* **2014**, *10*, 651-664.
70. Koehler, A. N. A complex task? Direct modulation of transcription factors with small molecules. *Curr Opin Chem Biol* **2010**, *14*, 331-40.
71. Stockwell, B. R. Exploring biology with small organic molecules. *Nature* **2004**, *432*, 846-854.
72. Arkin, M. Protein–protein interactions and cancer: small molecules going in for the kill. *Curr Opin Chem Biol* **2005**, *9*, 317-324.
73. Pagliaro, L.; Felding, J.; Audouze, K.; Nielsen, S. J.; Terry, R. B.; Krog-Jensen, C.; Butcher, S. Emerging classes of protein–protein interaction inhibitors and new tools for their development. *Curr Opin Chem Biol* **2004**, *8*, 442-449.

74. Arkin, M. R.; Wells, J. A. Small-molecule inhibitors of protein-protein interactions: progressing towards the dream. *Nat Rev Drug Discov* **2004**, *3*, 301-317.
75. Yap, J. L.; Chauhan, J.; Jung, K.-Y.; Chen, L.; Prochownik, E. V.; Fletcher, S. Small-molecule inhibitors of dimeric transcription factors: Antagonism of protein-protein and protein-DNA interactions. *MedChemComm* **2012**, *3*, 541-551.
76. Glanzer, J. G.; Liu, S.; Oakley, G. G. Small molecule inhibitor of the RPA70 N-terminal protein interaction domain discovered using in silico and in vitro methods. *Bioorg Med Chem* **2011**, *19*, 2589-95.
77. Berg, T. Modulation of Protein-Protein Interactions with Small Organic Molecules. *Angew Chem Int Edit* **2003**, *42*, 2462-2481.
78. Yin, H.; Hamilton, A. D. Strategies for Targeting Protein-Protein Interactions With Synthetic Agents. *Angew Chem Int Edit* **2005**, *44*, 4130-4163.
79. Hong, J. A.; Neel, D. V.; Wassaf, D.; Caballero, F.; Koehler, A. N. Recent discoveries and applications involving small-molecule microarrays. *Curr Opin Chem Biol* **2014**, *18*, 21-28.
80. Pop, M. S.; Stransky, N.; Garvie, C. W.; Theurillat, J.-P.; Hartman, E. C.; Lewis, T. A.; Zhong, C.; Culyba, E. K.; Lin, F.; Daniels, D. S.; Pagliarini, R.; Ronco, L.; Koehler, A. N.; Garraway, L. A. A Small Molecule That Binds and Inhibits the ETV1 Transcription Factor Oncoprotein. *Mol Cancer Ther* **2014**, *13*, 1492-1502.
81. Berg, T.; Cohen, S. B.; Desharnais, J.; Sonderegger, C.; Maslyar, D. J.; Goldberg, J.; Boger, D. L.; Vogt, P. K. Small-molecule antagonists of Myc/Max dimerization

inhibit Myc-induced transformation of chicken embryo fibroblasts. *Proc Natl Acad Sci USA* **2002**, 99, 3830-3835.

82. Rishi, V.; Potter, T.; Laudeman, J.; Reinhart, R.; Silvers, T.; Selby, M.; Stevenson, T.; Krosky, P.; Stephen, A. G.; Acharya, A.; Moll, J.; Oh, W. J.; Scudiero, D.; Shoemaker, R. H.; Vinson, C. A high-throughput fluorescence–anisotropy screen that identifies small molecule inhibitors of the DNA binding of B-ZIP transcription factors. *Anal Biochem* **2005**, 340, 259-271.

83. Moellering, R. E.; Cornejo, M.; Davis, T. N.; Bianco, C. D.; Aster, J. C.; Blacklow, S. C.; Kung, A. L.; Gilliland, D. G.; Verdine, G. L.; Bradner, J. E. Direct inhibition of the NOTCH transcription factor complex. *Nature* **2009**, 462, 182-188.

84. Bargonetti, J.; Manfredi, J. J. Multiple roles of the tumor suppressor p53. *Curr Opin Oncol* **2002**, 14, 86-91.

85. Harris, S. L.; Levine, A. J. The p53 pathway: positive and negative feedback loops. *Oncogene* **2005**, 24, 2899-2908.

86. Bernal, F.; Wade, M.; Godes, M.; Davis, T. N.; Whitehead, D. G.; Kung, A. L.; Wahl, G. M.; Walensky, L. D. A stapled p53 helix overcomes HDMX-mediated suppression of p53. *Cancer Cell* **2010**, 18, 411-22.

87. Ravindranathan, P.; Lee, T.-K.; Yang, L.; Centenera, M. M.; Butler, L.; Tilley, W. D.; Hsieh, J.-T.; Ahn, J.-M.; Raj, G. V. Peptidomimetic targeting of critical androgen receptor–coregulator interactions in prostate cancer. *Nat Commun* **2013**, 4, 1923.

88. Ahn, J. M.; Boyle, N. A.; Macdonald, M. T.; Janda, K. D. Peptidomimetics and peptide backbone modifications. *Mini Rev Med Chem* **2002**, 2, 463-473.

89. Garcia, R.; Bowman, T. L.; Niu, G.; Yu, H.; Minton, S.; Muro-Cacho, C. A.; Cox, C. E.; Falcone, R.; Fairclough, R.; Parsons, S.; Laudano, A.; Gazit, A.; Levitzki, A.; Kraker, A.; Jove, R. Constitutive activation of Stat3 by the Src and JAK tyrosine kinases participates in growth regulation of human breast carcinoma cells. *Oncogene* **2001**, *20*, 2499.
90. Chen, J.; Bai, L.; Bernard, D.; Nikolovska-Coleska, Z.; Gomez, C.; Zhang, J.; Yi, H.; Wang, S. Structure-Based Design of Conformationally Constrained, Cell-Permeable STAT3 Inhibitors. *ACS Med Chem Lett* **2010**, *1*, 85-89.
91. Trauger, J. W.; Baird, E. E.; Dervan, P. B. Recognition of DNA by designed ligands at subnanomolar concentrations. *Nature* **1996**, *382*, 559-561.
92. Chenoweth, D. M.; Poposki, J. A.; Marques, M. A.; Dervan, P. B. Programmable oligomers targeting 5'-GGGG-3' in the minor groove of DNA and NF-kappaB binding inhibition. *Bioorg Med Chem* **2007**, *15*, 759-70.
93. Nickols, N. G.; Dervan, P. B. Suppression of androgen receptor-mediated gene expression by a sequence-specific DNA-binding polyamide. *Proc Natl Acad Sci* **2007**, *104*, 10418-10423.
94. Bochman, M. L.; Paeschke, K.; Zakian, V. A. DNA secondary structures: stability and function of G-quadruplex structures. *Nat Rev Genet* **2012**, *13*, 770-780.
95. Balasubramanian, S.; Hurley, L. H.; Neidle, S. Targeting G-quadruplexes in gene promoters: a novel anticancer strategy? *Nat Rev Drug Discov* **2011**, *10*, 261-275.
96. Dias, N.; Stein, C. A. Antisense Oligonucleotides: Basic Concepts and Mechanisms. *Mol Cancer Ther* **2002**, *1*, 347-355.

97. Rao, D. D.; Vorhies, J. S.; Senzer, N.; Nemunaitis, J. siRNA vs. shRNA: similarities and differences. *Adv Drug Deliv Rev* **2009**, 61, 746-59.
98. Deng, Y.; Wang, C. C.; Choy, K. W.; Du, Q.; Chen, J.; Wang, Q.; Li, L.; Chung, T. K.; Tang, T. Therapeutic potentials of gene silencing by RNA interference: principles, challenges, and new strategies. *Gene* **2014**, 538, 217-27.
99. Matranga, C.; Tomari, Y.; Shin, C.; Bartel, D. P.; Zamore, P. D. Passenger-strand cleavage facilitates assembly of siRNA into Ago2-containing RNAi enzyme complexes. *Cell* **2005**, 123, 607-20.
100. Hong, D. S.; Younes, A.; L. Fayad, e. a. A phase I study of ISIS 481464 (AZD9150), a first-in-human, first-in-class, antisense oligonucleotide inhibitor of STAT3, in patients with advanced cancers. *J Clin Oncol* **2013**, 31, Supplement, abstract 8523.
101. Seth, P. P.; Siwkowski, A.; Allerson, C. R.; Vasquez, G.; Lee, S.; Prakash, T. P.; Kinberger, G.; Migawa, M. T.; Gaus, H.; Bhat, B.; Swayze, E. E. Design, Synthesis And Evaluation Of Constrained Methoxyethyl (cMOE) and Constrained Ethyl (cEt) Nucleoside Analogs. *Nucl Acid S* **2008**, 52, 553-554.
102. Janssen, S.; Cuvier, O.; Müller, M.; Laemml, U. K. Specific Gain- and Loss-of-Function Phenotypes Induced by Satellite-Specific DNA-Binding Drugs Fed to *Drosophila melanogaster*. *Mol Cell* **2000**, 6, 1013-1024.
103. Lee, T.-H.; Maheshri, N. A regulatory role for repeated decoy transcription factor binding sites in target gene expression. *Mol Sys Biol* **2012**, 8, 576-576.

104. Liu, X.; Wu, B.; Szary, J.; Kofoed, E. M.; Schaufele, F. Functional Sequestration of Transcription Factor Activity By Repetitive DNA. *J Biol Chem* **2007**, 282, 10.1074/jbc.M702547200.
105. Gambari, R. New trends in the development of transcription factor decoy (TFD) pharmacotherapy. *Curr Drug Targets* **2004**, 5, 419-30.
106. Weintraub, S. J.; Prater, C. A.; Dean, D. C. Retinoblastoma protein switches the E2F site from positive to negative element. *Nature* **1992**, 358, 259-261.
107. Wingender, E.; Chen, X.; Fricke, E.; Geffers, R.; Hehl, R.; Liebich, I.; Krull, M.; Matys, V.; Michael, H.; Ohnhäuser, R.; Prüß, M.; Schacherer, F.; Thiele, S.; Urbach, S. The TRANSFAC system on gene expression regulation. *Nucleic Acids Res* **2001**, 29, 281-283.
108. Faist, S.; Meyer, S. Compilation of vertebrate-encoded transcription factors. *Nucleic Acids Res* **1992**, 20, 3-26.
109. Beaucage, S. L.; Caruthers, M. H. Deoxynucleoside phosphoramidites—A new class of key intermediates for deoxypolynucleotide synthesis. *Tetrahedron Lett* **1981**, 22, 1859-1862.
110. McBride, L. J.; Caruthers, M. H. An investigation of several deoxynucleoside phosphoramidites useful for synthesizing deoxyoligonucleotides. *Tetrahedron Lett* **1983**, 24, 245-248.
111. Tomita, N.; Morishita, R.; Higaki, J.; Aoki, M.; Nakamura, Y.; Mikami, H.; Fukamizu, A.; Murakami, K.; Kaneda, Y.; Ogihara, T. Transient Decrease in High Blood

Pressure by In Vivo Transfer of Antisense Oligodeoxynucleotides Against Rat Angiotensinogen. *Hypertension* **1995**, 26, 131-136.

112. Tomita, N.; Morishita, R.; Higaki, J.; Tomita, S.; Aoki, M.; Ogihara, T.; Kaneda, Y. In vivo gene transfer of insulin gene into neonatal rats by the HVJ-liposome method resulted in sustained transgene expression. *Gene Ther* **1996**, 3, 477-482.

113. Morishita, R.; Gibbons, G. H.; Kaneda, Y.; Ogihara, T.; Dzau, V. J. Pharmacokinetics of antisense oligodeoxyribonucleotides (cyclin B1 and CDC 2 kinase) in the vessel wall in vivo: enhanced therapeutic utility for restenosis by HVJ-liposome delivery. *Gene* **1994**, 149, 13-19.

114. Morishita, R.; Gibbons, G. H.; Ellison, K. E.; Nakajima, M.; Zhang, L.; Kaneda, Y.; Ogihara, T.; Dzau, V. J. Single intraluminal delivery of antisense cdc2 kinase and proliferating-cell nuclear antigen oligonucleotides results in chronic inhibition of neointimal hyperplasia. *Proc Natl Acad Sci USA* **1993**, 90, 8474-8478.

115. Taniyama, Y.; Tachibana, K.; Hiraoka, K.; Namba, T.; Yamasaki, K.; Hashiya, N.; Aoki, M.; Ogihara, T.; Yasufumi, K.; Morishita, R. Local Delivery of Plasmid DNA Into Rat Carotid Artery Using Ultrasound. *Circulation* **2002**, 105, 1233-1239.

116. Morishita, R.; Gibbons, G. H.; Pratt, R. E.; Tomita, N.; Kaneda, Y.; Ogihara, T.; Dzau, V. J. Autocrine and paracrine effects of atrial natriuretic peptide gene transfer on vascular smooth muscle and endothelial cellular growth. *J Clin Invest* **1994**, 94, 824-829.

117. Tomita, N.; Higaki, J.; Kaneda, Y.; Yu, H.; Morishita, R.; Mikami, H.; Ogihara, T. Hypertensive rats produced by in vivo introduction of the human renin gene. *Circ Res* **1993**, 73, 898-905.

118. Tomita, N.; Higaki, J.; Morishita, R.; Kato, K.; Mikami, H.; Kaneda, Y.; Ogihara, T. Direct in vivo gene introduction into rat kidney. *Biochem Biophys Res Co* **1992**, 186, 129-134.
119. Chu, B. C.; Orgel, L. E. The stability of different forms of double-stranded decoy DNA in serum and nuclear extracts. *Nucleic Acids Res* **1992**, 20, 5857-8.
120. Bielinska, A.; Shivdasani, R. A.; Zhang, L.; Nabel, G. J. Regulation of Gene Expression with Double-Stranded Phosphorothioate Oligonucleotides. *Science* **1990**, 250, 997-1000.
121. Stein, C. A.; Subasinghe, C.; Shinozuka, K.; Cohen, J. S. Physicochemical properties of phosphorothioate oligodeoxynucleotides. *Nucleic Acids Res* **1988**, 16, 3209-3221.
122. Agrawal, S.; Jiang, Z.; Zhao, Q.; Shaw, D.; Cai, Q.; Roskey, A.; Channavajjala, L.; Saxinger, C.; Zhang, R. Mixed-backbone oligonucleotides as second generation antisense oligonucleotides: In vitro and in vivo studies. *Proc Natl Acad Sci USA* **1997**, 94, 2620-2625.
123. Zon, G. Oligonucleotide Analogues as Potential Chemotherapeutic Agents. *Pharm Res* **1988**, 5, 539-549.
124. Singh, S.; Koshkin, A.; Wengel, J.; Nielsen, P. LNA (locked nucleic acids): synthesis and high-affinity nucleic acid recognition. *Chem Commun* **1998**, 455-456.
125. Crinelli, R.; Bianchi, M.; Gentilini, L.; Magnani, M. Design and characterization of decoy oligonucleotides containing locked nucleic acids. *Nucleic Acids Res* **2002**, 30, 2435-2443.

126. Nielsen, P. E.; Egholm, M.; Berg, R. H.; Buchardt, O. Sequence-Selective Recognition of DNA by Strand Displacement with a Thymine-Substituted Polyamide. *Science* **1991**, 254, 1497-1500.
127. Egholm, M.; Buchardt, O.; Nielsen, P. E.; Berg, R. H. Peptide nucleic acids (PNA). Oligonucleotide analogs with an achiral peptide backbone. *J Am Chem Soc* **1992**, 114, 1895-1897.
128. Borgatti, M.; Finotti, A.; Romanelli, A.; Saviano, M.; Bianchi, N.; Lampronti, I.; Lambertini, E.; Penolazzi, L.; Nastruzzi, C.; Mischiati, C.; Piva, R.; Pedone, C.; Gambari, R. Peptide Nucleic Acids (PNA)-DNA Chimeras Targeting Transcription Factors as a Tool to Modify Gene Expression. *Curr Drug Targets* **2004**, 5, 735-744.
129. Lee, I. K.; Ahn, J. D.; Kim, H. S.; Park, J. Y.; Lee, K. U. Advantages of the Circular Dumbbell Decoy in Gene Therapy and Studies of Gene Regulation. *Curr Drug Targets* **2003**, 4, 619-623.
130. Ahn, J. D.; Morishita, R.; Kaneda, Y.; Lee, S.-J.; Kwon, K.-Y.; Choi, S.-Y.; Lee, K.-U.; Park, J.-Y.; Moon, I.-J.; Park, J.-G.; Yoshizumi, M.; Ouchi, Y.; Lee, I.-K. Inhibitory Effects of Novel AP-1 Decoy Oligodeoxynucleotides on Vascular Smooth Muscle Cell Proliferation In Vitro and Neointimal Formation In Vivo. *Circ Res* **2002**, 90, 1325-1332.
131. Hosoya, T.; Takeuchi, H.; Kanesaka, Y.; Yamakawa, H.; Miyano-Kurosaki, N.; Takai, K.; Yamamoto, N.; Takaku, H. Sequence-specific inhibition of a transcription factor by circular dumbbell DNA oligonucleotides. *FEBS Letters* **1999**, 461, 136-140.

132. Souissi, I.; Ladam, P.; Cognet, J. A. H.; Le Coquil, S.; Varin-Blank, N.; Baran-Marszak, F.; Metelev, V.; Fagard, R. A STAT3-inhibitory hairpin decoy oligodeoxynucleotide discriminates between STAT1 and STAT3 and induces death in a human colon carcinoma cell line. *Mol Cancer* **2012**, 11, 12-12.
133. Tadlaoui Hbib, A.; Laguillier, C.; Souissi, I.; Lesage, D.; Le Coquil, S.; Cao, A.; Metelev, V.; Baran-Marszak, F.; Fagard, R. Efficient killing of SW480 colon carcinoma cells by a signal transducer and activator of transcription (STAT) 3 hairpin decoy oligodeoxynucleotide – interference with interferon- γ -STAT1-mediated killing. *FEBS Journal* **2009**, 276, 2505-2515.
134. Tomita, N.; Ogihara, T.; Morishita, R. Transcription Factors as Molecular Targets: Molecular Mechanisms of Decoy ODN and their Design. *Curr Drug Targets* **2003**, 4, 603-608.
135. Mann, M. J. Transcription Factor Decoys: A New Model for Disease Intervention. *Ann NY Acad Sci* **2005**, 1058, 128-139.
136. D'Acquisto, F.; Ialenti, A.; Ianaro, A.; Di Vaio, R.; Carnuccio, R. Local administration of transcription factor decoy oligonucleotides to nuclear factor- κ B prevents carrageenin-induced inflammation in rat hind paw. *Gene Ther* **2000**, 7, 1731.
137. Matsuda, N.; Hattori, Y.; Takahashi, Y.; Nishihira, J.; Jesmin, S.; Kobayashi, M.; Gando, S. Therapeutic effect of in vivo transfection of transcription factor decoy to NF- κ B on septic lung in mice. *Am J Physiol-Lung C* **2004**, 287, L1248-L1255.
138. Ahn, J. D.; Morishita, R.; Kaneda, Y.; Kim, H. J.; Kim, Y. D.; Lee, H. J.; Lee, K. U.; Park, J. Y.; Kim, Y. H.; Park, K. K.; Chang, Y. C.; Yoon, K. H.; Kwon, H. S.; Park,

- K. G.; Lee, I. K. Transcription factor decoy for AP-1 reduces mesangial cell proliferation and extracellular matrix production in vitro and in vivo. *Gene Ther* **2004**, 11, 916-923.
139. Quarcoo, D.; Weixler, S.; Groneberg, D.; Joachim, R.; Ahrens, B.; Wagner, A. H.; Hecker, M.; Hamelmann, E. Inhibition of signal transducer and activator of transcription 1 attenuates allergen-induced airway inflammation and hyperreactivity. *J Allergy Clin Immun* **2004**, 114, 288-295.
140. Finotti, A.; Borgatti, M.; Bezzerri, V.; Nicolis, E.; Lampronti, I.; Dechecchi, M.; Mancini, I.; Cabrini, G.; Saviano, M.; Avitabile, C.; Romanelli, A.; Gambari, R. Effects of decoy molecules targeting NF-kappaB transcription factors in Cystic fibrosis IB3-1 cells. *Artif DNA PNA XNA* **2012**, 3, 97-104.
141. Wang, J.; Cheng, H.; Li, X.; Lu, W.; Wang, K.; Wen, T. Regulation of Neural Stem Cell Differentiation by Transcription Factors HNF4-1 and MAZ-1. *Mol Neurobiol* **2013**, 47, 228-240.
142. Xie, S.; Nie, R.; Wang, J.; Li, F.; Yuan, W. Transcription factor decoys for activator protein-1 (AP-1) inhibit oxidative stress-induced proliferation and matrix metalloproteinases in rat cardiac fibroblasts. *Transl Res* **2009**, 153, 17-23.
143. Feeley, B. T.; Miniati, D. N.; Park, A. K.; Grant Hoyt, E.; Robbins, R. C. Nuclear Factor-kappaB Transcription Factor Decoy Treatment Inhibits Graft Coronary Artery Disease After Cardiac Transplantation in Rodents. *Transplantation* **2000**, 70, 1560-1568.
144. Desmet, C.; Gosset, P.; Pajak, B.; Cataldo, D.; Bentires-Alj, M.; Lekeux, P.; Bureau, F. Selective Blockade of NF- κ B Activity in Airway Immune Cells Inhibits the Effector Phase of Experimental Asthma. *J Immunol* **2004**, 173, 5766-5775.

145. Kawauchi, M.; Suzuki, J.; Wada, Y.; Morishita, R.; Kaneda, Y.; Isobe, M.; Amano, J.; Takamoto, S. Downregulation of nuclear factor kappa B expression in primate cardiac allograft arteries after E2F decoy transfection. *Transpl P* **2001**, *33*, 451.
146. Mann, M. J.; Whittemore, A. D.; Donaldson, M. C.; Belkin, M.; Conte, M. S.; Polak, J. F.; Orav, E. J.; Ehsan, A.; Dell'Acqua, G.; Dzau, V. J. Ex-vivo gene therapy of human vascular bypass grafts with E2F decoy: the PREVENT single-centre, randomised, controlled trial. *The Lancet* **1999**, *354*, 1493-1498.
147. Nishimura, A.; Akeda, K.; Matsubara, T.; Kusuzaki, K.; Matsumine, A.; Masuda, K.; Gemba, T.; Uchida, A.; Sudo, A. Transfection of NF- κ B decoy oligodeoxynucleotide suppresses pulmonary metastasis by murine osteosarcoma. *Cancer Gene Ther* **2011**, *18*, 250-259.
148. Novak, E. M.; Metzger, M.; Chammas, R.; da Costa, M.; Dantas, K.; Manabe, C.; Pires, J.; de Oliveira, A. C.; Bydlowski, S. P. Downregulation of TNF-[alpha] and VEGF expression by Sp1 decoy oligodeoxynucleotides in mouse melanoma tumor. *Gene Ther* **2003**, *10*, 1992-1997.
149. Souissi, I.; Najjar, I.; Ah-Koon, L.; Schischmanoff, P. O.; Lesage, D.; Le Coquil, S.; Roger, C.; Dusanter-Fourt, I.; Varin-Blank, N.; Cao, A.; Metelev, V.; Baran-Marszak, F.; Fagard, R. A STAT3-decoy oligonucleotide induces cell death in a human colorectal carcinoma cell line by blocking nuclear transfer of STAT3 and STAT3-bound NF- κ B. *BMC Cell Biology* **2011**, *12*, 14-14.
150. Cogoi, S.; Zorzet, S.; Rapozzi, V.; Géci, I.; Pedersen, E. B.; Xodo, L. E. MAZ-binding G4-decoy with locked nucleic acid and twisted intercalating nucleic acid

modifications suppresses KRAS in pancreatic cancer cells and delays tumor growth in mice. *Nucleic Acids Res* **2013**, 41, 4049-4064.

151. Kuratsukuri, K.; Sugimura, K.; Harimoto, K.; Kawashima, H.; Kishimoto, T. "Decoy" of Androgen-Responsive Element Induces Apoptosis in LNCaP Cells. *Prostate* **1999**, 41, 121-126.

152. Wang, L. H.; Yang, X. Y.; Zhang, X.; Mihalic, K.; Xiao, W.; Farrar, W. L. The cis Decoy against the Estrogen Response Element Suppresses Breast Cancer Cells via Target Disrupting c-fos not Mitogen-activated Protein Kinase Activity. *Cancer Res* **2003**, 63, 2046-2051.

153. Leong, P. L.; Andrews, G. A.; Johnson, D. E.; Dyer, K. F.; Xi, S.; Mai, J. C.; Robbins, P. D.; Gadiparthi, S.; Burke, N. A.; Watkins, S. F.; Grandis, J. R. Targeted inhibition of Stat3 with a decoy oligonucleotide abrogates head and neck cancer cell growth. *Proc Natl Acad Sci USA* **2003**, 100, 4138-4143.

154. Chan, K. S.; Sano, S.; Kiguchi, K.; Anders, J.; Komazawa, N.; Takeda, J.; DiGiovanni, J. Disruption of Stat3 reveals a critical role in both the initiation and the promotion stages of epithelial carcinogenesis. *J Clin Invest* **2004**, 114, 720-728.

155. Liu, W. M.; Scott, K. A.; Shahin, S.; Propper, D. J. The in vitro effects of CRE-decoy oligonucleotides in combination with conventional chemotherapy in colorectal cancer cell lines. *Eur J Bioch* **2004**, 271, 2773-2781.

156. Alper, Ö.; Bergmann-Leitner, E.; Abrams, S.; Cho-Chung, Y. Apoptosis, growth arrest and suppression of invasiveness by CRE-decoy oligonucleotide in ovarian cancer

cells: Protein kinase A downregulation and cytoplasmic export of CRE-binding proteins.

Mol Cell Biochem **2001**, 218, 55-63.

157. Penolazzi, L., Magri, E., Lambertini, E., Calò, G., Cozzani, M., Siciliani, G., Piva, R., Gambari, R. Local in vivo administration of a decoy oligonucleotide targeting NF- κ B induces apoptosis of osteoclasts after application of orthodontic forces to rat teeth. *Int J Mol Med* **2006**, 18, 807-811.

158. Morishita, R.; Gibbons, G. H.; Horiuchi, M.; Ellison, K. E.; Nakama, M.; Zhang, L.; Kaneda, Y.; Ogihara, T.; Dzau, V. J. A gene therapy strategy using a transcription factor decoy of the E2F binding site inhibits smooth muscle proliferation in vivo. *Proc Natl Acad Sci USA* **1995**, 92, 5855-5859.

159. Sen, M.; Thomas, S. M.; Kim, S.; Yeh, J. I.; Ferris, R. L.; Johnson, J. T.; Duvvuri, U.; Lee, J.; Sahu, N.; Joyce, S.; Freilino, M. L.; Shi, H.; Li, C.; Ly, D.; Rapireddy, S.; Etter, J. P.; Li, P.-K.; Wang, L.; Chiosea, S.; Seethala, R. R.; Gooding, W. E.; Chen, X.; Kaminski, N.; Pandit, K.; Johnson, D. E.; Grandis, J. R. First-in-human trial of a STAT3 decoy oligonucleotide in head and neck tumors: implications for cancer therapy. *Cancer Discov* **2**, 694-705.

160. Kaplan, J. H.; Forbush, B.; Hoffman, J. F. Rapid photolytic release of adenosine 5'-triphosphate from a protected analog: utilization by the sodium:potassium pump of human red blood cell ghosts. *Biochemistry* **1978**, 17, 1929-1935.

161. Forbush, B. Na⁺ movement in a single turnover of the Na pump. *Proc Natl Acad Sci USA* **1984**, 81, 5310-5314.

162. Rajasekharan Pillai, V. N. Photoremovable Protecting Groups in Organic Synthesis. *Synthesis* **1980**, 1980, 1-26.
163. Mayer, G.; Heckel, A. Biologically Active Molecules with a “Light Switch”. *Angew Chem Int Ed* **2006**, 45, 4900-4921.
164. Brieke, C.; Rohrbach, F.; Gottschalk, A.; Mayer, G.; Heckel, A. Light-Controlled Tools. *Angew Chem Int Ed* **2012**, 51, 8446-8476.
165. Lee, H.-M.; Larson, D. R.; Lawrence, D. S. Illuminating the Chemistry of Life: Design, Synthesis, and Applications of “Caged” and Related Photoresponsive Compounds. *ACS Chem Biol* **2009**, 4, 409-427.
166. Deiters, A. Principles and Applications of the Photochemical Control of Cellular Processes. *ChemBioChem* **2010**, 11, 47-53.
167. Callaway, E. M.; Yuste, R. Stimulating neurons with light. *Curr Opin Neurobiol* **2002**, 12, 587-592.
168. Bennett, I. M.; Farfano, H. M. V.; Bogani, F.; Primak, A.; Liddell, P. A.; Otero, L.; Sereno, L.; Silber, J. J.; Moore, A. L.; Moore, T. A.; Gust, D. Active transport of Ca²⁺ by an artificial photosynthetic membrane. *Nature* **2002**, 420, 398-401.
169. Pelliccioli, A. P.; Wirz, J. Photoremovable protecting groups: reaction mechanisms and applications. *Photoch Photobio Sci* **2002**, 1, 441-458.
170. Givens, R.; Kotala, M. B.; Lee, J.-I. Mechanistic Overview of Phototriggers and Cage Release. In *Dynamic Studies in Biology*, Wiley-VCH Verlag GmbH & Co. KGaA: 2005; pp 95-129.

171. Corrie, J. E. T.; Furuta, T.; Givens, R.; Yousef, A. L.; Goeldner, M. Photoremovable Protecting Groups Used for the Caging of Biomolecules. In *Dynamic Studies in Biology*, Wiley-VCH Verlag GmbH & Co. KGaA: 2005; pp 1-94.
172. Il'ichev, Y. V.; Schwörer, M. A.; Wirz, J. Photochemical Reaction Mechanisms of 2-Nitrobenzyl Compounds: Methyl Ethers and Caged ATP. *J Am Chem Soc* **2004**, 126, 4581-4595.
173. Aujard, I.; Benbrahim, C.; Gouget, M.; Ruel, O.; Baudin, J.-B.; Neveu, P.; Jullien, L. o-Nitrobenzyl Photolabile Protecting Groups with Red-Shifted Absorption: Syntheses and Uncaging Cross-Sections for One- and Two-Photon Excitation. *Chem Eur J* **2006**, 12, 6865-6879.
174. Petit, M.; Tran, C.; Roger, T.; Gallavardin, T.; Dhimane, H.; Palma-Cerda, F.; Blanchard-Desce, M.; Acher, F. C.; Ogden, D.; Dalko, P. I. Substitution Effect on the One- and Two-photon Sensitivity of DMAQ "Caging" Groups. *Org Lett* **2012**, 14, 6366-6369.
175. Yu, H.; Li, J.; Wu, D.; Qiu, Z.; Zhang, Y. Chemistry and biological applications of photo-labile organic molecules. *Chem Soc Rev* **2010**, 39, 464-473.
176. Adams, S. R.; Kao, J. P. Y.; Tsien, R. Y. Biologically useful chelators that take up calcium(2+) upon illumination. *J Am Chem Soc* **1989**, 111, 7957-7968.
177. Wieboldt, R.; Gee, K. R.; Niu, L.; Ramesh, D.; Carpenter, B. K.; Hess, G. P. Photolabile precursors of glutamate: synthesis, photochemical properties, and activation of glutamate receptors on a microsecond time scale. *Proc Natl Acad Sci* **1994**, 91, 8752-8756.

178. Singh, A.; Khade, P. Synthesis and Photochemical Properties of Nitro-Naphthyl Chromophore and the Corresponding Immunoglobulin Bioconjugate. *Bioconjugate Chem* **2002**, 13, 1286-1291.
179. Momotake, A.; Lindegger, N.; Niggli, E.; Barsotti, R. J.; Ellis-Davies, G. C. R. The nitrodibenzofuran chromophore: a new caging group for ultra-efficient photolysis in living cells. *Nat Meth* **2006**, 3, 35-40.
180. Blanc, A.; Bochet, C. G. Bis(o-nitrophenyl)ethanediol: A Practical Photolabile Protecting Group for Ketones and Aldehydes. *J Org Chem* **2003**, 68, 1138-1141.
181. Yip, R. W.; Sharma, D. K.; Giasson, R.; Gravel, D. Photochemistry of the o-nitrobenzyl system in solution: evidence for singlet-state intramolecular hydrogen abstraction. *J Phys Chem* **1985**, 89, 5328-5330.
182. Papageorgiou, G.; Ogden, D. C.; Barth, A.; Corrie, J. E. T. Photorelease of Carboxylic Acids from 1-Acyl-7-nitroindolines in Aqueous Solution: Rapid and Efficient Photorelease of l-Glutamate¹. *J Am Chem Soc* **1999**, 121, 6503-6504.
183. Matsuzaki, M.; Honkura, N.; Ellis-Davies, G. C. R.; Kasai, H. Structural basis of long-term potentiation in single dendritic spines. *Nature* **2004**, 429, 761-766.
184. Warther, D.; Gug, S.; Specht, A.; Bolze, F.; Nicoud, J. F.; Mourot, A.; Goeldner, M. Two-photon uncaging: New prospects in neuroscience and cellular biology. *Bioorg Med Chem* **2010**, 18, 7753-7758.
185. Abate-Pella, D.; Zeliadt, N. A.; Ochocki, J. D.; Warmka, J. K.; Dore, T. M.; Blank, D. A.; Wattenberg, E. V.; Distefano, M. D. Photochemical Modulation of Ras-

Mediated Signal Transduction Using Caged Farnesyltransferase Inhibitors: Activation by One- and Two-Photon Excitation. *ChemBioChem* **2012**, 13, 1009-1016.

186. Liu, Q.; Deiters, A. Optochemical Control of Deoxyoligonucleotide Function via a Nucleobase-Caging Approach. *Accounts Chem Res* **2014**, 47, 45-55.

187. Ceo, L. M.; Koh, J. T. Photocaged DNA Provides New Levels of Transcription Control. *ChemBioChem* **2012**, 13, 511-513.

188. Rodrigues-Correia, A.; Koeppel, M.; Schäfer, F.; Joshi, K. B.; Mack, T.; Heckel, A. Comparison of the duplex-destabilizing effects of nucleobase-caged oligonucleotides. *Anal Bioanal Chem* **2011**, 399, 441-447.

189. Mayer, G.; Kröck, L.; Mikat, V.; Engeser, M.; Heckel, A. Light-Induced Formation of G-Quadruplex DNA Secondary Structures. *ChemBioChem* **2005**, 6, 1966-1970.

190. Heckel, A.; Buff, M. C. R.; Raddatz, M.-S. L.; Müller, J.; Pötzsch, B.; Mayer, G. An Anticoagulant with Light-Triggered Antidote Activity. *Angew Chem Int Ed* **2006**, 45, 6748-6750.

191. Lusic, H.; Young, D. D.; Lively, M. O.; Deiters, A. Photochemical DNA Activation. *Org Lett* **2007**, 9, 1903-1906.

192. Kröck, L.; Heckel, A. Photoinduced Transcription by Using Temporarily Mismatched Caged Oligonucleotides. *Angew Chem Int Ed* **2005**, 44, 471-473.

193. Chou, C.; Young, D. D.; Deiters, A. Photocaged T7 RNA Polymerase for the Light Activation of Transcription and Gene Function in Pro- and Eukaryotic Cells. *ChemBioChem* **2010**, 11, 972-977.

194. Casey, J. P.; Blidner, R. A.; Monroe, W. T. Caged siRNAs for Spatiotemporal Control of Gene Silencing. *Mol Pharm* **2009**, 6, 669-685.
195. Deiters, A. Light activation as a method of regulating and studying gene expression. *Curr Opin Chem Biol* **2009**, 13, 678-686.
196. Deiters, A.; Garner, R. A.; Lusic, H.; Govan, J. M.; Dush, M.; Nascone-Yoder, N. M.; Yoder, J. A. Photocaged Morpholino Oligomers for the Light-Regulation of Gene Function in Zebrafish and Xenopus Embryos. *J Am Chem Soc* **2010**, 132, 15644-15650.
197. Ordoukhanian, P.; Taylor, J.-S. Design and Synthesis of a Versatile Photocleavable DNA Building Block. Application to Phototriggered Hybridization. *J Am Chem Soc* **1995**, 117, 9570-9571.
198. Young, D. D.; Lively, M. O.; Deiters, A. Activation and Deactivation of DNAzyme and Antisense Function with Light for the Photochemical Regulation of Gene Expression in Mammalian Cells. *J Am Chem Soc* **2010**, 132, 6183-6193.
199. Shah, S.; Rangarajan, S.; Friedman, S. H. Light-Activated RNA Interference. *Angew Chem Int Ed* **2005**, 44, 1328-1332.
200. Mikat, V.; Heckel, A. Light-dependent RNA interference with nucleobase-caged siRNAs. *RNA* **2007**, 13, 2341-2347.
201. Govan, J. M.; Lively, M. O.; Deiters, A. Photochemical control of DNA decoy function enables precise regulation of nuclear factor kappaB activity. *J Am Chem Soc* **2011**, 133, 13176-82.
202. Buttiglieri, C.; Tucci, M.; Bertaglia, V.; Vignani, F.; Bironzo, P.; Di Maio, M.; Scagliotti, G. V. Understanding and overcoming the mechanisms of primary and acquired

resistance to abiraterone and enzalutamide in castration resistant prostate cancer. *Cancer Treat Rev* **2015**.

203. Denayer, S.; Helsen, C.; Thorrez, L.; Haelens, A.; Claessens, F. The Rules of DNA Recognition by the Androgen Receptor. *Mol Endocrinol* **2010**, *24*, 898-913.

204. Zhang, P.; Zhang, J.; Young, C. Y. F.; Kao, P. C.; Chen, W.; Jiang, A.; Zhang, L.; Guo, Q. Decoy Androgen-Responsive Element DNA Can Inhibit Androgen Receptor Transactivation of the PSA Promoter Gene. *Ann Clin Lab Sci* **2005**, *35*, 278-284.

205. Lusic, H.; Deiters, A. A New Photocaging Group for Aromatic N-Heterocycles. *Synthesis* **2006**, 2006, 2147-2150.

206. Young, D. D.; Lusic, H.; Lively, M. O.; Yoder, J. A.; Deiters, A. Gene Silencing in Mammalian Cells with Light-Activated Antisense Agents. *ChemBioChem* **2008**, *9*, 2937-2940.

207. Mergny, J. L.; Lacroix, L. Analysis of thermal melting curves. *Oligonucleotides* **2003**, *13*, 515-37.

208. Young, D. D.; Edwards, W. F.; Lusic, H.; Lively, M. O.; Deiters, A. Light-triggered polymerase chain reaction. *Chem Commun* **2008**, 462-464.

209. Lusic, H.; Young, D. D.; Lively, M. O.; Deiters, A. Photochemical DNA activation. *Org Lett* **2007**, *9*, 1903-6.

210. Usman, N., Ogilvie, K.K., Jiang, M.Y., Cedergren, R.J. Automated Chemical Synthesis of Long Oligoribonucleotides Using 2'-O-Silylated Ribonucleoside 3'-O-Phosphoramidites on a Controlled-Pore Glass Support: Synthesis of a 43-Nucleotide

Sequence Similar to the 3'-Half Molecule of an Escherichia coli Formylmethionine tRNA. *J Am Chem Soc* **1987**, 109, 7845.

211. Chenoweth, D. M.; Harki, D. A.; Phillips, J. W.; Dose, C.; Dervan, P. B. Cyclic Pyrrole-Imidazole Polyamides Targeted to the Androgen Response Element. *J Am Chem Soc* **2009**, 131, 7182-7188.

212. Yang, B.; Chang, Y.; Weyers, A. M.; Sterner, E.; Linhardt, R. J. Disaccharide analysis of glycosaminoglycan mixtures by ultra-high-performance liquid chromatography-mass spectrometry. *J Chromatogr* **2012**, 1225, 91-8.

213. Kuhn, H. J.; Braslavsky, S. E.; Schmidt, R. Chemical Actinometry. *Pure Appl Chem* **2004**, 76, 2105-2146.

214. Demas, J. N.; Bowman, W. D.; Zalewski, E. F.; Velapoldi, R. A. Determination of the quantum yield of the ferrioxalate actinometer with electrically calibrated radiometers. *J Phys Chem* **1981**, 85, 2766-2771.

215. Zhu, Y.; Pavlos, C. M.; Toscano, J. P.; Dore, T. M. 8-Bromo-7-hydroxyquinoline as a Photoremovable Protecting Group for Physiological Use: Mechanism and Scope. *J Am Chem Soc* **2006**, 128, 4267-4276.

216. Sweeney, C.; Li, L.; Shanmugam, R.; Bhat-Nakshatri, P.; Jayaprakasan, V.; Baldrige, L. A.; Gardner, T.; Smith, M.; Nakshatri, H.; Cheng, L. Nuclear Factor- κ B Is Constitutively Activated in Prostate Cancer In vitro and Is Overexpressed in Prostatic Intraepithelial Neoplasia and Adenocarcinoma of the Prostate. *Clin Cancer Res* **2004**, 10, 5501-5507.

217. Zhang, L.; Altuwaijri, S.; Deng, F.; Chen, L.; Lal, P.; Bhanot, U. K.; Korets, R.; Wenske, S.; Lilja, H. G.; Chang, C.; Scher, H. I.; Gerald, W. L. NF- κ B Regulates Androgen Receptor Expression and Prostate Cancer Growth. *Am J Pathol* **2009**, *175*, 489-499.
218. Nelson, D. E.; Ihekweba, A. E. C.; Elliott, M.; Johnson, J. R.; Gibney, C. A.; Foreman, B. E.; Nelson, G.; See, V.; Horton, C. A.; Spiller, D. G.; Edwards, S. W.; McDowell, H. P.; Unitt, J. F.; Sullivan, E.; Grimley, R.; Benson, N.; Broomhead, D.; Kell, D. B.; White, M. R. H. Oscillations in NF- κ B Signaling Control the Dynamics of Gene Expression. *Science* **2004**, *306*, 704-708.
219. Sung, M.-H.; Salvatore, L.; De Lorenzi, R.; Indrawan, A.; Pasparakis, M.; Hager, G. L.; Bianchi, M. E.; Agresti, A. Sustained Oscillations of NF- κ B Produce Distinct Genome Scanning and Gene Expression Profiles. *PLoS ONE* **2009**, *4*, e7163.
220. O'Shaughnessy, E. C.; Sarkar, C. A. Analyzing and engineering cell signaling modules with synthetic biology. *Curr Opin Biotech* **2012**, *23*, 785-790.
221. Pluvinet, R.; Olivar, R.; Krupinski, J.; Herrero-Fresneda, I.; Luque, A.; Torras, J.; Cruzado, J. M.; Grinyo, J. M.; Sumoy, L.; Aran, J. M. CD40: an upstream master switch for endothelial cell activation uncovered by RNAi-coupled transcriptional profiling. *Blood* **2008**, *112*, 3624-37.
222. Cho, Y. S.; Kim, M.-K.; Cheadle, C.; Neary, C.; Park, Y. G.; Becker, K. G.; Cho-Chung, Y. S. A genomic-scale view of the cAMP response element-enhancer decoy: A tumor target-based genetic tool. *Proc Natl Acad Sci* **2002**, *99*, 15626-15631.

223. Ahn, J. D.; Morishita, R.; Kaneda, Y.; Kim, H. S.; Chang, Y. C.; Lee, K. U.; Park, J. Y.; Lee, H. W.; Kim, Y. H.; Lee, I. K. Novel E2F decoy oligodeoxynucleotides inhibit in vitro vascular smooth muscle cell proliferation and in vivo neointimal hyperplasia. *Gene Ther* **2002**, *9*, 1682-92.
224. Karamouzis, M. V.; Gorgoulis, V. G.; Papavassiliou, A. G. Transcription Factors and Neoplasia: Vistas in Novel Drug Design. *Clin Cancer Res* **2002**, *8*, 949-961.
225. Lenox, H. J.; McCoy, C. P.; Sheppard, T. L. Site-Specific Generation of Deoxyribonolactone Lesions in DNA Oligonucleotides. *Org Lett* **2001**, *3*, 2415-2418.
226. Trzuppek, J. D.; Sheppard, T. L. Photochemical Generation of Ribose Abasic Sites in RNA Oligonucleotides. *Org Lett* **2005**, *7*, 1493-1496.
227. Wang, Y.; Sheppard, T. L.; Tornaletti, S.; Maeda, L. S.; Hanawalt, P. C. Transcriptional Inhibition by an Oxidized Abasic Site in DNA. *Chem Res Toxicol* **2006**, *19*, 234-241.
228. Kotera, M.; Bourdat, A. G.; Defrancq, E.; Lhomme, J. A highly efficient synthesis of oligodeoxycyribonucleotides containing the 2'-deoxyribonolactone lesion. *J Am Chem Soc* **1998**, *120*, 11810-11811.
229. Kotera, M.; Roupioz, Y.; Defrancq, E.; Bourdat, A. G.; Garcia, J.; Coulombeau, C.; Lhomme, J. The 7-nitroindole nucleoside as a photochemical precursor of 2'-deoxyribonolactone: access to DNA fragments containing this oxidative abasic lesion. *Chem Eur J* **2000**, *6*, 4163-9.

230. Roupioz, Y.; Lhomme, J.; Kotera, M. Chemistry of the 2-deoxyribonolactone lesion in oligonucleotides: cleavage kinetics and products analysis. *J Am Chem Soc* **2002**, *124*, 9129-35.
231. Brennan, P.; Donev, R.; Hewamana, S. Targeting transcription factors for therapeutic benefit. *Mol Biosyst* **2008**, *4*, 909-19.
232. Loakes, D.; Brown, D. M. 5-Nitroindole as an universal base analogue. *Nuc Acids Res* **1994**, *22*, 4039-4043.
233. Crey-Desbiolles, C.; Berthet, N.; Kotera, M.; Dumy, P. Hybridization properties and enzymatic replication of oligonucleotides containing the photocleavable 7-nitroindole base analog. *Nucleic Acids Res* **2005**, *33*, 1532-1543.
234. Kotera, M., Roupioz, Y., Defracq, E., Bourday, A., Garcia, J., Coulombeau, C., Lhomme, J. The 7-nitroindole nucleoside as a photochemical precursor of 2'-deoxyribonolactone: access to DNA fragments containing this oxidative abasic lesion. *Chem Eur J* **2000**, *6*, 4163.
235. Hayden, M. S.; Ghosh, S. NF- κ B, the first quarter-century: remarkable progress and outstanding questions. *Gene Dev* **2012**, *26*, 203-234.
236. Morishita, R.; Sugimoto, T.; Aoki, M.; Kida, I.; Tomita, N.; Moriguchi, A.; Maeda, K.; Sawa, Y.; Kaneda, Y.; Higaki, J.; Ogihara, T. In vivo transfection of cis element "decoy" against nuclear factor- κ B binding site prevents myocardial infarction. *Nat Med* **1997**, *3*, 894-9.
237. Penolazzi, L.; Magri, E.; Lambertini, E.; Calò, G.; M., C.; Siciliani, G.; Piva, R.; Gambari, R. Local in vivo administration of a decoy oligonucleotide targeting NF- κ B

induces apoptosis of osteoclasts after application of orthodontic forces to rat teeth. *Int J Mol Med* **2006**, 18, 807-811.

238. Metelev, V. G.; Kubareva, E. A.; Oretskaya, T. S. Regulation of activity of transcription factor NF- κ B by synthetic oligonucleotides. *Biochem (Moscow)* **2013**, 78, 867-878.

239. Lee, H. M.; Larson, D. R.; Lawrence, D. S. Illuminating the chemistry of life: design, synthesis, and applications of "caged" and related photoresponsive compounds. *ACS Chem Biol* **2009**, 4, 409-27.

240. Ceo, L. M.; Koh, J. T. Photocaged DNA provides new levels of transcription control. *Chembiochem* **2012**, 13, 511-3.

241. Chen, F. E.; Huang, D. B.; Chen, Y. Q.; Ghosh, G. Crystal structure of p50/p65 heterodimer of transcription factor NF-kappa B bound to DNA. *Nature* **1998**, 391, 410-413.

242. Sun, L.; Carpenter, G. Epidermal growth factor activation of NF- κ B is mediated through I κ B α degradation and intracellular free calcium. *Oncogene* **1998**, 16, 2095.

243. Phelps, C. B.; Sengchanthalangsy, L. L.; Malek, S.; Ghosh, G. Mechanism of κ B DNA binding by Rel/NF- κ B dimers. *J Biol Chem* **2000**, 275, 24392-24399.

244. Kotera, M.; Bourdat, A.; Defracq, E.; Lhomme, J. A Highly efficient synthesis of oligodeoxyribonucleotides containing the 2'-deoxyribonolactone lesion. *J Am Chem Soc* **1998**, 120, 11810-11811.

245. Heckel, A. Nucleobase-caged phosphoramidites for oligonucleotide synthesis. *Curr Protoc Nucleic Acid Chem* **2007**, Chapter 1, Unit 1 17.

246. Hexum, J. K.; Tello-Aburto, R.; Struntz, N. B.; Harned, A. M.; Harki, D. A. Bicyclic Cyclohexenones as Inhibitors of NF-kappaB Signaling. *ACS Med Chem Lett* **2012**, 3, 459-464.
247. Lawson, C. L.; Berman, H. M. Chapter 4 Indirect Readout of DNA Sequence by Proteins. In *Protein-Nucleic Acid Interactions: Structural Biology*, The Royal Society of Chemistry: 2008; pp 66-90.
248. Settles, S.; Wang, R.-W.; Fronza, G.; Gold, B. Effect of N3-Methyladenine and an Isosteric Stable Analogue on DNA Polymerization. *J Nucleic Acids* **2010**, 2010, 14.
249. Saito, Y.; Taguchi, H.; Fujii, S.; Sawa, T.; Kida, E.; Kabuto, C.; Akaike, T.; Arimoto, H. 8-Nitroguanosines as chemical probes of the protein S-guanylation. *Chem Commun (Camb)* **2008**, 5984-6.
250. Kunieda, K.; Tsutsuki, H.; Ida, T.; Kishimoto, Y.; Kasamatsu, S.; Sawa, T.; Goshima, N.; Itakura, M.; Takahashi, M.; Akaike, T.; Ihara, H. 8-Nitro-cGMP Enhances SNARE Complex Formation through S-Guanylation of Cys90 in SNAP25. *ACS Chem Neurosci* **2015**, 6, 1715-1725.
251. Leonard, N. J.; Neelima. 1,1,1,3,3,3-Hexafluoro-2-propanol for the removal of the 4,4'-Dimethoxytrityl protecting group from the 5'-hydroxyl of acid-sensitive nucleosides and nucleotides. *Tetrahedron Lett* **1995**, 36, 7833-7836.
252. Borkakoti, N. The active Site of Ribonuclease A from the Crystallographic Studies of Ribonuclease-A-Inhibitor Complexes. *Eur J Biochem* **1983**, 132, 89-94.

253. Cheng, K. C.; Cahill, D. S.; Kasai, H.; Nishimura, S.; Loeb, L. A. 8-Hydroxyguanine, an abundant form of oxidative DNA damage, causes G----T and A----C substitutions. *J Biol Chem* **1992**, *267*, 166-172.
254. Watson, J. D.; Crick, F. H. C. Genetical Implications of the Structure of Deoxyribonucleic Acid. *Nature* **1953**, *171*, 964-967.
255. Krishnamurthy, R. Role of pKa of Nucleobases in the Origins of Chemical Evolution. *Accounts Chem Res* **2012**, *45*, 2035-2044.
256. Topal, M. D.; Fresco, J. R. Complementary base pairing and the origin of substitution mutations. *Nature* **1976**, *263*, 285-289.
257. Abdul-Masih, M. T.; Bessman, M. J. Biochemical studies on the mutagen, 6-N-hydroxylaminopurine. Synthesis of the deoxynucleoside triphosphate and its incorporation into DNA in vitro. *J Biol Chem* **1986**, *261*, 2020-2026.
258. Budowsky, I. Mechanism of the mutagenic action of hydroxylamine. VII. Functional activity and specificity of cytidine triphosphate modified with hydroxylamine and O-methylhydroxylamine. *Biochim et biophys acta* **1972**, *287*, 195-210.
259. Brown, D. M.; Hewlins, M. J. E.; Schell, P. The tautomeric state of N(4)-hydroxy- and of N(4)-amino-cytosine derivatives. *J Chem Soc C* **1968**, 1925-1929.
260. Hill, F.; Williams, D. M.; Loakes, D.; Brown, D. M. Comparative mutagenicities of N6-methoxy-2,6-diaminopurine and N6-methoxyaminopurine 2'-deoxyribonucleosides and their 5'-triphosphates. *Nucleic Acids Res* **1998**, *26*, 1144-1149.
261. Morozov, Y. V.; Savin, F. A.; Chekhov, V. O.; Budowsky, E. I.; Yakovlev, D. Y. Photochemistry of N6-methoxyadenosine and of N4-hydroxycytidine and its methyl

derivatives I: spectroscopic and quantum chemical investigation of ionic and tautomeric forms: syn-anti isomerization. *J Photochem* **1982**, 20, 229-252.

262. Reeves, S. T.; Beattie, K. L. Base-pairing properties of N4-methoxydeoxycytidine 5'-triphosphate during DNA synthesis on natural templates, catalyzed by DNA polymerase I of *Escherichia coli*. *Biochemistry* **1985**, 24, 2262-2268.

263. Singer, B.; Fraenkel-Conrat, H.; Abbott, L. G.; Spengler, S. J. N4-Methoxydeoxycytidine triphosphate is in the imino tautomeric form and substitutes for deoxythymidine triphosphate in primed poly d[A-T] synthesis with *E. coli* DNA polymerase I. *Nucleic Acids Res* **1984**, 12, 4609-4619.

264. Harris, V. H.; Smith, C. L.; Jonathan Cummins, W.; Hamilton, A. L.; Adams, H.; Dickman, M.; Hornby, D. P.; Williams, D. M. The Effect of Tautomeric Constant on the Specificity of Nucleotide Incorporation during DNA Replication: Support for the Rare Tautomer Hypothesis of Substitution Mutagenesis. *J Mol Biol* **2003**, 326, 1389-1401.

265. Moore, M. H.; Van Meervelt, L.; Salisbury, S. A.; Kong Thoo Lin, P.; Brown, D. M. Direct Observation of Two Base-pairing Modes of a Cytosine-Thymine Analogue with Guanine in a DNAZ-form Duplex: Significance for Base Analogue Mutagenesis. *J Mol Biol* **1995**, 251, 665-673.

266. Lin, P. K.; Brown, D. M. Synthesis and duplex stability of oligonucleotides containing cytosine-thymine analogues. *Nucleic Acids Res* **1989**, 17, 10373-10383.

267. Podolyan, Y.; Gorb, L.; Leszczynski, J. Rare Tautomer Hypothesis Supported by Theoretical Studies: Ab Initio Investigations of Prototropic Tautomerism in the N-Methyl-P Base. *J Phys Chem A* **2005**, 109, 10445-10450.

268. Schuerman, G. S.; Van Meervelt, L.; Loakes, D.; Brown, D. M.; Kong Thoo Lin, P.; Moore, M. H.; Salisbury, S. A. A thymine-like base analogue forms wobble pairs with adenine in a Z-DNA duplex1. *J Mol Biol* **1998**, 282, 1005-1011.
269. Graci, J. D.; Harki, D. A.; Korneeva, V. S.; Edathil, J. P.; Too, K.; Franco, D.; Smidansky, E. D.; Paul, A. V.; Peterson, B. R.; Brown, D. M.; Loakes, D.; Cameron, C. E. Lethal Mutagenesis of Poliovirus Mediated by a Mutagenic Pyrimidine Analogue. *J Virol* **2007**, 81, 11256-11266.
270. Hill, F.; Loakes, D.; Brown, D. M. Polymerase recognition of synthetic oligodeoxyribonucleotides incorporating degenerate pyrimidine and purine bases. *Proc Natl Acad Sci* **1998**, 95, 4258-4263.
271. Moriyama, K.; Otsuka, C.; Loakes, D.; Negishi, K. Highly Efficient Random Mutagenesis in Transcription-reverse-transcription Cycles by a Hydrogen Bond Ambivalent Nucleotide 5'-Triphosphate Analogue: Potential Candidates for a Selective Anti-retroviral Therapy. *Nucleosides Nucleotides Nucleic Acids* **2001**, 20, 1473.
272. Chiu, T. K.; Dickerson, R. E. 1 A crystal structures of B-DNA reveal sequence-specific binding and groove-specific bending of DNA by magnesium and calcium. *J Mol Biol* **2000**, 301, 915-45.
273. Jones, K. L. P., A.; Hall, A.; Woodrow, M.D.; Tomkinson, N.C.O. . Copper-Catalyzed Coupling of Hydroxylamines with Aryl Iodides. *Org. Lett.* **2008**, 10, 797.
274. Hayden, M. S.; Ghosh, S. Shared principles in NF-kappaB signaling. *Cell* **2008**, 132, 344-362.

275. Ruland, J. Return to homeostasis: downregulation of NF- κ B responses. *Nature Immunology* **2011**, 12, 709-714.
276. Sen, R.; Baltimore, D. Multiple Nuclear Factors Interact with the Immunoglobulin Enhancer Sequences. *Cell* **1986**, 46, 705-716.
277. Karin, M.; Greten, F. R. NF-kappaB: linking inflammation and immunity to cancer development and progression. *Nat Rev Immunol* **2005**, 5, 749-759.
278. Naugler, W. E.; Karin, M. NF-kappaB and cancer-identifying targets and mechanisms. *Curr Opin Genet Devel* **2008**, 18, 19-26.
279. Aggarwal, B. B. Nuclear factor-kappaB: the enemy within. *Cancer Cell* **2004**, 6, 203-208.
280. Bremner, P.; Heinrich, M. Natural products as targeted modulators of the nuclear factor-kappaB pathway. *J Pharm Pharmacol* **2002**, 54, 453-472.
281. Folmer, F.; Harrison, W. T. A.; Tabudravu, J. N.; Jaspars, M.; Aalbersberg, W.; Feussner, K.; Wright, A. D.; Dicato, M.; Diederich, M. NF-kappaB-inhibiting naphthopyrones from the Fijian echinoderm *Comanthus parvicirrus*. *J Nat Prod* **2008**, 71, 106-111.
282. Müller, S.; Murillo, R.; Castro, V.; Brecht, V.; Merfort, I. Sesquiterpene lactones from *Montanoa hibiscifolia* that inhibit the transcription factor NF-kappa B. *J Nat Prod* **2004**, 67, 622-630.
283. Rüngeler, P.; Castro, V.; Mora, G.; Gören, N.; Vichnewski, W.; Pahl, H. L.; Merfort, I.; Schmidt, T. J. Inhibition of transcription factor NF-kappaB by sesquiterpene

- lactones: a proposed molecular mechanism of action. *Bioorg Med Chem* **1999**, *7*, 2343-2352.
284. Nam, N.-H. Naturally occurring NF-kappaB inhibitors. *Mini-Rev Med Chem* **2006**, *6*, 945-951.
285. Merfort, I. Perspectives on sesquiterpene lactones in inflammation and cancer. *Curr Drug Targets* **2011**, *12*, 1560-1573.
286. Singh, J.; Petter, R. C.; Baillie, T. A.; Whitty, A. The resurgence of covalent drugs. *Nat Rev Drug Discov* **2011**, *10*, 307-317.
287. Dumontet, V. New cytotoxic flavonoids from *Cryptocarya infectoria*. *Tetrahedron* **2001**, *57*, 6189-6196.
288. Govindachari, T. R.; Parthasarathy, P. C. Cryptocaryone, a novel 5',6'-dihydrochalcone, from *Cryptocarya bourdilloni* gamb. *Tetrahedron Lett* **1972**, *13*, 3419-3420.
289. Maddry, J. A.; Joshi, B. S.; Gary Newton, M.; William Pelletier, S.; Parthasarathy, P. C. Cryptocaryone: A revised structure. *Tetrahedron Lett* **1985**, *26*, 5491-5492.
290. Meragelman, T. L.; Scudiero, D. A.; Davis, R. E.; Staudt, L. M.; McCloud, T. G.; Cardellina, J. H., 2nd; Shoemaker, R. H. Inhibitors of the NF-kappaB activation pathway from *Cryptocarya rugulosa*. *J Nat Prod* **2009**, *72*, 336-339.
291. Fujioka, H.; Nakahara, K.; Oki, T.; Hirano, K.; Hayashi, T.; Kita, Y. The first asymmetric total syntheses of both enantiomers of cryptocaryone. *Tetrahedron Lett* **2010**, *51*, 1945-1946.

292. Franck, G. r.; Brödner, K.; Helmchen, G. n. Enantioselective Modular Synthesis of Cyclohexenones: Total Syntheses of (+)-Crypto- and (+)-Infectocaryone. *Org Lett* **2010**, 12, 3886-3889.
293. Tello-Aburto, R.; Harned, A. M. Palladium-catalyzed reactions of cyclohexadienones: regioselective cyclizations triggered by alkyne acetoxylation. *Org Lett* **2009**, 11, 3998-4000.
294. Palayoor, S. T.; Youmell, M. Y.; Calderwood, S. K.; Coleman, C. N.; Price, B. D. Constitutive activation of IkappaB kinase alpha and NF-kappaB in prostate cancer cells is inhibited by ibuprofen. *Oncogene* **1999**, 18, 7389-7394.
295. Suh, J.; Payvandi, F.; Edelstein, L. C.; Amenta, P. S.; Zong, W.-X.; Gélinas, C.; Rabson, A. B. Mechanisms of constitutive NF-kappaB activation in human prostate cancer cells. *The Prostate* **2002**, 52, 183-200.
296. Webber, M. M. Normal and benign human prostatic epithelium in culture. I. Isolation. *In Vitro* **1979**, 15, 967-982.
297. Webber, M. M.; Bello, D.; Quader, S. Immortalized and tumorigenic adult human prostatic epithelial cell lines: characteristics and applications. Part I. Cell markers and immortalized nontumorigenic cell lines. *The Prostate* **1996**, 29, 386-394.
298. Teahan, O.; Bevan, C. L.; Waxman, J.; Keun, H. C. Metabolic signatures of malignant progression in prostate epithelial cells. *Int J Biochem Cell Biol* **2011**, 43, 1002-1009.
299. Moraski, G. C.; Markley, L. D.; Hipskind, P. A.; Boshoff, H.; Cho, S.; Franzblau, S. G.; Miller, M. J. Advent of Imidazo [1, 2-a] pyridine-3-carboxamides with potent

multi-and extended drug resistant antituberculosis activity. *ACS Med Chem Lett* **2011**, 6, 466-470.

300. Bello, D.; Webber, M. M.; Kleinman, H. K.; Waringer, D. D.; Rhim, J. S. Androgen responsive adult human prostatic epithelial cell lines immortalized by human papillomavirus 18. *Carcinogenesis* **1997**, 18, 1215-1223.

301. Li, X. C.; Babu, K. S.; Jacob, M. R.; Khan, S. I.; Agarwal, A. K.; Clark, A. M. Natural Product-Based 6-Hydroxy-2, 3, 4, 6-tetrahydropyrrolo [1, 2-a] pyrimidinium Scaffold as a New Antifungal Template. *ACS Med Chem Lett* **2011**, 5, 391-395.

302. Raj, L.; Ide, T.; Gurkar, A. U.; Foley, M.; Schenone, M.; Li, X.; Tolliday, N. J.; Golub, T. R.; Carr, S. A.; Shamji, A. F.; Stern, A. M.; Mandinova, A.; Schreiber, S. L.; Lee, S. W. Selective killing of cancer cells by a small molecule targeting the stress response to ROS. *Nature* **2011**, 475, 231-234.

303. Chen, Y.-C.; Kung, F.-L.; Tsai, I.-L.; Chou, T.-H.; Chen, I.-S.; Guh, J.-H. Cryptocaryone, a Natural Dihydrochalcone, Induces Apoptosis in Human Androgen Independent Prostate Cancer Cells by Death Receptor Clustering in Lipid Raft and Nonraft Compartments. *J Urology* **2010**, 183, 2409-2418.

304. Avonto, C.; Tagliatela-Scafati, O.; Pollastro, F.; Minassi, A.; Di Marzo, V.; De Petrocellis, L.; Appendino, G. An NMR spectroscopic method to identify and classify thiol-trapping agents: revival of Michael acceptors for drug discovery? *Angew Chem Int Ed Engl* **2011**, 50, 467-471.

305. Kunsch, C.; Rosen, C. A. NF-kappa B subunit-specific regulation of the interleukin-8 promoter. *Mol Cell Biol* **1993**, 13, 6137-6146.

306. Xie, K. Interleukin-8 and human cancer biology. *Cytokine & Growth Factor Rev* **2001**, 12, 375-391.
307. Lindenmeyer, M. T.; Hrenn, A.; Kern, C.; Castro, V.; Murillo, R.; Müller, S.; Laufer, S.; Schulte-Mönting, J.; Siedle, B.; Merfort, I. Sesquiterpene lactones as inhibitors of IL-8 expression in HeLa cells. *Bioorg Med Chem* **2006**, 14, 2487-2497.
308. Singh, R. K.; Lokeshwar, B. L. Depletion of intrinsic expression of Interleukin-8 in prostate cancer cells causes cell cycle arrest, spontaneous apoptosis and increases the efficacy of chemotherapeutic drugs. *Mol Cancer* **2009**, 8, 57-57.
309. Galli, R.; Starace, D.; Busà, R.; Angelini, D. F.; Paone, A.; De Cesaris, P.; Filippini, A.; Sette, C.; Battistini, L.; Ziparo, E.; Riccioli, A. TLR stimulation of prostate tumor cells induces chemokine-mediated recruitment of specific immune cell types. *J Immunol* **2010**, 184, 6658-6669.
310. Lötscher, D.; Rupprecht, S.; Stoeckli-Evans, H.; von Zelewsky, A. Enantioselective catalytic cyclopropanation of styrenes by copper complexes with chiral pinene-[5,6]-bipyridine ligands. *Tetrahedron Asymmetr* **2000**, 11, 4341-4357.
311. Karin, M. Nuclear factor-kappaB in cancer development and progression. *Nature* **2006**, 441, 431-436.
312. Verri, A.; Montecucco, A.; Gosselin, G.; Boudou, V.; Imbach, J. L.; Spadari, S.; Focher, F. L-ATP is recognized by some cellular and viral enzymes: does chance drive enzymic enantioselectivity? *Biochem J* **1999**, 337, 585-590.

313. Focher, F.; Spadari, S.; Maga, G. Antivirals at the mirror: The lack of stereospecificity of some viral and human enzymes offers novel opportunities in antiviral drug development. *Curr Drug Targets* **2003**, *3*, 41-53.
314. Spadari, S.; Maga, G.; Verri, A.; Focher, F. Molecular basis for the antiviral and anticancer activities of unnatural L-beta-nucleosides. *Expert Opin Investig Drugs* **1998**, *7*, 1285-300.
315. Maury, G. The enantioselectivity of enzymes involved in current antiviral therapy using nucleoside analogues: a new strategy? *Antivir Chem Chemoth* **2000**, *11*, 165-189.
316. Zemlicka, J. Enantioselectivity of the antiviral effects of nucleoside analogues. *Pharmacol Therapeut* **2000**, *85*, 251-266.
317. Mathe, C.; Gosselin, G. L-Nucleoside enantiomers as antivirals drugs: a mini-review. *Antivir Res* **2006**, *71*, 276-281.
318. Gray, N. M. M., C.L.P.; Penn, C.R.; Cameron, J.M.; Bethell, R.C. The Intracellular Phosphorylation of (-)-2'-Deoxy-3'-thiacytidine (3CT) and the Incorporation of 3TC 5'-monophosphate into DNA by HIV-1 Reverse Transcriptase and Human DNA Polymerase γ . *Biochem Pharm* **1995**, *50*, 1043-1051.
319. Christopherson, R. I.; Lyons, S. D.; Wilson, P. K. Inhibitors of de novo nucleotide biosynthesis as drugs. *Accounts Chem Res* **2002**, *35*, 961-971.
320. Ishikawa, H. Mizaribine and mycophenolate mofetil. *Curr Med Chem* **1999**, *6*, 575-597.
321. Nakamura, J.; Lou, L. Biochemical characterization of human GMP synthetase. *J Biol Chem* **1995**, *270*, 7347-7353.

322. Kusumi, T. T., M.; Katsunuma, T.; Yamamura, M. Dual Inhibitory Effect of Bredinin. *Cell Biochem Fun* **1988**, 7, 201-204.
323. McConkey, G. A. Plasmodium falciparum: Isolation and Characterisation of a Gene Encoding Protozoan GMP Synthase. *Exp Parasitol* **2000**, 94, 23-32.
324. Chittur, S. V.; Klem, T. J.; Shafer, C. M.; Davisson, V. J. Mechanism for acivicin inactivation of triad glutamine amidotransferases. *Biochemistry* **2001**, 40, 876-887.
325. Salaski, E. J., Maag, H. GMP Synthetase: Synthesis and Biological Evaluation of a Stable Analog of the Proposed AMP-XMP Reaction Intermediate. *Synlett* **1999**, S1, 897-900.
326. Nakamura, J.; Straub, K.; Wu, J.; Lou, L. The glutamine hydrolysis function of human GMP synthetase-identification of an essential active site cysteine. *J Biol Chem* **1995**, 270, 23450-23455.
327. Tesmer, J. J. G.; Stemmler, T. L.; Pennerhahn, J. E.; Davisson, V. J.; Smith, J. L. Preliminary X-ray analysis of Escherichia coli GMP Synthetase: determination of anomalous scattering factors for a cysteinyl mercury derivative. *Proteins* **1994**, 18, 394-403.
328. Tesmer, J. G.; Klem, T. J.; Deras, M. L.; Davisson, V. J.; Smith, J. L. The crystal structure of GMP synthetase reveals a novel catalytic triad and is a structural paradigm for two enzyme families. *Nat Struct Biol* **1996**, 3, 74-86.
329. Spector, T. Studies with GMP Synthetase from Ehrlich Ascites Cells. *J Biol Chem* **1975**, 250, 7372-7376.

330. Forsman, J. J.; Warna, J.; Murzin, D. Y.; Leino, R. Reaction kinetics and mechanism of acid-catalyzed anomerization of 1-O-acetyl-2,3,5-tri-O-benzoyl-L-ribofuranose. *Carbohydr Res* **2009**, 344, 1102-1109.
331. Vorbruggen, H.; Krolikiewicz, K.; Bennua, B. Nucleoside Syntheses 22. Nucleoside synthesis with trimethylsilyl triflate and perchlorate as catalysts. *Chem Ber-Recl* **1981**, 114, 1234-1255.
332. Nishimura, T. I., I. . Studies of Synthetic Nucleosides. I. Trimethylsilyl Derivative of Pyrimidines and Purines. *Chem Phar Bull* **1964**, 12, 352-356.
333. Yoshikawa, M.; Kato, T.; Takenishi, T. A novel method for phosphorylation of nucleosides to 5'-nucleotides. *Tetrahedron Lett* **1967**, 50, 5065-5068.
334. Sakamoto, N. GMP Sythetase (Escherichia coli). *Method Enzymol* **1978**, 51, 213-218.
335. Abbott, J. L.; Newell, J. M.; Lightcap, C. M.; Olanich, M. E.; Loughlin, D. T.; Weller, M. A.; Lam, G.; Pollack, S.; Patton, W. A. The Effects of Removing the GAT Domain from E. coli GMP Synthetase. *Protein J* **2006**, 25, 483-491.
336. Hirst, M.; Haliday, E.; Nakamura, J.; Lou, L. Human GMP synthetase. Protein purification, cloning, and functional expression of cDNA. *J Biol Chem* **1994**, 269, 23830-23837.
337. Lou, L.; Nakamura, J.; Tsing, S.; Nguyen, B.; Chow, J.; Straub, K.; Chan, H.; Barnett, J. High-level production from a baculovirus expression system and biochemical characterization of human GMP synthetase. *Protein Expres Purif* **1995**, 6, 487-495.

338. Bhat, J. Y. S., B.G.; Balaram, H. Kinetic and biochemical characterization of plasmodium falciparum GMP synthetase. *Biochem J* **2008**, 409, 263-273.
339. Spector, T.; Jones, T. E.; Krenitsky, T. A.; Harvey, R. J. Guanosine monophosphate synthetase from Ehrlich ascites cells-multiple inhibition by pyrophosphate and nucleosides. *Biochim Biophys Acta* **1976**, 452, 597-607.
340. Rodriguez-Suarez, R.; Xu, D. M.; Veillette, K.; Davison, J.; Sillaots, S.; Kauffman, S.; Hu, W. Q.; Bowman, J.; Martel, N.; Trosok, S.; Wang, H.; Zhang, L.; Huang, L. Y.; Li, Y.; Rahkhodaee, F.; Ransom, T.; Gauvin, D.; Douglas, C.; Youngman, P.; Becker, J.; Jiang, B.; Roemer, T. Mechanism-of-action determination of GMP synthase inhibitors and target validation in *Candida albicans* and *Aspergillus fumigatus*. *Chem Biol* **2007**, 14, 1163-1175.
341. Christopherson, R. I.; Lyons, S. D.; Wilson, P. K. Inhibitors of de Novo Nucleotide Biosynthesis as Drugs. *Acc Chem Res* **2002**, 35, 961-971.
342. Perigaud, C.; Gosselin, G.; Imbach, J. L. Nucleoside analogs as chemotherapeutic agents: a review. *Nucleos Nucleot* **1992**, 11, 903-945.
343. Berman, P. A.; Human, L.; Freese, J. A. Xanthine oxidase inhibits growth of Plasmodium falciparum in human erythrocytes in vitro. *J Clin Invest* **1991**, 88, 1848-1855.
344. McConkey, G. A. Plasmodium falciparum: Isolation and Characterisation of a Gene Encoding Protozoan GMP Synthase. *Exp Parasitol* **2000**, 94, 23-32.

345. Deras, M. L. C., S.V.; Davisson, V.J. N2-Hydroxyguanosine 5'-Monophosphate Is a Time-Dependent Inhibitor of Escherichia coli Guanosine Monophosphate Synthetase. *Biochemistry* **1999**, 38, 303-310.
346. Pietta, P. M., P.; Pace, M. . HPLC Assay of Enzymatic Activities. *Chromatographia* **1987**, 24, 439-441.
347. Pettersen, E. F.; Goddard Td Fau - Huang, C. C.; Huang Cc Fau - Couch, G. S.; Couch Gs Fau - Greenblatt, D. M.; Greenblatt Dm Fau - Meng, E. C.; Meng Ec Fau - Ferrin, T. E.; Ferrin, T. E. UCSF Chimera--a visualization system for exploratory research and analysis. *J Comput Chem* **2004**, 25, 1605-1612.

Appendix A

INHIBITION OF GUANOSINE MONOPHOSPHATE SYNTHETASE BY THE SUBSTRATE ENANTIOMER L-XMP

This work has been published by John Wiley & Sons:
Struntz, N. B.; Hu, T.; White, B. R.; Olson, M. E.; Harki, D. A. Inhibition of guanosine
monophosphate synthetase by the substrate enantiomer L-XMP. *ChemBioChem* **2012**, 13,
2517-20.

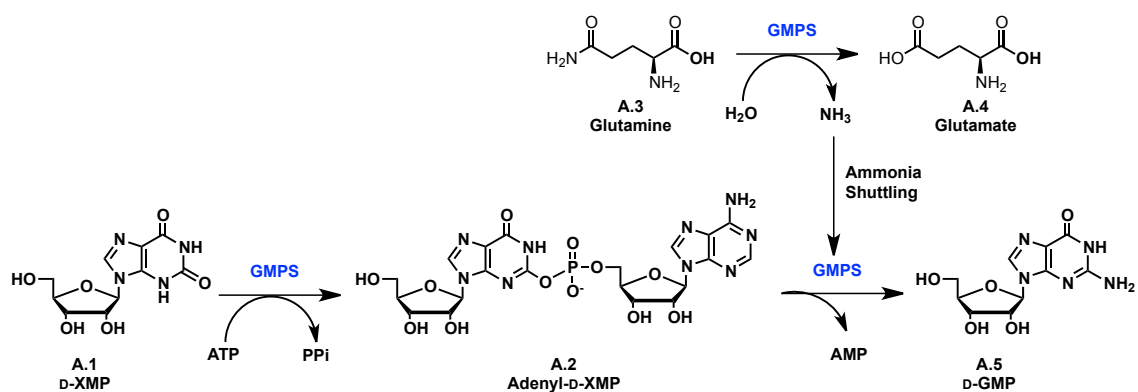
The full text is reprinted with permission.
Copyright Clearance License: 3738291108006

This work was performed in collaboration with Dr. Tianshun Hu, Dr. Brian R. White, Dr. Margaret E. Olson, and Professor Daniel A. Harki. We acknowledge the Swiss Tropical and Public Health Institute (Swiss TPH) for the antimalarial testing of compounds.

A.1 Rationale

Studies with mirror-image L-enantiomer nucleosides and nucleotides have revealed relaxed enantioselectivities of several cellular kinases and viral polymerases.^{312,313} This feature of enzyme-ligand molecular recognition has been exploited in the design of efficacious antiviral L-nucleoside drugs, which have lowered host cell toxicity.³¹⁴⁻³¹⁷ For example, lamivudine (2',3'-dideoxy-3'-thiacytidine, 3TC), an L-nucleoside drug, exploits the relaxed enantioselectivity of HIV reverse transcriptase to inhibit viral replication.³¹⁸ Conversely, the enantioselectivities of the majority of nucleotide biosynthesis enzymes have not been characterized. The depletion of cellular nucleotide pools has been shown to result in antiproliferative, antibacterial, and immunosuppressive effects.³¹⁹⁻³²²

GMP Synthetase (GMPS), an enzyme in *de novo* nucleotide biosynthesis, catalyzes the amination of xanthosine 5'-monophosphate (XMP, **A.1**) to guanosine 5'-



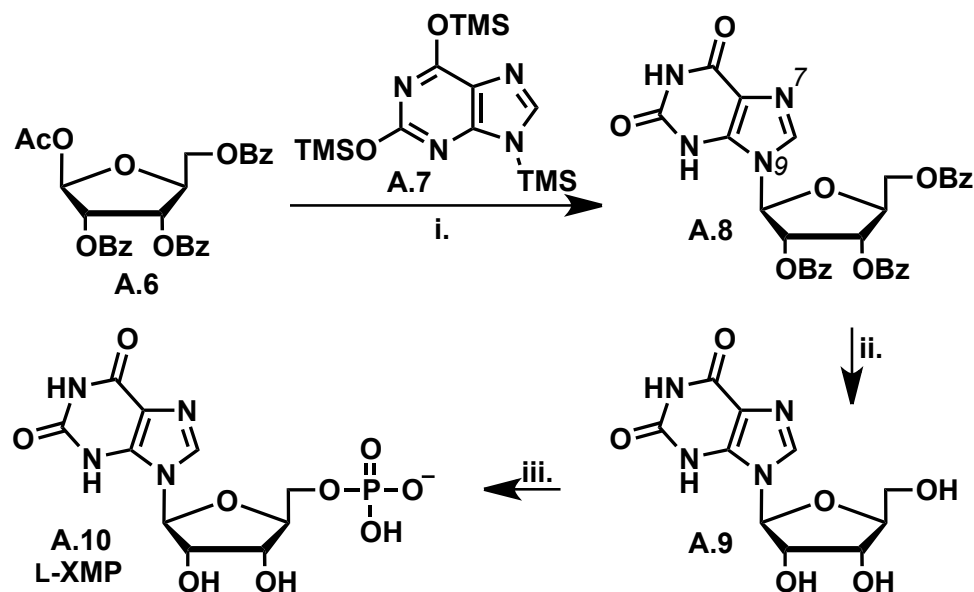
Scheme A.1. Enzymatic reaction catalyzed by GMPS. D-XMP **A.1** is adenylated in the synthetase active site by ATP, yielding **A.2**, which causes a conformational shift, allowing ammonia to be liberated in the amidotransferase active site **A.3** to **A.4**. GMPS then catalyzes aminolysis of the adenylated D-XMP to afford D-GMP **A.5**.

monophosphate (GMP, **A.5**) in the presence of glutamine (the amine source) and ATP (**Scheme A.1**).^{315,316} GMPS possesses two active sites that are separated by approximately 30 Å, suggesting that GMPS undergoes a significant conformational change during catalysis.³²³ In the amidotransferase active site, a glutamine residue **A.3** is hydrolyzed to glutamate **A.4** and liberates ammonia, which subsequently functions as the nucleophile in the amination of XMP.³²⁴ In the synthetase active site, the 2-carbonyl of XMP is adenylated with ATP to activate the aromatic ring for subsequent aminolysis (**A.2**).^{320,323,325} Formation of this intermediate is believed to trigger glutamine hydrolysis in the amidotransferase active site.³²⁶

A crystal structure of *E. coli* GMPS has been solved that reveals a large solvent-accessible synthetase pocket with considerable surface area.^{327,328} Several base-modified D-XMP analogues have been shown to function as substrates for GMPS and be converted to their amine derivatives.³²⁹ Based on this structural information and our interest in characterizing for the first time the enantioselectivity of GMPS, we hypothesized that L-XMP, the enantiomer of native ligand D-XMP, could target GMPS and modulate enzymatic activity. We hypothesized that L-XMP could incorporate into the synthetase active site and inhibit enzyme function, or less likely, L-XMP could function as a substrate for GMPS and undergo aminolysis to yield L-GMP. In either case, the biosynthesis of D-GMP would be affected, either by direct enzyme inhibition or by the activity of a suicide substrate. Given the central importance of GMPS in eukaryote and prokaryote biochemistry, we examined the enantioselectivity of the enzyme.

A.2 L-XMP Synthesis

Preceding this work, a synthesis of L-XMP (**A.10**), the enantiomer of natural ligand D-XMP, had not been reported. Our synthesis of L-XMP (**A.10**) started from L-arabinose, which was elaborated to 1-*O*-acetyl-2,3,5-tri-*O*-benzoyl- β -L-ribofuranoside (**A.6**) by reported methods (**Scheme A.2**).³³⁰ A Vorbrüggen coupling with trimethylsilyl protected xanthine **A.7** gave a separable mixture protected L-xanthosine isomer **A.8** (N^9 isomer, N^7 isomer not shown).^{331,332} Deprotection of the benzoyl protecting groups of **A.8** using ammonia afforded L-xanthosine (**A.9**). Selective



Scheme A.2. Synthesis of L-XMP **A.10**: Reagents and conditions: (i) TMSOTf, DCE, reflux, 70% (for **A.8**), 21% (**A.11** for N^7 -isomer, not shown); (ii) NH_3 , MeOH, 55 °C (sealed tube), 93%; (iii) POCl_3 , $\text{PO}(\text{OMe})_3$, Proton-Sponge; aq. TEAB, 25%.

phosphorylation of the 5'-OH of **A.9** utilizing phosphorous oxychloride gave L-XMP (**A.10**).³³³

A.3 GMPS Expression and Kinetic Analysis of GMPS by HPLC and UV-Vis

E. coli GMPS was overexpressed and purified (**Figure A.6**) and an HPLC-based assay was developed to quantitate enzymatic reaction products. GMPS was incubated with test substrates and NH₄OAc (ammonia source), and the reaction was terminated at various time points by addition of EDTA. GMPS protein was then removed by a molecular weight spin-column (30 kDa), and enzymatic reaction products were analyzed by reverse-phase HPLC. Surprisingly, we found that incubation of L-XMP and GMPS yielded a new peak of identical retention time as D-GMP (**Figure A.1a**).

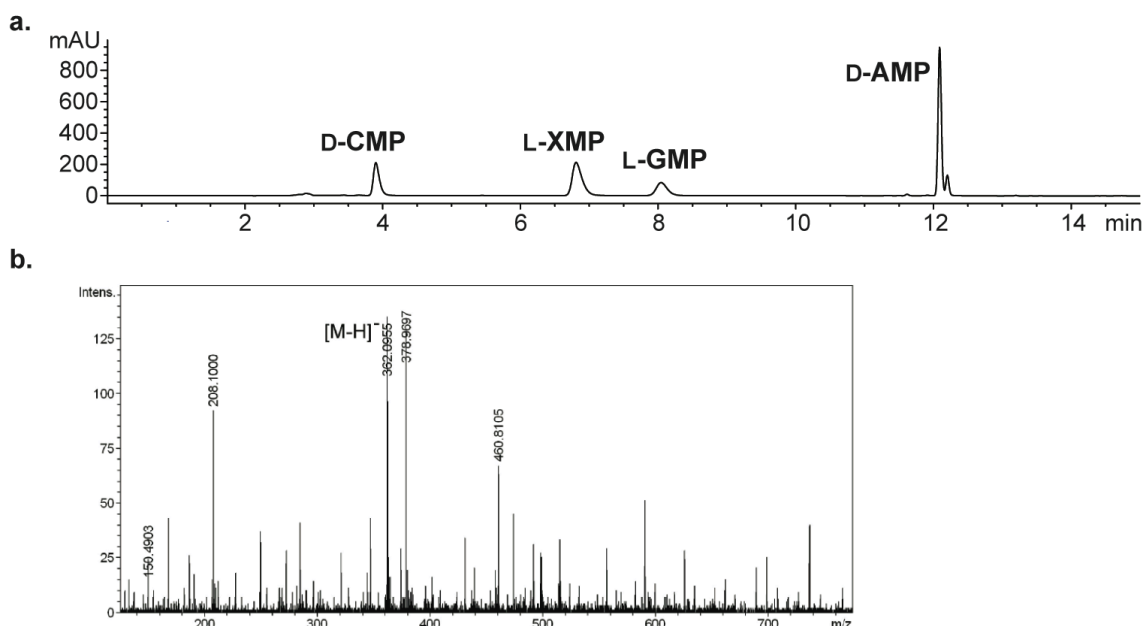


Figure A.1. (a) HPLC analysis of L-XMP conversion to L-GMP by GMPS (254 nm) (b) MS analysis of L-GMP peak.

Characterization of this new peak (MS analysis, **(Figure A.1b)**) confirmed that L-XMP was converted to L-GMP by GMPS, demonstrating that turnover of the opposite enantiomer substrate was possible.

Biochemical characterization of the kinetics of L-XMP conversion to L-GMP by GMPS, as well as D-XMP conversion to D-GMP, was measured by fitting the individual GMP/CMP (cytosine 5'-monophosphate, an external standard) ratios from each sample into the slope-intercept equation from the calibration plot. Initial velocity measurements of GMP production as a function of time were measured at a variety of substrate (XMP) concentrations, and at fixed saturating concentrations of the non-varied substrates ATP and NH₄OAc (**Figure A.2a**). Fitting these data to the Michaelis-Menten equation and analysis by non-linear regression allowed measurement of kinetic parameters (**Table A.1**).

Analysis of D-XMP revealed an apparent K_m of 35.3 μM , which was similar to previously reported K_m values for *E. coli* GMPS (29 μM and 166 μM).^{334,335} The turnover number (k_{cat}) was found to be $5.6 \times 10^{-2} \text{ s}^{-1}$, which was comparable to a previous report of $9.4 \times 10^{-2} \text{ s}^{-1}$,³³⁵ but 100-fold lower than human GMPS.^{336,337} Analysis of L-XMP revealed an apparent K_m of 316.7 μM , which is ~10-fold higher than the natural enantiomer. Surprisingly, the k_{cat} was measured at $3.8 \times 10^{-5} \text{ s}^{-1}$, which is a 1000-fold difference in turnover number compared to D-XMP. The specific activity (k_{cat}/K_m) of L-XMP decreased 13,000-fold from the natural enantiomer ($1.6 \times 10^{-3} \mu\text{M}^{-1}\text{s}^{-1}$ for D-XMP versus $1.2 \times 10^{-7} \mu\text{M}^{-1}\text{s}^{-1}$ for L-XMP). These results suggest that L-XMP may also inhibit GMPS.

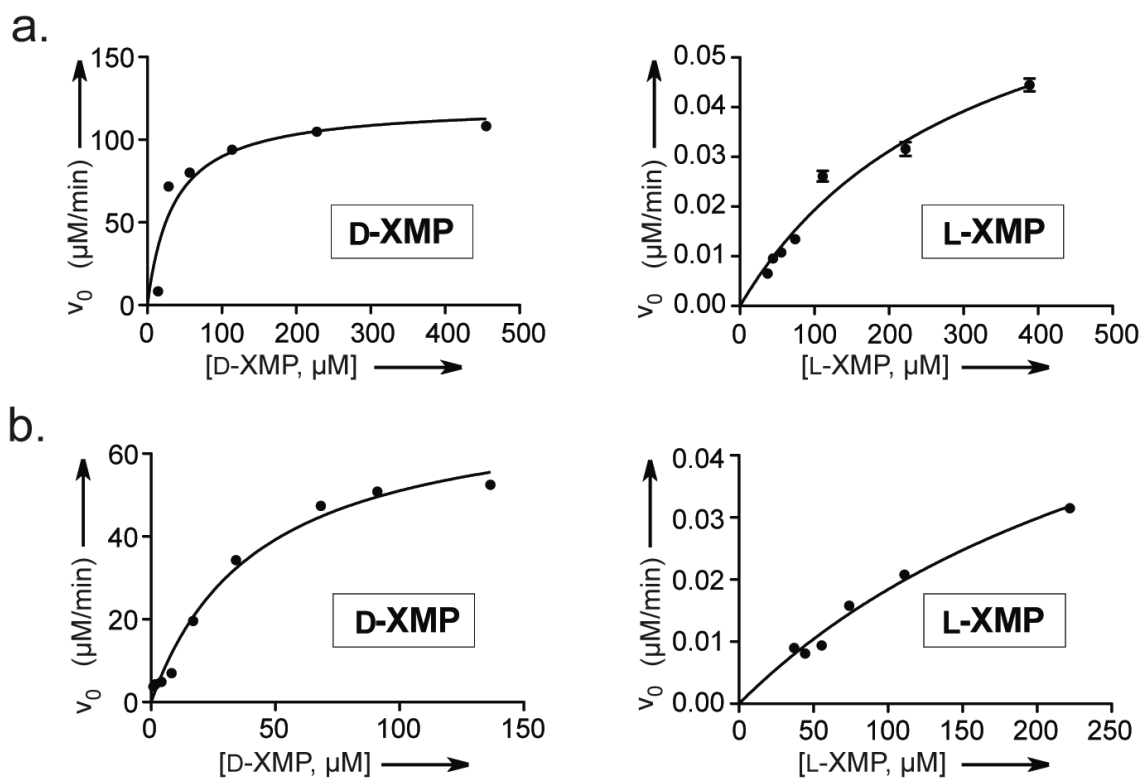


Figure A.2. Initial velocities versus substrate plots for D-XMP and L-XMP as measured by (a) HPLC analysis and (b) UV-Vis analysis.

Table A.1. Kinetic parameters of GMPS enantiomer substrates D-XMP and L-XMP.			
Substrate	k_{cat} (s^{-1})	K_m (μM)	k_{cat}/K_m ($\mu\text{M}^{-1} \text{s}^{-1}$)
D-XMP ^[a]	$5.6 (\pm 0.4) \times 10^{-2}$	35.3 ± 8.5	1.6×10^{-3}
D-XMP ^[b]	$5.1 (\pm 0.8) \times 10^{-2}$	24.9 ± 6.6	2.0×10^{-3}
L-XMP ^[a]	$3.8 (\pm 0.4) \times 10^{-5}$	316.7 ± 55.6	1.2×10^{-7}
L-XMP ^[b]	$3.7 (\pm 0.8) \times 10^{-5}$	329.9 ± 104.9	1.1×10^{-7}
[a] HPLC Analysis [b] UV-Vis Analysis			

To confirm the values derived from the HPLC assay, a known continuous UV spectrophotometric assay was also employed.^{334,338} This assay monitors a reduction in 290 nm absorbance resulting from conversion of XMP ($\epsilon_{290} = 4800 \text{ M}^{-1} \text{ cm}^{-1}$) to GMP ($\epsilon_{290} = 3300 \text{ M}^{-1} \text{ cm}^{-1}$). UV-based kinetic data was calculated analogously to the HPLC-derived data (**Figure A.2b**). Analysis of both D-XMP and L-XMP revealed nearly identical results to the HPLC assay (for L-XMP: $k_{\text{cat}}/K_m = 1.1 \times 10^{-7} \mu\text{M}^{-1} \text{s}^{-1}$ (UV) versus $1.2 \times 10^{-7} \mu\text{M}^{-1} \text{s}^{-1}$ (HPLC); **Table A.1**).

A.4 Inhibition of GMPS by L-XMP

Although L-XMP conversion to L-GMP by GMPS was demonstrated, the weak affinity of L-XMP for GMPS, coupled with its slow turnover number, suggested possible enzyme inhibition by this ligand. To probe for GMPS inhibition, we performed

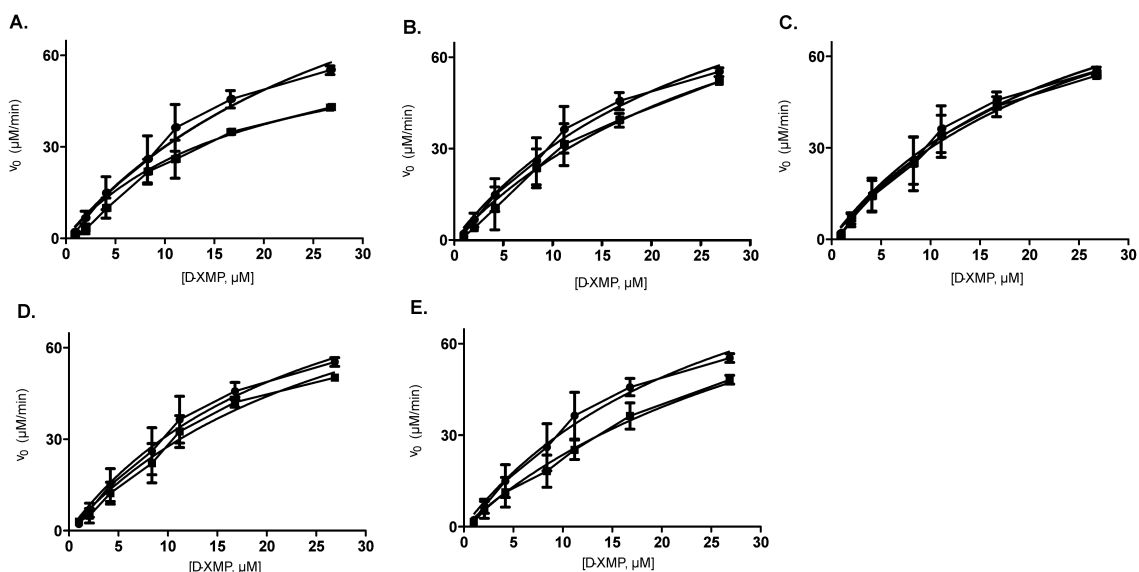


Figure A.3. Inhibition experiment plots of initial velocity versus substrate concentration for (A) decoyinine (B) mizoribine (C) D-xanthosine (D) L-xanthosine (E) L-XMP. Circles denote [Inhibitor] = 0 μM and squares denote [Inhibitor] = (A) 43 μM , (B) 0.4 μM , (C) 100 μM , (D) 100 μM , and (E) 3.2 μM .

enzymatic activity experiments with our xanthosine-based molecules to demonstrate reduction of GMPS-mediated amination of D-XMP (**Figure A.3**). Addition of a fixed concentration of inhibitor to varying D-XMP concentrations, followed by analysis by UV-Vis and fitting to the competitive inhibition equation (or uncompetitive for decoyinine towards XMP),³²¹ yielded the K_i data shown in **Table A.2**. Evaluation of the known GMPS uncompetitive inhibitor decoyinine revealed a $K_i = 54.1 \mu\text{M}$, which was similar to a previous report ($26 \mu\text{M}$).³³⁹ Mizoribine, a known GMPS competitive inhibitor, was found to be more potent in our hands ($K_i = 1.8 \mu\text{M}$), and this activity is similar to reports of the same compound against *E. brefeldianum* GMPS (K_i of $10 \mu\text{M}$).^{320,337} L-XMP (**6**) inhibition results were quite interesting, revealing that L-XMP is almost 7-fold more potent than decoyinine inhibition against *E. coli* GMPS ($K_i = 7.5 \mu\text{M}$). Both D-xanthosine and L-xanthosine nucleosides were also tested and neither molecule inhibited GMPS, suggesting that 5'-monophosphorylation is required for inhibition. Mizoribine does not require phosphorylation for GMPS inhibition. Our results suggest that L-XMP can inhibit GMPS enzymatic activity with potency similar to or slightly better than other known inhibitors.^{320,337,339,340}

Table A.2. GMPS inhibition data of known inhibitors and xanthosine analogues.	
Inhibitor	K_i (μM)
Decoyinine	54.1 ± 14.5
Mizoribine	1.8 ± 0.7
D-Xanthosine	> 1500
L-Xanthosine	> 500
L-XMP	7.5 ± 1.8

A.5 Docking Analysis of L-XMP

To understand the molecular interactions of D-XMP and L-XMP within the GMPS active site, energy minimized three-dimensional conformations of the biochemical reaction intermediates (adenyl-D-XMP and adeny-L-XMP; **Figure A.4a**) were docked (Surflex-dock in the SYBYL software suite) into the crystal structure of *E. coli* GMPS (PDB 1GPM).^{327,328} The molecule of AMP observed in the x-ray crystal structure was extracted and re-docked into GMPS with a calculated similarity of 0.908 (1.0 is the

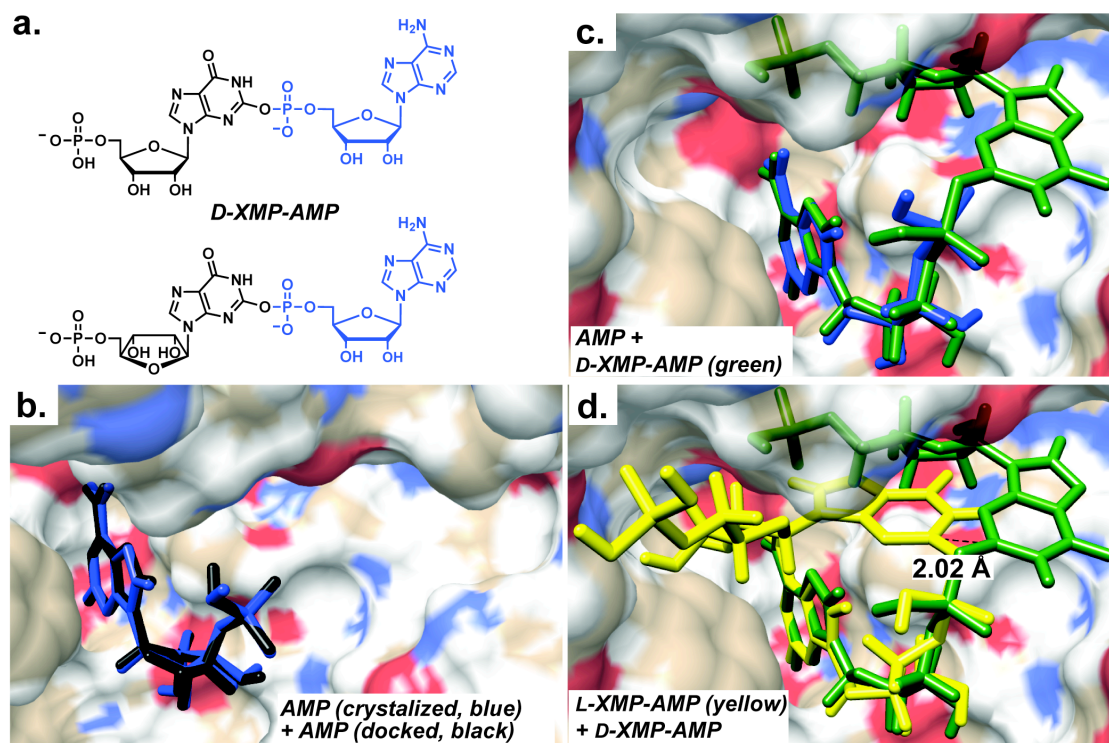


Figure A.4. (a) Structures of adenylylated D-XMP, the known intermediate in GMPS biosynthesis, and the putative adenylylated L-XMP intermediate in the synthesis of L-GMP by GMPS (b) Bound ligand AMP (blue) from X-ray crystal structure of *E. coli* GMPS was extracted from the structure and re-docked into the GMPS binding pocket overlaid with the crystallized AMP (black) (residues 207-406, pdb 1GPM) (c) Adenylylated D-XMP (green) docked into the GMPS binding pocket demonstrating docking accuracy of intermediates (d) Adenylylated L-XMP (yellow) and adenylylated D-XMP (green) docked into the GMPS binding pocket demonstrating a 2.0 Å conformational shift in xanthine nucleobases.

theoretical maximum), showing reliability in docking accuracy of the program (**Figure A.4b**). The docking of adenylyl-D-XMP and adenylyl-L-XMP over AMP demonstrated accuracy of the intermediates (**Figure A.4c-d**). Several stabilizing molecular interactions were observed between adenylyl-D-XMP and GMPS, such as hydrogen bonds between

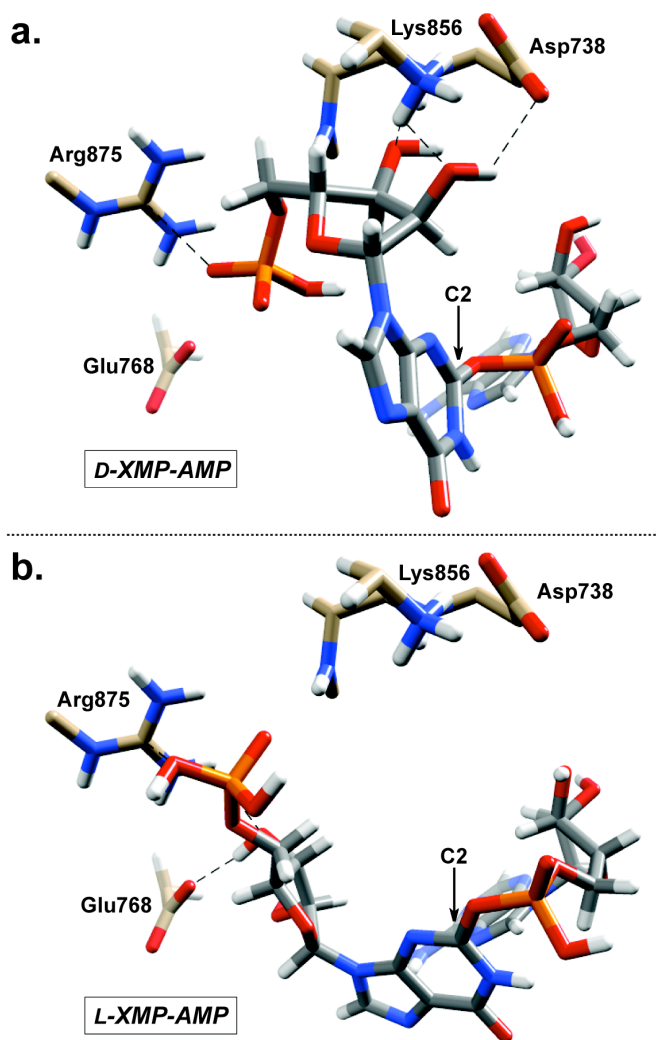


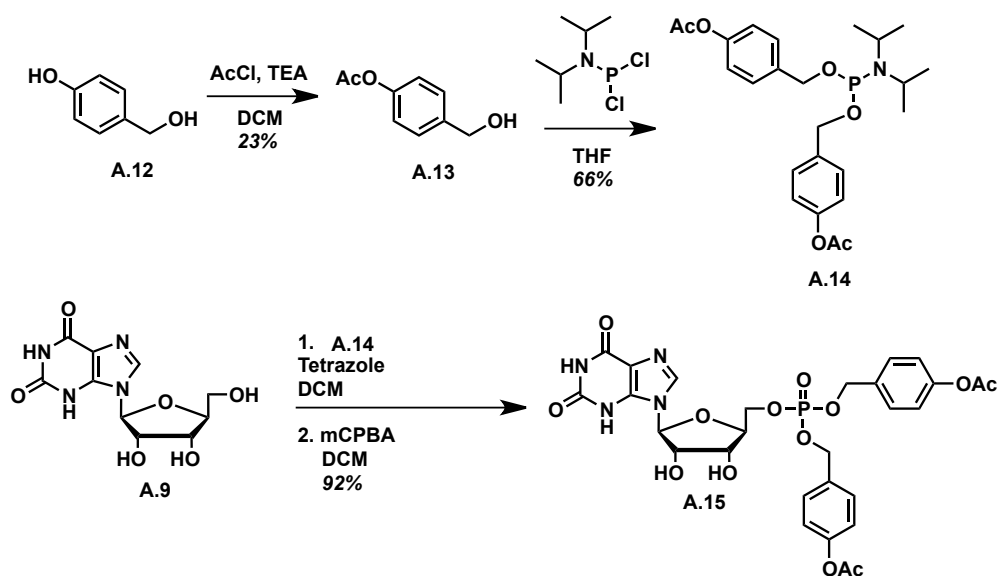
Figure A.5. Docking of (a) adenylyl-D-XMP and (b) adenylyl-L-XMP intermediates into the *E. coli* GMPS synthetase binding pocket. Key hydrogen-bonding interactions between the adenylylated ligands and GMPS are marked with dashed lines. The 2-position of the xanthine nucleobase is marked (2.0 Å conformational shift).

Lys856 and the xanthine nucleobase; Arg785, Arg765, and Glu768 to ribose alcohols; and Asn761 to the phosphate of D-XMP (**Figure A.5a**). The considerable size of the GMPS synthetase pocket readily accommodated the docking of adenylyl-L-XMP; however, the L-ribose sugar occupied a substantially different position within the synthetase domain (**Figure A.5b**). No longer present were many of the key molecular interactions between the nucleobase and ribose alcohols as evident by a decreased in consensus score, which is an estimate of the overall ligand binding affinity (CScore = 7.68 for D-XMP versus 6.16 for L-XMP). One compensating molecular interaction was observed for adenylyl-L-XMP, which was a hydrogen bond between Asn761 to a ribose alcohol. The conformation of the L-ribose sugar in adenylyl-L-XMP also forces C^2 of the nucleobase to be positioned approximately 2.0 Å away from the region in space occupied by natural adenylyl-D-XMP ligand. This perturbation to nucleobase conformation may deter aminolysis of the adenylylated unnatural monophosphate, thereby slowing enzyme turnover. Additionally, the loss of key hydrogen-bonding interactions may also contribute to the loss in enzyme efficiency. Nonetheless, our observation of the synthesis of L-GMP from L-XMP implies the large size of the synthetase pocket must allow some movement of adenylyl-L-XMP to obtain the correct conformation for amination.

A.6 Anti-malarial Activity of L-XMP Analogues

Inhibitors of enzymes that catalyze *de novo* nucleotide biosynthesis can be effective drugs against cancer, inflammatory disorders, and infections, especially if the

target is dependent on the pathway.³⁴¹ All parasitic protozoa rely on salvage of nucleic acids for cell division because of the limited access to purines and therefore, are sensitive to imbalances in dNTP pools, with depletion of one dNTP halting DNA synthesis altogether.^{319,342} Hence, drugs that deplete intracellular dNTPs have the potential to starve parasites of necessary reagents for cell division. For example, parasitic growth is inhibited in *Plasmodium falciparum* by degradation of exogenous hypoxanthine.³⁴³ Since a crucial step in the *de novo* synthesis 2'-deoxyguanosine triphosphates (dGTP) is the *de novo* synthesis of guanosine monophosphate by GMPS, the inhibition of GMPS is hypothesized to confer to antiparasitic activity.³⁴⁴ Since the pharmacokinetics of phosphate compounds are generally poor, we synthesized a prodrug of **A.10** that masked the negative charges on the phosphates and would hydrolyze to yield **A.10** within cells (**Scheme A.3**). 4-Hydroxyl benzyl alcohol **A.12** was acetylated to yield the intermediate **A.13**, which was reacted with diisopropylphosphoramidous dichloride to afford the 4-



Scheme A.3. Synthesis of L-XMP prodrug **A.15**.

acetoxyl benzyl phosphoramidite **A.14**. L-Xanosine **A.9** was reacted with the phosphoramidite **A.14** and oxidized to the phosphate to yield the L-XMP prodrug **A.15**.

Because *P. falciparum* is the parasite that causes malaria in humans, we sent **A.9**, **A.10**, and the prodrug **A.15** to the Swiss Tropical and Public Health Institute for antimalarial testing. Both L-Xanosine **A.9** and L-XMP **A.10** did not demonstrate any antimalarial activity (greater than 10000 nM) compared to the 3.9 and 9.2 nM activity of the known antimalarial drugs Artesunate and Chloroquine (**Table A.3**). The L-XMP prodrug **A.15**, however, exhibited weak antimalarial activity ($IC_{50} = 6.3 \mu\text{M}$), which could be overall toxicity due to release of the quinone methide from the masked phosphate. We concluded that although antimalarial activity was observed, it is unclear if it was due to modulation of dNTP levels.

Table A.3. Antimalarial data of known inhibitors and xanthosine analogues.	
Inhibitor	IC_{50} (nM)
Artesunate	3.9
Chloroquine	9.2
A.9	> 10000
A.10	> 10000
A.15	6324

A.7 Conclusions and Future Work

In conclusion, the biochemical conversion of L-GMP from L-XMP provides new insight into the substrate promiscuity of GMPS. GMPS was also inhibited

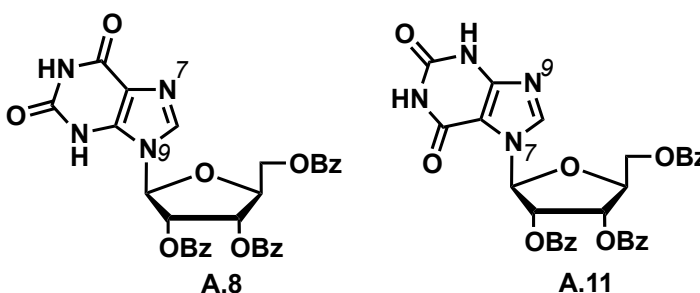
by L-XMP at low micromolar levels, which is comparable to other known inhibitors. This inhibition lead to a low micromolar antimalarial activity against *Plasmodium falciparum* strain NF54. These results provide new insight into GMPS-ligand interactions that will be useful for future inhibitor designs.

A.8 Experimental Section

A.8.1 Chemical Synthesis.

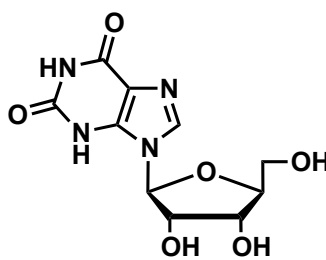
General. Chemical reagents were typically from Sigma-Aldrich or Acros and used without additional purification unless explicitly noted. Triethylammonium acetate (TEAA, 1 M aq. solution) and triethylammonium bicarbonate (TEAB, 1 M aq. solution) buffers were from Sigma-Aldrich. Bulk solvents were from Fisher Scientific and anhydrous 1,2-dichloroethane was purchased from Sigma-Aldrich. Buffers for HPLC purification and analysis were prepared and diluted with distilled and deionized H₂O (ddH₂O) and the pH was adjusted with HCl (1 N aq. soln). Reactions were performed under an atmosphere of dry N₂ unless otherwise noted. Silica gel chromatography was performed on a Teledyne-Isco Combiflash Rf-200 instrument utilizing Redisep Rf Gold High Performance silica gel columns (Teledyne-Isco) or self-packed columns with SiliaFlash 60Å silica gel (SiliCycle). Analytical HPLC analysis and semi-preparative HPLC purifications were performed on an Agilent 1200 series instrument equipped with a diode array detector and a Zorbax SB-AQ column (4.6 x 150 mm, 3.5 µm, Agilent Technologies) for analytical-scale analysis or a Zorbax SB-AQ column (9.4 x 250 mm, 5

μm , Agilent Technologies) for semi-preparative purification. Nuclear magnetic resonance (NMR) spectroscopy employed a Bruker AvanceII+ instrument operating at 400 MHz (for ^1H), 100 MHz (for ^{13}C), or 161 MHz (for ^{31}P) at ambient temperature. Chemical shifts are reported in parts per million and normalized to internal solvent peaks or tetramethylsilane. High-resolution mass spectrometry (HRMS) was recorded in either positive-ion or negative-ion mode on a Bruker BioTOF II instrument. (see Appendix B for chromatograms).



9-(2',3',5'-tri-*O*-benzoyl- β -L-ribo-furanosyl)xanthine (A.8) and 7-(2',3',5'-tri-*O*-benzoyl- β -L-ribofuranosyl)xanthine (A.11). Vorbrüggen coupling conditions were used to prepare protected nucleosides **A.8** and **A.11**.³³¹ In brief, a solution of 1-*O*-acetyl-2,3,5-tri-*O*-benzoyl- β -L-ribofuranose^{341,343} (**A.6**, 150.0 mg, 0.30 mmol) and tris(trimethylsilyl)xanthine³⁴⁴ (**A.7**, 243.3 mg, 0.66 mmol) in anhydrous 1,2-dichloroethane (5 mL) was treated with TMSOTf (65 μL , 0.36 mmol) and heated to reflux for 1 h. The mixture was then diluted with dichloromethane (10 mL), washed with aqueous NaHCO_3 (sat'd, 20 mL), and the aqueous layer was extracted with additional dichloromethane (10 mL, 3x). The combined organic layers were dried over Na_2SO_4 , concentrated *in vacuo*, and SiO_2 purified (gradient 50 to 80% acetone in hexanes) to give

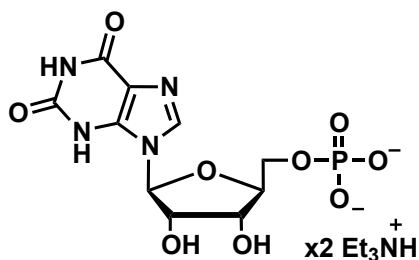
A.8 (124.0 mg, 70%) and **A.11** (37.5 mg, 21%) as white foams. **9-(2', 3', 5'-tri-*O*-benzoyl- β -L-ribofuranosyl)-xanthine (A.8).** ^1H NMR (MeOH- d_4): δ 7.96-7.94 (m, 2H), 7.90-7.88 (m, 2H), 7.85-7.81 (m, 3H), 7.53-7.45 (m, 3H), 7.39-7.25 (m, 6H), 6.31 (d, J = 5.3 Hz, 1H), 6.03 (t, J = 5.5 Hz, 1H), 5.94-5.91 (m, 1H), 4.79-4.73 (m, 2H), 4.64 (dd, J = 11.9, 4.1 Hz, 1H); ^{13}C NMR (MeOH- d_4): δ 176.5, 167.6, 166.8, 166.7, 160.5, 154.6, 145.1, 135.6, 135.2, 135.0, 134.8, 131.0, 130.82, 130.76, 130.2, 129.9, 129.8, 117.3, 87.5, 82.0, 75.8, 72.7, 64.8; HRMS (ESI $^+$) calc'd for $\text{C}_{31}\text{H}_{24}\text{N}_4\text{NaO}_9$ [$\text{M}+\text{Na}$] $^+$, 619.1441; found 619.1448. **7-(2',3',5'-tri-*O*-benzoyl- β -L-ribofuranosyl)-xanthine (A.11)** ^1H NMR (MeOH- d_4): δ 8.13 (s, 1H), 8.00-7.92 (m, 2H), 7.90-7.85 (m, 2H), 7.83-7.80 (dd, J = 9.9, 2.7 Hz, 2H), 7.51-7.46 (m, 3H), 7.38-7.24 (m, 6H), 6.47 (d, J = 4.9 Hz, 1H), 6.15-6.07 (m, 1H), 6.01-5.98 (m, 1H), 4.77-4.71 (m, 2H), 4.72-4.64 (m, 1H); ^{13}C NMR (MeOH- d_4): δ 167.7, 166.8, 166.6, 157.0, 153.4, 152.2, 143.7, 135.0, 134.9, 134.6, 131.0, 130.92, 130.85, 130.7, 130.3, 130.1, 129.8, 129.7, 129.6, 108.0, 90.8, 81.5, 76.4, 72.6, 65.1; HRMS (ESI $^+$) calc'd for $\text{C}_{31}\text{H}_{24}\text{N}_4\text{NaO}_9$ [$\text{M}+\text{Na}$], 619.1441; found 619.1427.



A.9

L-xanthosine (L-Xao, A.9). Protected L-xanthosine **A.8** (102.0 mg, 0.17 mmol) was dissolved in ammonia in methanol (~7 N, 5 mL) in a sealed tube and heated to 50 $^{\circ}\text{C}$

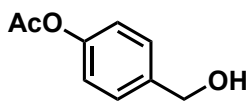
overnight. The reaction was cooled to RT, concentrated *in vacuo*, and SiO₂ purified (33% MeOH in CH₂Cl₂) to afford **A.9** (45.1 mg, 93%) as a white solid. ¹H NMR (DMSO-*d*₆): δ 11.74 (br s, 1H), 10.88 (br s, 1H), 7.88 (s, 1H), 5.75 (d, *J* = 6.9 Hz, 1H), 5.41 (br s, 3H), 4.22 (dd, *J* = 6.8, 5.1 Hz, 1H), 4.06 (dd, *J* = 5.0, 2.1 Hz, 1H), 4.03 – 3.98 (m, 1H), 3.66 (d, *J* = 2.5 Hz, 2H); ¹³C NMR (DMSO-*d*₆): δ 157.9, 150.5, 139.4, 135.7, 116.2, 88.7, 86.1, 74.0, 70.9, 61.3; HRMS (ESI⁺) calc'd for C₁₀H₁₂N₄NaO₆ [M+Na]⁺, 307.0655; found 307.0651.



A.10

L-Xanthosine-5'-monophosphate triethylammonium salt (L-XMP, A.10). This compound was prepared by a modification to the previously reported synthesis of D-Xanthosine-5'-monophosphate (D-XMP).³³³ To a partially dissolved solution of L-xanthosine (**A.9**, 62.5 mg, 0.22 mmol) in trimethyl phosphate (2.2 mL) was added proton-sponge (83.0 mg, 0.39 mmol). The solution was cooled to 2 °C and POCl₃ (50 μL, 0.54 mmol) was added dropwise. After stirring at 2 °C for 2 h, triethylammonium bicarbonate (TEAB, 1.0 M, 5 mL) was added and the crude material was concentrated *in vacuo*. The crude monophosphate was purified by stepwise semi-preparative HPLC. The HPLC purification method (flow rate = 4.5 mL/min) involved isocratic triethylammonium acetate buffer (TEAA, 20 mM, pH = 6, 0 to 5 min), followed by linear

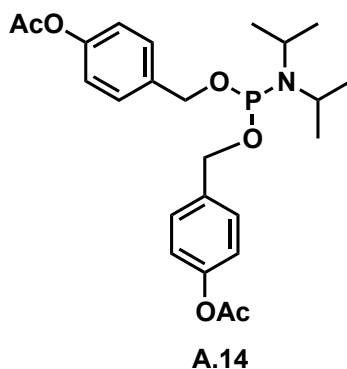
gradients of 0% to 15% CH₃CN in TEAA buffer (5 to 15 min) and 15% to 90% CH₃CN in TEAA buffer (15 to 20 min). The material eluting broadly from 7-10 minutes was collected and lyophilized to dryness. The crude material was purified an additional time by the semi-preparative HPLC utilizing this method and the material eluting broadly from 6-9.5 minutes was collected and lyophilized to dryness. The residual material was re-dissolved in ddH₂O (10 mL), frozen, and then lyophilized to dryness to give L-XMP (55.3 mg, 19%) as a white syrup. By ¹H NMR analysis, approximately 10 equivalents of TEA salt were associated with each equivalent of L-XMP. ¹H NMR (D₂O): δ 7.89 (s, 1H), 5.87 (d, *J* = 6.4 Hz, 1H), 4.46 – 4.38 (m, 1H), 4.26 (d, *J* = 2.9 Hz, 1H), 3.90 (dd, *J* = 13.0, 2.7 Hz, 1H), 3.81 (dd, *J* = 12.9, 3.4 Hz, 1H), 3.16 (q, *J* = 7.3 Hz, 12H), 1.27 (t, *J* = 7.3 Hz, 18H); ¹³C NMR (D₂O): δ 160.4, 156.4, 148.1, 136.1, 115.1, 86.9, 84.3, 74.3, 70.5, 64.4, 46.6, 22.9, 8.2; ³¹P NMR (D₂O): δ 0.48. HRMS (ESI⁻) calc'd for C₁₀H₁₂N₄O₉P [M-H]⁻, 363.0347; found 363.0343. The regiochemistry of phosphorylation was additionally verified by analytical HPLC analysis of a co-injection of L-XMP and commercial D-XMP. A singly eluting peak was observed (data not shown).



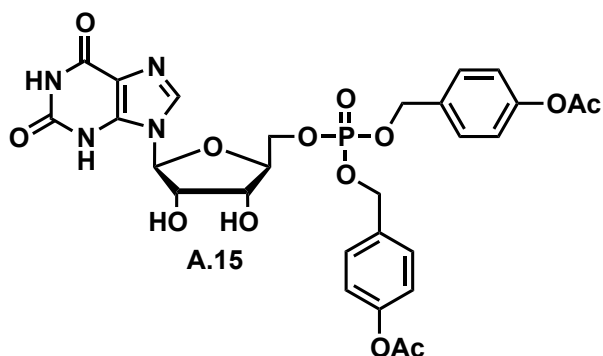
A.13

Acetoxybenzyl alcohol (A.13). Acetylchloride (1.95 mL, 25.0 mmol) was added dropwise to a solution of 4-hydroxybenzyl alcohol **A.12** (3.10 g, 25.0 mmol) and TEA (3.50 mL, 25.0 mmol) in DCM (100 mL) at 0 °C and stirred for 24 hours. The solution

was extracted with saturated sodium bicarbonate (100 mL) and DCM (100 mL), concentrated *in vacuo*, and SiO₂ purified (gradient of 0-10% methanol in DCM) to afford **A.13** as an oil (960 mg, 23%). ¹H NMR (CDCl₃): δ = 7.35 (d, 2H, *J* = 6.76 Hz), 7.06 (d, 2H, *J* = 6.84 Hz), 4.64 (s, 2H), 2.29 (s, 3H); ¹³C NMR (CDCl₃): δ = 169.7, 150.0, 138.6, 128.1, 121.6, 64.6, 21.1; HRMS-ESI⁺ m/z [M+Na]⁺ calc'd for C₉H₁₀O₃Na⁺: 189.0522, found: 189.0618.



1,1-Diacetoxybenzylalcohol-*N,N*-diisopropylphosphinamine (A.14). A mixture of **A.13** (71 mg, 0.43 mmol) and TEA (0.07 mL, 0.49 mmol) in THF (1.0 mL) was added dropwise to diisopropylphosphoramidous dichloride (0.04 mL, 0.21 mmol) in THF (1.0 mL) at -80 °C. The reaction was warmed to RT, concentrated *in vacuo*, and SiO₂ purified (gradient of 0-70% ethyl acetate in hexanes) to afford **A.14** as an oil (92 mg, 66%). ¹H NMR (CDCl₃): δ = 7.28 (d, 4H, *J* = 8.08 Hz), 6.97 (d, 4H, *J* = 8.12 Hz), 3.42 (s, 4H), 2.23 (s, 6H), 1.97 (s, 2H), 1.14 (s, 6H), 1.12 (s, 6H); ¹³C NMR (CDCl₃): δ = 128.6, 128.0, 121.6, 121.3, 67.98, 45.8, 25.6, 22.6, 21.1; ³¹P NMR (CDCl₃): δ = 147.94 (s, 1P); HRMS-ESI⁻ m/z [M-2H]²⁻ calc'd for C₂₄H₃₀NO₆P²⁻: 229.5911, found: 229.0383.



L-Xanthosine-5'-1,1-Diacetoxybenzylalcohol monophosphate (A.15).

Phosphoramidite **A.14** (13 mg, 0.03 mmol) was added to a solution of L-xanthosine **A.9** (8.0 mg, 0.03 mmol) in DCM (5 mL) and molecular sieves. Tetrazole (0.27 mL, 0.47 M in acetonitrile) was added and it was stirred at room temperature for 24 hours. The reaction was poured into brine (10 mL), extracted with DCM (10 mL), and concentrated *in vacuo*. The crude phosphine was immediately dissolved in DCM (5 mL) and mCPBA (14 mg, 0.06 mmol) was added and stirred at room temperature for 24 hours. The reaction was poured into H₂O:NaHCO₃ (10 mL, 1:1), extracted with DCM (10 mL), and SiO₂ purified (gradient of 0-40% ethyl acetate in hexanes) to afford **A.15** as a white solid (17 mg, 92%). ¹H NMR (CDCl₃): δ = 7.76 (s, 1H), 7.30 (d, 4H, *J* = 10.1 Hz), 7.05 (d, 4H, *J* = 10.2 Hz), 5.77 (d, 1H), 5.13-5.00 (m, 2H), 4.05 (m, 1H), 3.69 (m, 1H), 3.56 (m, 1H), 3.42 (s, 4H), 2.10 (s, 6H); ¹³C NMR (CDCl₃): δ = 151.0, 150.3, 149.7, 136.2, 130.1, 129.2, 128.7, 123.8, 121.9, 121.6, 100.0, 99.5, 87.2, 66.7, 47.5, 30.8, 21.0; ³¹P NMR (CDCl₃): δ = 8.46; HRMS-ESI⁻ *m/z* [M-H]⁻ calc'd for C₂₈H₂₉N₄O₁₃P⁻: 659.1396, found: 659.1410.

A.8.2 Sequencing of *E. coli* GMP Synthetase. The pET28a plasmid bearing the *E. coli* GuaA gene with a hexahistidine tag on the 5' end was a generous gift from Professor

Janet Smith (University of Michigan).^{327,328} To verify that we purified a plasmid containing the *guaA* gene, we utilized two forward sequencing primers – 5'-GGAAAACATTCATAAGC-3' and 5'-CGTATTCGTCGACAACG-3' for automated sequencing at the University of Minnesota Biomedical Genomics Center. Sequencing results from each primer were aligned with the *E. coli* K12 genome using BLASTn. Positive alignment along with manually overlapping the two sequences yielded a large portion of the *guaA* sequence containing one silent mutation at proline 404 (CCG → CCA). The overlapping sequence was assembled and aligned against the nonredundant protein database using BLASTx, confirming that the sequence derived from the plasmid indeed codes for *E. coli* GMPS.

A.8.3 Overexpression and Purification of *E. coli* GMP Synthetase. Two x 10 mL LB-Kanamycin (LB-Kan, 50 µg/mL Kan) media was inoculated with single colonies from freshly transformed BL21 (DE3) *E. coli*. After overnight incubation at 37 °C with shaking at 250 rpm, these cultures were used to inoculate 2 x 1 L LB-Kan cultures. Protein expression was induced when the OD₆₀₀ of the culture reached 1.2 via the addition of 1 mM IPTG. Cultures were incubated overnight at 37 °C with shaking at 250 rpm. Cells were recovered via centrifugation at 7500 x g for 15 minutes at 4 °C. The cell pellets (~4 g each) were frozen in a dry ice/EtOH bath, then thawed and resuspended in 10 mL buffer A (0.25 M KCl, 10 mM KH₂PO₄, 10 mM imidazole, 1 mM DTT, pH 7.4) with 1 mg/mL lysozyme and a protease inhibitor tablet (Roche). The cell suspension was incubated for 30 minutes at room temperature with shaking. The cell paste was then

sonicated (VibraCell VCX-750 sonicator with temperature probe, Sonics and Materials, Inc.) for 12 pulses of 15 s with a 45 s rest period between pulses, taking care to keep the temperature of the lysate from exceeding 20 °C. Cell debris was removed via centrifugation at 40,000 x g for 45 min at 4 °C. The supernatants from both cultures were combined at this point and directly loaded onto a Ni-NTA column, washed with 200 mL of buffer A, then eluted with buffer B (0.25 M KCl, 10 mM KH₂PO₄, 150 mM Imidazole, 1 mM DTT, pH 7.4). An Econo gradient pump and fraction collector (Bio-Rad) was used for chromatography. Fractions with measurable A₂₈₀ and an A₂₈₀/A₂₆₀ ratio of >1.4 were pooled, concentrated to ~10 mg/mL, and stored as a 25% glycerol stock at -80 °C. Typical yields of ~50 mg protein/L of culture were obtained. Protein purities were >95% as evidenced by gel electrophoresis (**Figure A.6**).

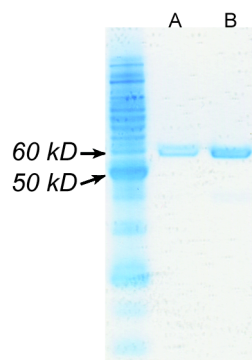


Figure A.6. Purified GMPS. (a) Ni-NTA purified. (b) Mono-Q purified.

A.8.4 UV-Vis Spectrophotometric Assay for GMPS Enzymatic Activity. GMPS enzymatic activity was measured spectrophotometrically utilizing a previously reported assay.³³⁸ In brief, this assay monitors a reduction in 290 nm absorbance resulting from conversion of XMP ($\epsilon = 4800 \text{ M}^{-1} \text{ cm}^{-1}$) to GMP ($\epsilon = 3300 \text{ M}^{-1} \text{ cm}^{-1}$) by the enzyme. A $\Delta\epsilon$

value of $1500 \text{ M}^{-1} \text{ cm}^{-1}$ was used to calculate the amount of GMP formed. Aqueous solutions (800 μL) of XMP (1, 2, 4, 8, 11, 17, and 27 μM) and GMPS (0.65 μM for D-XMP or 6.5 μM for L-XMP) were diluted into ddH₂O and pre-incubated in microcentrifuge tubes for two hours. The pre-incubated solutions were transferred to quartz cuvettes and incubated for 3 min at 37 °C in a heat block. 200 μL of an aqueous solution of Tris/HCl (75 mM, pH 8.5), ATP (1.25 mM), (NH₄)₂SO₄ (60 mM), and MgSO₄ (10 mM) was added to the pre-incubated solution of XMP and GMPS. The cuvettes were mixed, and ΔA_{290} was recorded at 37 °C using a temperature-controlled Agilent Cary 100 UV-Vis spectrophotometer. GMP production as a function of time was measured at a variety of substrate (XMP) concentrations. These discrete initial velocity values ($\mu\text{M}/\text{min}$) were obtained by plotting a tangential line to the first (approximately) 15% of data points, followed by dividing the slope of the resulting line to the difference in molar extinction coefficient between XMP and GMP ($\Delta\epsilon$ value of $1500 \text{ M}^{-1}\text{cm}^{-1}$ at 290 nm). This series of experiments yielded initial velocity values of GMP production at a variety of XMP concentrations. The measured initial velocity values of different XMP concentrations were fitted to the Michaelis-Menten equation (eq. 1) and analyzed by non-linear regression using the software GraphPad Prism 5 to determine the K_m and V_{max} . Each experiment was performed in triplicate and mean K_m and V_{max} values (with standard deviation) were calculated.

(Equation 1) $v = V_{max}[S]/(K_m + [S])$

A.8.5 Substrate Competition Experiments with GMPS. The inhibition constants were measured utilizing the above spectrophotometric assay. Previous studies with nucleoside inhibitors of GMPS have demonstrated progressive-type inhibition, therefore, pre-incubation of D-XMP, inhibitor, and GMPS was required before addition of the amine source.^{321,345} Two known GMPS inhibitors (decoyinine (Santa Cruz Biotechnology) and Mizoribine (Sigma-Aldrich)) were used in this assay. In brief, aqueous solutions (800 μ L) of D-XMP (1, 2, 4, 8, 11, 17, and 27 μ M), GMPS (0.65 μ M), and inhibitor (constant concentrations, shown below) were diluted into ddH₂O and pre-incubated in microcentrifuge tubes for two hours. The pre-incubated solutions were transferred to quartz cuvettes and incubated for 3 min at 37 °C in a heat block. 200 μ L of an aqueous solution of Tris/HCl (75 mM, pH 8.5), ATP (1.25 mM), (NH₄)₂SO₄ (60 mM), and MgSO₄ (10 mM) was added to the pre-incubated solution of XMP, GMPS, and inhibitor. The cuvettes were mixed, and ΔA_{290} was recorded at 37 °C as described above. The measured initial velocity values of different D-XMP concentrations were fitted to the uncompetitive Michaelis-Menten equation for decoyinine³²¹ (eq. 2) or competitive Michaelis-Menten equation for all other inhibitors (eq. 3) and analyzed by non-linear regression to determine the K_i . Each experiment was performed in triplicate and mean K_i values (with standard deviation) were calculated.

$$\text{(Equation 2)} \quad v = V_{\max}[\text{S}]/(K_{m,app} + [\text{S}]) \quad K_{m,app} = K_m/(1+[\text{I}]/\alpha K_i);$$

$$V_{\max,app} = V_{\max}/(1+[\text{I}]/\alpha K_i)$$

(Equation 3) $v = V_{\max}[S]/(K_{m,app} + [S])$ $K_{m,app} = K_m/(1+[I]/\alpha Ki)$

A.8.6 HPLC Assay for GMPS Enzymatic Activity. GMPS enzymatic activity was also measured by quantifying the amount of aminated products (D-GMP or L-GMP) formed from reaction of D-XMP or L-XMP with GMPS by analytical HPLC analysis. Modifying a previously reported HPLC assay of enzymatic activities,³⁴⁶ the enzymatic reactions were carried out in microcentrifuge tubes and contained aqueous solutions with the following components (final volume of 500 μ L): Tris/HCl (75 mM, pH 8.5), ATP (1.25 mM), $(\text{NH}_4)_2\text{SO}_4$ (60 mM), and MgSO_4 (10 mM), myokinase (5 IU/mL, Sigma-Aldrich) and varying concentrations of XMP. The solutions were incubated for 3 min at 37 $^{\circ}$ C to permit myokinase to convert all the ADP (present in commercial preparations of ATP) to ATP. The concentration of ATP remains constant throughout the reaction. Reactions were initiated by the addition of GMPS (0.65 μ M for D-XMP as ligand or 6.5 μ M for L-XMP as ligand), the tubes were gently mixed, and the reaction was allowed to proceed at 37 $^{\circ}$ C. At different time points, 500 μ L of a solution of cytosine 5'-monophosphate (CMP, 1.6 mM, external standard, Sigma-Aldrich) and EDTA (100 mM) was added to stop the reaction. The final mixtures were filtered through a Millipore centrifugal filter (Amicon Ultra – 0.5 mL, 30 kDa molecular weight cutoff) to remove proteins and triplicate injections of 40 μ L of filtrate were then analyzed by HPLC.

An Agilent 1200 series instrument equipped with a diode array detector and a Zorbax SB-AQ column (4.6 x 150 mm, 3.5 μ m, Agilent Technologies) at 22 $^{\circ}$ C was used

for analysis. The mobile phase comprised aqueous triethylammonium acetate buffer (TEAA, 20 mM, pH = 6, 0 to 5 min), followed by 0 to 50% CH₃CN in TEAA buffer (5 to 15 min) at a flow-rate 1.0 mL/min. A representative HPLC chromatogram is shown in **Figure A.1a**. The formation of L-GMP (LRMS (ESI⁻) calcd for C₁₀H₁₂N₄O₉P [M-H]⁻, 362.05; found 362.09) was verified by mass spectral analysis (Figure S2). CMP was used as an external standard in this assay (see above), and a linear plot of GMP/CMP absorbance (measured by area integration of respective peaks at 260 nm) versus [GMP, mM] was created (yielding a slope-intercept equation, R² > 0.99). The concentration of GMP formed from the test samples was determined by fitting the individual GMP/CMP ratios from each sample into the slope-intercept equation from the calibration plot. GMP production as a function of time was measured at a variety of substrate (XMP) concentrations. This series of experiments yielded initial velocity values of GMP production at a variety of XMP concentrations. Three sets of initial velocity experiments were acquired for each XMP concentration tested. The measured initial velocities values of different XMP concentrations were fitted to the Michaelis-Menten equation (eq. 1) and analyzed by non-linear regression using the software GraphPad Prism 5 to determine the K_m and V_{max} .

A.8.7 Docking Studies of L-XMP into GMPS Active Site. Energy minimized three-dimensional conformations were generated for each compound using the Minimize Molecule function of the SYBYL 8.0 discovery software suite (Tripos, Inc.) with Gasteiger-Marsili charges. The three dimensional compounds were docked into GMPS

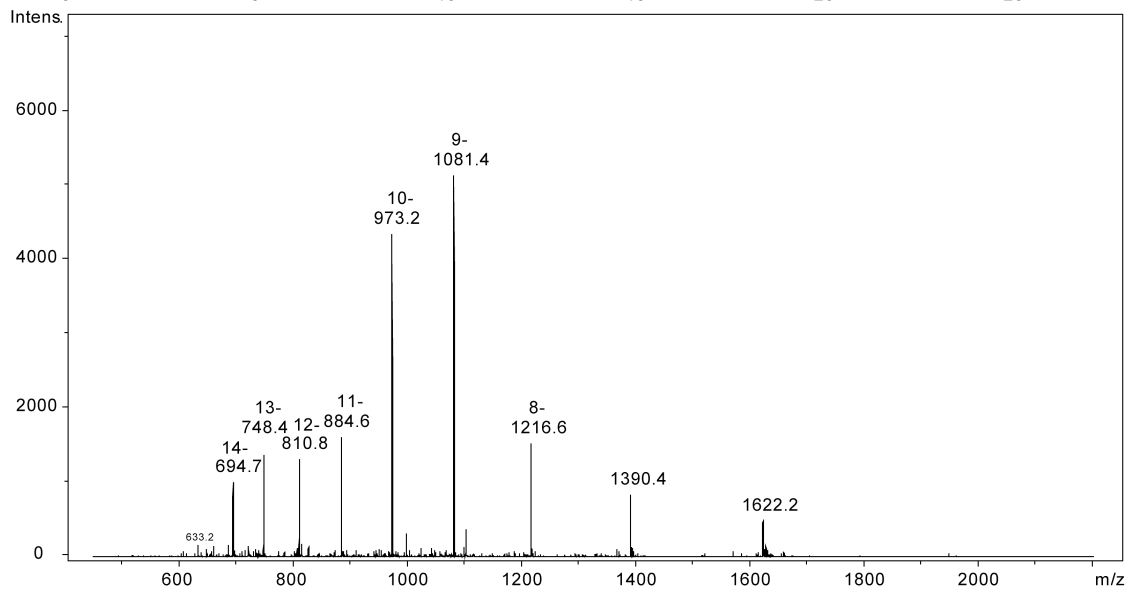
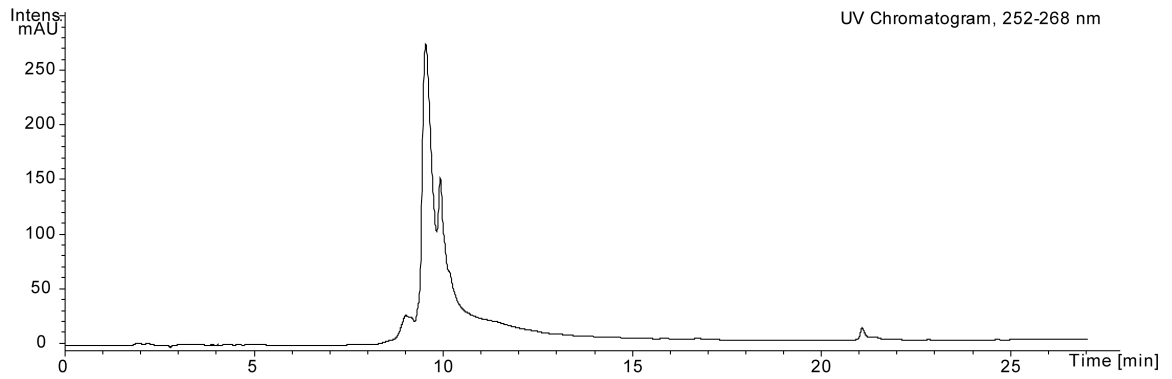
(PDB: 1GPM)³²⁸ using Surflex-Dock function in the SYBYL software suite. In Surflex-Dock, the cocrystallized AMP ligand was used to guide the protomol generation required for docking. Docking accuracy was verified by extracting the bound ligand AMP (blue) from X-ray crystal structure and re-docking it into the GMPS binding pocket, which yielded a calculated similarity of 0.908 to the bound ligand (1.0 being identical structures)(**Figure A.4b**). Parameters of 0.3 and 2 were used for docking threshold and bloat, respectively. The maximum number of conformations per compound fragment and the maximum number of poses per ligand were both set to their default values of 20, and the maximum number of rotatable bonds per molecule was set to 100. All calculations were done on Minnesota Supercomputing Institute (MSI) workstations running under the Suse Linux Enterprise Desktop 10.2 operating system. Visualizations were rendered using UCSF Chimera.³⁴⁷

Appendix B

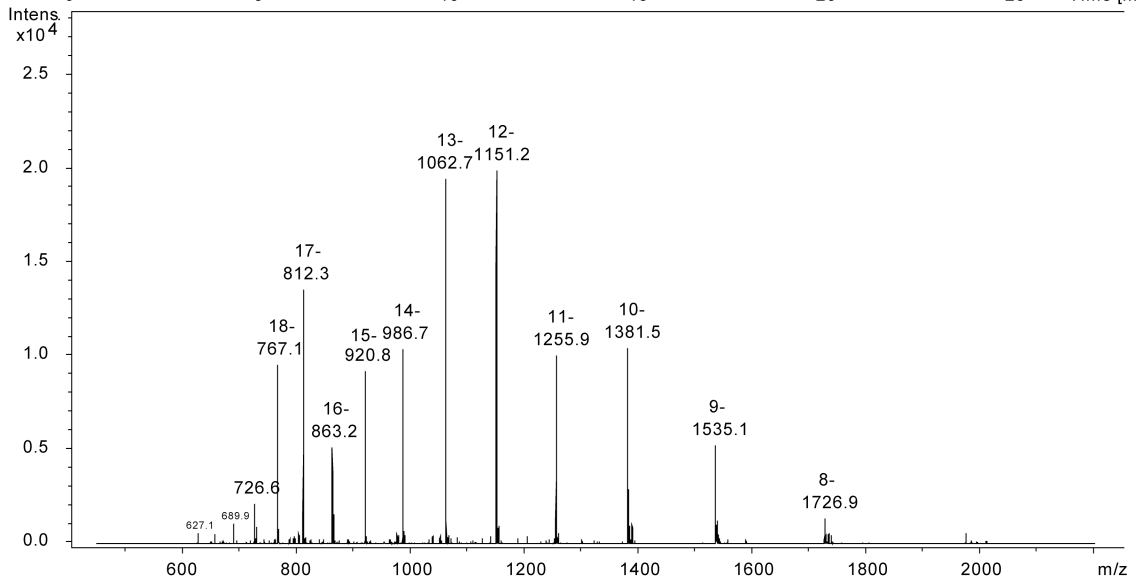
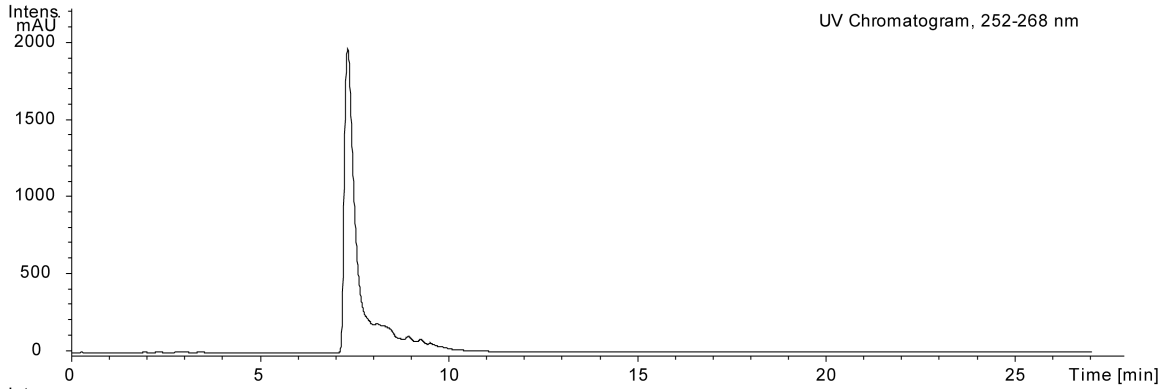
SPECTRAL DATA FOR SYNTHESIZED COMPOUNDS

B.1 Chapter 2 Compounds

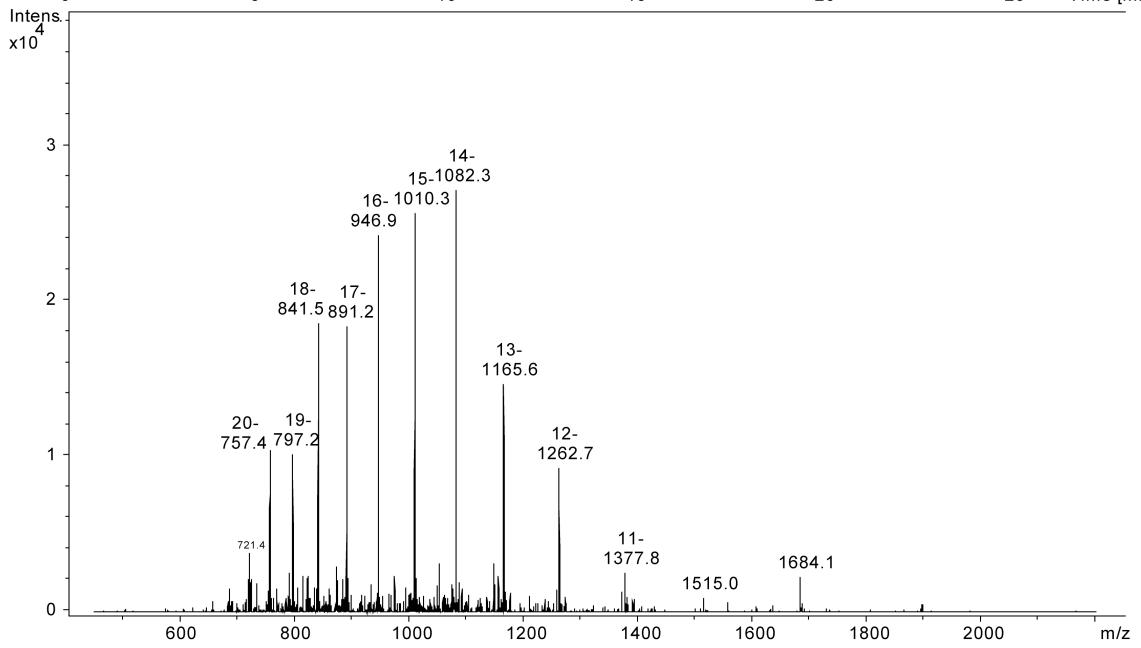
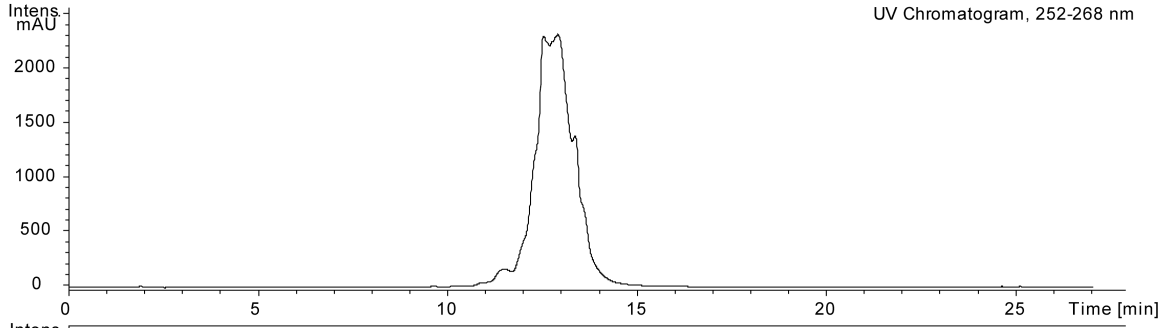
5'-TGGGGACTTTCAGTTTCTGGAAAGTCCCCA-3' (2.1)
m/z calc'd (Parent): 9741.1
m/z found (Parent): 9741.6



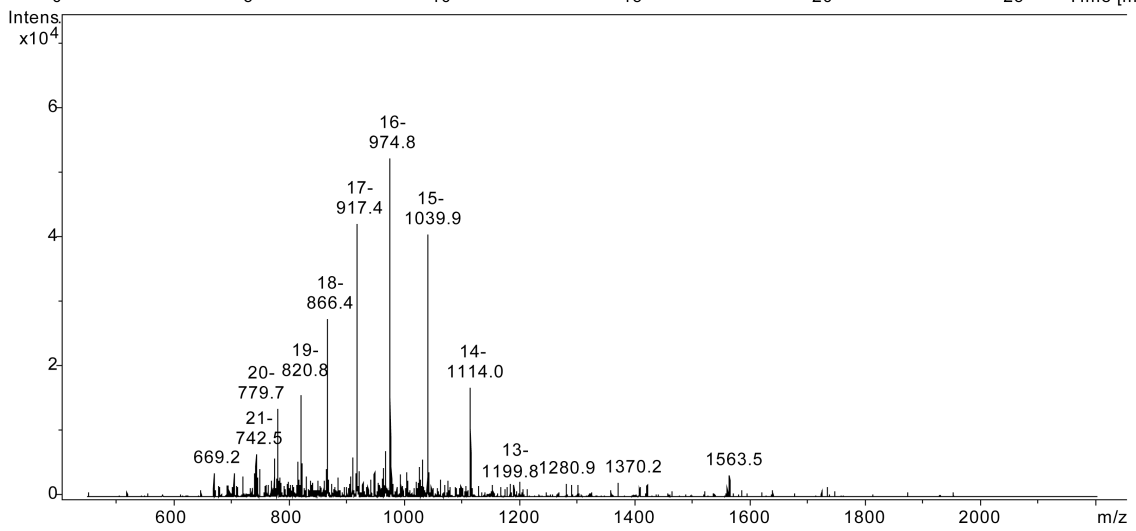
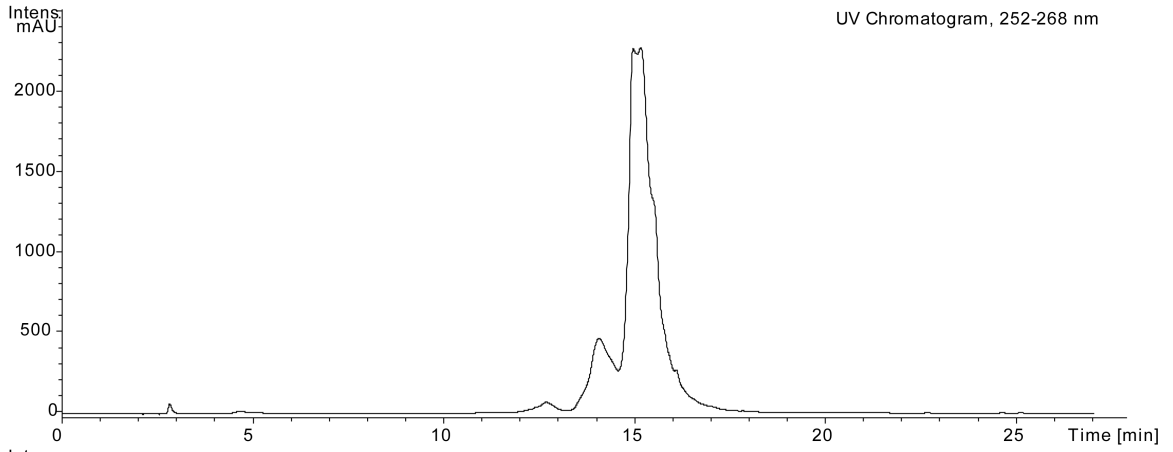
5'-TGCAGAACAGCAAGTGCTAGCTTTGCTAGCACTTGCTGTTCTGCA-3' (2.2)
m/z calc'd (Parent): 13827.0
m/z found (Parent): 13827.8



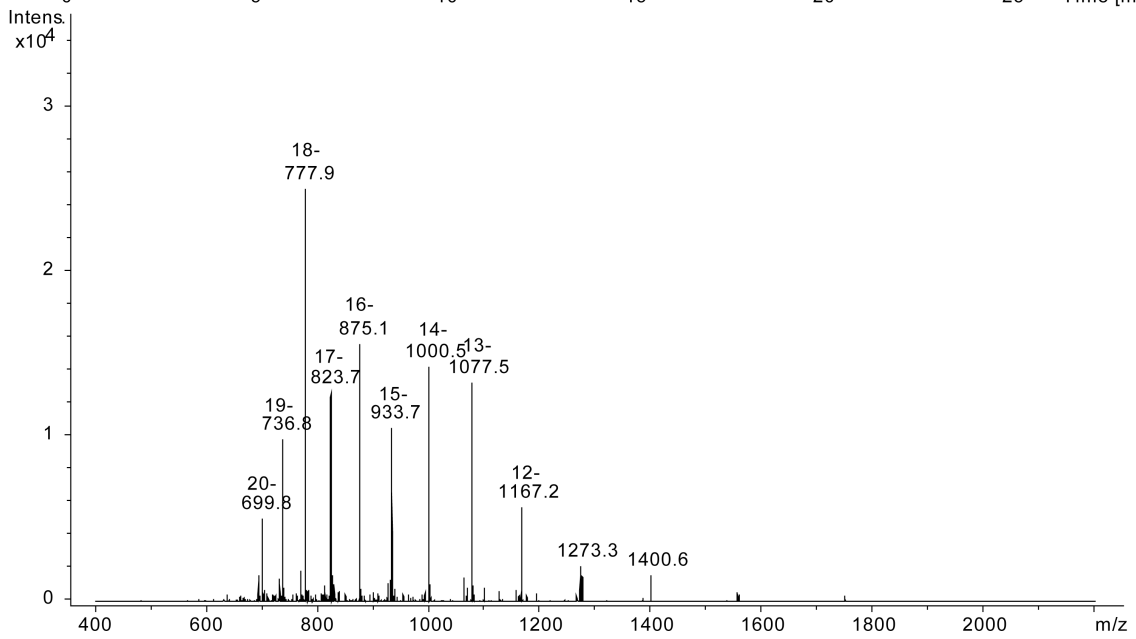
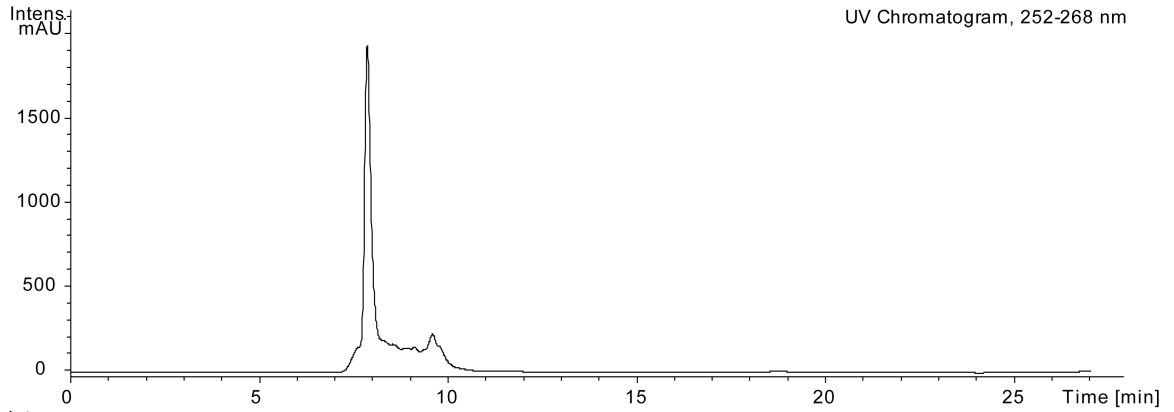
5'-XGCAGAACAGCAAGXGCTAGCTTTGCXAGCACXTGCXGTTXGCA-3' (2.3)
m/z calc'd (Parent): 13827.0
m/z found (Parent): 13827.8



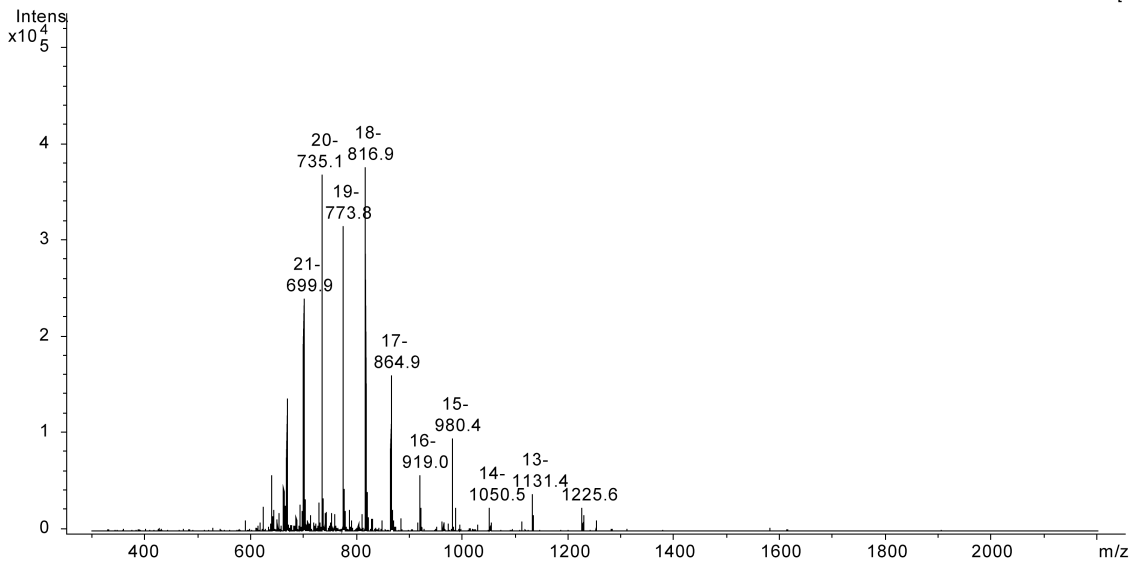
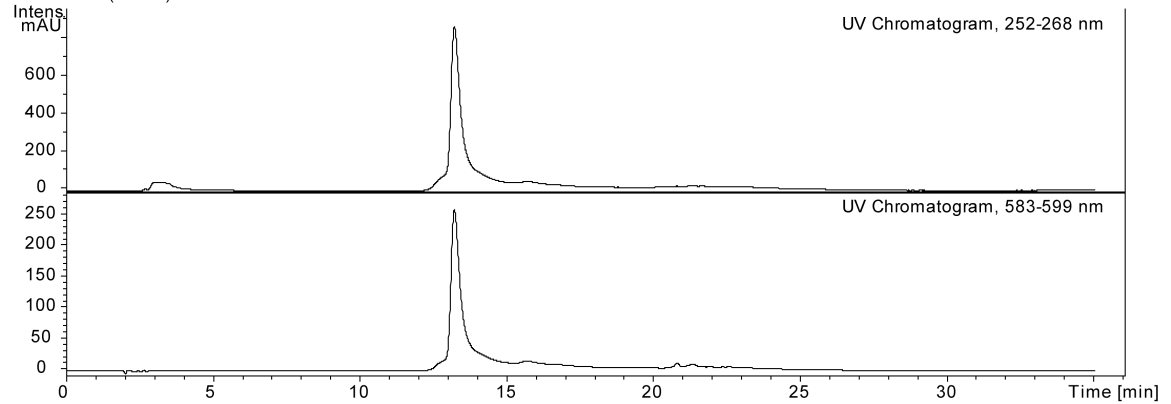
5'-XGCAGAACAGCAAGXGCXAGCTTTGCXAGCACXTGCXGXTXCXGCA-3' (2.4)
m/z calc'd (Parent): 15609.2
m/z found (Parent): 15610.4



5'-C6-Amino-TGCAGAACAGCAAGTGCTAGCTTTGCTAGCACTTGCTGTTCTGCA-3' (2.10)
m/z calc'd (Parent): 14015.2
m/z found (Parent): 14015.7



5'-TR-C6--TGCAGAACAGCAAGTGCTAGCTTTGCTAGCACTTGCTGTTCTGCA-3' (2.11)
m/z calc'd (Parent): 14708.0
m/z found (Parent): 14721.2

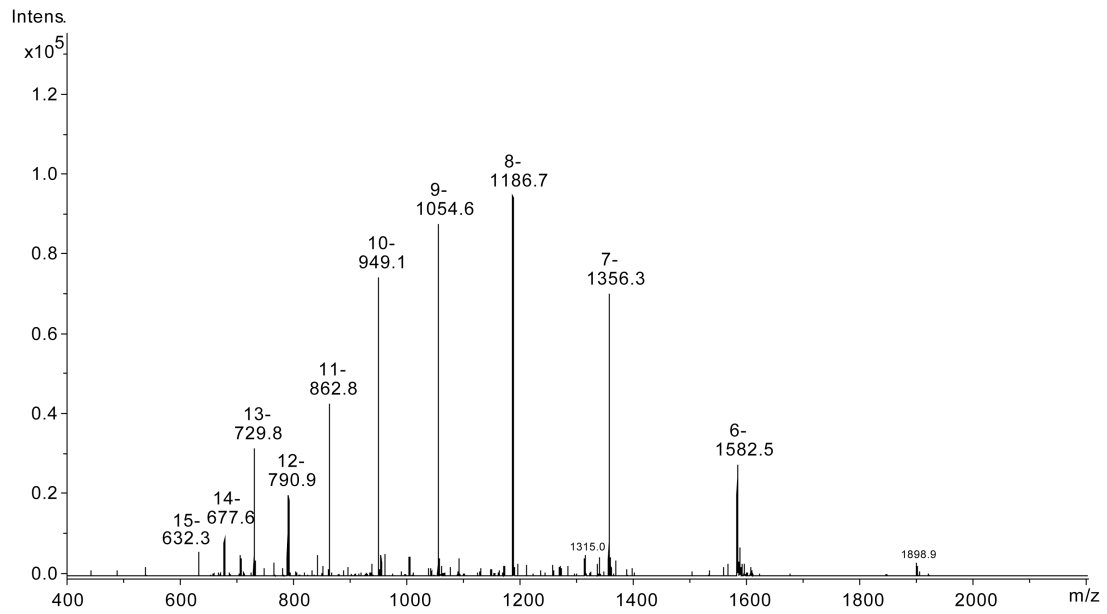
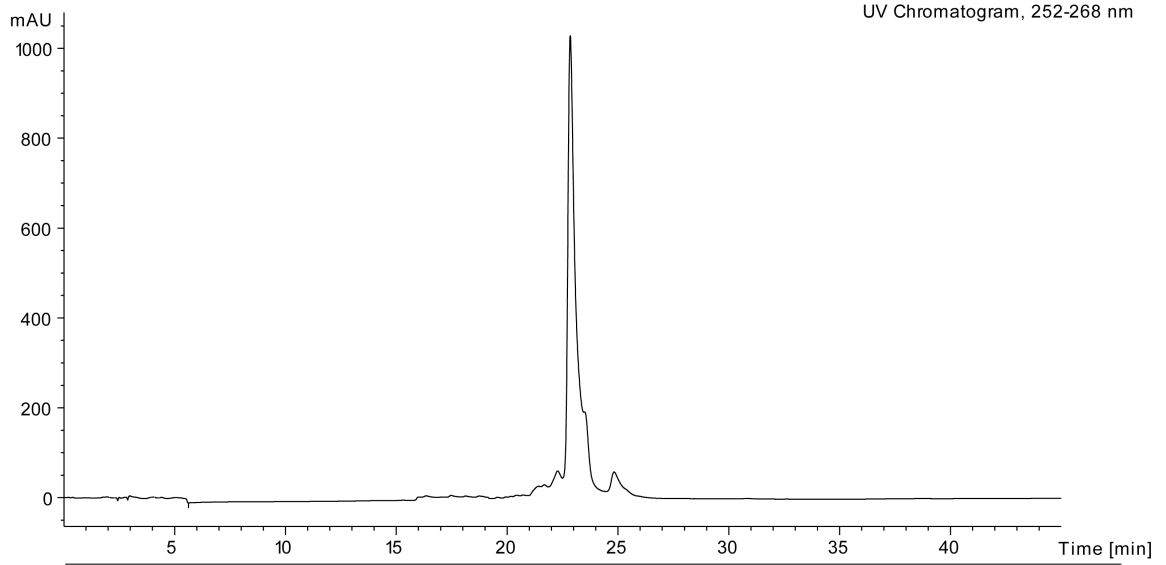


B.2 Chapter 3 Compounds

5'-TGGGGACTTTCCAGTTTCTGGAAAGTCCCA-3' (**3.10**)

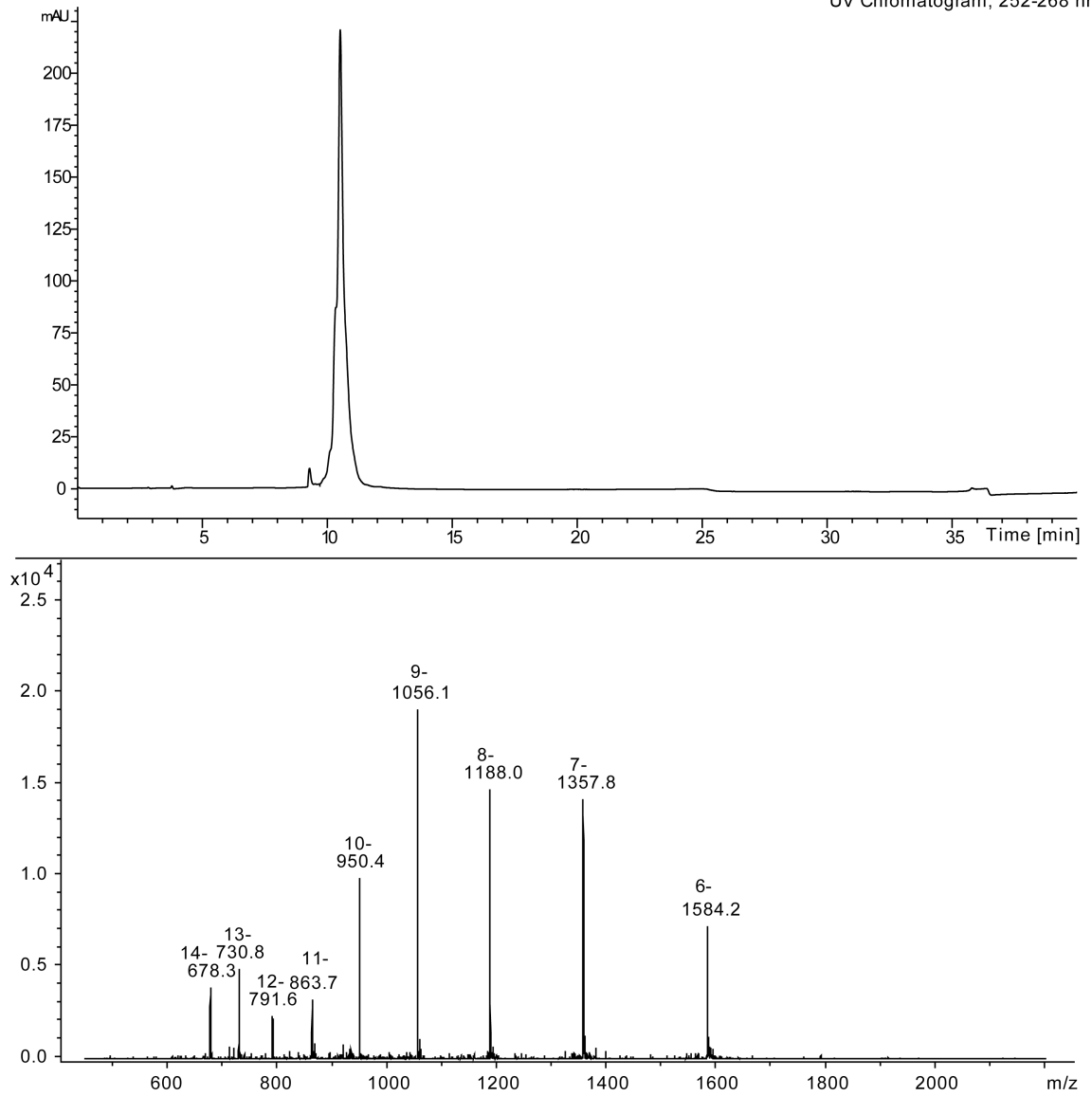
m/z calc'd (Parent): 9502.2

m/z found (Parent): 9501.6



5'-TGG(7-NI)GACTTTCCAGTTTCTGAAAGTCCCCA-3' (3.11)
m/z calc'd (Parent): 9513.2
m/z found (Parent): 9513.9

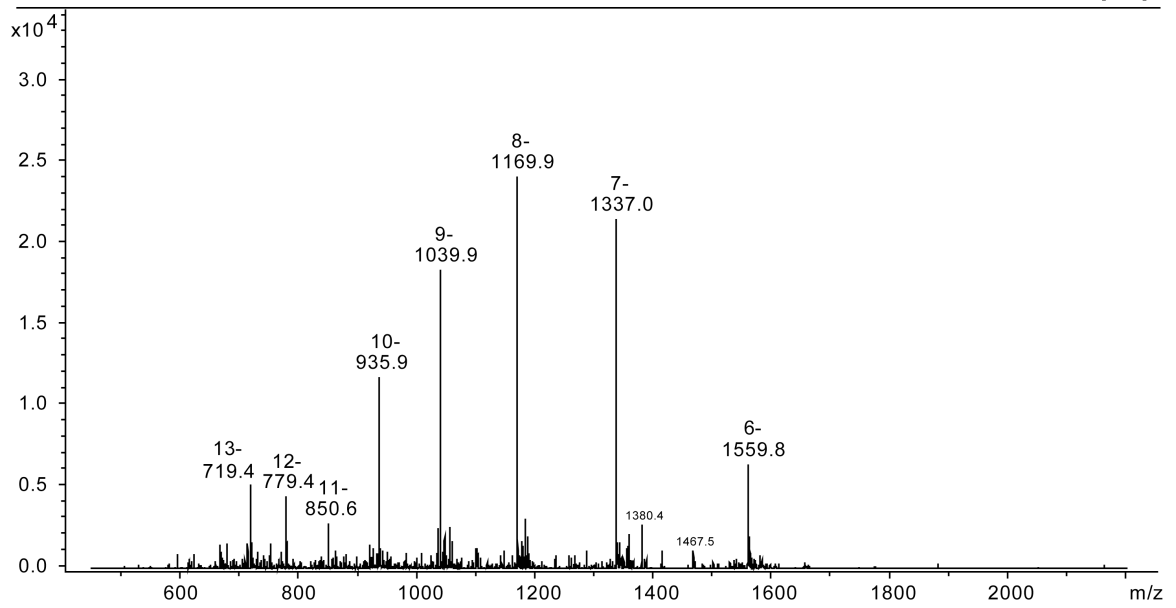
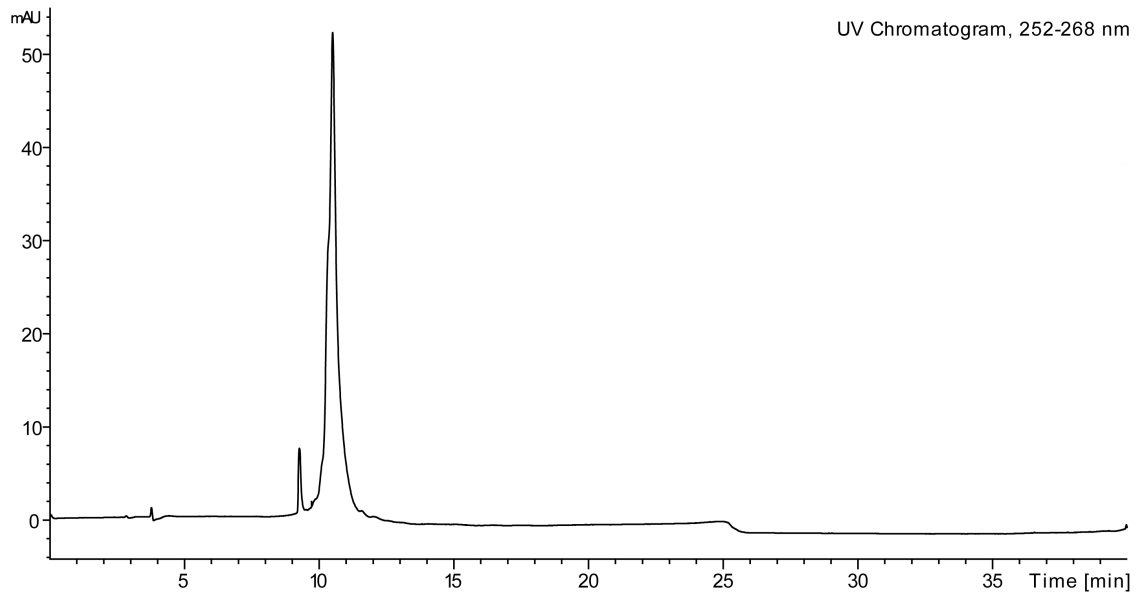
UV Chromatogram, 252-268 nm



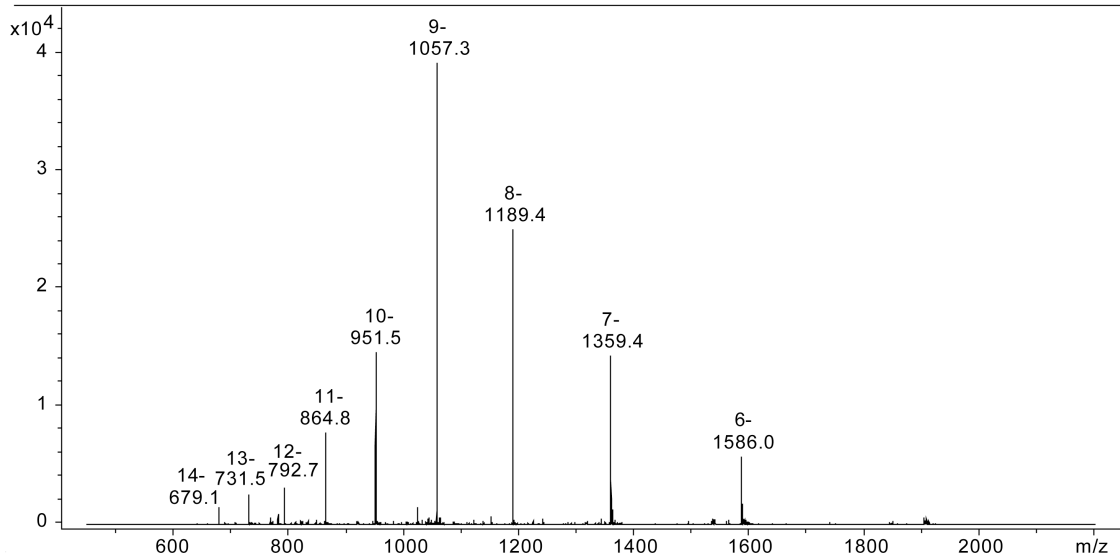
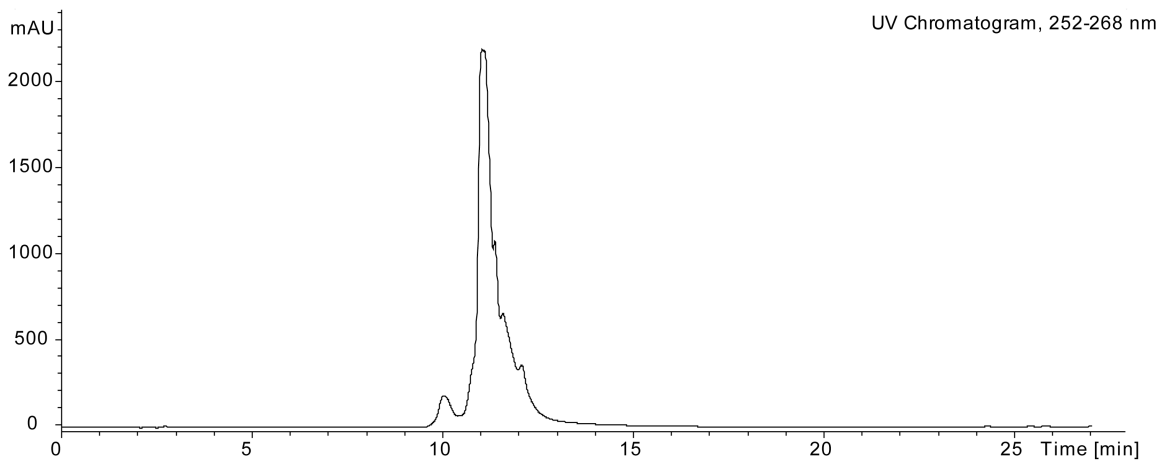
5'-TGG_GACTTTCAGTTTCTGGAAAGTCCCCA-3' (3.12)

m/z calc'd (Parent): 9367.1

m/z found (Parent): 9368.1

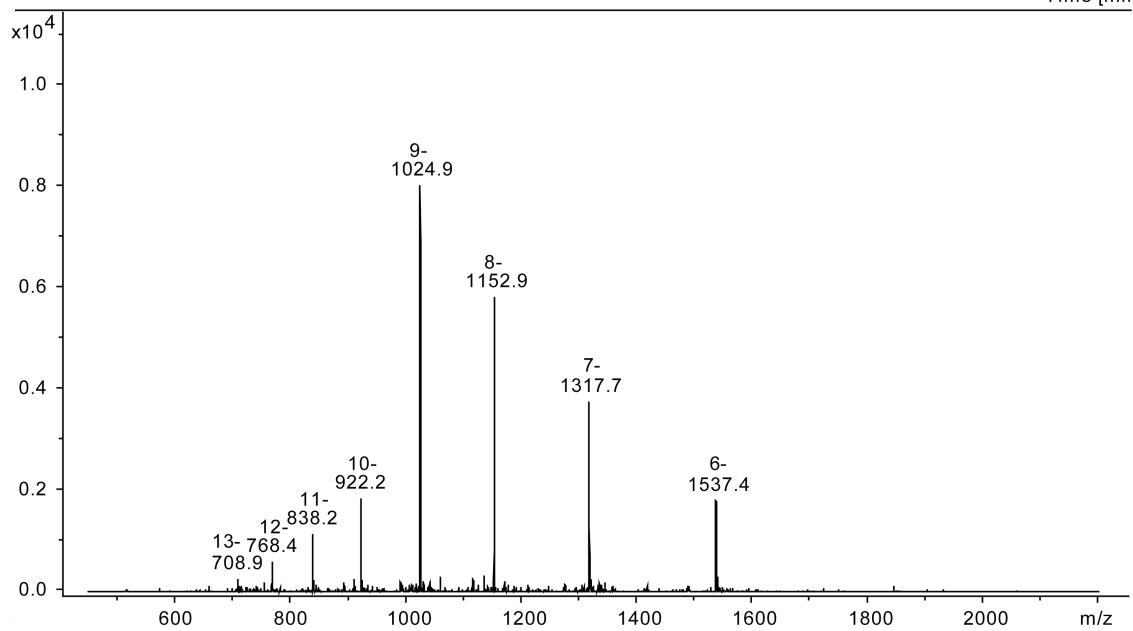
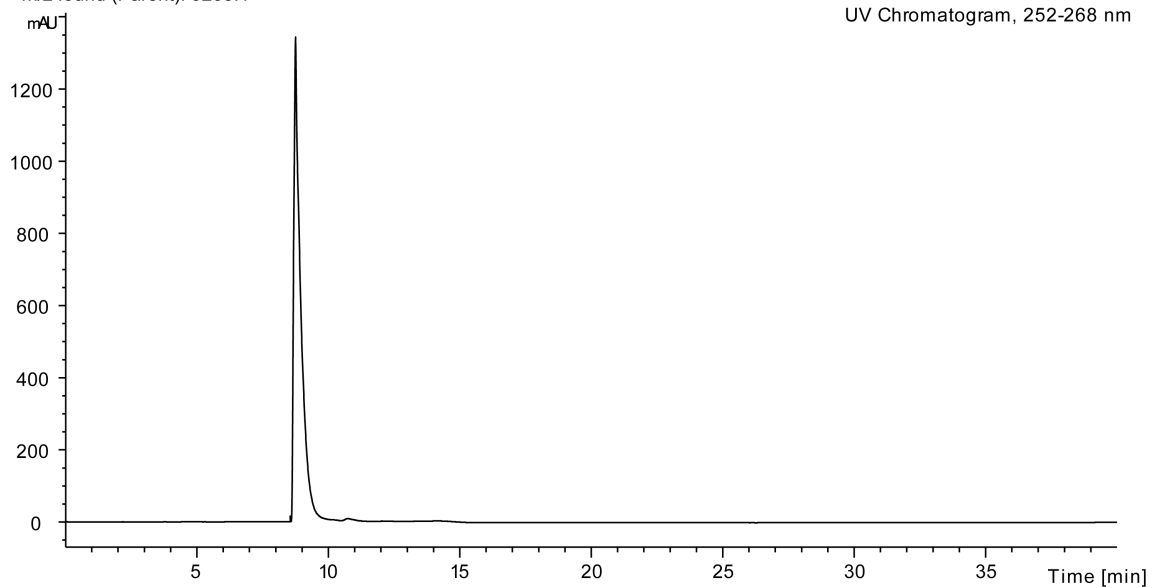


5'-TG(7-NI)G(7-NI)ACTTCCAGTTTCTGGAAAGTCCCA-3' (3.13)
m/z calc'd (Parent): 9524.2
m/z found (Parent): 9524.7

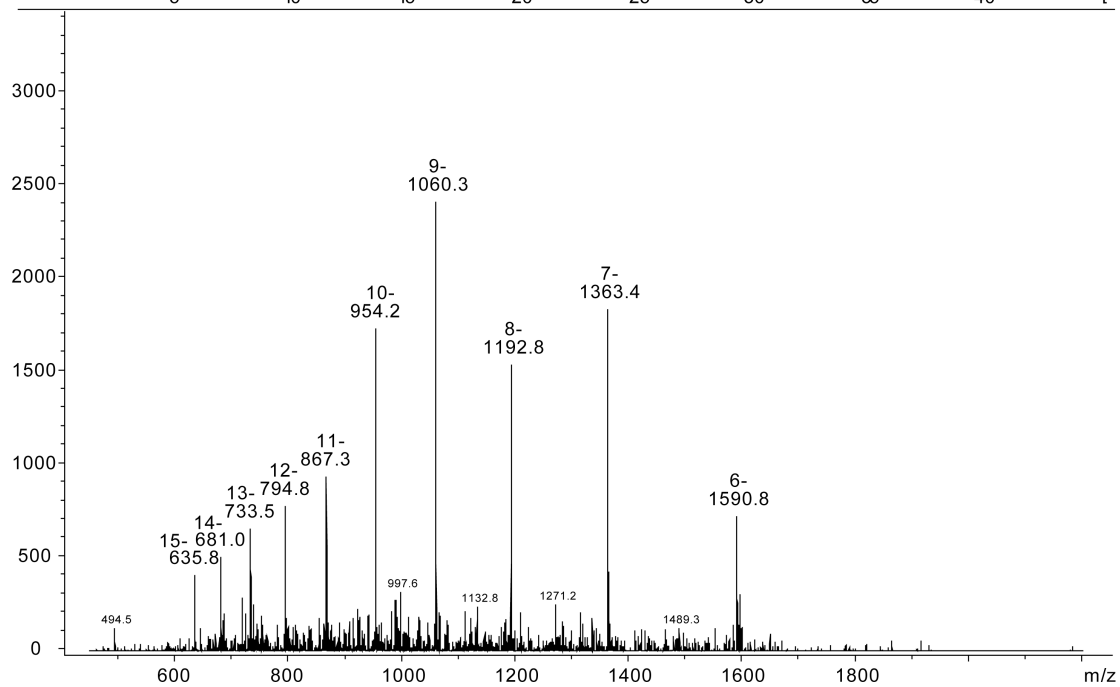
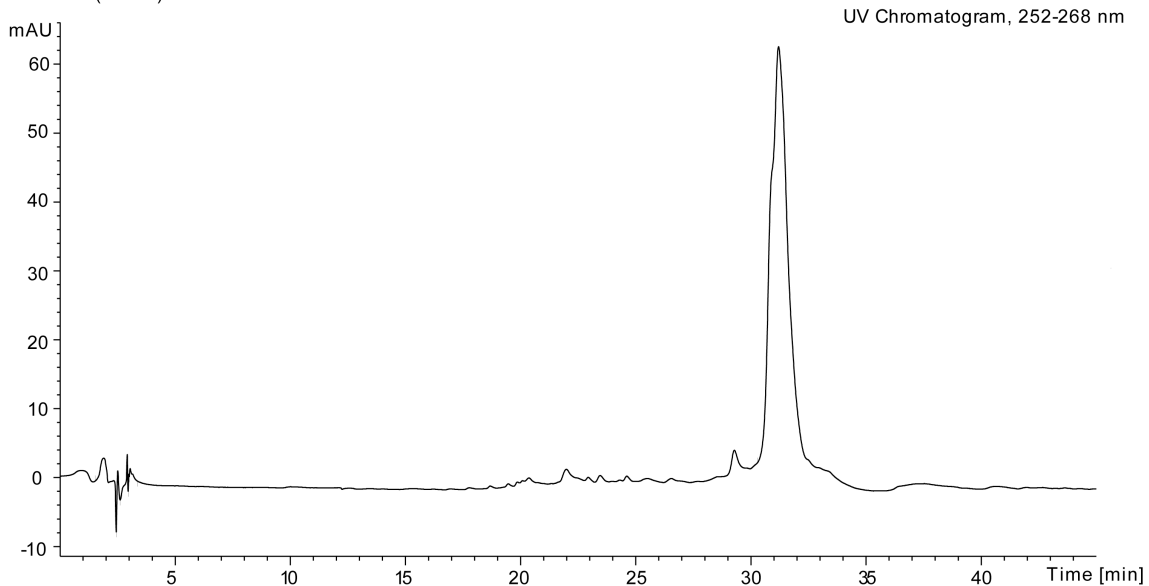


5'-TG_G_ACTTTCCAGTTTCTGGAAAGTCCCCA-3' (3.14)
m/z calc'd (Parent): 9232.9
m/z found (Parent): 9233.1

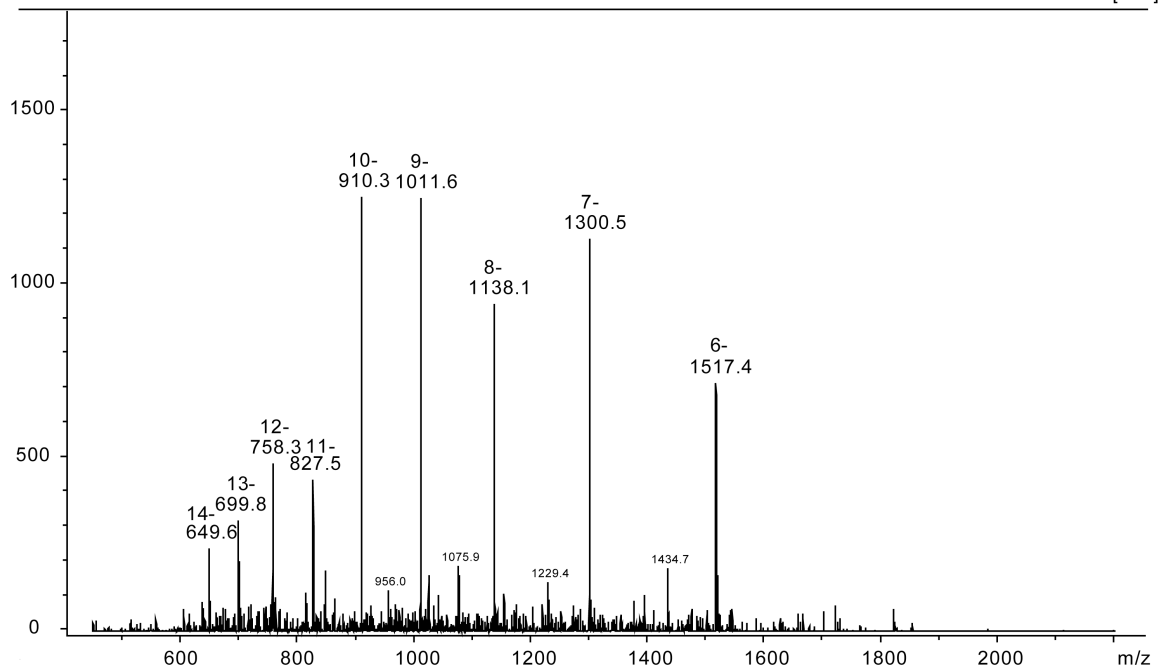
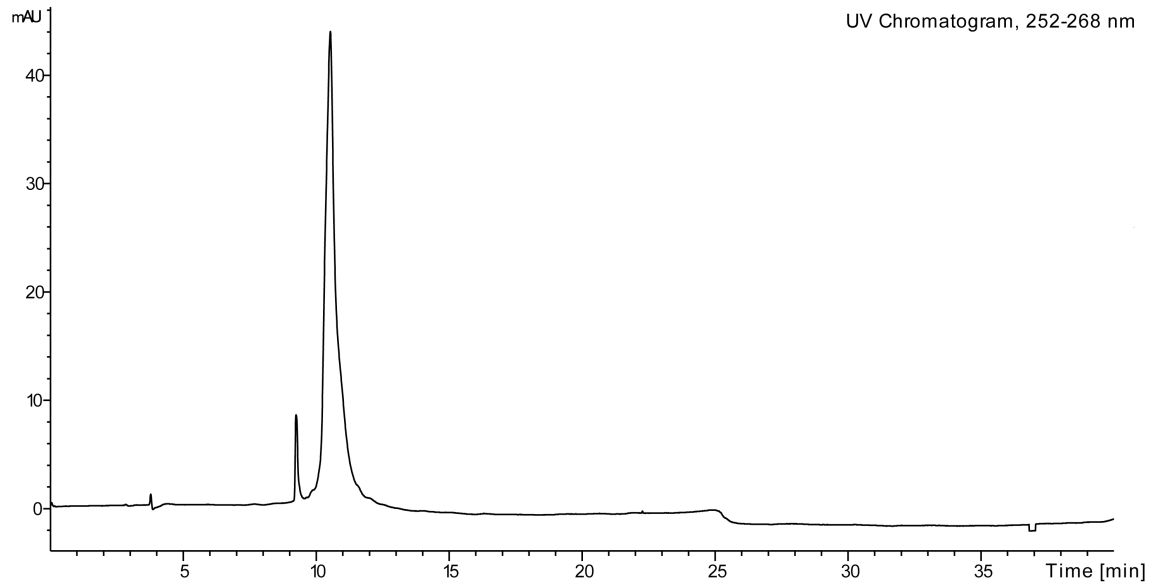
UV Chromatogram, 252-268 nm



5'-T(7-NI)G(7-NI)G(7-NI)CTTCCAGTTTCTGGAAAGTCCCCA-3' (3.15)
m/z calc'd (Parent): 9551.2
m/z found (Parent): 9551.7

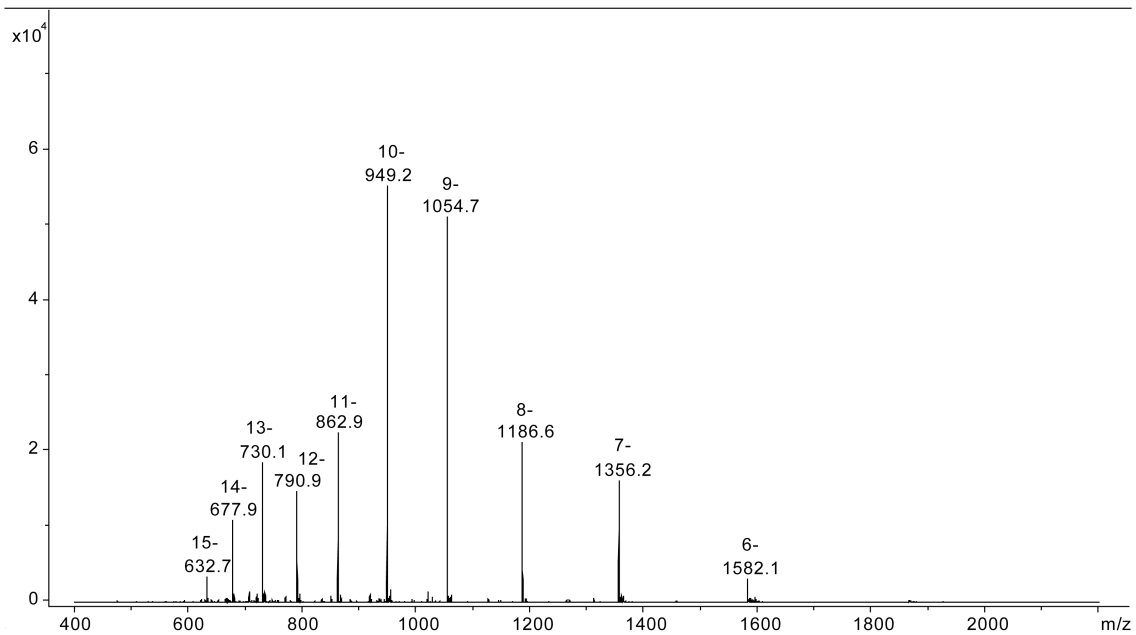
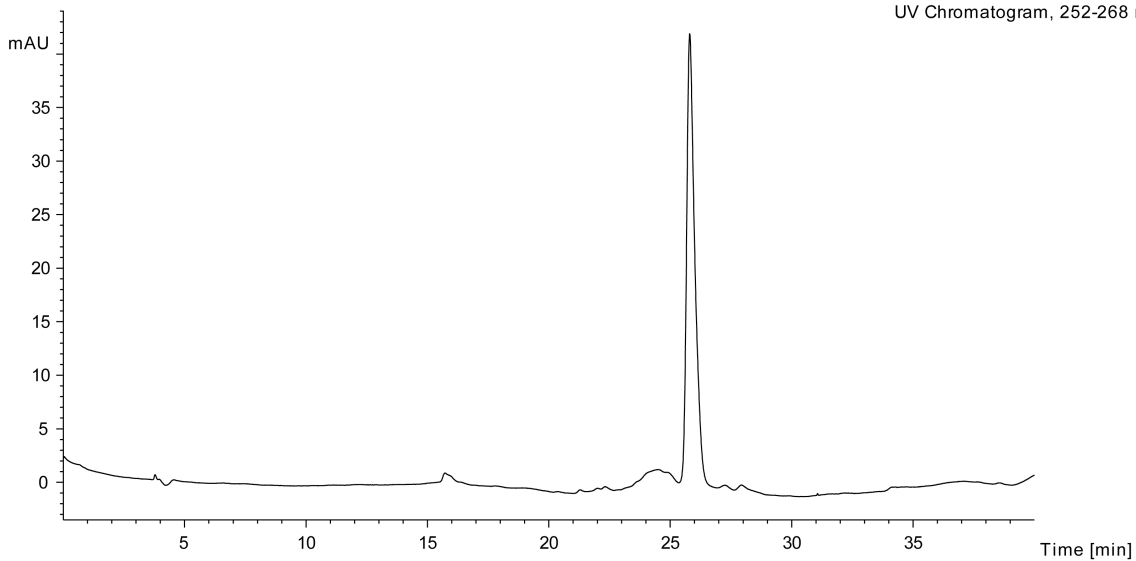


5'-T_G_G_CTTTCCAGTTTCTGGAAAGTCCCCA-3' (3.16)
m/z calc'd (Parent): 9114.8
m/z found (Parent): 9113.5



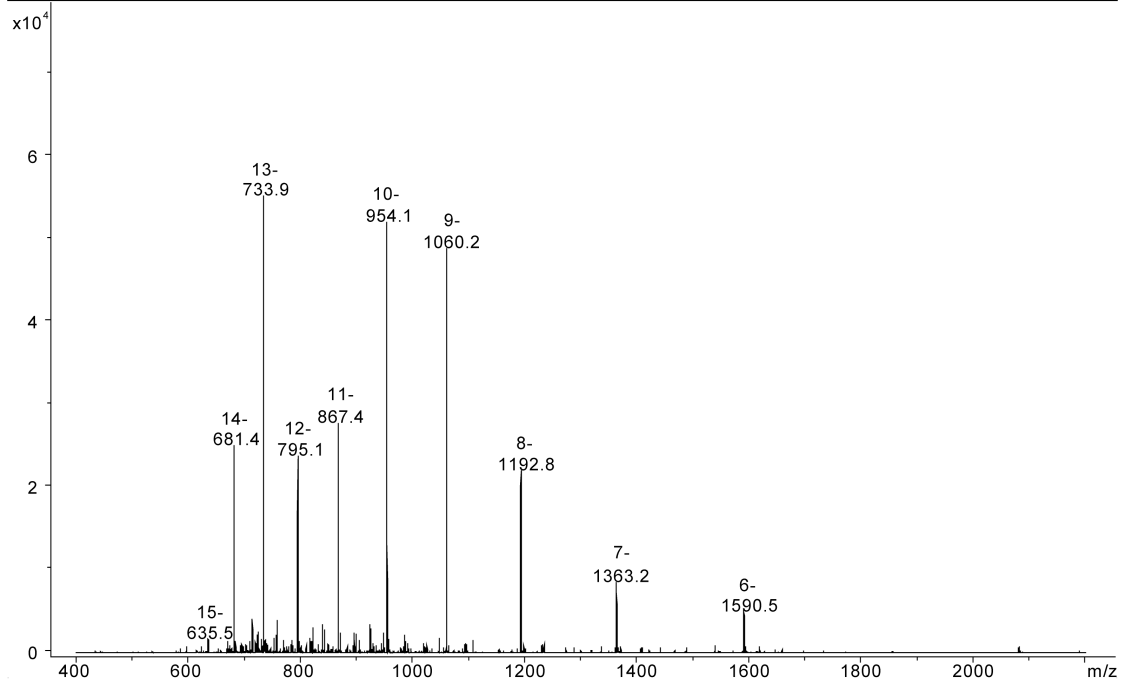
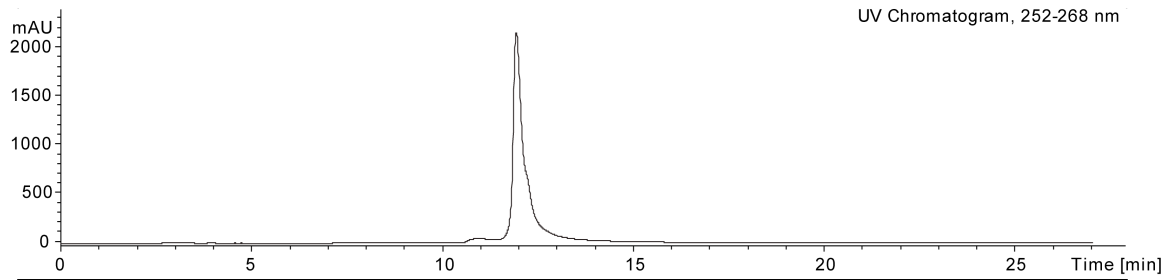
5'-TTGCCGTACCTGACTTTGTCAGGTACGGCAA-3' (3.17)
m/z calc'd (Parent): 9502.2
m/z found (Parent): 9502.0

UV Chromatogram, 252-268 nm



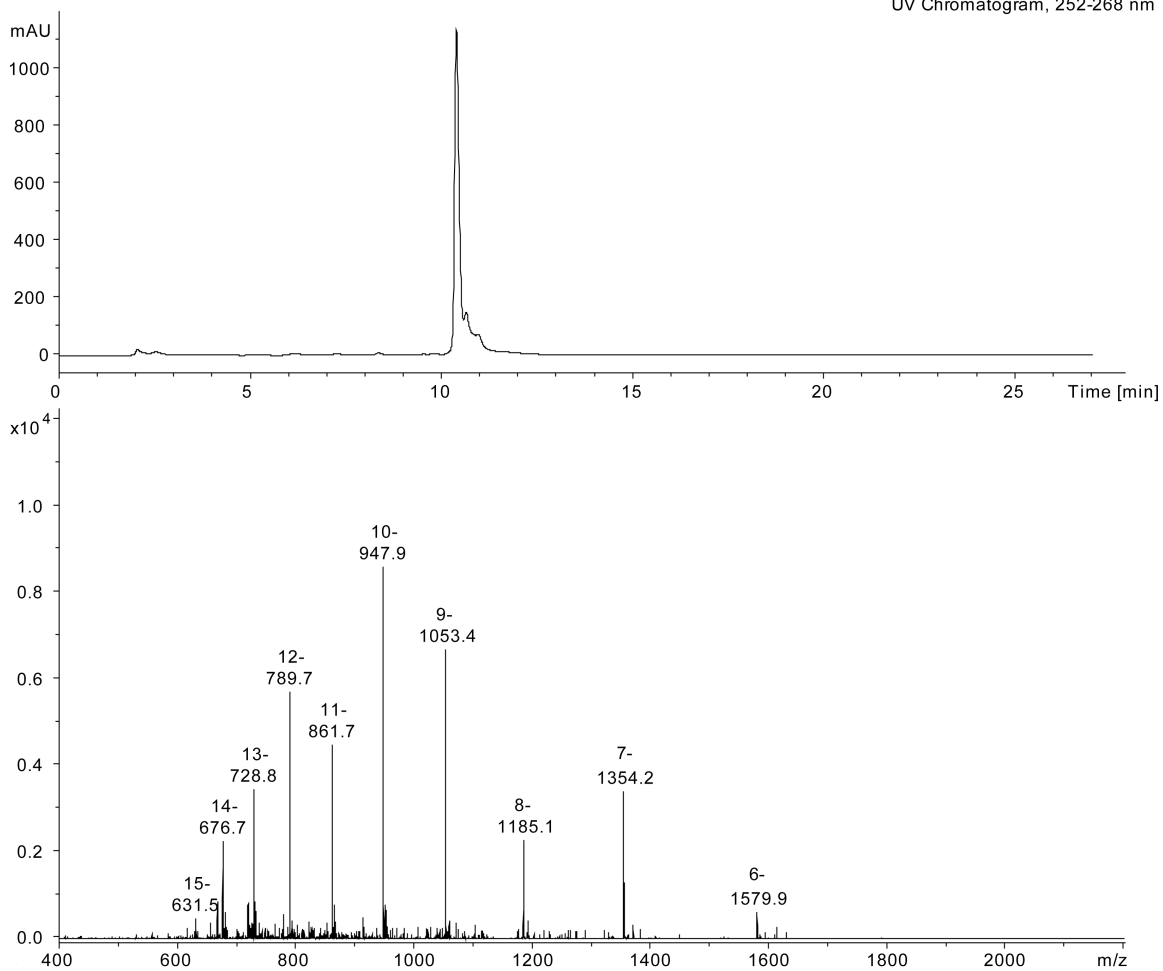
5'-TT(7-NI)CC(7-NI)T(7-NI)CCTGACTTTGTCAGGTACGGCAA-3' (3.18)
m/z calc'd (Parent): 9551.2
m/z found (Parent): 9550.8

UV Chromatogram, 252-268 nm

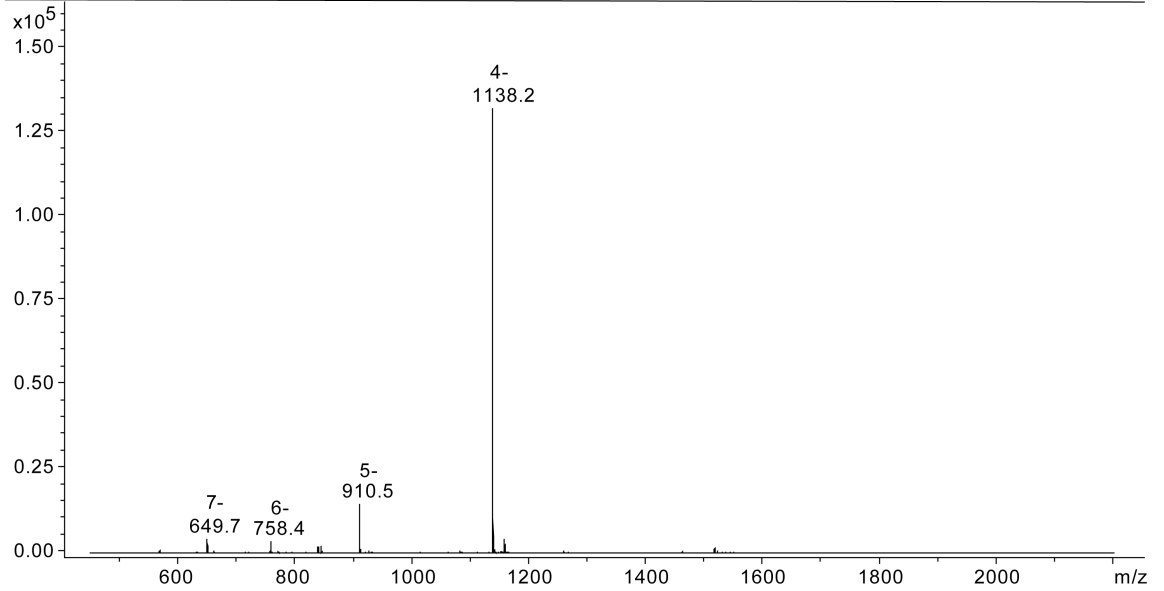
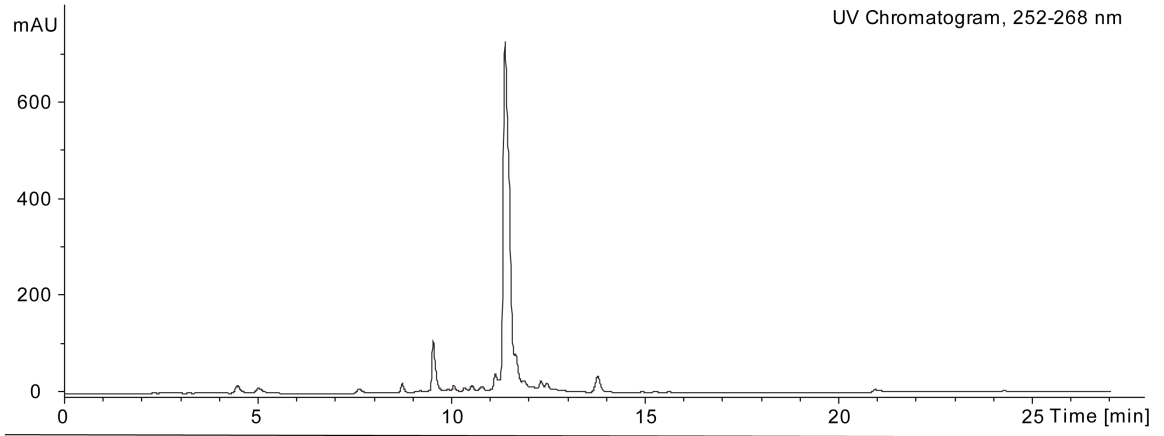


5'-TAGAGGCTTTCCAGTTTCTGGAAAGTCCCA-3' (3.19)
m/z calc'd (Parent): 9486.2
m/z found (Parent): 9486.4

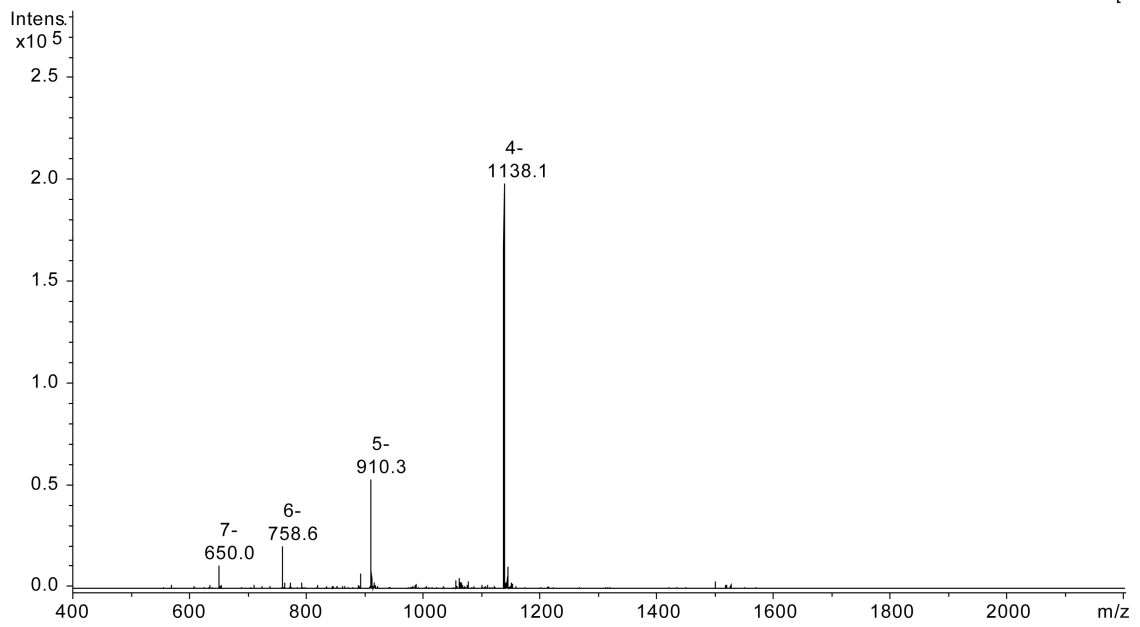
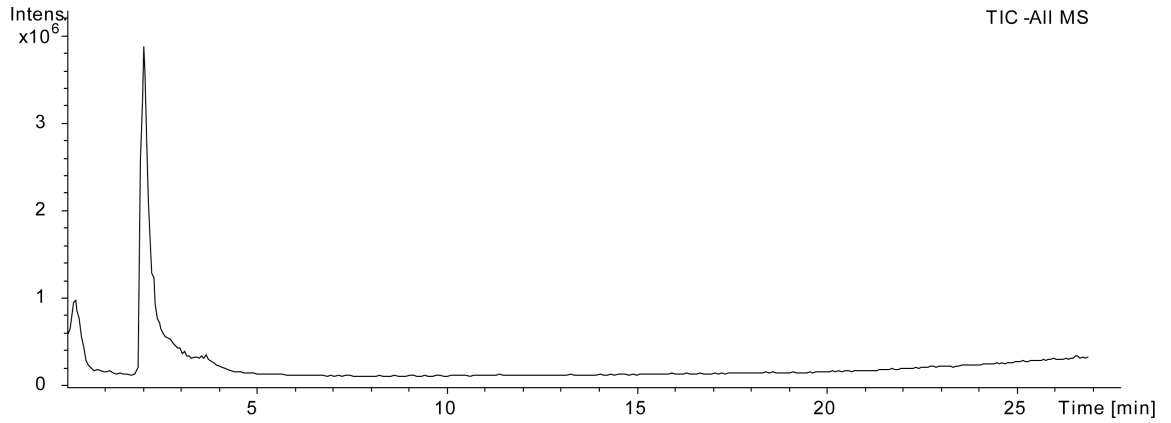
UV Chromatogram, 252-268 nm



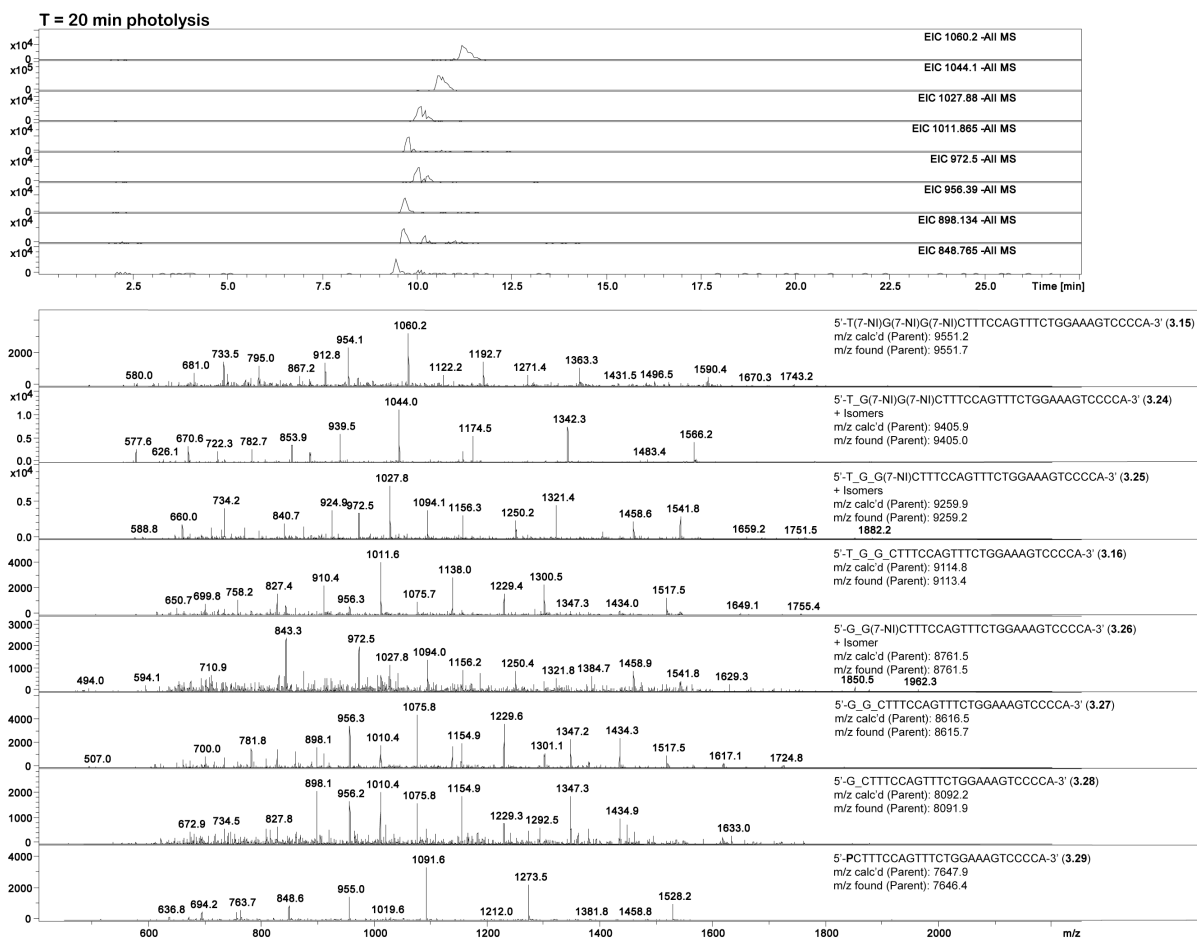
5'-CCTTTT(7-N)AAAAAGG-3' (3.21)
m/z calc'd (Parent): 4557.0
m/z found (Parent): 4556.8



5'-CCTTTT(6-NI)AAAAAGG-3' (3.23)
m/z calc'd (Parent): 4557.0
m/z found (Parent): 4556.8



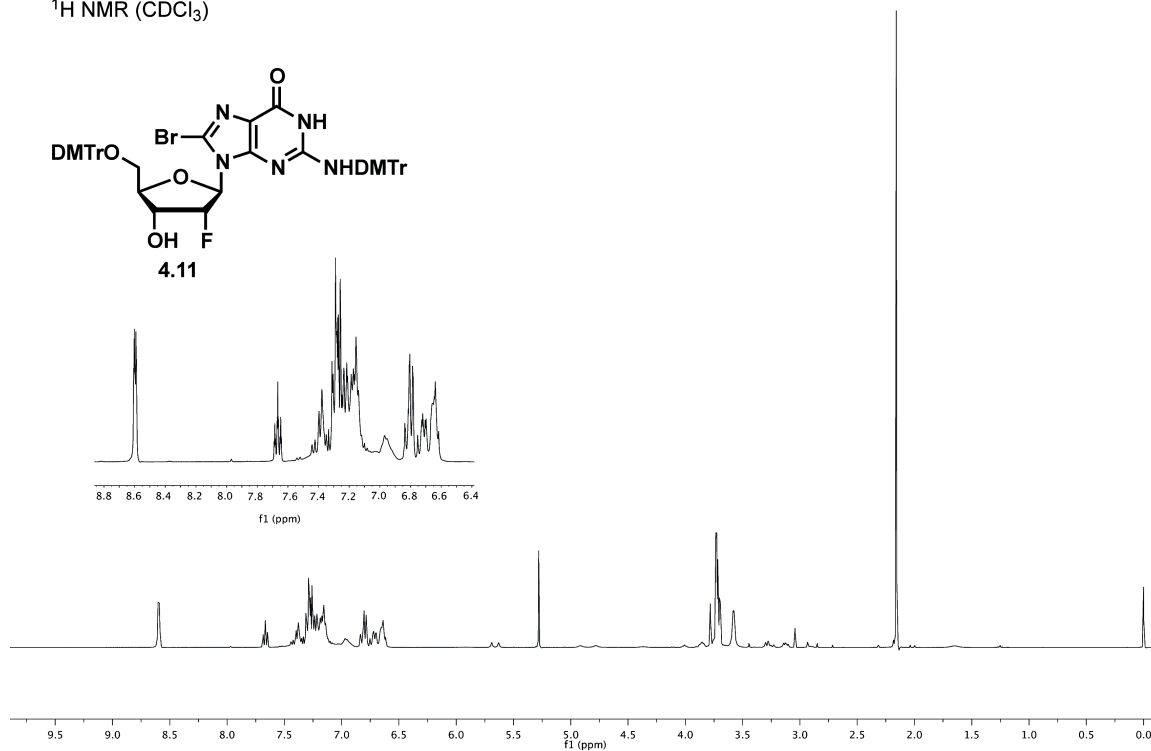
Products Formed From the Photolysis of 3.15.



B.3 Chapter 4 Compounds

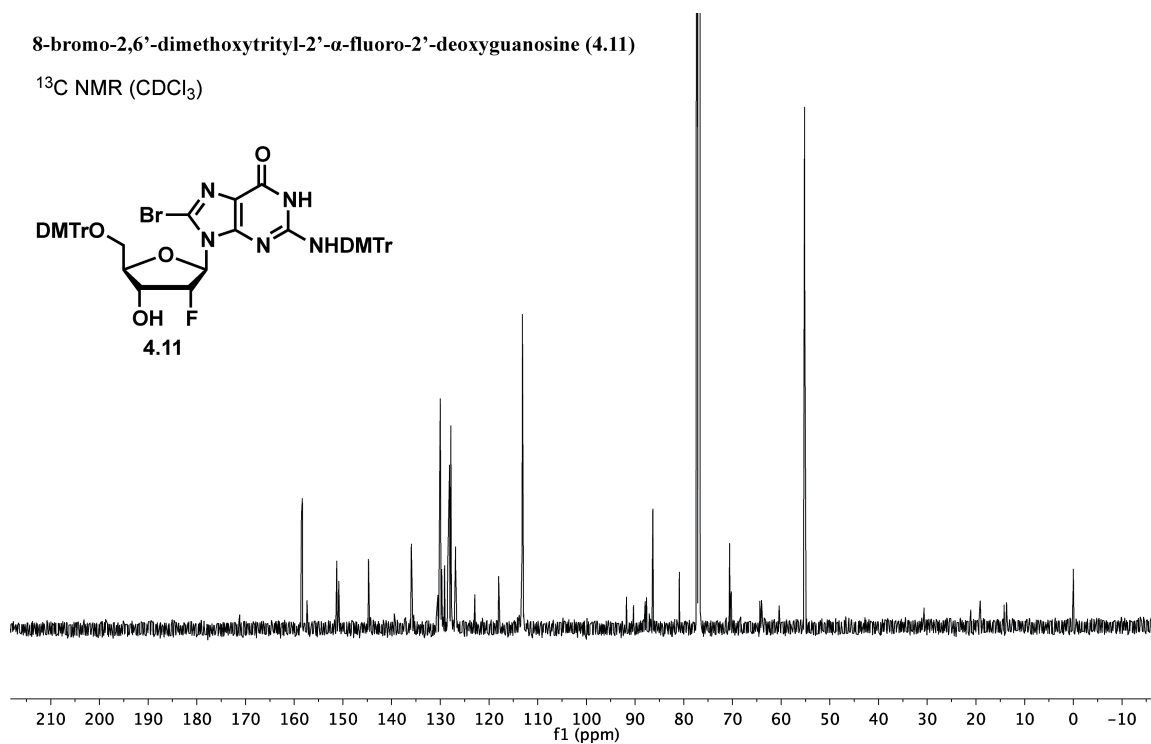
8-bromo-2,6'-dimethoxytrityl-2'- α -fluoro-2'-deoxyguanosine (4.10)

^1H NMR (CDCl_3)



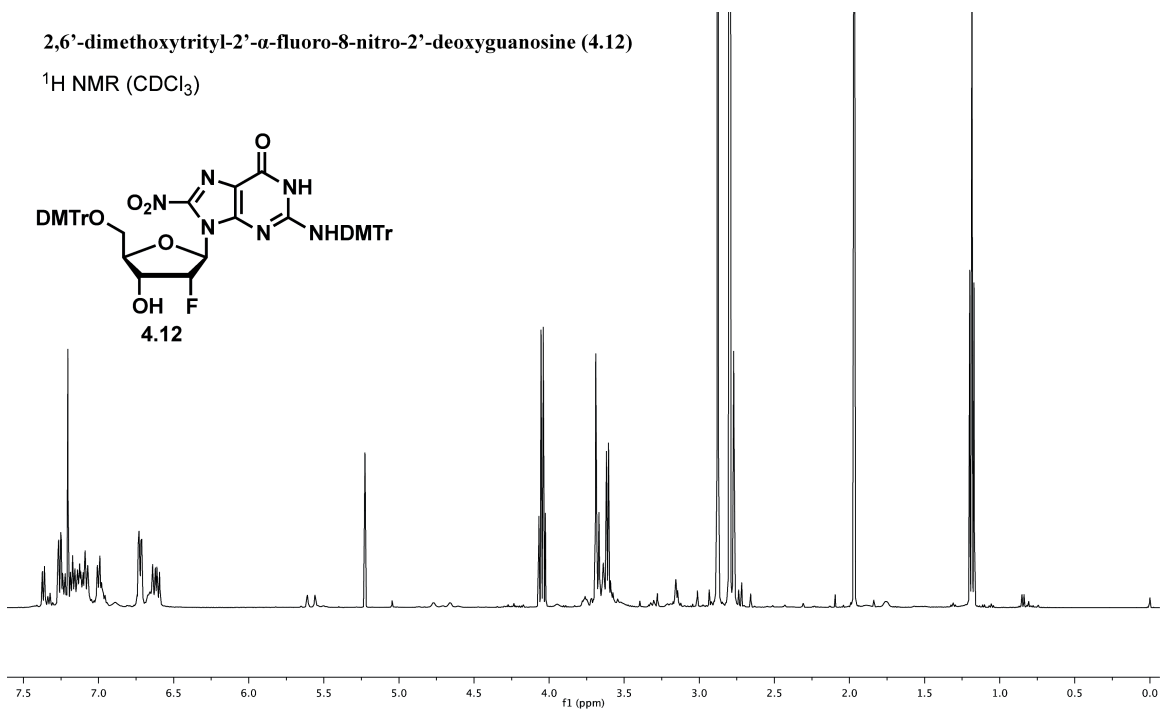
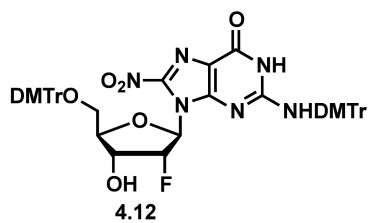
8-bromo-2,6'-dimethoxytrityl-2'- α -fluoro-2'-deoxyguanosine (4.11)

^{13}C NMR (CDCl_3)



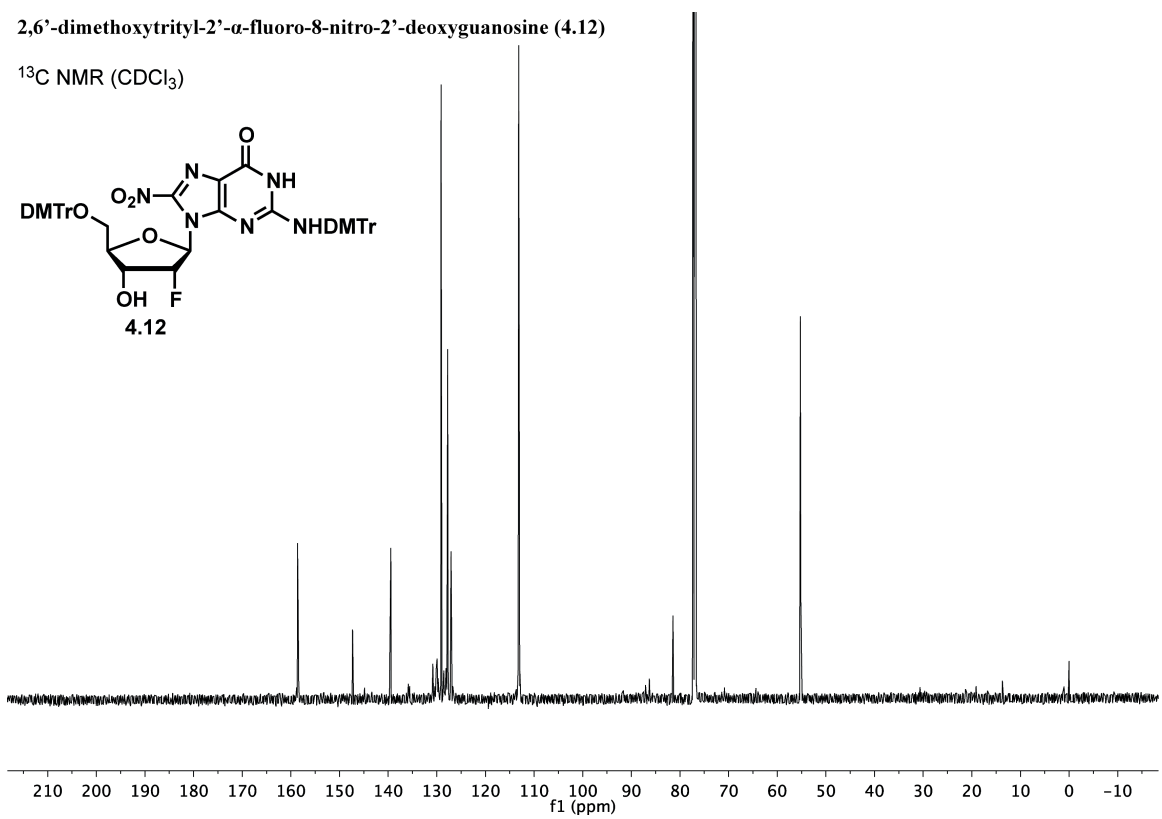
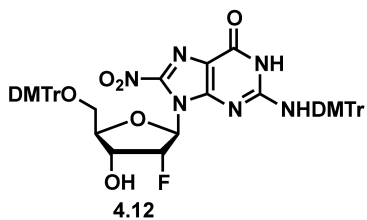
2,6'-dimethoxytrityl-2'- α -fluoro-8-nitro-2'-deoxyguanosine (4.12)

^1H NMR (CDCl_3)



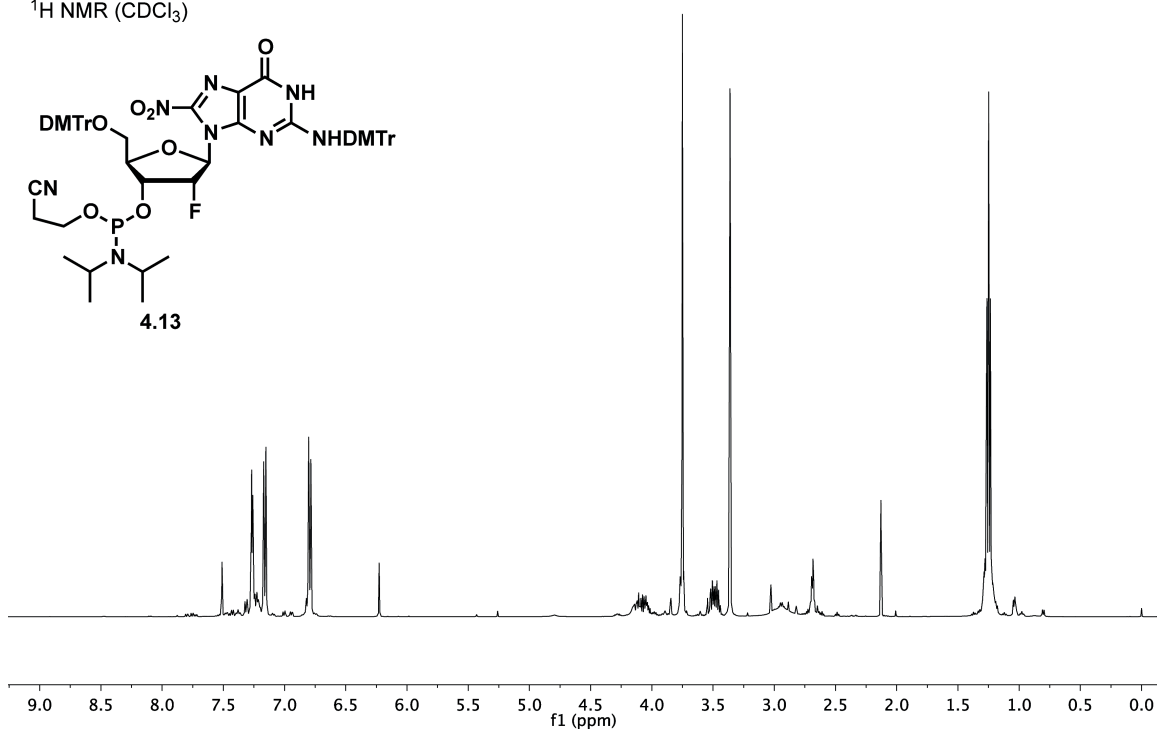
2,6'-dimethoxytrityl-2'- α -fluoro-8-nitro-2'-deoxyguanosine (4.12)

^{13}C NMR (CDCl_3)



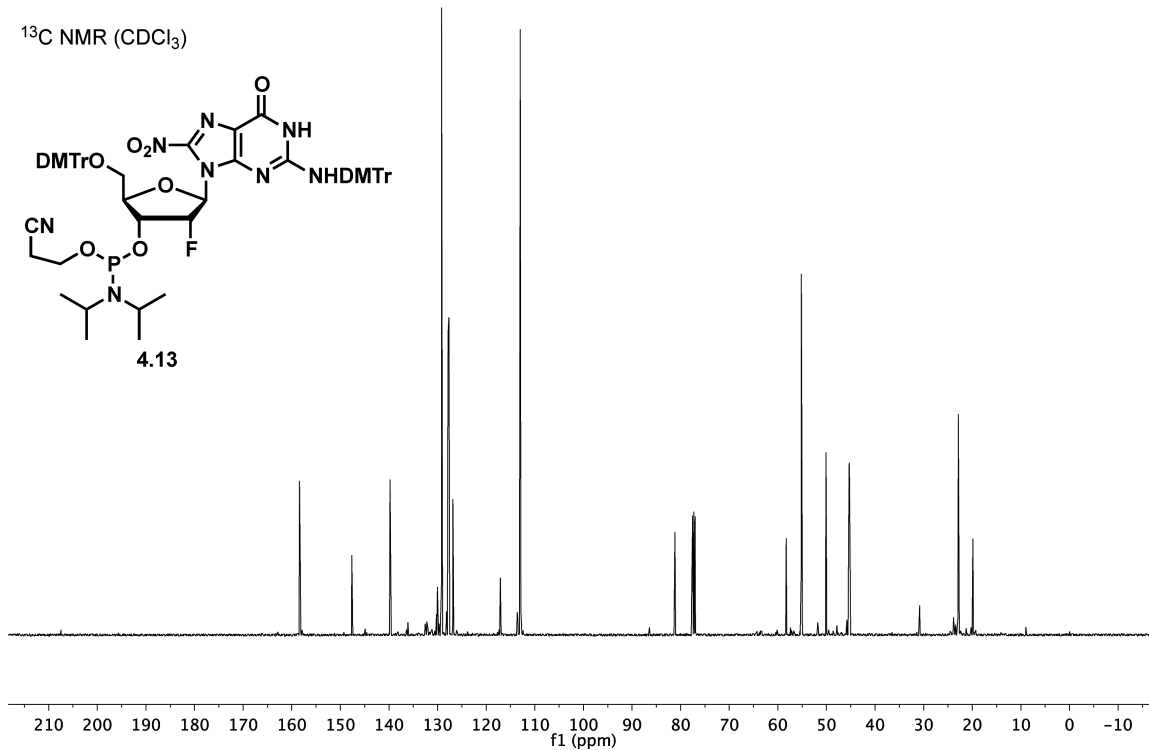
2-Cyanoethyl-N,N-diisopropylphosphoramidite-2,6'-dimethoxytrityl-2'- α -fluoro-8-nitro-2'-deoxyguanosine (4.13)

^1H NMR (CDCl_3)



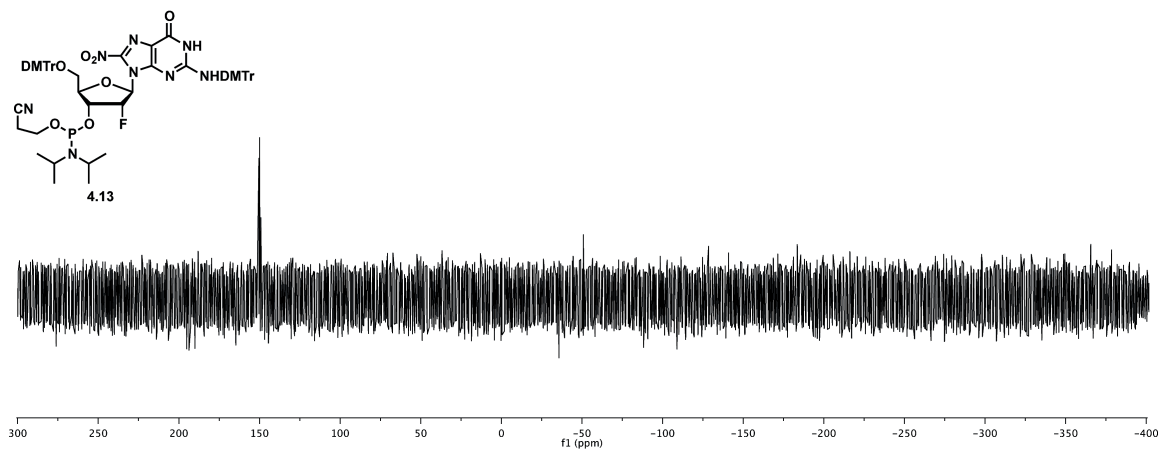
2-Cyanoethyl-N,N-diisopropylphosphoramidite-2,6'-dimethoxytrityl-2'- α -fluoro-8-nitro-2'-deoxyguanosine (4.13)

^{13}C NMR (CDCl_3)

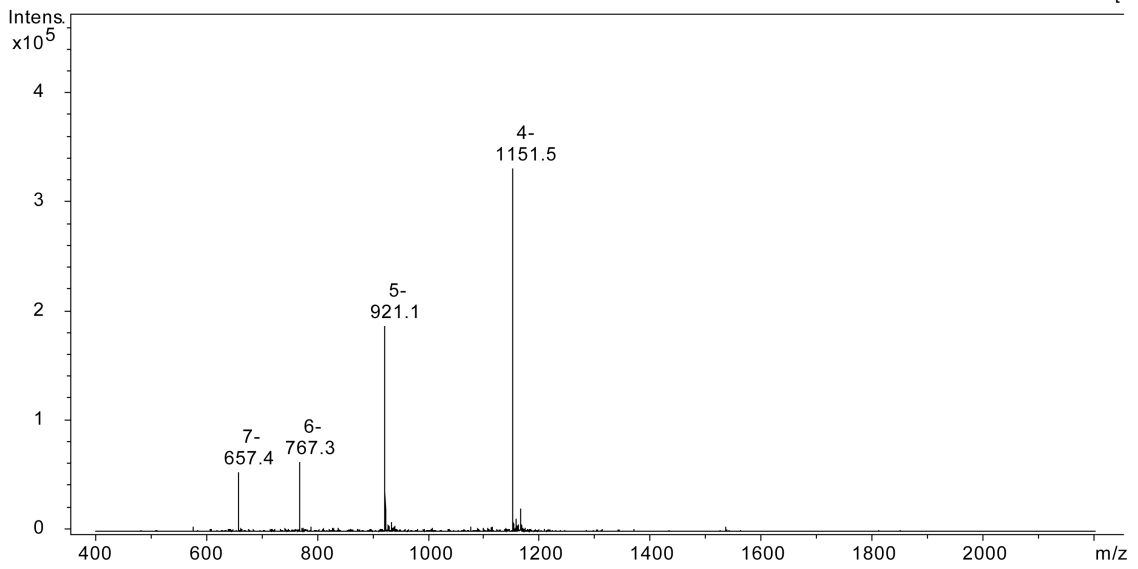
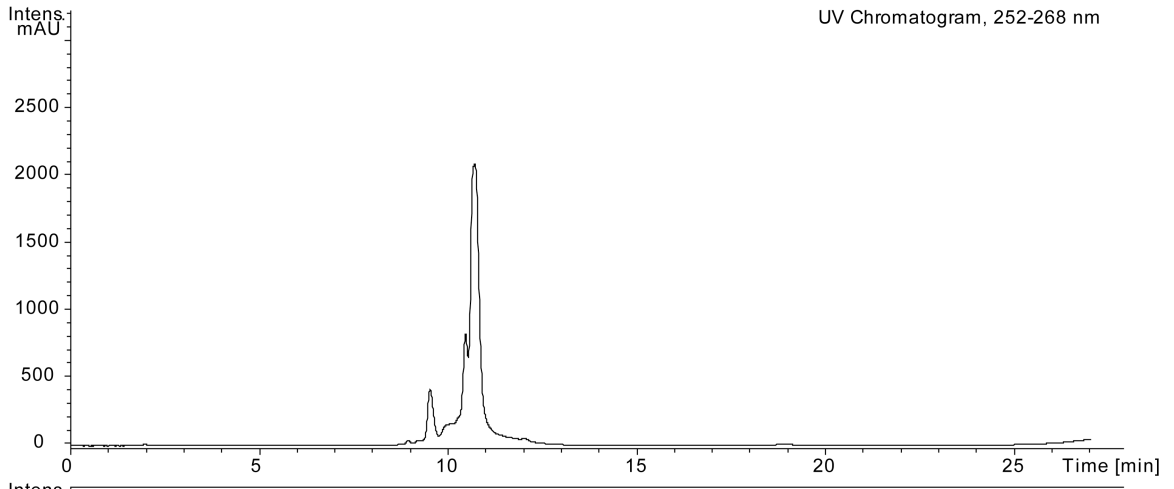


2-Cyanoethyl-N,N-diisopropylphosphoramidite-2,6'-dimethoxytrityl-2'- α -fluoro-8-nitro-2'-deoxyguanosine (4.13)

^{31}P NMR (CDCl_3)

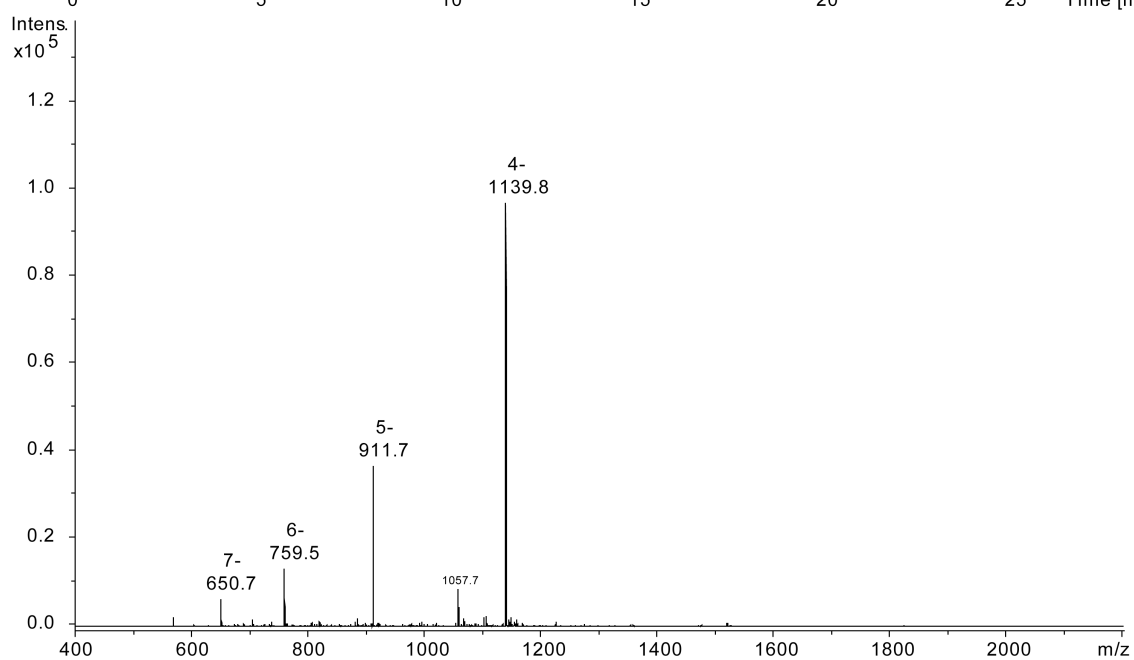
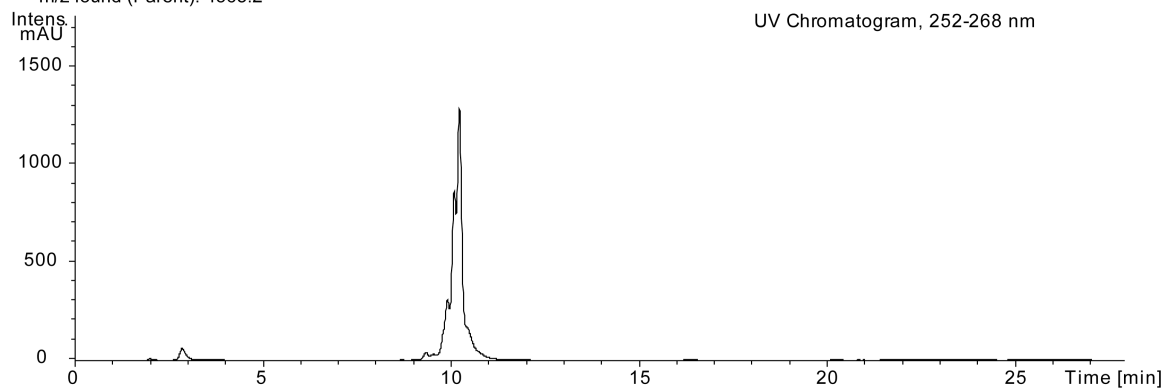


5'-CCTTTT(8-NG)AAAAAGG-3' (4.14)
m/z calc'd (Parent): 4608.9
m/z found (Parent): 4609.5



5'-CCTTTT(8-OG)AAAAAGG-3' (4.15)
m/z calc'd (Parent): 4561.9
m/z found (Parent): 4563.2

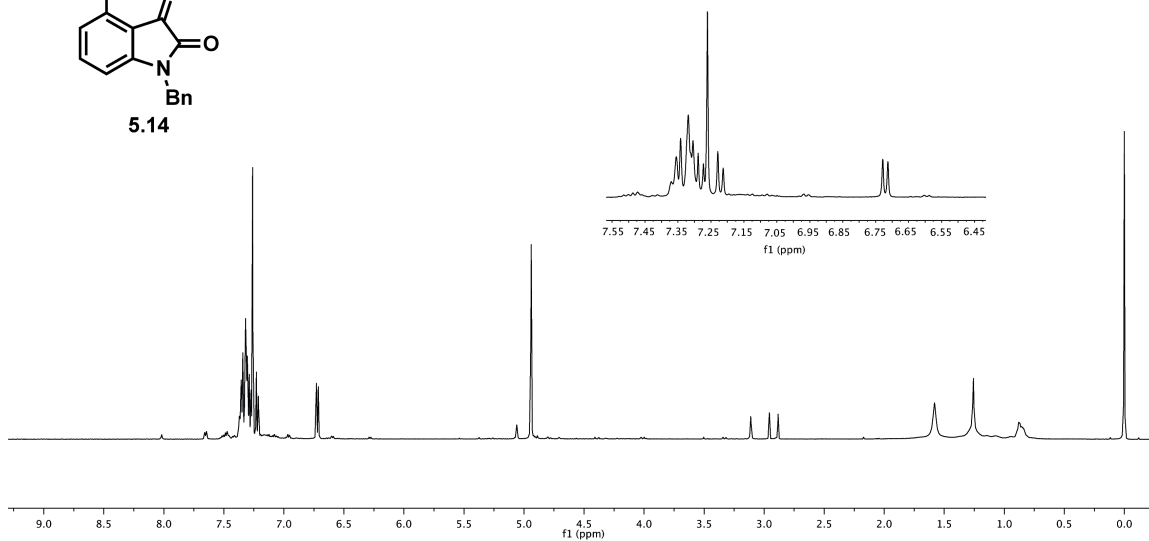
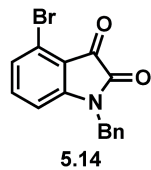
UV Chromatogram, 252-268 nm



B.4 Chapter 5 Compounds

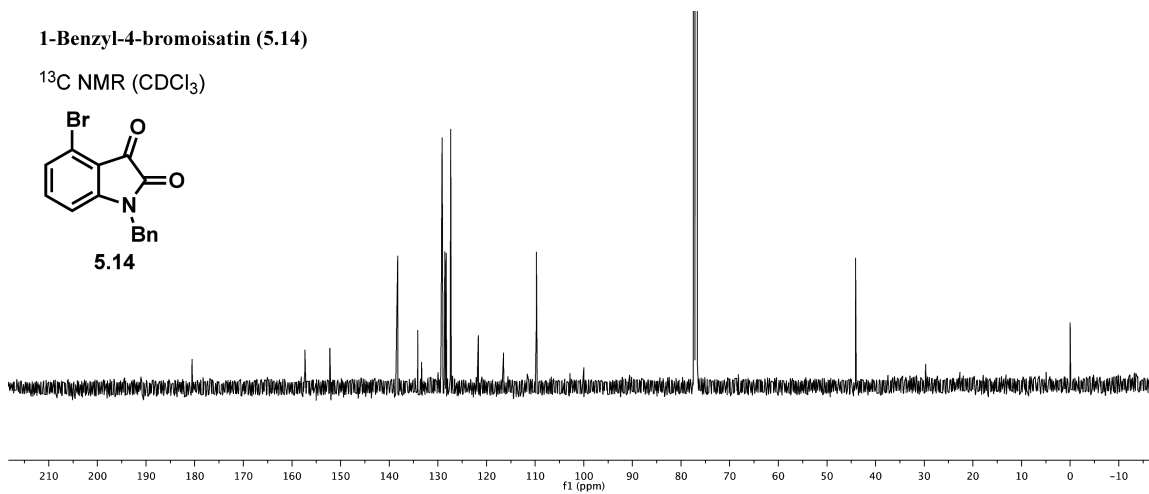
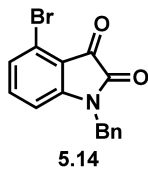
1-Benzyl-4-bromoisatin (5.14)

^1H NMR (CDCl_3)



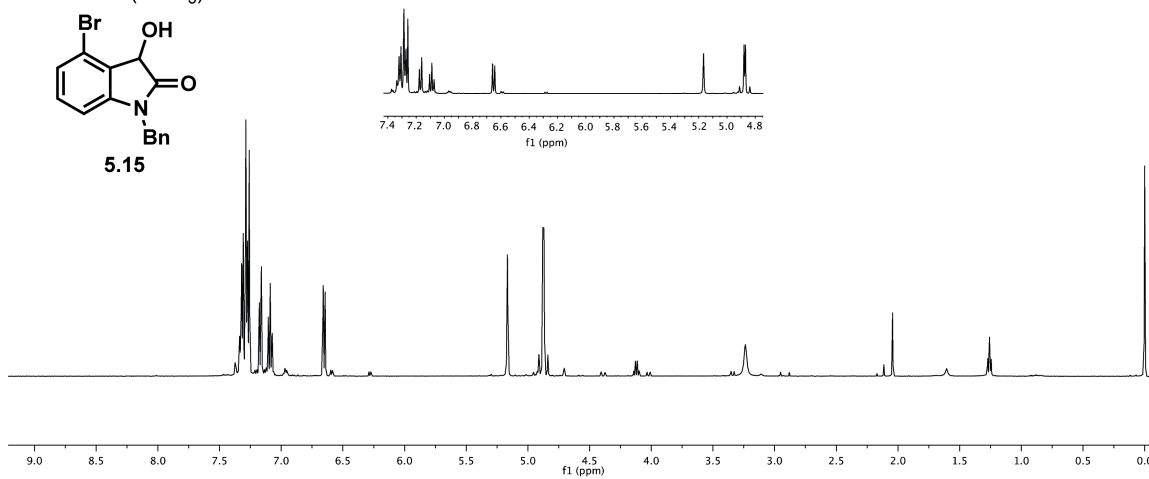
1-Benzyl-4-bromoisatin (5.14)

^{13}C NMR (CDCl_3)



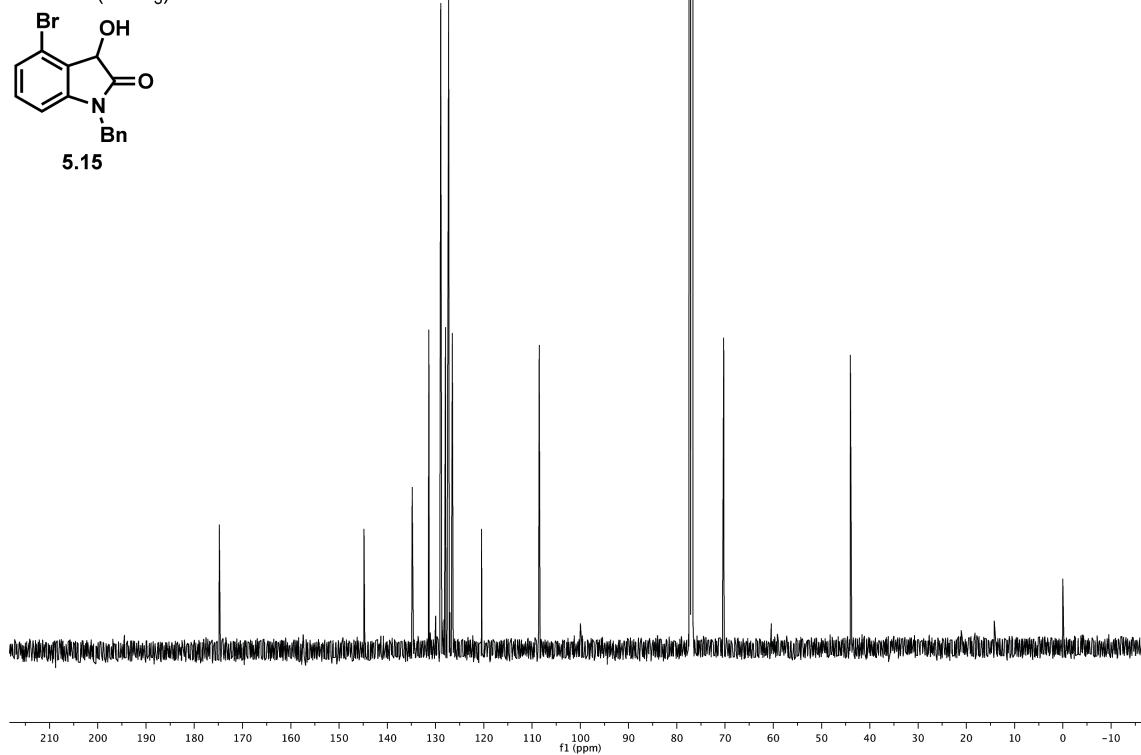
1-Benzyl-4-bromo-3-hydroxy-isatin (5.15)

¹H NMR (CDCl₃)



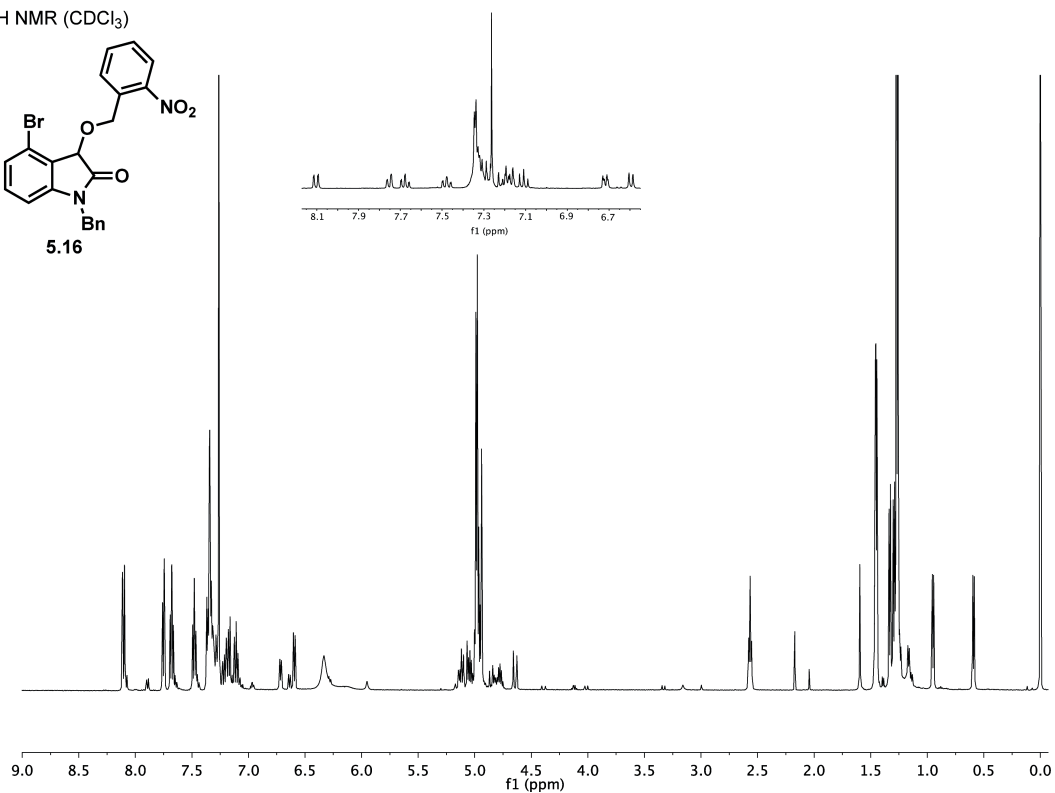
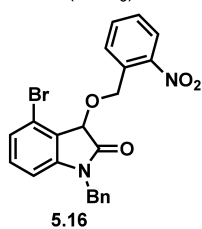
1-Benzyl-4-bromo-3-hydroxy-isatin (5.15)

¹³C NMR (CDCl₃)



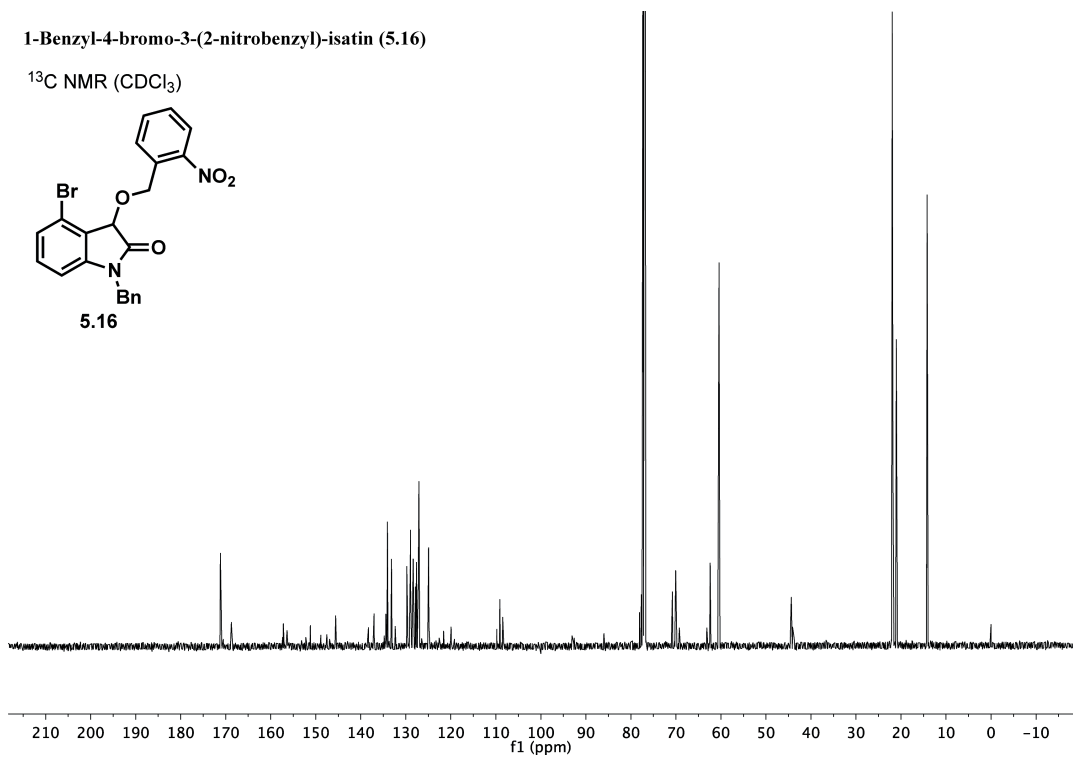
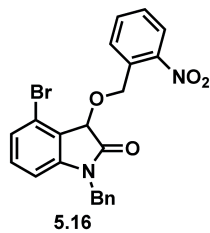
1-Benzyl-4-bromo-3-(2-nitrobenzyl)-isatin (5.16)

¹H NMR (CDCl₃)



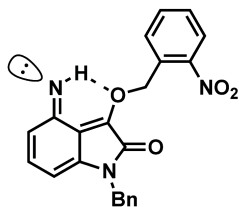
1-Benzyl-4-bromo-3-(2-nitrobenzyl)-isatin (5.16)

¹³C NMR (CDCl₃)

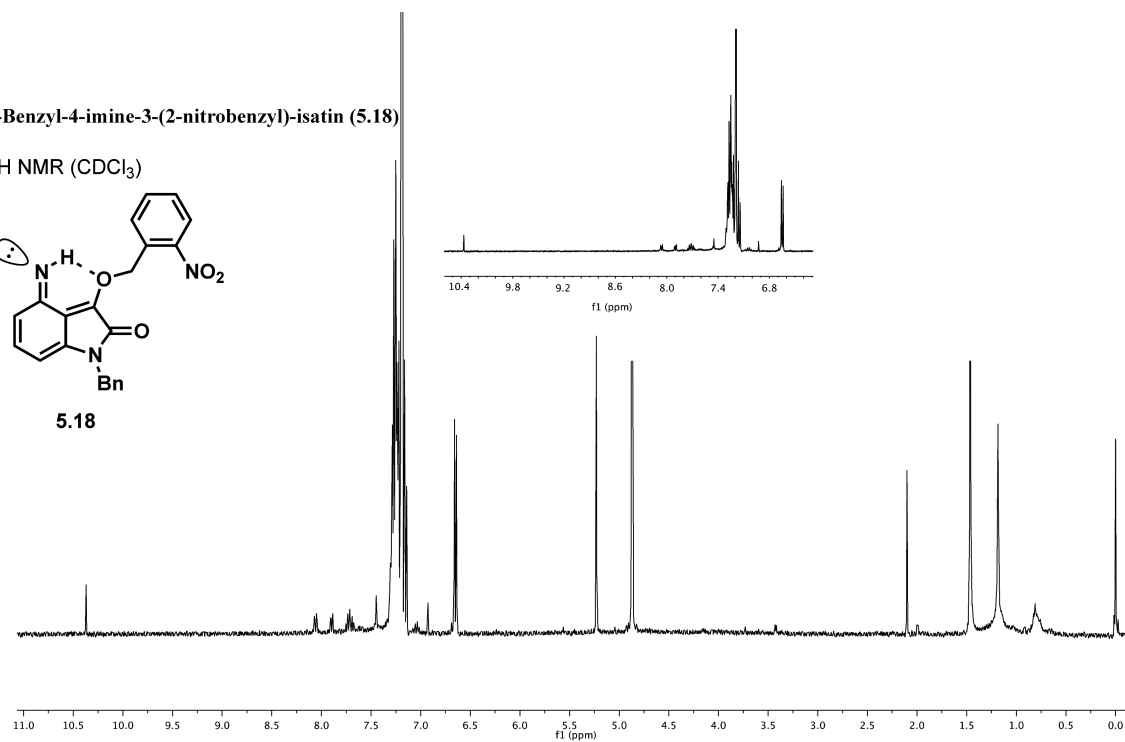


1-Benzyl-4-imine-3-(2-nitrobenzyl)-isatin (5.18)

¹H NMR (CDCl₃)

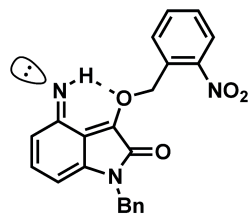


5.18

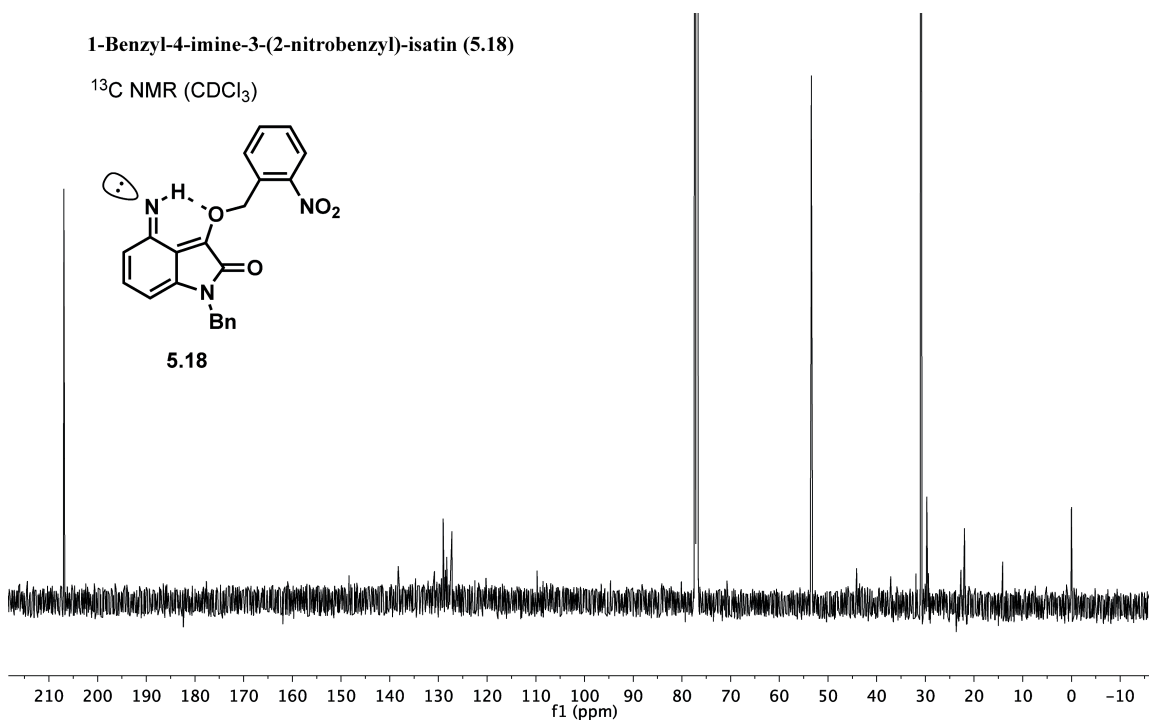


1-Benzyl-4-imine-3-(2-nitrobenzyl)-isatin (5.18)

¹³C NMR (CDCl₃)



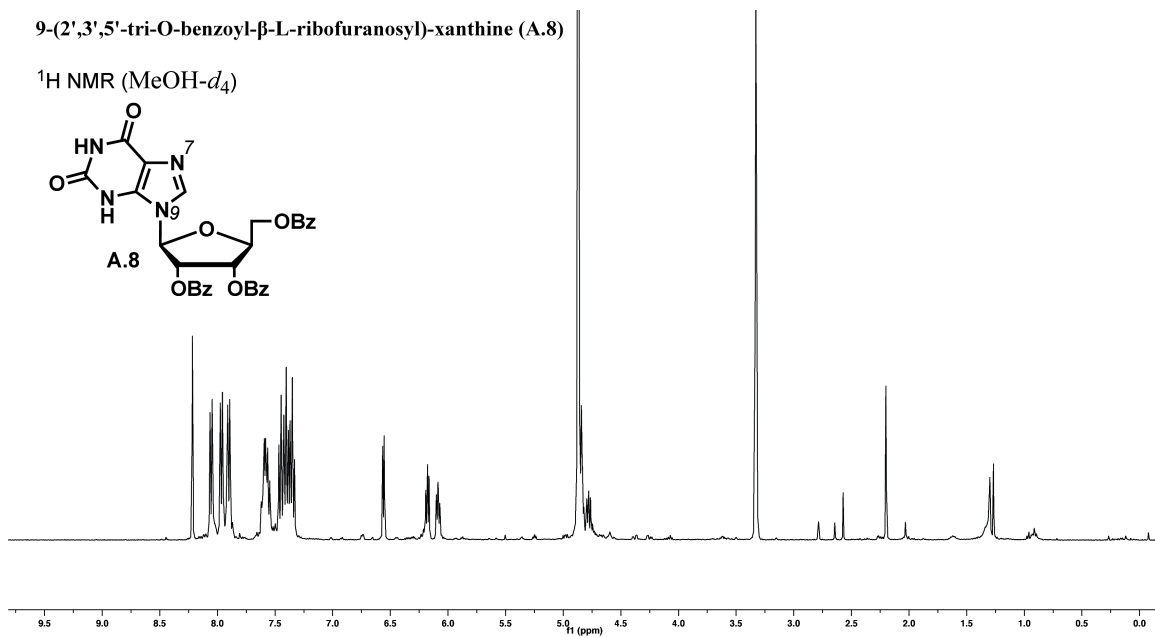
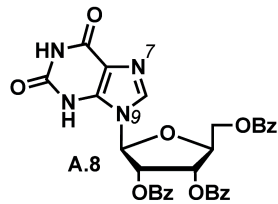
5.18



B.5 Appendix A Compounds

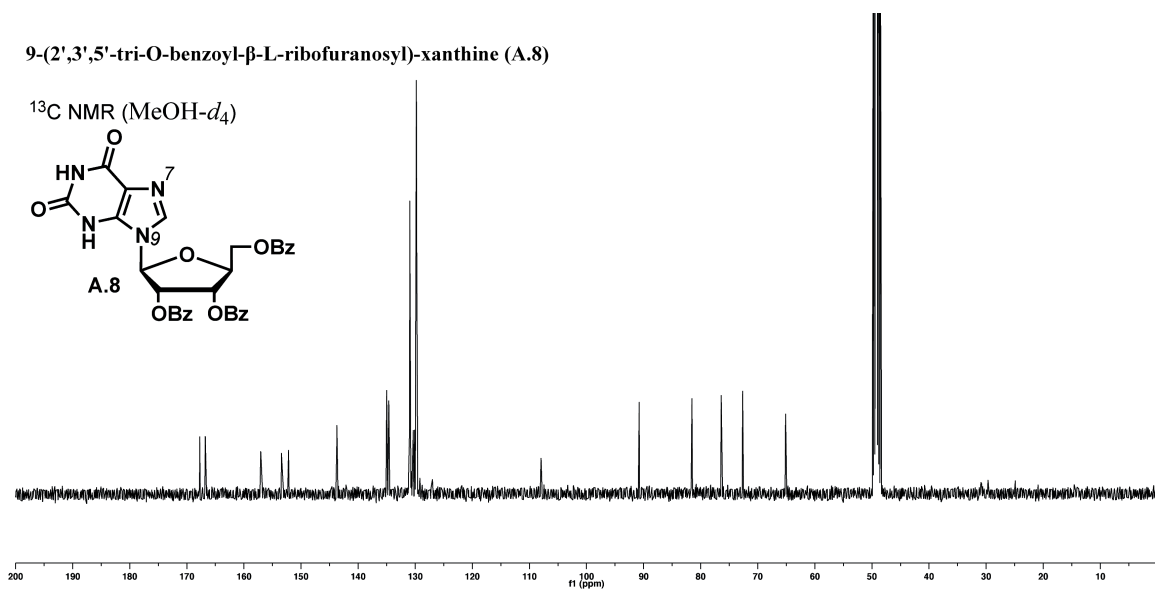
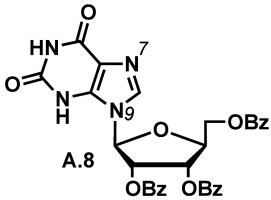
9-(2',3',5'-tri-O-benzoyl-β-L-ribofuranosyl)-xanthine (A.8)

¹H NMR (MeOH-*d*₄)



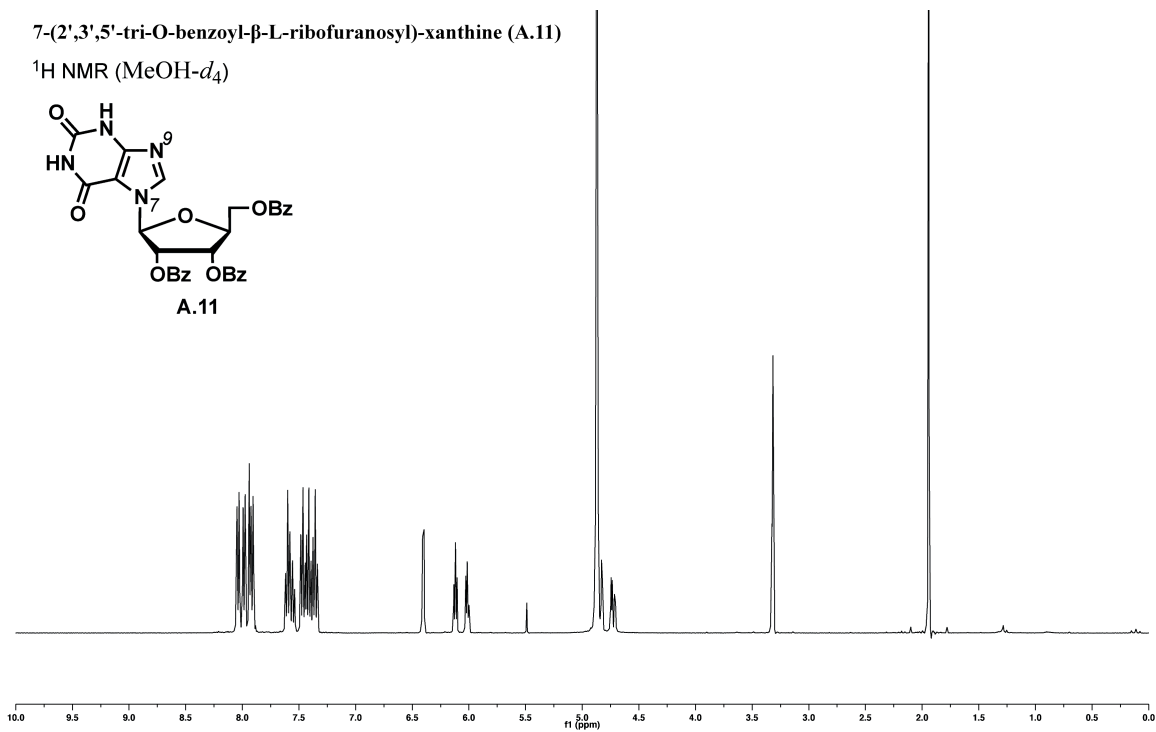
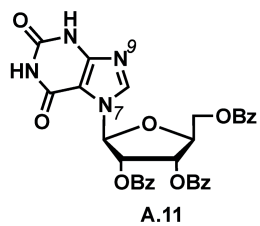
9-(2',3',5'-tri-O-benzoyl-β-L-ribofuranosyl)-xanthine (A.8)

¹³C NMR (MeOH-*d*₄)



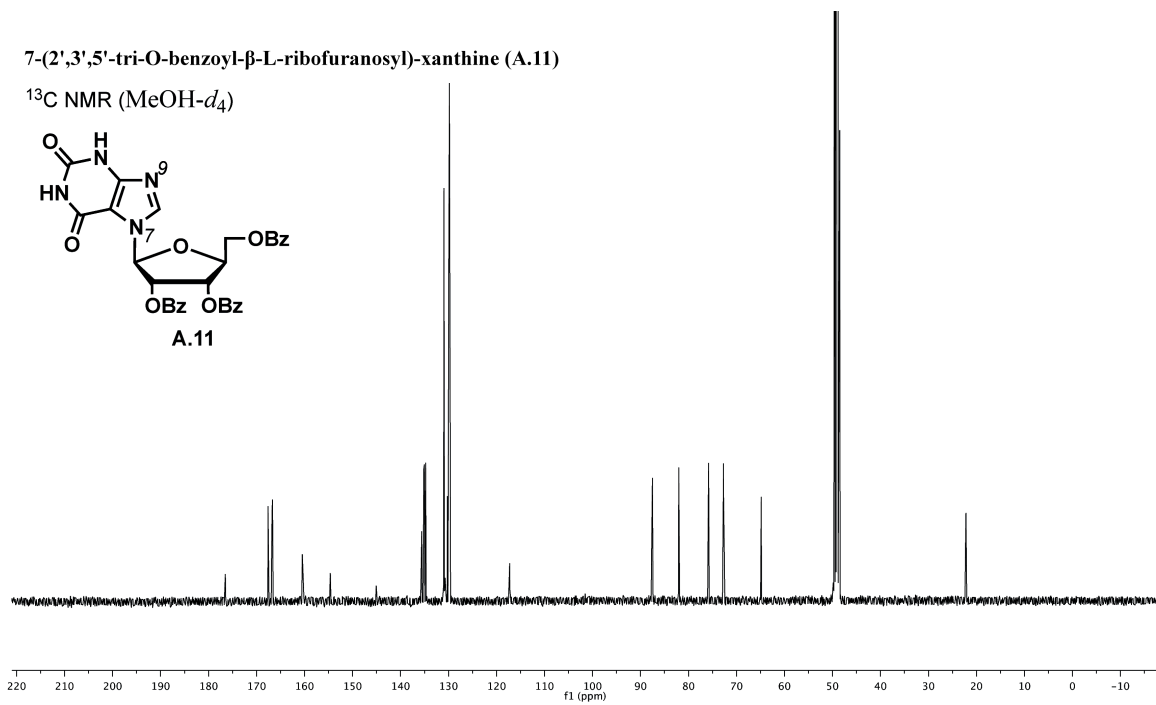
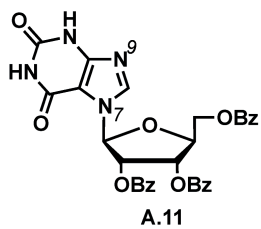
7-(2',3',5'-tri-O-benzoyl-β-L-ribofuranosyl)-xanthine (A.11)

¹H NMR (MeOH-*d*₄)



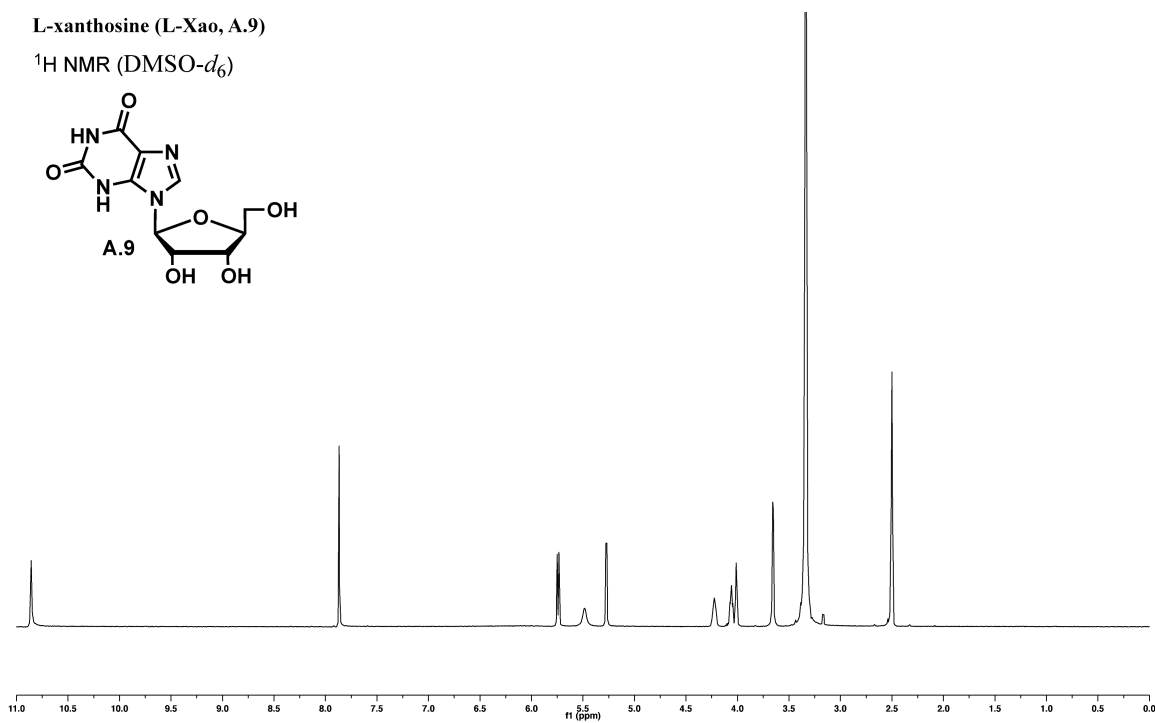
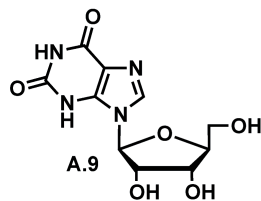
7-(2',3',5'-tri-O-benzoyl-β-L-ribofuranosyl)-xanthine (A.11)

¹³C NMR (MeOH-*d*₄)



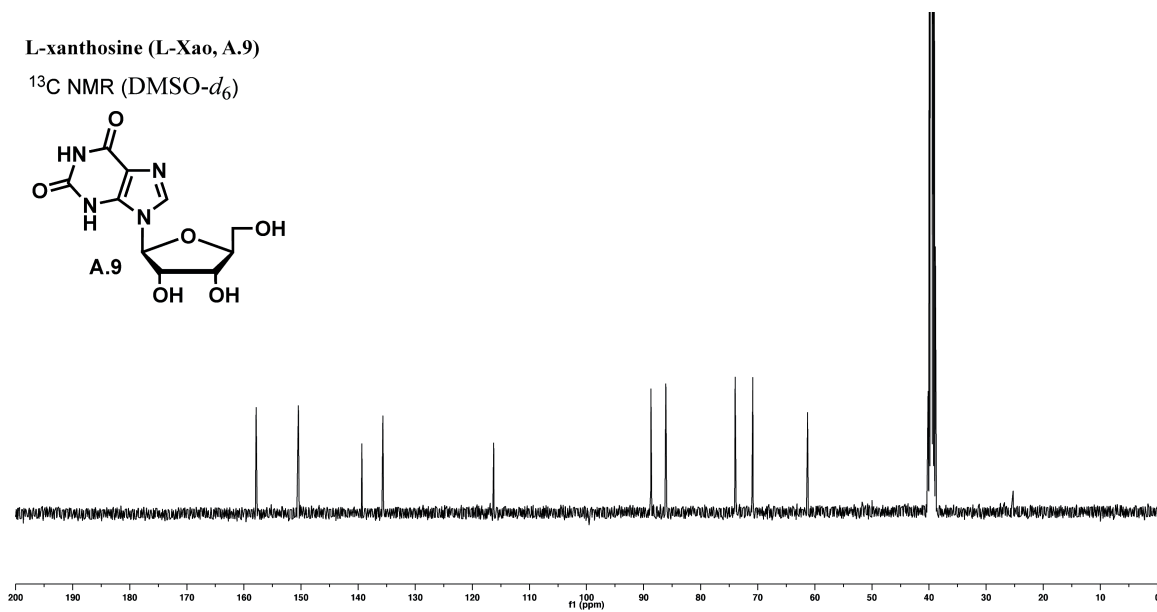
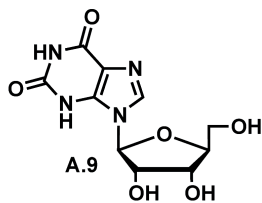
L-xanthosine (L-Xao, A.9)

^1H NMR (DMSO- d_6)



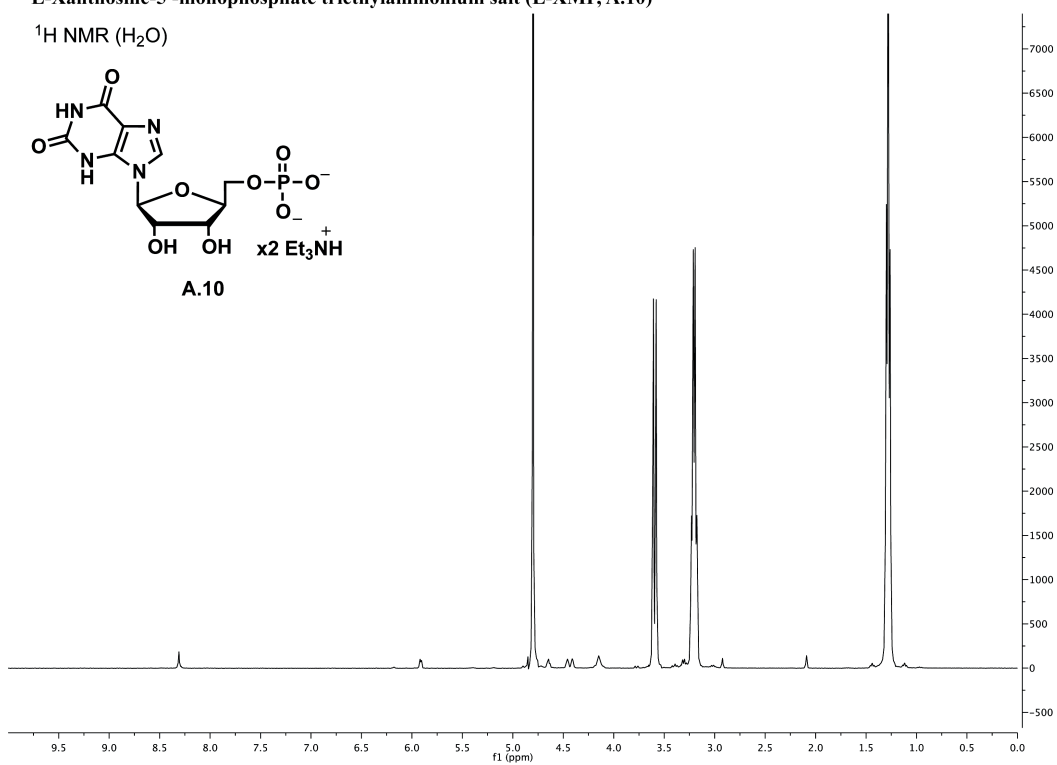
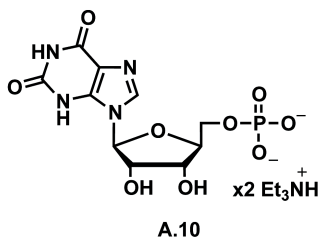
L-xanthosine (L-Xao, A.9)

^{13}C NMR (DMSO- d_6)



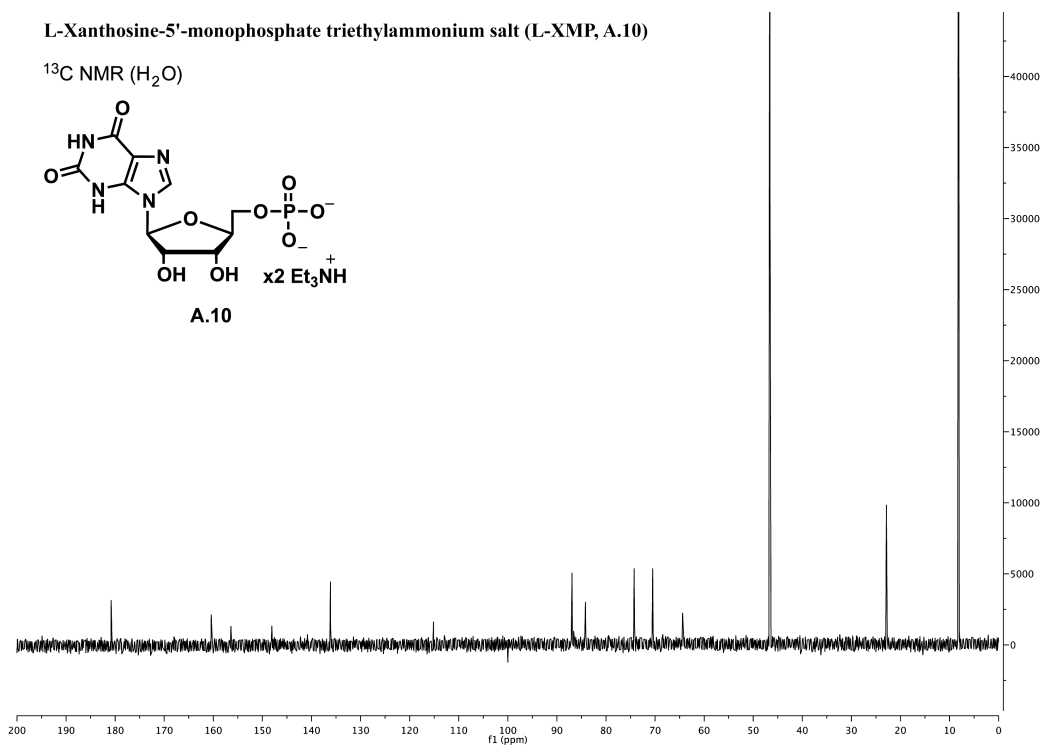
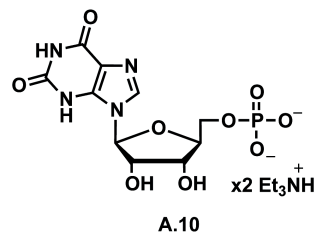
L-Xanthosine-5'-monophosphate triethylammonium salt (L-XMP, A.10)

^1H NMR (H_2O)



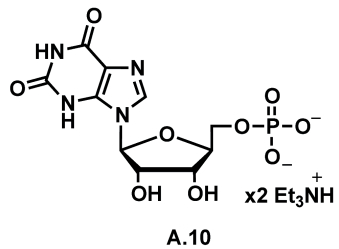
L-Xanthosine-5'-monophosphate triethylammonium salt (L-XMP, A.10)

^{13}C NMR (H_2O)

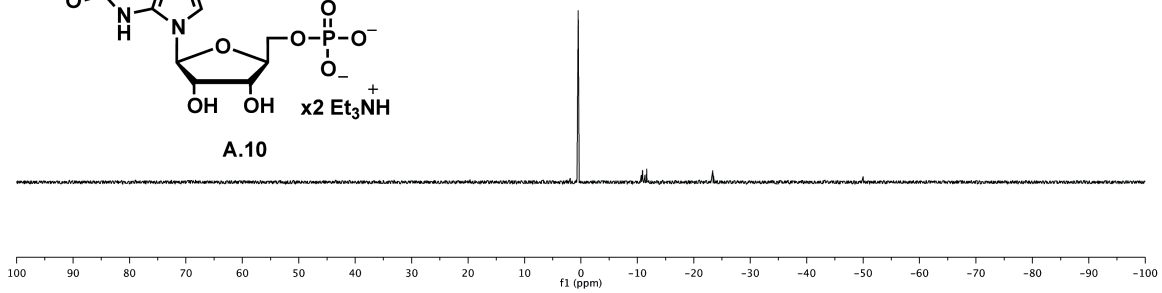


L-Xanthosine-5'-monophosphate triethylammonium salt (L-XMP, A.10)

^{31}P NMR (H_2O)

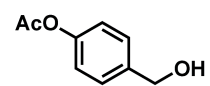


A.10

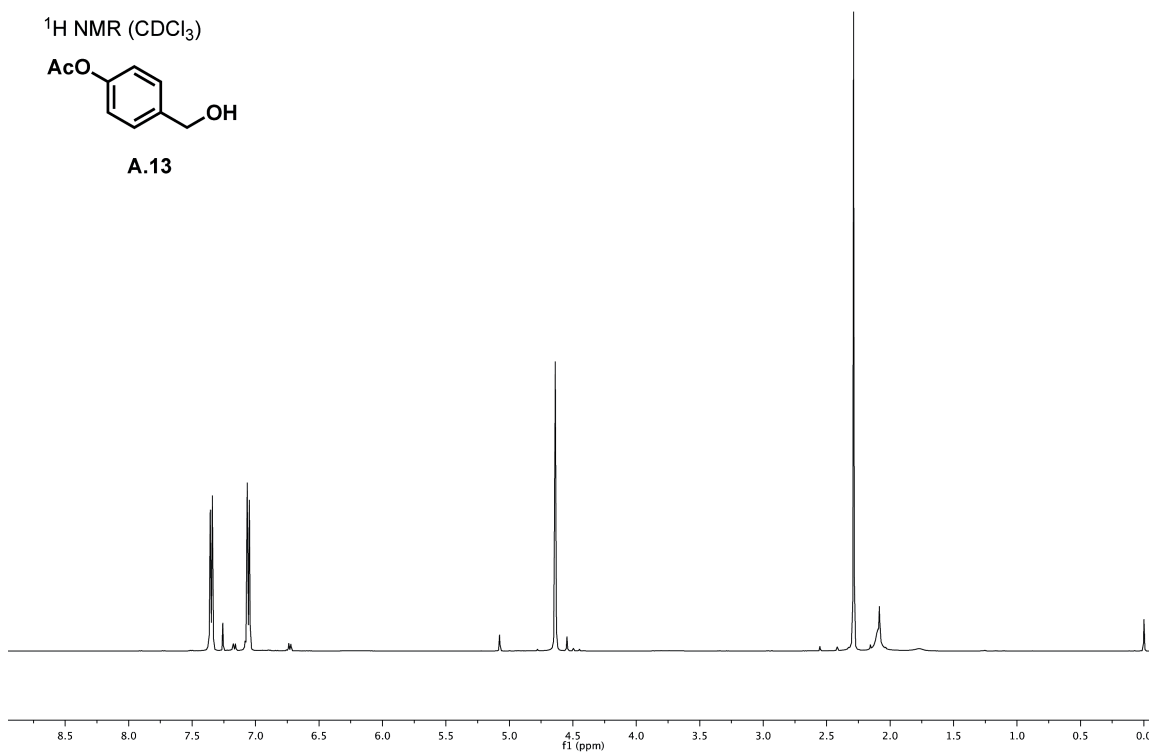


Acetoxybenzyl alcohol (A.13)

^1H NMR (CDCl_3)

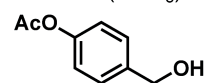


A.13

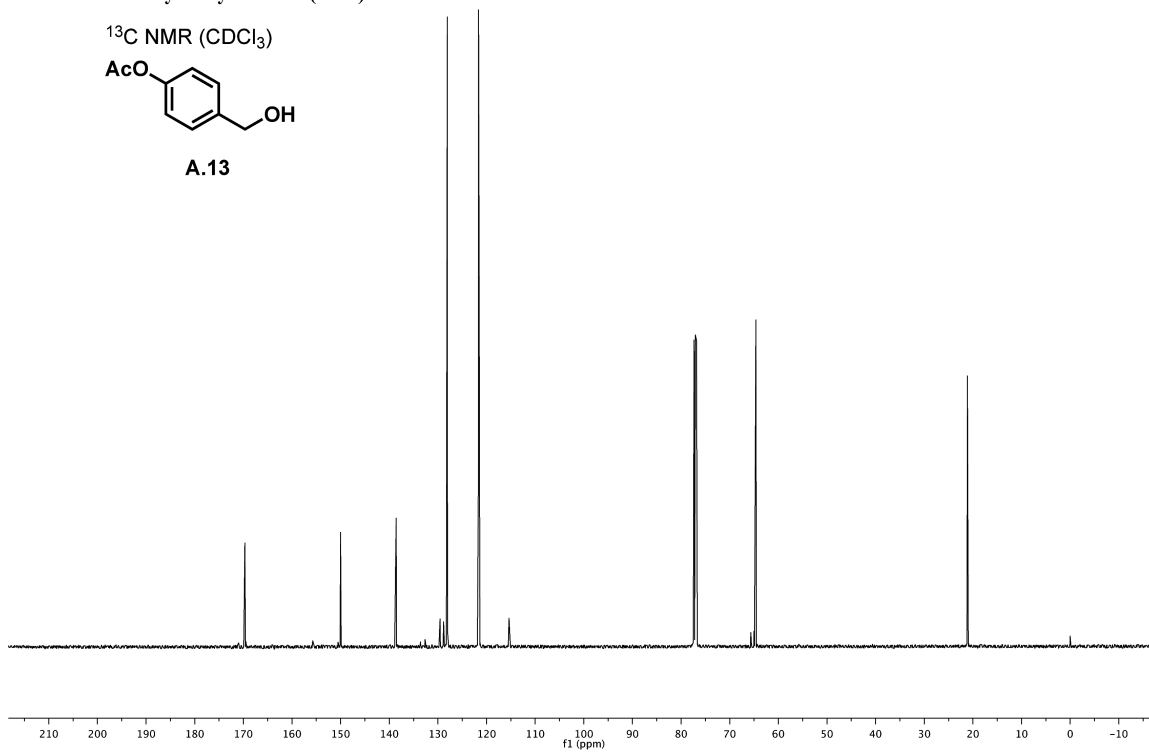


Acetoxybenzyl alcohol (A.13)

^{13}C NMR (CDCl_3)

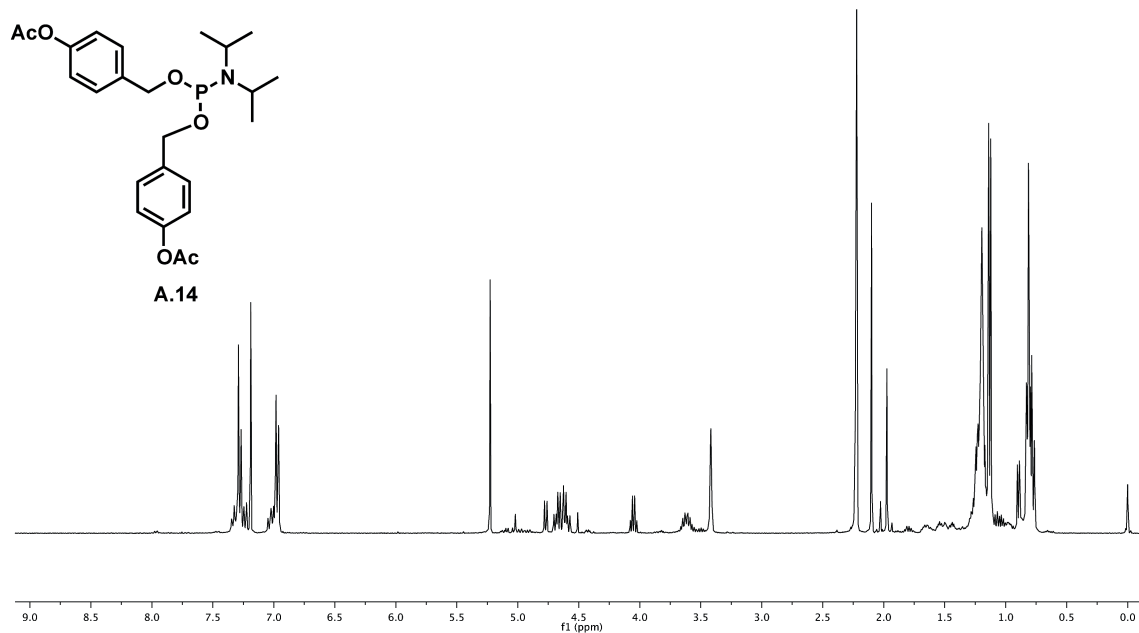


A.13



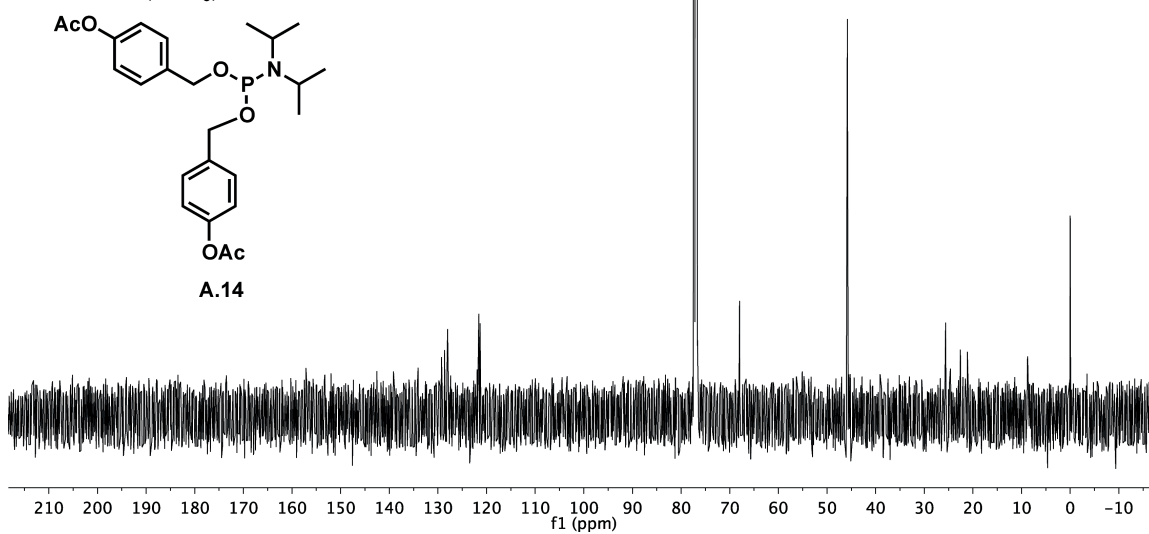
1,1-Diacetoxybenzylalcohol-N,N-diisopropylphosphinamine (A.14)

¹H NMR (CDCl₃)



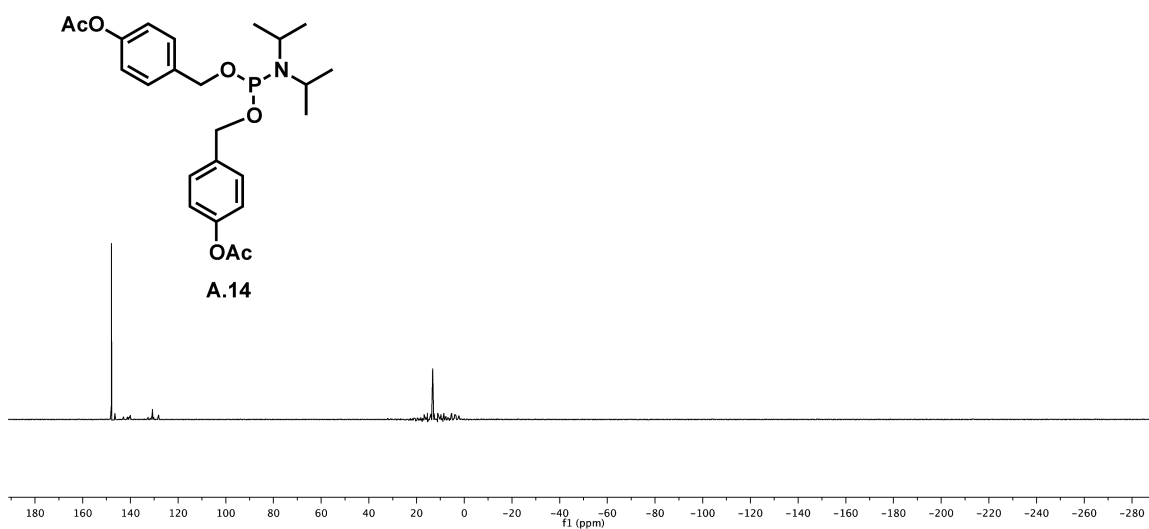
1,1-Diacetoxybenzylalcohol-N,N-diisopropylphosphinamine (A.14)

¹³C NMR (CDCl₃)



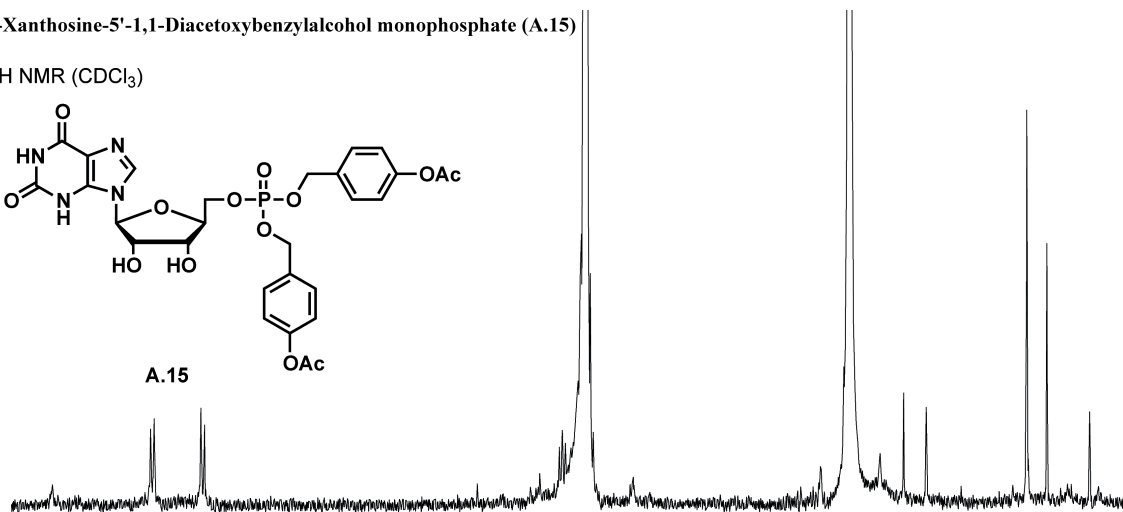
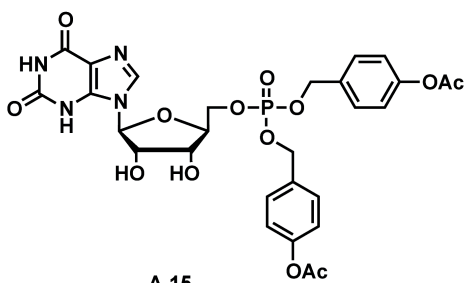
1,1-Diacetoxymethyl-4-(4-acetoxymethylphenyl)phosphinamine (A.14)

^{31}P NMR (CDCl_3)



L-Xanthosine-5'-I,1-Diacetoxybenzylalcohol monophosphate (A.15)

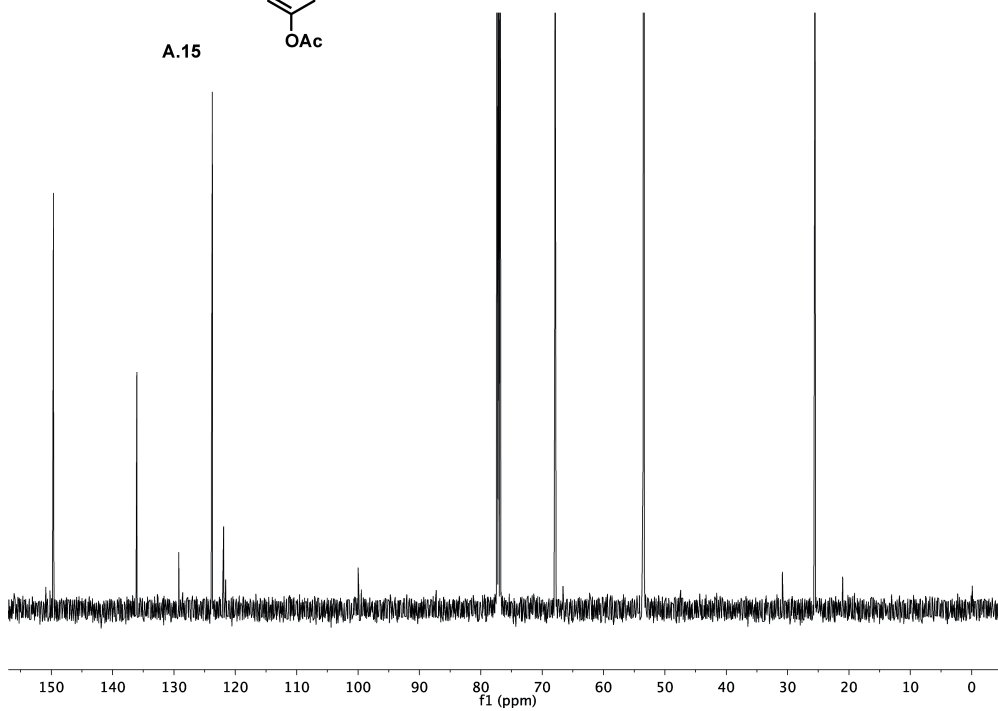
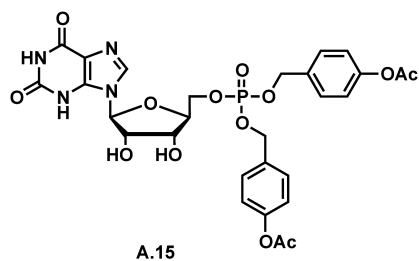
¹H NMR (CDCl₃)



8.0 7.8 7.6 7.4 7.2 7.0 6.8 6.6 6.4 6.2 6.0 5.8 5.6 5.4 5.2 5.0 4.8 4.6 4.4 4.2 4.0 3.8 3.6 3.4 3.2 3.0 2.8 2.6 2.4 2.2 2.0 1.8 1.6

L-Xanthosine-5'-I,1-Diacetoxybenzylalcohol monophosphate (A.15)

¹³C NMR (CDCl₃)



L-Xanthosine-5'-1,1-Diacetoxybenzylalcohol monophosphate (A.15)

^{31}P NMR (CDCl_3)

